CRAS 2019

Proceedings of the 9th Joint Workshop on New Technologies for Computer/Robot Assisted Surgery

March 21-22, 2019
Tower Genova Airport Hotel, Genoa, Italy

CRAS 2019

Proceedings of the 9th Joint Workshop on New Technologies for Computer/Robot Assisted Surgery

Proceedings of the 9th Joint Workshop on New Technologies for Computer/Robot Assisted Surgery, Genoa, Italy, March 21 – 22, 2019

www.cras-eu.org

ISBN 9789491857041

30° CONGRESSO NAZIONALE SPIGC

9th CRAS
Joint Workshop on Computer/Robot Assisted Surgery

ENCOURAGING YOUNG SURGEONS AND ENGINEERS

March 21 – 22, 2019 - Genoa, Italy

CRAS+SPIGC 2019

Joining Efforts – Progressing Faster

Robotic surgery is one of the most appealing fields of modern robotics. With over 3 decades history, more than 3.800 systems installed worldwide and over 600.000 robot-assisted interventions conducted per year, the field of robotic surgery is considered well established. Despite these impressive figures and increasing popularity in research labs all over the world, the list of technological advances that made it into the operating room (OR) during this last decade is fairly limited. Long expected techniques such as 3D reconstruction, motion compensation, virtual guidance and haptic feedback still have not made into the market.

CRAS seeks to give a clear view on the status and recent trends of assistive surgical robotic technologies. It aims to support and propose concrete measures to accelerate research and innovation in this field. To this end, the ninth edition of CRAS has brought engineers and surgeons together to exchange experiences, ideas and rethink the future of surgical technologies.

For the first time, the 9th edition of the Joint Workshop on New Technologies for Computer/Robot Assisted Surgery (CRAS) was completely merged with a medical conference, the National Congress of the Italian Polispecialistic Society of Young Surgeons (SPIGC). The result was a large conference dedicated to ENCOURAGE YOUNG SURGEONS AND ENGINEERS. This joint event offered a unique opportunity for multi-cultural interactions, for identifying surgical needs and potential engineering solutions, and for the establishment of new multi-disciplinary collaborations.

CRAS+SPIGC 2019 aimed at fostering the transformation of surgery into an INNOVATIVE, INTERACTIVE, TECHNOLOGICAL and EDUCATIONAL process, stimulating discussions about this vision through joint sessions, round-tables and hands-on demonstrations of the latest research prototypes and technological innovations.

Location

Tower Genova Airport Hotel
Via Pionieri e Aviatori d'Italia, 44
16154 Genova, Italy

Organization Secretariat

Pro.Forma
Via Baroni, 2/3 s.d.
16129 Genova, Italy

Tel. +39 010 59 54 382
www.pro-forma.org
info@pro-forma.org

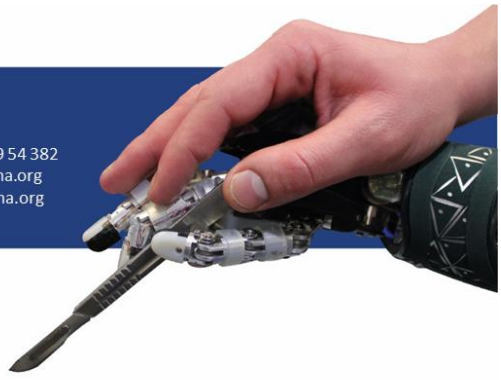

With the support of:

OSPEDALE POLICLINICO SAN MARTINO · iit ISTITUTO ITALIANO DI TECNOLOGIA · UNIVERSITÀ DEGLI STUDI DI GENOVA · REGIONE LIGURIA

Venue

The CRAS+SPIGC 2019 joint conference was held at the Tower Genova Airport Hotel, in Genoa, Italy.

Tower Genova Airport

Hotel & Conference Center

Via Pionieri ed Aviatori D'Italia, 44

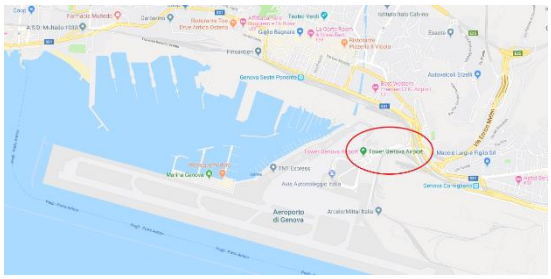

Tower Genova Airport Hotel & Conference Center is conveniently located near the airport and the city, 6 km from the historic center and 15 minutes' walk from the Marina di Genova.

Genoa

Genoa is the capital of Liguria and the sixth largest city in Italy. It is one of Europe's largest cities on the Mediterranean Sea and the largest seaport in Italy. Genoa has been nicknamed "la Superba" due to its glorious past and impressive landmarks. Part of the city's old town is included in the World Heritage List (UNESCO). The city's rich art, music, gastronomy, architecture and history allowed it to become the 2004 European Capital of Culture. It is the birthplace of Cristoforo Colombo. Genoa is located in the Italian Riviera, near other major Italian tourist destinations such as Portofino and the Cinque Terre. It is also a short train ride away from Milan, Turin, Pisa and Florence.

(Adapted from *Wikipedia*)

CRAS+SPIGC 2019 Joint Conference Chairs

Leonardo Mattos
Dept. of Advanced Robotics
Istituto Italiano di Tecnologia
Via Morego 30
16163 Genoa, Italy

Davide Pertile
Oncologic Surgery Unit
Ospedale Policlinico San Martino
Largo R. Benzi 10
16132 Genoa, Italy

Stefano Scabini
Oncologic Surgery Unit
Ospedale Policlinico San Martino
Largo R. Benzi 10
16132 Genoa, Italy

Domenico Palombo
Dipartimento di Scienze Chirurgiche e Diagnostiche Integrate
Università degli Studi di Genova
Viale Benedetto XV, 6
16132 Genoa, Italy

CRAS 2019 Co-Chairs

Paolo Fiorini
Università di Verona
Computer Science Department
Ca' Vignal 2
37134 Verona, Italy

Emmanuel Vander Poorten
University of Leuven
Dept. of Mechanical Engineering
Celestijnenlaan 300B
B-3001 Heverlee, Belgium

CRAS 2019 Organizing Committee

Salih Abdelaziz
LIRMM - Université de Montpellier

Alperen Acemoglu
IIT

Kaspar Althoefer
Queen Mary University of London

Christos Bergeles
UCL

Gianni Borghesan
KU Leuven

Alicia Casals
IBEC

Zhuoqi Cheng
IIT

Gastone Ciuti
SSSA

Giulio Dagnino
ICL

Jenny Dankelman
TU Delft

Helge Wurdemann
UCL

Brian Davies
ICL, IIT

Elena De Momi
POLIMI

Kathleen Denis
KU Leuven

Nikhil Deshpande
IIT

Giancarlo Ferrigno
POLIMI

Fanny Ficuciello
Univ. Napoli

Paolo Fiorini
Univ. Verona

Ioannis Georgilas
University of Bath

Edward Grant
NCSU

Yassine Haddab
LIRMM - Université de Montpellier

Nabil Zemiti
LIRMM - Université de Montpellier

Matteo Laffranchi
IIT

Chao Liu
LIRMM – CNRS

Leonardo Mattos
IIT

Evangelos Mazomenos
UCL

Arianna Menciassi
SSSA, Pisa

Sara Moccia
Università Politecnica delle Marche, IIT

George Mylonas
ICL

Ilana Nisky
Ben-Gurion Univ

Sebastien Ourselin
UCL

Veronica Penza
IIT

Loredana Zollo
Università Campus Bio-Medico di Roma

Benoit Herman
UCLouvain

Tim Horeman
TU Delft

Pierre Jannin
Université de Rennes

Jelizaveta Konstantinova
Queen Mary University of London

Philippe Poignet
LIRMM - Université de Montpellier

E. Vander Poorten
KU Leuven

Ferdinando Rodriguez Y Baena
ICL

Benoit Rosa
ICube, Strasbourg

Bruno Siciliano
Univ. Napoli

Danail Stoyanov
UCL

Program

In this joint conference, all science and engineering presentations from CRAS were embedded into closely related medically oriented sessions. The session topics included:

- Minimally invasive surgery
- Robotic surgery
- Surgical staplers and suturing technologies
- Trauma and resuscitation
- Endoscopy and endoscopic surgery
- Microsurgery
- Endovascular surgery
- Rehabilitation and enhanced recovery after surgery
- Imaging and diagnosis
- Health Technology Assessment (HTA)
- High energy surgical devices
- Surgical training
- Tracers, surgical guidance and augmented reality
- Transplantation and regenerative medicine
- ''Low cost" technologies
- New technologies, novel methods and future applications
- New technologies demonstrations and competition

For details on the CRAS+SPIGC 2019 conference program, please refer to CRAS website

https://www.cras-eu.org/cras-2019/program.html

Open-Access License Information

CRAS 2019 Abstract index

VRViz: Native VR Visualization of ROS Topics

J. O'Neill[1], S. Ourselin[1], T. Vercauteren[1], L. da Cruz[2]*, and C. Bergeles[1]*,

[1]*School of Biomedical Engineering and Imaging Sciences, King's College London,*

[2]*Moorfields Eye Hospital* **Equal Contribution*

christos.bergeles@kcl.ac.uk

INTRODUCTION

With Virtual Reality (VR) hardware becoming readily available, the promise of unparalleled data visualization and immersion using VR is coming within reach. Further, the Robot Operating System, or ROS [1], has matured to a point where it is considered key to the development of robotic systems, including simulation and sensor processing. In this paper we present our openly accessible framework to introduce the ROS-based 3D models of a robot into an active VR environment, therefore merging the advantages of the breadth of tools that ROS offers on kinematics and simulation with the immersion that VR offers. We anticipate that our tool can offer key insights during the robot design evaluation stage, as it provides the possibility for the robot to interact with its surroundings, while providing the operator with a realistic overview of its visual or ergonomic considerations. There have been several attempts to bring the benefits of virtual reality to the ROS framework, however these either depend on obsolete hardware [2] or require the use of a separate PC running Windows [3] in order to use the Oculus drivers on the Windows computer. We present here an open source ROS node which provides visualization of ROS topics in virtual environment, with similar functionality to RViz while running natively on Ubuntu.

MATERIALS AND METHODS

The software is written in C++ using OpenGL. VRViz depends on Steam & SteamVR being installed, which are freely available from Valve Corporation. Linked dependencies include OpenVR and SDL2, which are included in the repository as catkin libraries to match the ROS catkin ecosystem. The VRViz Node itself extends an example class in order to ease integration of updates to the OpenVR SDK, which is useful as the OpenVR SDK is still under active development. The software is available open sorce on GitHub at https://github.com/RViMLab/vrviz.

VRViz is under active development, and currently supports the following message types:

- **Image:** Stereo or normal image;
- **Point Cloud:** Colored points in 3D space;
- **Robot Description:** URDF description, including 3D meshes;
- **Transforms**: Display axes for transformations;
- **Visualization Markers:** shapes, text & meshes.

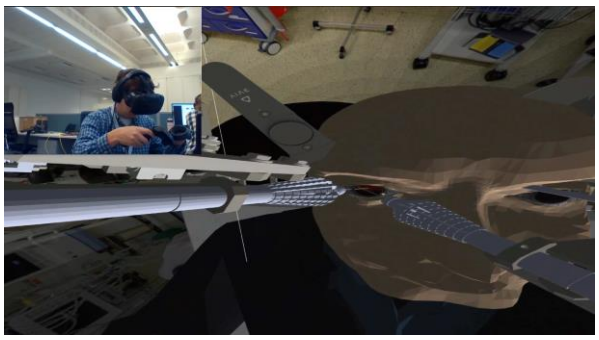

Figure. 1. Preliminary design-stage retinal surgery robot being manipulated and visualized in virtual reality. The inset shows the user, and the large view shows the left eye image sent to the headset.

For the 3D interaction in the virtual world, the "Ground" of VR space connected to ROS space. This world coordinate frame can be manipulated with buttons on the Steam-VR wand to explore large scenes or when seated but this can cause some disorientation. The user can also walk around the scene, and the buttons and position and orientation of the VR-headset and VR-wands poses are published back to ROS as transform messages to be used for control, with millimeter-level accuracy. The size of the 3D world is scalable from ROS→VR, to allow both large or small scenes to be comfortably explored.

As a test case, the authors used a model of a retinal surgical system currently being designed by the Robotics and Vision in Medicine Lab and Moorfields Eye Hospital [4]. This model was converted from SolidWorks into ROS using the standard URDF format. Further context, such as the surrounding surgical suite and the operating table, was also added. Kinematics nodes were created for every robot joint, enabling the manipulation of a robot designed in Solidworks via ROS in VR. Once in ROS, the robotic system was evaluated in 3D by both the engineers designing the system and the clinicians who will ultimately use the system.

The virtual reality system was then further extended by adding a simple retinal surgery game and used for outreach events. The system was shown to the general public at New Scientist Live, a science exposition in London. The system was also demonstrated to potential patients at the UK Macular Society's London Conference, providing an opportunity for the patient community to get a first understanding of scientific research and development in robotics.

In order to demonstrate the adaptability of the system, two other robots were also tested with the system. The Turtlebot [5] is a widely used mobile robot which is well supported in ROS. This was used running in Gazebo, a physics simulator which works with ROS. A full body surgical robot which is under development, CORVUS [6], was used with inverse kinematics to show the motion and dexterity of the robot with an operating table.

RESULTS

The virtual reality system with the retinal surgical robot, shown in Figure 1, received positive feedback both from the engineers designing the robot, as well as from the clinicians who were advising on the robot's design.

Figure. 2. Members of the public interacting with the VRViz demo at New Scientist Live.

The outreach event to the general public at New Scientist Live is shown in Figure 2. This event received positive feedback from most of the eventgoers. However, it should be noted that very young children found the virtual reality unsettling, and some users lacked good vision in both eyes due to medical issues which reduced the value in the 3D stereoscopic effect. This was also true among many members of the Macular Society, however the ability to move around in 3D still provided enough depth cues to those lacking stereo vision that they were able to get some value out of the demo.

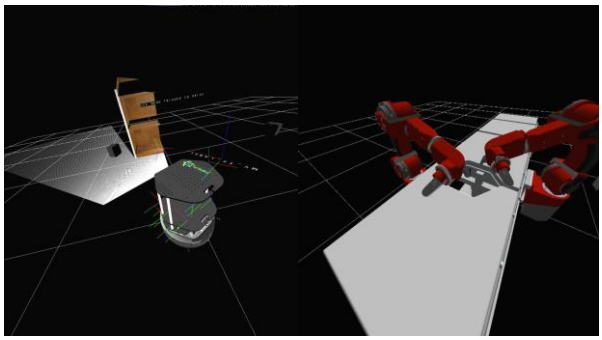

Figure. 3. Left: Turtlebot simulated in Gazebo, being visualized in virtual reality. **Right:** CORVUS full body surgical robot being controlled in virtual reality.

The additional robots tested can be seen in Figure 3. The Turtlebot and a point cloud it is scanning of a virtual environment are shown on the left, and the CORVUS robot can be seen on the right where the two arms are following the position of the wands.

CONCLUSION AND DISCUSSION

The VRViz node provides a significant benefit to engineers who are already using ROS for their development of robots for medical or other purposes. The ability to run natively in Ubuntu allows a lower barrier to entry than earlier systems, and the open source nature of the software means that additional or custom features can easily be added. Future work includes a more detailed user study including evaluation by clinicians.

An additional benefit of the system is providing an entertaining and educational outreach tool with minimal additional effort once the system is set up. This can allow the valuable research into medical robotics to be shared with a wider audience to elicit feedback and keep target markets appraised of design progress prior to the construction of a physical prototype.

The VRViz software should work with any headset supported by both OpenVR and Ubuntu, however the authors have only tested with a standard Vive headset and therefore cannot make any claims beyond that. As the software is still in development there are many opportunities for further work, including extending support for more ROS messages and testing the software with different robot designs. We welcome contributions from interested researchers in what we hope can become a useful platform for our community.

The research was funded by the NIHR Invention for Innovation Programme (II-LB-0716-20002). The views expressed are those of the author(s) and not necessarily those of the NHS, the NIHR or the Department of Health and Social Care.

REFERENCES

[1] M. Quigley, et al. ROS: an open-source robot operating system. In *ICRA workshop on open source software*, volume 3, page 5. Kobe, 2009.

[2] oculus_rviz_plugins: Oculus plugins for RViz [online] Available: https://github.com/ros-visualization/oculus_rviz_plugins.

[3] D. Whitney, et al. "Comparing Robot Grasping Teleoperation across Desktop and Virtual Reality with ROS Reality." *Proceedings of the International Symposium on Robotics Research*. 2017.

[4] A. Mablekos-Alexiou, et al. "Requirements Based Design and End-to-End Dynamic Modeling of a Robotic Tool for Vitreoretinal Surgery." *ICRA*. IEEE, 2018.

[5] Garage, Willow. "Turtlebot." *Website: http://turtlebot.com* last visited 2018

[6] J. O'Neill and T. Kowalewski. Online free anatomy registration via non-contact skeletal tracking for collaborative human/robot interaction in surgical robotics. *ASME Journal of Medical Devices*, 8(3), 2014.

Calibration of Optical See-Through Head Mounted Display for Augmented Reality Surgery

Nadia Cattari[1,*], Umberto Fontana[1,2], Fabrizio Cutolo[2], Sara Condino[2], Mauro Ferrari[1], Vincenzo Ferrari[1,2]

[1]*EndoCAS Center, Department of Translational Research and New Technologies in Medicine and Surgery, University of Pisa, Italy*

[2]*Department of Information Engineering, University of Pisa, Italy*

[*]*nadia.cattari@endocas.unipi.it*

INTRODUCTION

The growing availability of new medical imaging modalities together with the need to reduce the invasiveness of surgical procedures, has encouraged the research for new 3D visualization modalities of patient-specific virtual reconstructions of the anatomy that could act as a surgical guidance or tool for surgical training. In this context, Augmented Reality (AR) system based on head mounted displays (HMDs), such as Optical See-Through (OST) HMD, offer the most ergonomic solution, as they intrinsically provide the user with an egocentric and natural viewpoint and for this reason are deemed as the most efficient solution for those tasks manually performed under user's direct vision [1-4]. The introduction of such technology in the basic surgical workflow could remarkably improve the surgical outcomes, as it could lead to reductions in surgery times and improvements in surgical accuracy, reducing trauma to the patient.

Several attempts in this direction have already been done at the EndoCAS Research Center, where the Microsoft HoloLens have been used to develop an augmented reality training systems for two types of surgery: minimally invasive neurosurgery and orthopaedic open surgery [5, 6].

In both cases, a specific app was developed to run on the HoloLens device (Figure 1) and was used to test the suitability and efficacy of wearable AR displays as tool for surgical training. Either papers yielded positive and encouraging results.

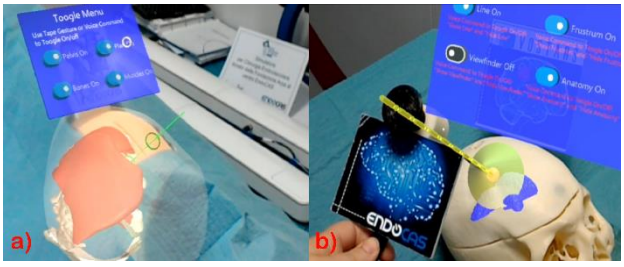

Figure 1. AR demo implementation Microsoft HoloLens based for: a) minimally invasive neurosurgery and b) orthopedic open surgery.

However, some of the problems that characterize the OST HMD systems have not yet been solved, which make them not robust enough to be used as a surgical tool on standard basis. The key problem that hinders the successful introduction of such devices in the surgical workflow pertains the correct registration between the real scene (e.g., patient anatomy) and the virtual enrichment. For a perfect combination between the real 3D world and the computer-generated 2D graphics projected onto the display, an accurate alignment between real and virtual content must be obtained on the display image plane. To this end, we must know the exact position of the user's eye within the HMD reference system and take it into account when performing the calibration of the OST display.

In this paper we suggest a solution for the aforementioned calibration based on a homographic transformation that encapsulates the eye position with respect to the display; according to Grubert et al [7], this solution can be classified as automatic closed-loop calibration method. For a more thorough analysis of the work presented in this paper, we refer the reader to our already published work [8].

MATERIAL AND METHODS

We focused on OST near-eye displays (NEDs) based on waveguides with focal plane at infinity. The common goal of all eye-NED calibration procedures is to define a proper projection matrix that yields a correct pixelwise mapping of the world points onto the display. We modeled the eye-NED as an on-axis pinhole camera, with principal point located in the middle of the display and focal length equal on both x and y axis. In our experiments, we substituted the user's eye with an internal camera.

The estimation of the projection matrix was divided into two steps: 1) world to eye/camera projection matrix and 2) eye/camera to display homography.

In the first step, we considered the eye position with respect to the world for the computation of the projection

matrix. The transformation is described by the following relation:

$$\tilde{p}_c = \lambda K_c \cdot T_W^C \cdot \tilde{P}_W \quad (1)$$

Where $\tilde{p}_c \in \mathbb{R}^{3x1}$ is the image point in homogeneous coordinates (in pixel) and $\tilde{P}_W \in \mathbb{R}^{4x1}$ is the world point in homogeneous coordinates (in mm). λ is a generic scale factor due to the equivalence of homogeneous coordinate rule. K_C is the intrinsic matrix of the eye/camera and T_W^C is the transformation matrix that transforms the world points in the eye/camera coordinate system.

The second step of the calibration is the computation of the homographic transformation between eye/camera and display in its central position. This step is essential for evaluating the correct projection matrix, as by applying this homography the correct registration between real world points and projected virtual points is recovered. The homography matrix is obtained as follows [9, 10]:

$$H_C^D = K_D \cdot (R_C^D + \frac{t_C^D \cdot n^T}{d_{c \to Waveguide}}) \cdot K_C^{-1} \quad (2)$$

As in [11], $H_C^D \in \mathbb{R}^{3x3}$ is a perspective preserving homography that depends on: the rotation matrix and translation vector between eye/camera and display coordinate system (R_C^D and t_C^D); the normal unit vector to the display waveguide (n^T); the intrinsic matrix of the display (K_D); the eye/camera distance from the display waveguide ($d_{c \to Waveguide}$). Moreover, we assumed that for a NED with infinity focus, K_D is not affected by the position of the eye with respect to the display (i.e. ideal on-axis camera model).

Thus, the final projection matrix is:

$$P_{def} = H_C^D \cdot K_C \cdot T_W^C \quad (3)$$

P_{def} can be broken down using RQ Givens decomposition as explained in [9], obtaining:

$$P_{def} = K_{eq} \cdot [R_{eq} | t_{eq}] \quad (4)$$

Where K_{eq} and $[R_{eq}|t_{eq}]$ represents the proper intrinsic and extrinsic matrices of the virtual rendering camera.

RESULTS

We assessed the accuracy of the calibration strategy by analyzing the disparities between the NED-projected landmarks and their real counterparts. For measuring the displacement, we exploited the hybrid nature of the HMD proposed in [12] and shown in Figure 2, placing a camera in arbitrary positions behind the NED to simulate the user's view.

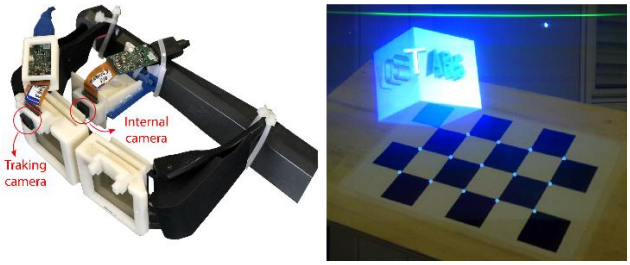

Figure 2. On the left: the HMD in detail. On the right: example of the OST view after the calibration.

The tests were performed in ten different configurations and led to the average results shown in Table 1:

Mean		Std. Dev.		Max Value		Euclidian Distance	
x axis	*y axis*	*x axis*	*y axis*	*x axis*	*y axis*	*Mean*	*Std. Dev*
0.99	1.32	1.07	1.19	4.76	5.45	1.85	1.37

Table 1. Average error values in pixels of the ten camera/display configurations.

It appears clear that the resulting errors are small, with a global average values of less than two pixels.

CONCLUSION AND DISCUSSION

In this work, we presented an automatic calibration technique for OST NED with infinity focus. We estimate the equivalent projective transformation that relates world points to image points on the display. The projective transformation accounts for the parallax between the real viewpoint and the ideal (display) viewpoint. We compensate this parallax through a homographic transformation.

Next step of our study will be the testing of our calibration method in case of a real user. To this aim, we are currently working at the integration of the device shown in Figure 2 with an eye tracking system, through which we will know the exact position of the user's eye and we will be able to insert this information in the homographic transformation.

It is worth mentioning that our method is suitable for OST systems with infinity focus; however, it would be interesting to test its functionality for visors with closer focus such as the HoloLens, whose focal plane is set at 2 meters.

REFERENCES

[1] F. Cutolo, C. Freschi, S. Mascioli, P. D. Parchi, M. Ferrari, and V. Ferrari, "Robust and Accurate Algorithm for Wearable Stereoscopic Augmented Reality with Three Indistinguishable Markers," *Electronics,* vol. 5, Sep 2016.

[2] F. Cutolo, A. Meola, M. Carbone, S. Sinceri, F. Cagnazzo, E. Denaro*, et al.*, "A new head-mounted display-based augmented reality system in neurosurgical oncology: a study on phantom," *Computer Assisted Surgery,* vol. 22, pp. 39-53, 2017.
[3] B. Fida, F. Cutolo, G. di Franco, M. Ferrari, and V. Ferrari, "Augmented reality in open surgery," *Updates in Surgery,* vol. 70, pp. 389-400, Sep 2018.
[4] F. Cutolo and V. Ferrari, "The Role of Camera Convergence in Stereoscopic Video See-through Augmented Reality Displays," *International Journal of Advanced Computer Science and Applications,* vol. 9, pp. 12-17, Aug 2018.
[5] M. Carbone, S. Condino, F. Cutolo, R. M. Viglialoro, O. Kaschke, U. W. Thomale*, et al.*, "Proof of Concept: Wearable Augmented Reality Video See-Through Display for Neuro-Endoscopy," Cham, 2018, pp. 95-104.
[6] S. Condino, G. Turini, P. D. Parchi, R. M. Viglialoro, N. Piolanti, M. Gesi*, et al.*, "How to Build a Patient-Specific Hybrid Simulator for Orthopaedic Open Surgery: Benefits and Limits of Mixed-Reality Using the Microsoft HoloLens," *Journal of Healthcare Engineering,* vol. 2018, p. 12, 2018.
[7] J. Grubert, Y. Itoh, K. Moser, and J. E. Swan, "A Survey of Calibration Methods for Optical See-Through Head-Mounted Displays," *Ieee Transactions on Visualization and Computer Graphics,* vol. 24, pp. 2649-2662, Sep 2018.
[8] U. Fontana, F. Cutolo, N. Cattari, and V. Ferrari, "Closed-Loop Calibration for Optical See-Through Near Eye Display with Infinity Focus," in *Adjunct Proceedings of the IEEE International Symposium for Mixed and Augmented Reality 2018 (To appear)*, ed, 2018.
[9] R. Hartley and A. Zisserman, *Multiple View Geometry in Computer Vision*, 2 ed. Cambridge: Cambridge University Press, 2004.
[10] P. Lothe, S. Bourgeois, E. Royer, M. Dhome, and S. Naudet-Collette, "Real-Time Vehicle Global Localisation with a Single Camera in Dense Urban Areas: Exploitation of Coarse 3D City Models," *2010 Ieee Conference on Computer Vision and Pattern Recognition (Cvpr),* pp. 863-870, 2010.
[11] F. Cutolo, U. Fontana, and V. Ferrari, "Perspective Preserving Solution for Quasi-Orthoscopic Video See-Through HMDs," *Technologies,* vol. 6, Mar 2018.
[12] F. Cutolo, U. Fontana, M. Carbone, R. D'Amato, and V. Ferrari, "Hybrid Video/Optical See-Through HMD," *Adjunct Proceedings of the 2017 Ieee International Symposium on Mixed and Augmented Reality (Ismar-Adjunct),* pp. 52-57, 2017.

Identification of Box-Jenkins Model for a Magnetically Actuated Fiber-Coupled Laser for Computer-Assisted Laser Microsurgery

Hamed Mohammadbagherpoor[1], Edward Grant[1]
[1]Department of Electrical and Computer Engineering,
North Carolina State University, Raleigh, NC
hmohamm2@ncsu.edu, egrant@ncsu.edu

I. INTRODUCTION

Since the introduction of the AESOP surgical robot in 1990 the medical field has continued to expand its use of robotics [1]. The first recorded application of a laser system in a surgical procedure was 1963, when a laser was used for retinal tears surgery [2]. The benefits obtained by using lasers in soft tissue surgeries include: (a) improved post-operative functionality, (b) decreased morbidity, (c) better homeostasis, and (d) reduce thermal damage to tissue [3]. Commonly, laser endoscopic tool positioning is controlled by the surgeon through a human computer interface, the control is open-loop and the interface is large. Giallo and Grant [4] were the first to develop a computer interface that precisely controlled a laser for tumor ablation. In [5], [6] the research in [4] was transitioned into an open-loop electromagnetically (EM) actuated laser fiber positioning system.

The focus of this research was the development of a closed-loop light laser optic fiber positioning system, one that would overcome control issues identified in [5], [6]. The research concentrated on applying an identification algorithm to the new closed-loop scanning system, one that would achieve consistent calibration and tuning. First, a dynamic model of the new closed-loop system had to be identified. Fig.1, shows a graphic of both the closed-loop laser scanning system and an image of the physical test-bed. For a clinical application the EM actuator system must be an integral part of endoscopic tool, which will lead to future design and scalability challenges. Currently, the scanning actuation system consists of four miniature electromagnetic coils and five ring permanent magnets; that are attached to a light lasers optic fiber. Magnetic actuators are robust, they operate at low voltages and can be controlled remotely. The forces used to actuate the lasers optic fiber are generated by the torque interaction that occurs within the EM fields. A photo-detector sensor was then introduced into the system. This feedback sensor measured the output position of the laser beam and compared it to a desired input value, the difference between the values was the input to the controller. Experiments with closed-loop feedback gave improved laser positioning accuracy and reduced output tracking error. An estimation algorithm was then used to: (a) identify the system's dynamic model, and (b) aid in the design of the controller. Experiments with input/output data and the system identication algorithm estimated the model of the system to be a second order system. A proportional-integral (PI) controller was then designed and tested on the closed-loop light laser scanning system test-bed. The results showed that the system operated within desired tolerances.

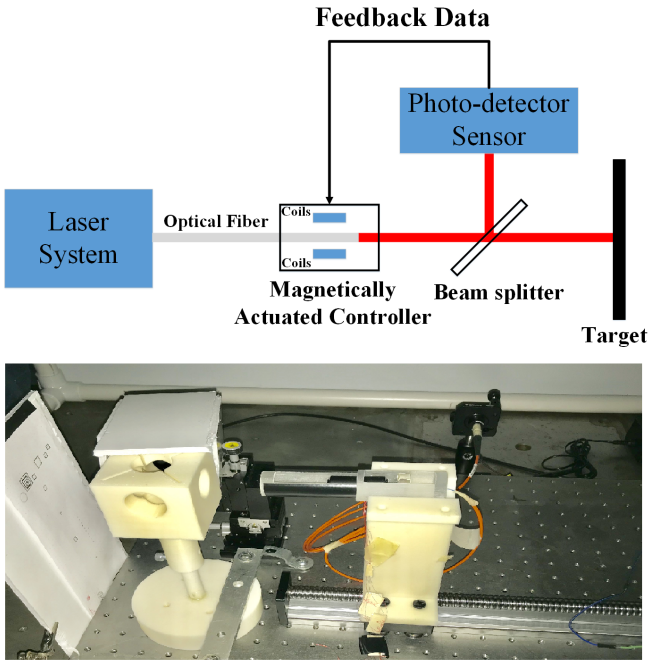

Fig. 1: The experimental test-bed of the closed-loop laser system

II. ESTIMATION OF THE MODEL

To begin the process, the system was considered to be a discrete-time linear system with input $u(k)$ and output $y(k)$, see [7].

$$y(k) = G(z)u(k) + H(z)e(k) \tag{1}$$

Where, $e(k)$ was zero mean white noise and the goal was to identify the transfer functions $G(z)$ and $H(z)$ using suitable input/output time series data. A Box-Jenkins model was used to identify the discrete model of the magnetically actuated fiber-coupled light laser. The output of the model was generated from an input/output data set, it is expressed by equ.(2),

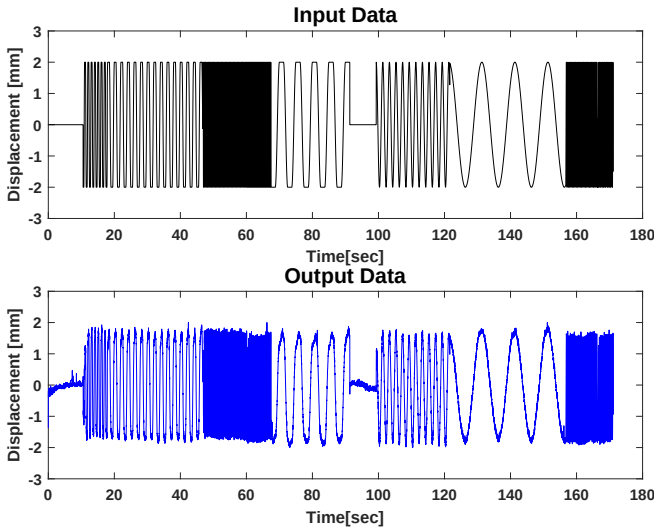

Fig. 2: An input/output data set

$$y(k) = \frac{B(z)}{F(z)}u(k) + \frac{C(z)}{D(z)}e(k) \tag{2}$$

$$\begin{aligned} F(z) &= 1 + f_1 z^{-1} + f_2 z^{-2} + \ldots + f_{n_f} z^{-n_f} \\ B(z) &= 1 + b_1 z^{-1} + b_2 z^{-2} + \ldots + b_{n_b} z^{-n_b} \\ C(z) &= 1 + c_1 z^{-1} + c_2 z^{-2} + \ldots + c_{n_c} z^{-n_c} \\ D(z) &= 1 + d_1 z^{-1} + d_2 z^{-2} + \ldots + d_{n_d} z^{-n_d} \end{aligned} \tag{3}$$

In order to identify the unknown parameters of a physical system (f_i,b_i,c_i,d_i) a recursive least square method was used. The objective function, from the Box-Jenkins model, was minimized using an input/output data set gathered by experimentation $\{u(k), y(k)\}_{k=1}^{N}$. That objective function is expressed as equ. (4).

$$J(\theta) := \min_{b_1, b_2, \ldots} \sum_{k=1}^{N} [y(k) - \hat{\varphi}^T(k)\theta]^2, \tag{4}$$

Where, $\hat{\varphi}(k)$ is a matrix of input, output, and estimated noise data, and θ is a vector of coefficients. The parameters are estimated by applying the recursive least square method to minimize the objective function. The noise model and its order are estimated by the user, so the risk of introducing error into the model is high. A common first step is to initialize the noise model as $H(z) = 1$, i.e., no noise model needs to be identified. Initially, the output of the system only includes the noise at the time of measurement and does not include noise samples from any previous time-steps. In order to accurately identify the system order the input signal was excited over a range of frequencies. The input/output data recorded was then used to train the Box-Jenkins algorithm and thereby determine the system's dynamic model, see Fig.2.

III. RESULTS

A Box-Jenkins algorithm within the MATLAB identification toolbox was used to identify the system parameters. The system proved to be second order model, equ. (5).

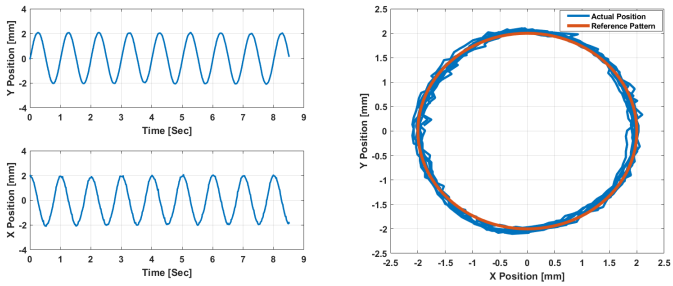

Fig. 3: Actual laser position vs. reference position for the closed-loop system

$$Y(s) = \frac{13.86s + 9.9e04}{s^2 + 27.7s + 9.889e04}U(s) \tag{5}$$

The identified model was then used to design a proportional plus integral (PI) controller for the system. The derived PI parameters controlled the system with 95% accuracy (6)

$$G_c(s) = K_p + \frac{K_I}{s} \tag{6}$$

where, $K_p = 0.08$ and $K_I = 16$. The derived controller parameters were implemented and verified on the physical test-bed. The result are shown in Fig.3. The result shows that the system is capable of track the reference signal with an accuracy of $60\mu m$.

IV. CONCLUSIONS

In conclusion, the research here used a system identification method to model a physical system, i.e., an EM actuated fiber optic system, to accurately position a light laser beam under closed-loop control. Experimentally derived input/output data, recorded over a range of frequencies, was applied to a Box-Jenkins algorithm and an identification model of the dynamic system was generated. The second order model generated by the Box-Jenkins algorithm was 95% accurate. That model was then used to design a PI controller that further improved the positioning accuracy of the closed-loop system to $60\mu m$.

REFERENCES

[1] R. J. O. Barrera, The Surgical Robot: Applications and Advantages in General Surgery, in Surgical Robotics, InTech, 2018.
[2] C. J. Campbell, K. S. Noyori, M. C. Rittler, and C. J. Koester, "Intraocular Temperature Changes Produced by Laser Coagulation*" Acta Ophthalmologica, vol. 41, no. S76, pp. 2231, May 2009.
[3] C. A. Solares and M. Strome, "Transoral Robot-Assisted CO2 Laser Supraglottic Laryngectomy: Experimental and Clinical Data," The Laryngoscope, vol. 117, no. 5, pp. 817820, May 2007.
[4] J. F. Giallo, "A medical robotic system for laser phonomicrosurgery," Ph.D. Thesis, North Carolina State University, 2008.
[5] A. Acemoglu and L. S. Mattos, "Magnetic laser scanner for endoscopic microsurgery," in 2017 IEEE International Conference on Robotics and Automation (ICRA), 2017.
[6] A. Acemoglu, N. Deshpande, and L. S. Mattos, "Towards a Magnetically-Actuated Laser Scanner for Endoscopic Microsurgeries," Journal of Medical Robotics Research, vol. 3, no. 2, p. 1840004, Jun. 2018.
[7] Y. Liu, D. Wang, and F. Ding, "Least squares based iterative algorithms for identifying BoxJenkins models with finite measurement data" Digital Signal Processing, vol. 20, no. 5, pp. 14581467, Sep. 2010.

SVEI: Smart Venous Entry Indicator

Z. Cheng[1], B. L. Davies[1,2], L. Guastini[3], D. G. Caldwell[1], L. S. Mattos[1]

[1]*Istituto Italiano di Tecnologia, Genova, Italy,*

[2]*Imperial College London, London, UK*

[3]*University of Genova, Genova, Italy*

zhuoqi.cheng @iit.it

INTRODUCTION

Peripheral IntraVenous Catheterization (PIVC) is a very common procedure for medicinal infusion and blood sampling, with over 2.7 million PIVCs taking place in the United States daily [3]. Unfortunately, this operation suffers from very low success rates, especially for children younger than 2 years old, because their veins are very small and fragile. The overall success rate for pediatric patients is reported to be around 60% [1].

During a pediatric PIVC, it is highly difficult to detect venipuncture. The traditional unassisted PIVC relies on the practitioner's haptic sensing of a small decrease in insertion force to detect this event. But this force change is small and noisy [2]. Thus, over-puncture is a common failure in pediatric PIVC.

This study presents a small device named SVEI (Smart Venous Entry Indicator) which is designed to overcome the challenge of venipuncture detection. This device can provide fast and accurate venous entry detection, and light on an LED to inform the operator at the exact moment this happens. Here, a pre-clinical experiment using a baby arm training phantom was conducted to evaluate the SVEI involving medical personnel. Details of the SVEI design and experiment are provided below.

MATERIALS AND METHODS

Figure 1(A) shows the prototype of SVEI. A concentric electrode needle (CEN) and a cannula can be directly plugged to the SVEI and use for PIVC operation. Figure 1(B) shows the configuration of SVEI. It includes a control unit (Atmega328P) which reads the electrical impedance measurements from an AD5933 impedance converter IC. Before the PIVC operation, the user needs to turn on the device by the switch. LED_PW is used to indicate whether the device is on or off. Another LED (LED_IV) in the front of the SVEI is used for indicating venous entry. After the SVEI is turned on, the control unit starts reading data from the AD5933 and processing the data continuously. When the measured value is found within the range of blood, LED_IV is lit. A battery is integrated into SVEI for power supply allowing the device to work cordless.

For the device evaluation, an experiment was conducted at the San Martino hospital, Genova, Italy. All subjects invited to this study had medical background. However, due to different job duties, some participants were not experienced in performing PIVC. Based on their experience, we divided the subjects into 2 groups: the Expert group and the Non-Expert group. The Expert group consisted of medical doctors and nurses, all of whom had >5 years experiences on PIVC operation. The subjects in the Non-Expert group included medical students, medical assistants and medical doctors, who claimed to have none or little experience in this task. This allowed us to compare the performance between two groups, and evaluate the effectiveness of SVEI for assisting different potential user groups of the technology.

Before the experiment, all subjects received verbal and written information describing the experiment and its goal. They were also asked to provide written informed consent according to recommendations from the Istituto Italiano di Tecnologia and the Declaration of Helsinki.

Then a 5 min tutorial video about the PIVC process was provided. In addition, the experimenters showed SVEI to the subjects and introduced its working principle with both verbal and video instructions.

Subsequently, each subject was required to perform 6 PIVC trials on the baby arm phantom in total. In either group, half participants were asked to perform 3 trials with an ordinary IV catheter first and then 3 more trials with SVEI. The other half participants were required to use SVEI in the first 3 trials and then use an IV catheter in the subsequent 3 trials. For each trial, we collected the result whether it is successful and the possible reason if it failed. This study also recorded the operation time for each trial. For result analysis, the time of failed trials were not considered since they are normally very long and cannot reflect the real time needed for a PIVC.

As shown in Figure 2, the experimental setup included a baby arm phantom, a pump for circulating a 0.5% saline solution inside the baby arm phantom, a SVEI, a regular 26G IV catheter (Terumo SURFLO-W), a Vein Finder (BVF-260), and a video camera for recording an overview of all trials performed during the experiment.

At the end of the experiment, the participants completed a questionnaire designed to collect data about their PIVC experience and satisfaction with SVEI.

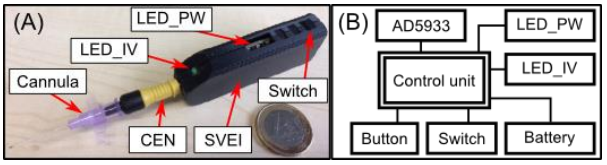

Figure. 1. (A) The prototype of SVEI; (B) the system configuration of SVEI.

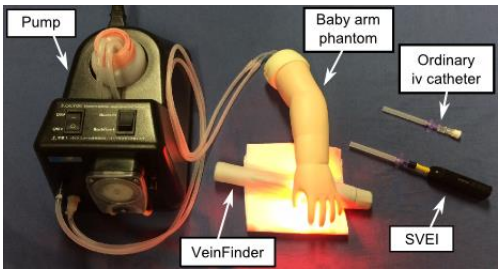

Figure. 2. (A) The 3D model of SVEI; (B) the system configuration of SVEI.

RESULTS

In total, this study had eight subjects in the Expert group and twelve subjects in the Non-Expert group. In both groups, the numbers of female subjects and male subjects were equal.

The experimental results demonstrated that the overall success rate of PIVC for all the subjects increased from 48.3% for the conventional way to 71.7% when SVEI was used. The difference between two methods was statistically significant (Welch Two Sample t-test, t = -2.6, p-value = 0.00088). Both experts and non-experts could greatly benefit from this medical device. It was noted that when SVEI was used, experts achieved 75% success rates, much higher than their performance in the conventional way (33.3%). As for non-experts, a considerably high success rate of 69.4% was achieved with SVEI compared to the success rate of 58.3% in the conventional way.

Moreover, the improvement of PIVC performance when using SVEI could also be observed through comparing the individual success rates of SVEI-assisted PIVC and unassisted PIVC. Specifically, for each subject, the numbers of successful insertions in 3 unassisted PIVC trials and 3 SVEI-assisted PIVC trials were collected respectively for comparison. The results revealed that all experts achieved better or equal results with SVEI than the traditional way. And in the Non-Expert group, 9 out of 12 subjects could also have better or equal PIVC performances when SVEI was used.

Another important evaluation metric is the first-stick accuracy. In the Expert group, the improvement of first-stick accuracy by SVEI is obvious as 5 out of 8 subjects succeeded their first trials with the assistance of SVEI. The others were successful at their second attempt. However, when they performed the PIVC insertion in the conventional way, only 2 experts could successfully insert the catheter at their first attempt. The others required three or more attempts to complete the task.

Among 12 non-expert subjects, 8 subjects succeeded the first attempts with the assistance of SVEI and 10 subjects could successful perform the PIVC insertion within 2 attempts. When trying the conventional way, 7 subjects succeed their first attempts, but only 1 more subject was successful in the second trial.

The reasons for the failed insertions in both Expert group and Non-Expert group were also collected. This results also show that SVEI has potential to effectively help both experts and non-experts to avoid catheter overshoot (OS) and undershoot (US) during the PIVC insertion. In the Expert group, the occurrence of OS and US was 8 cases and 5 cases respectively, during the unassisted PIVC trials. These numbers decreased to 2 cases and 3 cases when SVEI was used. Similar phenomena was observed in the Non-Expert group as the failed insertions due to OS reduced from 7 cases to 3 cases, failures of US reduced from 7 cases to 5 cases. In addition, 2 failed SVEI-assisted PIVC insertions were found due to miss-target (MT) by non-experts.

In addition, the experimental results revealed that the operation time for inserting catheter with the assistance of SVEI could be slightly faster than the conventional way. For experts, it took them 14.2 s (SD=3.1 s) on average to insert a regular catheter without SVEI, and 11.6 s (SD=3.6 s) to do the same task with SVEI. Also, in the Non-Expert group, the operation time was found to be 14.4 s (SD=5.2 s) in a conventional way and 10.6 s (2.9 s) for a SVEI-assisted PIVC.

The results of the SUS questionnaires showed that Experts were more satisfied with their performance with SVEI compared to their performance in the conventional PIVC way. They felt that the task becomes easier with SVEI than with only a regular catheter. As for the Non-Expert group, the subjects were overall satisfied their performances in both SVEI-assisted PIVC and unassisted PIVC. Nevertheless, they also agreed that SVEI could make the task easier for them compared to the conventional method. The satisfaction of the performance was found highly correlated to the success rates (r=0.893, p=0.0007). In addition, the questionnaire answers also revealed that SVEI was highly appreciated by both experts and non-experts under all dimensions of usability expressed by the SUS scales [4].

CONCLUSION AND DISCUSSION

The experimental results clearly show that SVEI can greatly improve the performance of pediatric PIVC for both experts and non-experts. They also confirm that PIVC operation is very difficult even for experienced medical personnel. With the help of SVEI, the challenging venipuncture detection procedure can be addressed, and thus PIVC performance of both experts and non-expert were found to be greatly improved. The future work of this study will focus on the clinical trials on patients with SVEI.

REFERENCES

[1] LA Myers, GM Arteaga, LJ Kolb, CM Lohse, and CS Russi. "Prehospital peripheral intravenous vascular access success rates in children." Prehospital Emergency Care 2013.

[2] R. Brewer. "Improving peripheral iv catheterization through robotics: From simple assistive devices to a fully-autonomous system." Thesis (Ph.D.), Stanford University 2015.

[3] M. Margaret, *et al*. "VASCULAR ACCESS MANAGEMENT 1: AN OVERVIEW." Journal of renal care 2008.

[4] Brooke, John. "SUS-A quick and dirty usability scale." Usability evaluation in industry 1996.

Convolutional network for multi-planar pose prediction in medical imaging

B. M. Maris[1], E. Ghignoni[1], P. Fiorini[1]

[1]*Department of Computer Science, University of Verona, Italy*
bogdan.maris@univr.it

INTRODUCTION

Image guided medical procedures may require the identification of the pose of a real-time acquired image, usually 2D, inside of a pre-operative 3D dataset. Once the pose is known, an instrument that was already calibrated with the imaging probe will perform the procedure precisely. The identification of the pose of a 2D image inside a 3D dataset with the highest precision and accuracy is therefore of paramount importance. The common tracking systems employed in clinical scenarios are optical and electromagnetic. Even if the accuracy of these systems is less than 1mm, they suffer of drawbacks: the optical system works on the line of sight, while the electromagnetic system can undergo interference. Moreover, they cannot track the movement of the organ of interest.

In this paper, we investigate the possibility to track a 2D medical image inside a 3D volume through the implementation of a neural network that learn the pose inside a dataset. Magnetic resonance images (MRI) of the prostate have been used. Our work took inspiration from [1], where a deep learning architecture was employed to learn the camera pose from a single RGB image. Compared with [1], our implementation makes use of different data, therefore the loss function for learning the image pose was changed, as described in the next section. The pose estimation in volumetric data using a deep learning approach was published in [2], but in a microscopic scenarios, where optical coherence tomography images were used.

The use of convolutional neural networks (CNN) in medical applications is still rare, also because of the difficulty to obtain large training sets [3].

MATERIALS AND METHODS

MRI data of the prostate from 47 patients was used. For each single patient dataset, we have performed arbitrary slicing through random translations and rotations (Figure 1). The slicing was limited to ¼ from the center of the volume to the maximum extension along x, y, z axis, respectively. We specify here that each patient dataset represents a 'scene', therefore the algorithm will train on 2D images taken from the same patient in order to learn the position and the orientation inside each 'scene'.

Since the MRI resolution of the prostate standard exam is low (512×512×35 voxels), we re-interpolated the starting volume to the resolution of 256×256×256 voxels along the directions x, y and z respectively.

The interpolation is required because slicing the volume in an arbitrary orientation should yield images with similar resolution, so that the training algorithm could work.

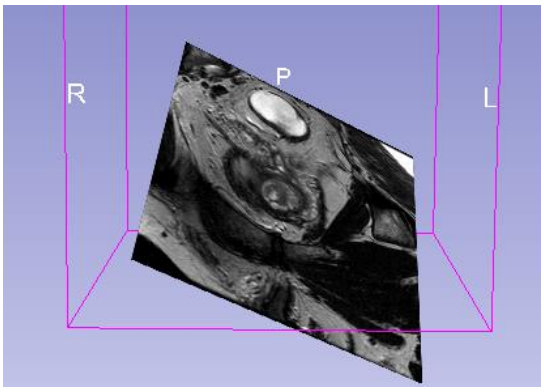

Figure. 1. A random slice from a 3D dataset (image captured with 3DSlicer).

We have used in this work the GoogLeNet Deep Learning architecture with a customized loss function, as follows. The neural network was implemented using Keras, a Python Deep Learning library and TensorFlow, which is an open source machine learning framework.

Training operations took more than one day on an Nvidia GTX 1060 graphical board. We have employed two loss functions: one based on a single parameter β, used for initialization (1), and a more precise loss (2), called reprojection error function, that fine-tunes the initial guess:

$$\mathcal{L}(I) = \|\hat{x} - x\|_1 + \beta \left\| q - \frac{\hat{q}}{\|\hat{q}\|_2} \right\|_1 \quad (1)$$

$$\mathcal{L}(I) = \frac{1}{SIZE^2} \sum_{v=1}^{SIZE} \sum_{u=1}^{SIZE} \|\pi(u,v) - \hat{\pi}(u,v)\|_1 \quad (2)$$

In these formulas, I is the image considered, x, q are the position and orientation quaternion respectively, and π is the projection function for each pixel (u, v) in the ground truth image:

$$\pi(u,v) = \begin{pmatrix} s_u & 0 & 0 \\ 0 & s_v & 0 \\ 0 & 0 & 1 \end{pmatrix} R \begin{pmatrix} u - \frac{SIZE}{2} \\ v - \frac{SIZE}{2} \\ 0 \end{pmatrix} + t \quad (3)$$

In (3), s_u and s_v are the scaling coefficients of the MRI taken from the DICOM header, R is the rotation matrix determined by the unit quaternion, t is the coordinate of the central pixel of the slices and gives the translation.

Loss function	Mean Error		Accuracy	
	Distance (mm)	Degrees	<1mm	<3˚
Training with (1)	0.85±0.32	1.82±1.3	≈90%	≈88%
Fine-tuning (2)	0.24±0.13	0.31±0.2	≈98%	≈99%

Table 1. Results of the proposed algorithm.

The 'hat' versions of the variables ($\hat{x}, \hat{q}, \hat{\pi}$) denote the predicted values.
The loss given by (1) balances between the positioning error and the orientation error, as in [1], when a suitable value for β is chosen.
By testing several values for β, we found a good estimation around $\beta = 200$.
There are two considerations to be mentioned here: the loss function (1) converges toward a global minimum that is not always optimal, meanwhile the loss function (2), based only on the reprojection error could stop in a local minimum or converges very slowly. The combination of both functions will lead to the best results.
For each patient dataset, we trained the algorithm with 11000 images, of which 0.1% were used for evaluation during the learning operations.

RESULTS

Table 1 shows the results achieved by our algorithm.
Since the loss (1) should bring the result toward a global minimum, we had to pay attention to the learning rate coefficient. We tried values ranging from 10^{-3} to 10^{-6}. The algorithm converges only with learning rates closer to the smallest limit of the interval, or even smaller.

For each patient, we evaluated the error on 100 arbitrary oriented slices that were not included in the training process. The slice positioning error was computed as the average Euclidean distance between the learned position and the ground truth (Table 1). To get the orientation error, we have transformed the quaternions in Euler angles and we computed the difference with the angles given by ground truth.

We have then averaged the results over the whole cohort of patients and we computed the standard deviation.

The last column of the table 1 reports the percentage of the images that reached an accuracy of less than 1mm in positioning and less than 3˚ in orientation.

These results confirm that the improvements achieved by the fine-tuning process are not insignificant; in very delicate cases, such as minimally invasive procedures, half a millimeter can determine the success of the intervention.

CONCLUSION AND DISCUSSION

We presented a preliminary work to compute the pose of a 2D slice inside a 3D medical image dataset. This is an innovative work that enlarge the spectrum of applications of deep learning in medical images, from mere segmentation of organs to intra-operative registration.
Future improvement that can be applied to obtain a better model are:
-change the fine-tuning formula (2) by considering not only the distance between pixels but also the differences among the intensities of pixels that belong to the same position;
- predict the pose of a slice taken from one patient, while the training was performed on several different patients;
- perform segmentation of the organ of interest and learn the pose of the slice taken from the segmentation. This will increase the speed and the precision of the algorithm.
A future iteration of this work will involve using better MRI images of the prostate (e.g. images acquired with a 3T MRI scanner) and ultrasound (US) imaging.
It would be also interesting to try our architecture with data coming from other organs (e.g. brain, breast).
The use of the pose prediction in conjunction with a tracking system may simplify the procedure of the loss function computation by substituting the initialization step with the tracked pose. The tracked pose is then refined by using only the fine-tuned loss function (2).
We envision that our work will open the way to new applications that support medical procedures and employ machine learning.
The final goal is to increase the intra-operative registration accuracy and precision from about 5 mm, as it is at the current state of the art, to 1 mm, which is desired in a high precision procedure, such as the biopsy or minimally invasive therapy of lesions smaller than 5 mm.

REFERENCES

[1] A. Kendall and R. Cipolla, "Geometric loss functions for camera pose regression with deep learning," in *Proceedings - 30th IEEE Conference on Computer Vision and Pattern Recognition, CVPR 2017*, 2017.

[2] N. Gessert, M. Schlüter, and A. Schlaefer, "A deep learning approach for pose estimation from volumetric OCT data," *Med. Image Anal.*, 2018.

[3] D. Bouget, M. Allan, D. Stoyanov, and P. Jannin, "Vision-based and marker-less surgical tool detection and tracking: a review of the literature," *Medical Image Analysis*. 2017.

Design and fabrication of synthetic, silicone-based tissue and organ models for surgical simulations

Burcin Ustbas Gul[1], Deniz Kilic Yanilmaz [2], Cem Yilmaz[3], Mehmet Bayramicli[4], and Ozge Akbulut[1]

[1] *Faculty of Engineering and Natural Sciences, Sabanci University, Istanbul, Turkey, burcinustbas@sabanciuniv.edu*

[2]*Surgitate Medikal Arge Sanayi ve Ticaret A. S., Kocaeli, Turkey, deniz.kilic@surgitate.com*

[3]*Istanbul Oncology Hospital, Istanbul, Turkey, drcemyilmaz@gmail.com*

[4]*Department of Plastic, Reconstructive and Aesthetic Surgery, Marmara University Hospital, Istanbul, Turkey, mbayramicli@marmara.edu.tr*

Corresponding author: ozgeakbulut@sabanciuniv.edu

INTRODUCTION

Lack of cadavers and organ models hinders the quality of medical education; therefore, there is a need for a reliable and sustainable training medium for ever-growing number of medical students and personnel. We design and fabricate silicone-based surgical models that are engineered to simulate mechanical responses of real organs to incision, dissection, and suturing. On these accessible platforms, surgeons-in-training can improve their skill sets and standardized evaluations of the trainees can be carried out.

Here, we present two of these platforms: i) breast model [1] and ii) microsurgery model [2].

Breast model. One in eight women experiences breast cancer in the world and the return of these women to their pre-cancer lives depends on the aesthetic and medical success of the surgery that they are going to go through. On this model, several different modern oncoplastic techniques can be practiced; a huge part of the model can be removed, the model can be sutured, and the position of the areola can be manipulated.

This model has a two-layered composite structure for dermis and epidermis layers as opposed to the single-layered torso models in the market. This structure provides better suturing retention as well as an enhanced undermining experience. Undermining, which is the separation of the dermal layer from the connective tissue, is a technique that the trainees should master.

Microsurgery model. Several disciplines such as plastic surgery, neurosurgery, and orthopaedic surgery have integrated microsurgery to their practice [3]. Long-term assessment of recovery of nerve injuries that are repaired through microsurgery indicates a faster healing process and retrieval of sensory and motor functions [4]. This model offers a standard medium for the repair of a fifth-degree nerve injury. Fresh tissues such as pig leg, human placenta, and avulsed skin are a few examples to fresh tissues that are used as practice media. Fresh tissues necessitate refrigeration and contain a high risk of transmissible diseases; hence, can be classified as biohazards and require vast amounts of effort for self-protection. Our model is designed to reflect necessary fragility, complexity, and hierarchical outlook of real tissues and offers a realistic platform for surgeons-in-training to simulate the repair of nerve injuries at their own pace. Current synthetic models in the market only consist of vessels which are embedded in a matrix.

MATERIALS AND METHODS

We have tracked a series of silicone and silicone-based composite formulations to mimic the cosmetic and mechanical properties of human tissues. Two-component liquid silicone elastomer; component A (SL-3358A) and B (SL-3358B), were obtained from KCC Corporation, Korea. Silicone oil was purchased from Sapar, Turkey (PMX200-350 CST). Cotton fibers were received from local providers. Dyes that were used in coloring were obtained from Wacker Chemie AG. The mechanical properties of the formulations for the microsurgery model were characterized via the Universal Testing Machine; the damage caused by the needle on the entry sites was assessed through scanning electron microscopy (SEM).

The design of the breast model was iterated through the feedback of expert surgeons. We used tear-drop shaped aluminum molds where, first, the inner tissue was cured, then a textile layer is employed to impart resistance to tearing during suturing. Thereafter, two outer silicone layers were applied to simulate dermis and epidermis. The areola is molded and colored separately, and attached to the breast after the curing of the outer layer. The back of the models was capped with Velcro to be attached to a wooden plane that provides four different angles of inclination. Anatomical landmarks like the clavicles and jugular notch can be marked on this plane for training purposes.

The structure of the microsurgery model was based on the human anatomy of the peripheral nervous system [5]. The model is aimed at ulnar, median and radial nerves in the upper extremity and contains a skin layer, fascia (the connective tissue layers between the skin, nerves, and the muscle layers), and the peripheral nerves (epineurium and fascicles). The simulated epineurium has an inner diameter of 3 mm with a wall thickness of 1 mm. It holds three fascicles which are 1 mm-thick composite structures that contain 0.1 wt % cotton fiber in their

formulation. Axons are excluded from the design, since on a benchtop, it would not be possible to fabricate fibers that are 1 μm in diameter.

RESULTS

We focused on the elastic modulus at the range of 3–10 MPa for the inner tissue of the breast model and optimized the mechanical properties for precise incision, epidermal undermining, suturing, and resisting suture tension after excision of a considerable mass.

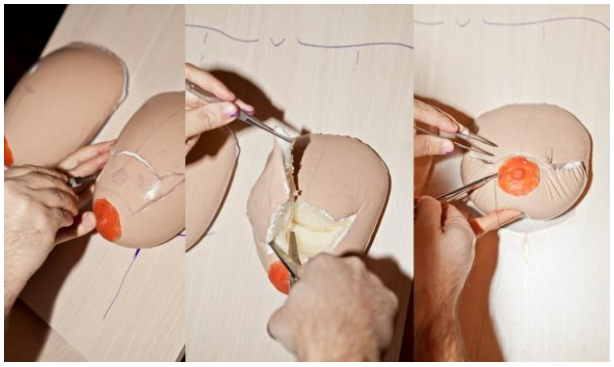

Figure 1. Simulation of batwing mammoplasty on the breast model

For the microsurgery model, mechanical properties of the formulations of silicone were tested to mimic human peripheral nerves. A formulation with 83.3 wt% silicone oil and 0.1 wt% cotton fiber was chosen to be used as nerve fascicles. Both 83.3 wt% silicone oil with cotton fiber and 66.6 wt% silicone oil without fiber provided a microsuturing response similar to that of epineurium at a wall thickness of 1 mm.

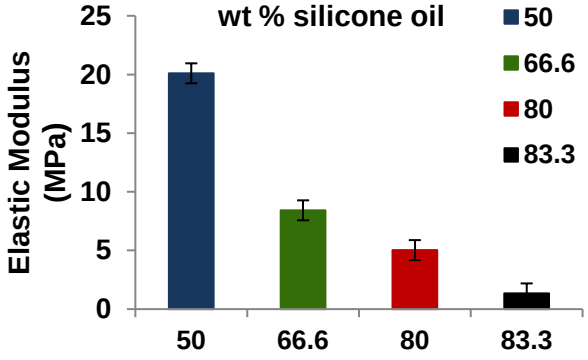

Figure 2. Comparison of elastic modulus of formulations with increasing wt % silicone oil

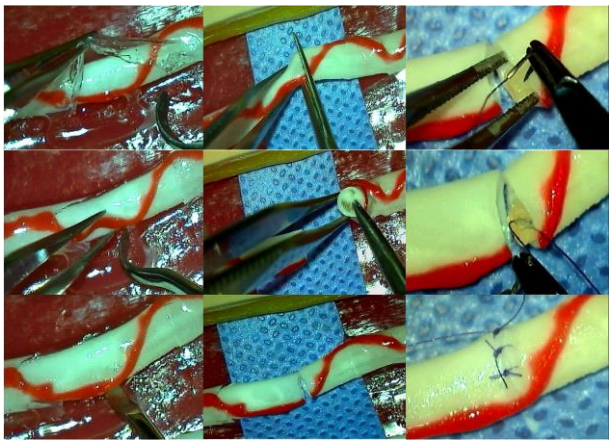

Figure 3. Simulation of repair of fifth degree peripheral nerve injury on the microsurgery phantom.

CONCLUSION AND DISCUSSION

These phantoms i) provide realistic responses to surgical interventions, ii) can be produced in a non-chemistry lab, and iii) have a potential to serve as a standardized test medium for assessing skill sets of surgeons. The surgeons can potentially improve their eye-hand coordination on these models, which in turn, may reduce the number of cadavers/animal models that are routinely used in surgical trainings.

REFERENCES

[1] Kilic D., Ustbas B., Budak E. P., Eyisoylu H., Yilmaz C., Eldem B., and Akbulut O. “Silicone-based composites as surgical breast models for oncoplasty training”, Procedia Engineering; 2016; 159: 104–107.

[2] Ustbas Gul B., Kilic Yanilmaz, D., Arslan D., Bayramicli M. and Akbulut, O. “Silicone-based simulation phantoms for peripheral nerve microsurgery”, Jour. of Plastic, Reconstructive & Aesthetic Surgery (article in press, Nov. 14, 2018).

[3] Chan W.Y., Matteucci P., Southern S.J. “Validation of microsurgical models in microsurgery training and competence: a review”, Microsurgery; 2007; 27: 494–499.

[4] Rutner T. W., Ziccardi V. B., Janal M. N. “Long-term outcome assessment for lingual nerve microsurgery”, J Oral Maxillofac Surg; 2005; 63 (08):1145–1149.

[5] Mai JK, Paxinos G. The human nervous system, United States: Elsevier, Academic Press; 2011 ISBN: 9780123742360.

Development of Different Grasp Type Handles for a Haptic Telemanipulator

E. I. Zoller[1], P. Salz[1], P. C. Cattin[2], A. Zam[3], G. Rauter[1]

{BIROMED-Lab[1], CIAN[2], BLOG[3]}, Dept. of Biomedical Engineering, University of Basel, CH
esther.zoller@unibas.ch

INTRODUCTION

In teleoperated minimally invasive laser osteotomy surgeons have to manoeuver a robotic endoscope to an accurate pose inside the patient's body such that the built-in laser can treat the target structure. The positioning of the endoscope has to be achieved within several physical limitations: the master and slave device mechanics, the anatomy of the operator's hand and wrist, and the anatomical environment at the surgical site [1]. Previous work has intensively investigated both mechanics and control algorithms of master devices (telemanipulators) and slave devices [2]. Although the handle is the part of the telemanipulator through which the user interacts with the teleoperation system, to date we have not found any detailed guidelines on how to design task-specific telemanipulator handles. However, it seems plausible that the handle design directly influences the surgeon's task performance. Therefore, the aim of this work was to develop different telemanipulator handle prototypes considering several geometric shapes and sizes. The set of developed prototypes was subsequently reduced based on different handle characteristics.

MATERIALS AND METHODS

A customized, 6 degrees of freedom, handleless lambda.6 haptic device (Force Dimension, Nyon, Switzerland) was used. While the delta-structure of the device defines the end-effector position, the attached serial links allow the rotation of the end-effector around the yaw, pitch, and roll axis (see Fig. 1).

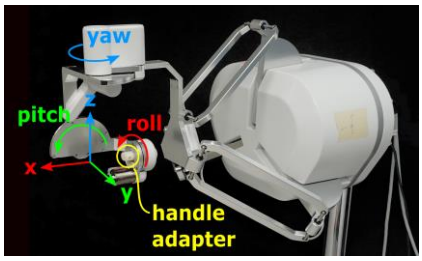

Figure 1. The lambda.6 can provide haptic feedback in 6 degrees of freedom (x, y, z, roll, pitch, yaw). An adapter at the end-effector allows mounting different handles.

In a first step, the prototype generation, eight different three-dimensional geometric shapes, all based on simple shapes such as circles, triangles or squares, were used (see Fig. 2a). For each of these shapes at least two different prototypes addressing two fundamental grasp types [3] were developed: one to be held with a precision grip and one to be held with a power grip. While for the precision grip the handle is held only with the fingers, the handle is to be held with a firm contact with both the palm of the hand and some of the fingers for the power grip (see Fig. 2b). Most geometric shapes allowed the creation of further handles by simply rotating the shape. Thus, an unequal number of prototypes was generated for each of the eight geometric shapes.

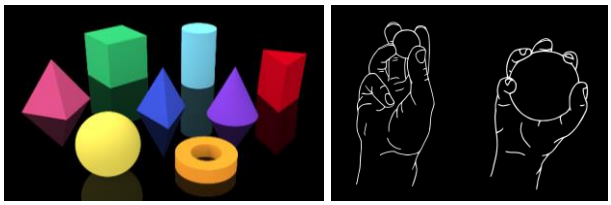

a) b)

Figure 2. a) The eight basic geometries on which the handle development was based on: square pyramid, sphere, cube, triangular pyramid, cylinder, ring, cone, and prism. b) Two basic grasp types: precision grip (left) and power grip (right).

In a second step, the prototype reduction, all resulting prototypes were mounted onto the lambda.6 using an adapter. To reduce the number of handle prototypes in a structured way, all prototypes were rated by the developers with respect to four different characteristics:

- Grasp intuitiveness, i.e. if it is clear how the handle is intended to be grasped.
- Home position ergonomics, i.e. how ergonomic the wrist and hand posture is when the handle is held at the center of the lambda.6 workspace with neutral angles and the lower arm aligned with the roll axis.
- Manipulation ergonomics, i.e. how ergonomic the wrist and hand positions are when the handle is moved throughout the workspace of the lambda.6.
- Association with everyday objects, i.e. how often objects with a similar shape are grasped in daily life.

Each handle was rated on a scale from one to five for each of the four characteristics, five being the highest score. All handles with a score of less than an arbitrary cutoff of 15 points were disregarded. Moreover, the grasp type used to hold each prototype was assessed according to the grasp taxonomy developed by Feix et al. [4]. For handles with the same grasp type, only the one with the highest score was eligible for further consideration. In a third step, the prototype refinement, all remaining handles were adapted to improve their ergonomics and grasp intuitiveness. These final adaptations included slight rotation and scaling of the prototypes, adding fingertip grooves, and filleting of sharp edges.

RESULTS

Overall, 41 different handle prototypes were developed based on 8 basic geometries in the prototype generation phase, i.e. two to nine different prototypes per geometric shape (see Fig. 3). Totally, these prototypes are held with 13 different grasp types as defined by Feix et al. [4].

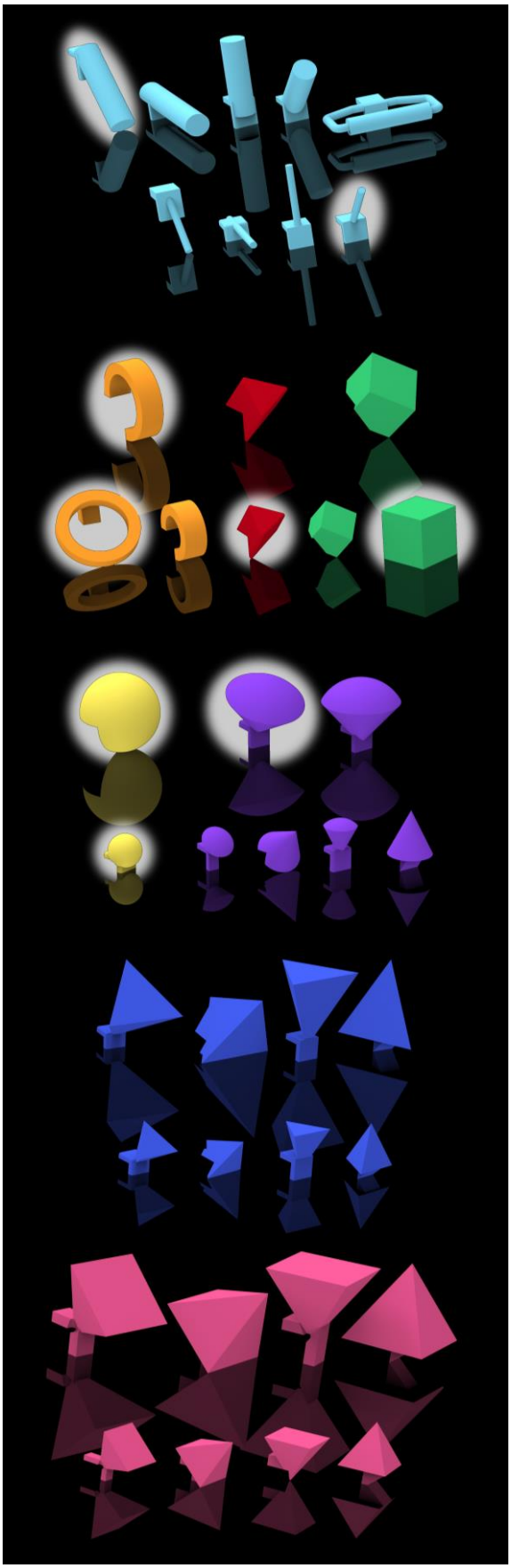

Figure 3. All 41 developed handle prototypes. The different prototypes originating from the same basic geometry are displayed in the same color and vary in size and orientation. The prototypes that were pursued further are highlighted.

Table 1 shows the results of the developers' rating of all prototypes that reached a minimum score of 15 points in the prototype reduction phase. These are also highlighted in Fig. 3. The selected nine prototypes are all held with different grasp types (five different precision grips and four different power grips) and are based on six of the original eight different geometric forms.

Grasp intuitiveness	4	5	4	4	5	3	4	5	4
Home position ergonomics	4	4	5	4	4	4	4	4	3
Manipulation ergonomics	4	3	3	4	4	4	4	3	4
Association with everyday objects	4	5	4	3	3	4	3	3	4
Total score	16	17	16	15	16	15	15	15	15

Table 1. Subjective evaluation of the preferred nine prototypes. The box coloring of the prototype renderings shows if they were designed to be held with a power grip (dark gray) or precision grip (light gray). The rated boxes are color-coded by score.

The adapted versions of the nine prototypes that resulted from the prototype refinement phase are shown in Fig. 4.

Figure 4. The final nine handle prototypes color-coded by the underlying geometric form.

CONCLUSION AND DISCUSSION

This work presents the structured development of several telemanipulator handles for different grasp types. In addition to existing work (e.g. [5]), we focused on generating handles that enforce different grasp types. This will allow us to assess which grasp types and handles are most suitable considering anatomical constraints of the human wrist and specific teleoperation tasks. Thus, this work documents a first necessary step towards task-specific guidelines on grasp types for teleoperation handle design.

REFERENCES

[1] K. Zareinia, Y. Maddahi, C. Ng, N. Sepehri and G. R. Sutherland, "Performance evaluation of haptic hand-controllers in a robot-assisted surgical system," *Int J Med Robotics Comput Assist Surg*, vol. 11, no. 4, p. 486–501, 2015.

[2] R. Muradore and P. Fiorini, "A review of bilateral teleoperation algorithms," *Acta Polytech Hung*, vol. 13, no. 1, p. 191–208, 2016.

[3] J. R. Napier, "The prehensile movements of the human hand," *J Bone Joint Surg*, vol. 38, no. 4, p. 902–913, 1956.

[4] T. Feix, J. Romero, H.-B. Schmiedmayer, A. M. Dollar and D. Kragic, "The grasp taxonomy of human grasp types," *IEEE Trans. Human-Mach. Syst.*, vol. 46, no. 1, p. 66–77, 2016.

[5] T. L. Brooks and A. K. Bejczy, "Hand controllers for teleoperation; A state-of-the-art technology survey and evaluation," JPL Publication 85-11, 1985.

Accuracy of 3D Modelling Techniques for the Human Knee

S.M. Forte[1,2], F. Tatti[2], F. Rodriguez y Baena[2]

[1]*Department of Information Engineering, University of Pisa, Italy*

[2]*Department of Mechanical Engineering, Imperial College London, UK*

s.forte1@studenti.unipi.it; {f.tatti, f.rodriguez}@imperial.ac.uk

INTRODUCTION

The use of computer-assisted orthopaedic surgery (CAOS) systems in the operating room has become more prevalent over the past 15 years [1]. As these systems increase in popularity, it is pivotal to understand the performance of key elements, and how these impact the accuracy of the overall system.

The creation of an accurate 3D model of the bone and joint is a crucial requirement for any CAOS system, and the basis for any and all surgical planning. This model can be obtained by using image-based or image-free techniques [2], [3]. Image-based techniques rely on the segmentation of pre-operative scans. Segmentation is typically done manually, which is a time-consuming process that requires technical expertise. Image-free techniques were developed to avoid this preoperative step and rely on intraoperative surface scanning and bone morphing algorithms to create a patient-specific model during surgery. Recent advances in machine learning have aided the development of novel segmentation algorithms, which may eventually enable automation of the segmentation process in image-based techniques [4].

In this work, we assessed the accuracy of digital models of a cadaveric femur obtained using three different systems (manual segmentation, a state-of-the-art machine learning algorithm and a commercial image-free surgical system), by comparing them to high resolution optical scans of the exposed femur, which is used here as the gold standard.

MATERIALS AND METHODS

Test sample and MRI scans

One cadaveric knee was used for this study. Ethical approval was obtained from the Imperial College Healthcare Tissue Bank (project R13066-3A) and the cadaveric knee was sourced from an approved supplier. The intact sample was scanned using a Siemens Spectra MRI system to obtain the images needed for the image-based procedures (Fig. 1, left).

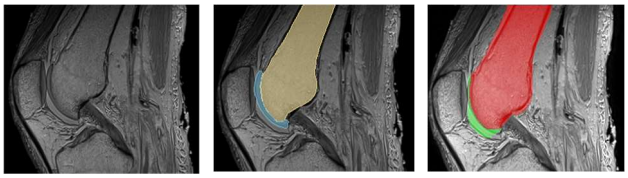

Figure 1. (*Left*) MRI scan of the cadaveric knee. (*Middle*) Manual segmentation: femur in yellow, femur cartilage in light blue. (*Right*) Automatic segmentation: femur in red, femur cartilage in green.

MRI segmentation

Manual segmentation of the femur bone and cartilage was performed in 3D-Slicer by thresholding, followed by manual adjustment (Fig. 1, middle). A 3D model of the segmented volume was then generated using the same software.

The automated segmentation was performed using the Convolutional Neural Network (CNN) architecture described in [5]. The neural network was trained to classify voxels into five categories (femur bone, femur cartilage, tibia bone, tibia cartilage, other) using 70 MRI volumes of the knee, available from the SKI10 challenge [6]. Training required approximately 41 hours on an NVIDIA Tesla K80 Graphic Processing Unit (GPU). After training, the same neural network was used to segment an MRI scan of the specimen (Fig. 1, right). The label maps obtained from the network were then converted into a 3D model using Matlab R2018a.

Digitisation using optical methods

The knee specimen was prepared for optical surface scanning by attaching it to a custom-made metal rig using bone cement and exposing the distal end of the femur by performing a vertical cut as in a Total Knee Arthroplasty (TKA).

To obtain a gold standard measurement, 12 high resolution scans of the visible part of the femur head were obtained from different positions and orientations, using a Polyga HDI C210 3D Scanner. The scans were then aligned and merged using the FlexScan3D software, available from the camera manufacturer.

The specimen was then digitised using a commercial

Figure 1. Digitisation of the cadaveric knee using the image-free system.

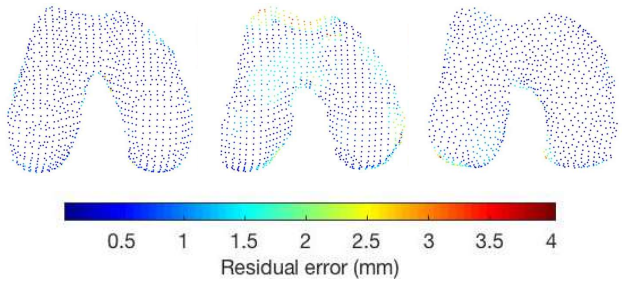

Figure 3. Residual error in mm between gold-standard and manual segmentation (left), automatic segmentation (middle), and image-free modelling (right).

image-free surgical system. To this end, a reference array was attached to the femur using bone pins and, after standard calibration, the visible part of the femur was digitised using the system's probe (Fig. 2). After this, the system's log files were downloaded to a USB drive to access the computed surface model.

RESULTS

The 3D models obtained with the different modalities were imported into Matlab as point clouds and manually cut to include only the distal end of the femur, as this was the only part accessible with the optical scanner and image-free system. Point clouds derived from the manual and automatic segmentation were uniformly down-sampled to ease comparison with the image-free method.

After this preliminary step, the point clouds obtained from manual and automated segmentation, and from the image-free system were registered to the gold standard using the Iterative Closest Point (ICP) method [7].

Fig. 3 shows the residual distance of each point from the gold standard, for the three methods analysed. To summarise the accuracy of each method, the root mean square error (RMSE) was computed for each modality and is reported in Table 1. The manual segmentation has the lowest RMSE, followed by the image-free method. The RMSE computed for the automatic segmentation is highest. Additionally, the results in Fig. 3 clearly highlight how the CNN struggled in certain regions (e.g. the intercondylar notch), where discriminating between bone and cartilage is particularly challenging.

Finally, the three techniques analysed require significantly different times to execute. While manual segmentation requires hours to complete, automated segmentation required approximately 1 minute on the same GPU used for training. The image-free procedure also executed in minutes, but required calibration of the system, and surface acquisition with the probe, pushing the overall time to about 20 min. It is important to note that the latter method does away with all preoperative imaging and related scanning time, which should be taken into account when comparing and contrasting these three different methods.

CONCLUSION AND DISCUSSION

Despite recent advances in the field, automatic segmentation of medical images remains a challenging task. Manual segmentation is confirmed here to be the most accurate method, but it requires expertise and time. Hence, in order to alleviate the task for clinicians, image-free systems have gained in popularity.

Manual	CNN	Image-free
0.4889 mm	1.1294 mm	0.7143 mm

Table 1. RMSE in mm resulting from the registration carried out between each point cloud and the gold-standard.

Our results show that the accuracy of a state-of-the-art machine-learning algorithm is still worse than with other methods, but inching towards the ballpark figure for image-free systems, albeit with the need for preoperative imaging of the patient, which would add time and cost to a navigated procedure.

It is worth noting that our algorithm was trained on a relatively small MRI dataset (70 volumes), and the use of a larger training dataset might improve performance.

These results suggest that machine-learning methods could become a powerful alternative to currently available segmentation techniques. With the attention that these methods have been receiving in recent years, and the rapid development of hardware and software tools for deep learning, the quality and speed of execution of these methods will continue to improve in the coming years, with a consequent impact on their speed, robustness, and overall accuracy.

ACKNOWLEDGEMENT

We thank Hadi El Daou and He Liu for their assistance with the cadaveric tests. This work was partially supported by INNOVATE UK under project number 103950.

REFERENCES

[1] V. Quack, S. Kathrein, B. Rath, M. Tingart, and C. Lüring, "Computer-assisted navigation in total knee arthroplasty: A review of literature," *Biomed. Tech.*, vol. 57, no. 4, pp. 269–275, 2012.

[2] N. Sugano, "Computer-assisted orthopaedic surgery and robotic surgery in total hip arthroplasty," *Clin. Orthop. Surg.*, vol. 5, no. 1, pp. 1–9, 2013.

[3] L. Nolte and T. Beutler, "Basic principles of CAOS," *Injury*, vol. 35, no. 1 SUPP, pp. 6–16, 2004.

[4] G. Litjens *et al.*, "A survey on deep learning in medical image analysis," *Med. Image Anal.*, vol. 42, no. December 2012, pp. 60–88, 2017.

[5] B. Kayalibay, G. Jensen, and P. van der Smagt, "CNN-based Segmentation of Medical Imaging Data," Jan. 2017.

[6] T. Heimann, B. J. Morrison, M. A. Styner, M. Niethammer, and S. Warfield, "Segmentation of Knee Images: A Grand Challenge," in *MICCAI 2010*, 2010, pp. 185–194.

[7] P. J. Besl and N. D. McKay, "Method for registration of 3-D shapes," 1992, vol. 1611, pp. 1611–1621.

Combining machine learning and kinematic analysis to control medical cable-driven flexible instruments

Rafael Aleluia Porto[1], Florent Nageotte[1], Philippe Zanne[1] and Michel de Mathelin[1]

[1]*ICube, University of Strasbourg, CNRS, France*
r.aleluiaporto@unistra.fr

INTRODUCTION

In the context of minimally invasive surgeries, cable-driven flexible instruments are essential tools. In robotic systems, cable transmission allows to control distal effectors from motors located at the proximal side, but non-linearities are introduced due to the interaction between the cables and the sheaths inside the endoscopic tools shafts [1]. A common effect that can be observed is the presence of a hysteresis shape between the position of the cables at the proximal side and the distal tip position.
A novel position inverse kinematic model (IKM) that is able to take into account complex non-linearities is proposed in this paper. The core concept of our method is to combine classic kinematic modeling with supervised machine learning techniques. This allows for a precise, yet efficient, IKM that can handle hysteresis effects. The positioning accuracy is improved compared to other learning-based approaches [2] with a much faster training phase as has been shown on experiments on the STRAS robotic platform.

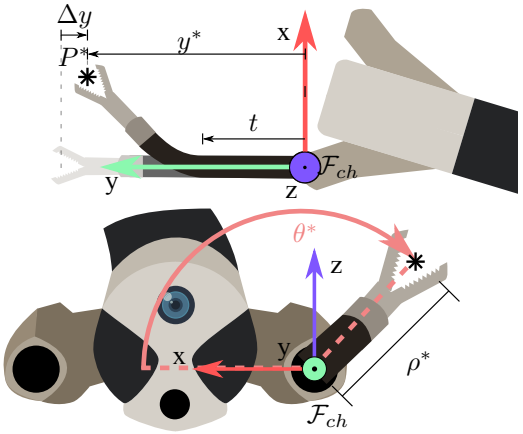

Figure 1: The cable-driven instrument passing through the channel of an endoscope. Top: top view, bottom: face view. Figure shows left channel frame, the degrees-of-freedom of the instrument and task space parameters. Adapted from [3].

MATERIALS AND METHODS

We consider a flexible instrument with 3 motorized DOFs: the bending of its distal part, the rotation and the translation of its shaft in the channel of the endoscope. The motor positions for each DOF are denoted q_{bend}, q_{rot} and q_{trans} respectively. For this system, a suitable parameterization of the task space is obtained by using the radius ρ, the depth y, which is a function of the translation t and depth difference Δy, and rotation θ with respect to the channel. These parameters can be seen in figure 1.
Our objective is to determine the motor positions allowing to achieve a reference position P^* defined in the channel frame $\mathcal{F}_{ch}$ despite the non-linearities introduced by the mechanical transmission.

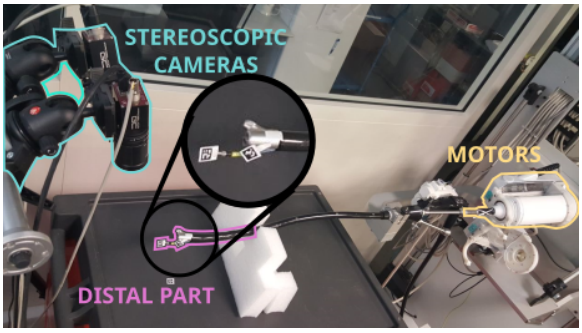

Figure 2: The experimental setup consists of the STRAS robotic platform that controls the endoscopic surgical tools and the external measurement system composed of two cameras (used only for training and validation).

The classic hypothesis used while modeling this kind of flexible system is that bending induces a constant curvature shape of the instrument [4]. On this basis, a 3-step IKM can be computed [5]. This model, however, does not represent the reality of such devices. The interaction between the cables and the sheaths coupled with the aging of the vertebrae of the distal tip can greatly impact the accuracy of the traditional IKM. Our approach to handle the imperfections of the mechanical transmission is to combine classic kinematic modeling with machine learning. The configuration of the tool is described by its geometry, but the impact of the actuators on each joint is modeled using data obtained by measurements from the system.
The distal parameters used to describe the configuration of the tool are θ, ρ, y and Δy. These parameters can be linked to the motors positions in a decoupled way [5]. The method can be described by two main steps:

Training step:

- Train the models linking the actuator space to the task space by obtaining the input/output pairs with an external sensor. The searched models are:
  1. $q_{rot} = f^{-1}(\theta)$ - inverse rotation model;
  2. $q_{bend} = g^{-1}(\rho)$ - inverse radius model;
  3. $\Delta y = h(q_{bend})$ - direct bending model;
  4. $q_{trans} = k^{-1}(y)$ - inverse translation model.

Prediction step:

- Given the reference position P^*, express the desired orientation θ^*, radius ρ^* and depth y^*.
- Find the actuator position by using the learned models in the following order: 1) $q^*_{rot} = f^{-1}(\theta^*)$, 2) $q^*_{bend} = g^{-1}(\rho^*)$ and 3) $q_{trans} = k^{-1}(y^* + h(q^*_{bend}))$.
- Apply the desired joint positions to the robotic system.

Note that the prediction step does not use any external measurement. A possible technique to obtain the models is the Extreme Learning Machine [6]. The input (ξ_i) and output space (ξ_o) for the inverse relations are defined as

$$\xi_i[k] = (\alpha[k], d^j[k]) \text{ and } \xi_o[k] = q^j[k]$$

where α is the considered distal parameter (θ, ρ or y), $d^j[k]$ is the displacement direction (coded as $+1/-1$) and q^j is the actuator position of the joint j. For the single direct relation h, the spaces are defined as

$$\xi_i[k] = (q_{bend}[k], d^{bend}[k]) \text{ and } \xi_o[k] = \Delta y[k].$$

A total of 700 positions is required to train all of the models (300 for direct and inverse bending models, 300 for the rotation model and 100 for the translation model). These data are acquired using the setup shown in figure 2.

RESULTS

The proposed approach was tested on one of the STRAS robot instruments. 2D and 3D trajectories were carried out twice to evaluate the precision and the repeatability of the technique. The 2D trajectories only involved the translation and bending of the tool. The paths performed by the tool were ellipses defined in the XY-plane with a major and minor axis of 44mm and 6mm respectively. Figure 3 illustrates the results of 3 different techniques. All the tests were performed in open-loop.

Our proposed approach gives very good results with a 2D RMS error of 0.72mm and a high repeatability. The statistics are reported on table 1, first column. It can be observed that our model is capable of generalizing well and can make up for the backlash.

The second technique tested consisted of training the previously mentioned models without taking into account the displacement direction. The error statistics can be found in the second column of table 1. The backlash cannot be properly modeled and, therefore, it cannot be compensated. Since the backlash of the bending joint greatly impacts both the motion on the x-direction and the prediction of Δy, large errors are observed on both directions.

The third method is a state-of-the-art, learning-based technique [2]. The training data was obtained by performing backward and forward motions of the bending joint while maintaining constant translations. A total of 1920 points, distributed on a $[30 \times 32]$ grid over the actuator space $[q_{trans} \times q_{bend}]$, were acquired. The errors are reported in table 1 (third column). The poor generalization shown by this method can be explained by the lack of features describing the hysteresis loop in its input space.

The 3D trajectory shown in figure 4 is shaped like a parabola in the XY-plane with a slight rotation around the Y-axis. A displacement of 40mm, 20mm, and 9mm alongside the X, Y and Z directions respectively defines the range of the desired movement. To perform this trajectory, all 3 DOFs must be actuated simultaneously. As detailed in table 1 (fourth column), the errors are larger than the ones obtained in the 2D case. Nevertheless, the obtained accuracy is similar to methods using an external sensor for feedback [7], whereas our approach only relies on encoders measurements.

Statistics	2D			3D
	our method	w/o backlash comp.	method of [2]	our method
RMS (mm)	0.72	6.87	7.92	2.92
Var (mm^2)	0.19	8.37	11.57	1.92
Max (mm)	4.0	12.9	14.1	5.86

Table 1: Statistics of the errors for the 2D and 3D trajectories for different position control methods

CONCLUSION AND DISCUSSION

The 2D experiments really showcase the potential of the proposed approach. It outperforms the approach from [2] by reducing the RMS error by 11 times. For the 3D experiments, even though the errors are larger, the results are still very promising.

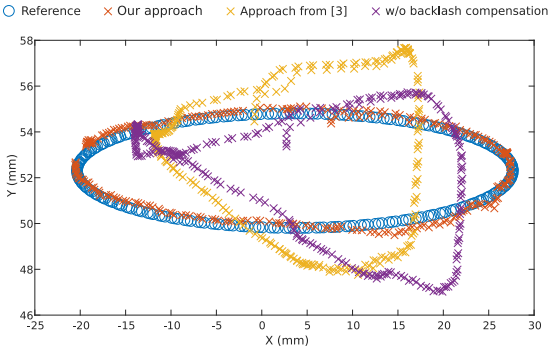

Figure 3: 2D trajectories on the XY-plane. Adapted from [3].

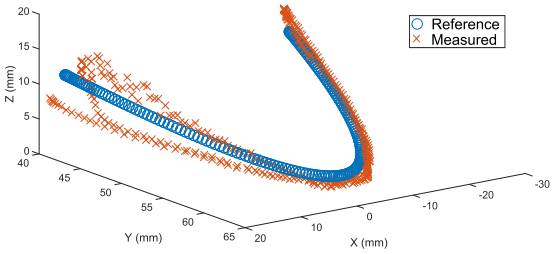

Figure 4: 3D trajectory performed in the task space.

ACKNOWLEDGEMENTS

This work has been supported by ITMO Cancer in the framework of "Plan Cancer" under project ROBOT and by French state funds within the Investissements d'Avenir program under the ANR-11-LABX-0004 (Labex CAMI).

REFERENCES

[1] V. Agrawal et al. "Modeling of transmission characteristics across a cable-conduit system" in IEEE Transactions on Robotics, vol. 26, no. 5, 914-924, 2010.

[2] W. Xu et al. "Data-driven methods towards learning the highly nonlinear inverse kinematics of tendon-driven surgical manipulators" in Int. Journ. of Medical Robotics and Computer Assisted Surgery, vol. 13, no. 3, 2017.

[3] R. A. Porto, F. Nageotte, P. Zanne and M. de Mathelin. "Position control of medical cable-driven flexible instruments by combining machine learning and kinematic analysis", in press.

[4] R. J. Webster et al. "Design and kinematic modeling of constant curvature continuum robots: A review" in The International Journal of Robotics Research, vol. 29, no. 13, 2010, 1661-1683.

[5] A. De Donno et al. "Master / Slave Control of Flexible Instruments for Minimally Invasive Surgery" in Proceedings of IEEE/RSJ International Conference on Intelligent Robots and Systems (IROS), Tokyo, 2013, 483-489.

[6] G.-B. Huang et al. "Extreme learning machine: a new learning scheme of feedforward neural networks" in Proceedings of IEEE International Joint Conference on Neural Networks, Budapest, Hungary, July 2004, 985-990.

[7] R. Reilink et al. "Pose reconstruction of flexible instruments from endoscopic images using markers" in Proceedings of IEEE International Conference on Robotics and Automation (ICRA), St. Paul, 2012, 2938-2943.

Depth Prediction and Implicit Domain Adaption for Endoscopy using Conditional Generative Adversarial Networks

A. Rau[1], P. J. Edwards[1], O. Ahmad[1], L. Lovat[1], D. Stoyanov[1]

[1] *Wellcome / EPSRC Centre for Interventional and Surgical Sciences (WEISS), University College London*

a.rau.16@ucl.ac.uk

INTRODUCTION

Colorectal cancer is the third most common cancer worldwide and the success of therapeutic treatment highly depends on early diagnosis through colonoscopy. The quality of the procedure, however, varies according to experience and expertise of the endoscopist [1]. In this work we develop a method to predict depth from endoscopic images. Depth information can be used to map the inner surface of the colon during colonoscopy improving navigation and thus polyp detection rates.

Because the colon is inflated and deformed during colonoscopy, ground truth from computer tomography (CT) cannot be obtained. While previous work has therefore focused on geometry cues [2], more recent work trains on synthetic images and uses unsupervised transformer networks to translate between the domains of synthetic and real images [3]. As these transformer networks are error-prone and do not allow backpropagation of the translation loss, we instead train an integrated conditional generative neural network (cGAN) that predicts depth directly from both synthetic and real images. We report promising results on synthetic data and qualitatively verify the robustness of the model on real clinical images.

MATERIALS AND METHODS

Data Generation – We generate a synthetic dataset based on a CT colonography scan. From the scan we extract a surface mesh. Using the game engine Unity we determine a camera path through the mesh and render RGB images and corresponding depth maps along the path (Figure 1). The virtual camera has a field of view of 110° and two attached virtual light sources to replicate a real colonoscope. We generate several subsets with different lighting-material configurations.

Conditional GANs [4] – GANs learn the distribution over a given set in an unsupervised manner and traditionally are used to generate random instances from the learned distribution. A standard GAN consists of a generator that draws samples from the current distribution and a discriminator that evaluates how real the sample looks. Let $y \coloneqq G(z|\theta_g)$ denote the output of the generator, where G is a convolutional neural network (CNN), θg are the parameters of the CNN, and z is noise. And let $D(y|\theta_d)$ denote the discriminator, with CNN parameters θ_d. Then by competing with one another in a minmax game, the discriminator becomes better at distinguishing

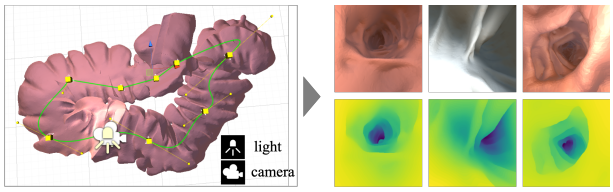

Figure 1. Data generation process. Left: colon segment within the Unity environment with a virtual camera, camera path, and light source; Right: examples of rendered RGB images with corresponding depth maps generated along camera path.

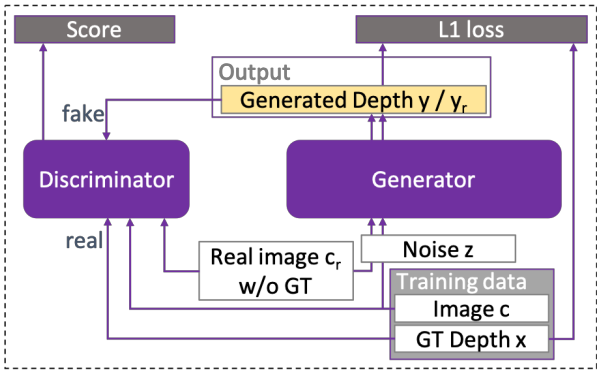

Figure 2. Scheme of our network architecture.

real images x from fake ones, and the generator learns to output more realistic looking instances. Eventually, an equilibrium is reached, and the generator

$$G^* = \arg\min_G \max_D E_{z\sim p_z(z)}[\log 1 - D(G(z))] + E_{x\sim p_{data}(x)}[\log D(x)]$$

learns to produce instances that are indistinguishable from real images in the training set.

In cGANs, the generator and discriminator are conditioned on an input image c, in our case the RGB colonoscopy image. Our base model is the cGAN pix2pix [5], that uses a convex loss to compare the generator output, in our case the predicted depth, to its ground truth. The generator then predicts depth from RGB images. The discriminator decides whether the depth looks realistic and the L1-Loss between ground truth depth and generated depth is backpropagated to the generator. In its equilibrium we then obtain

$$G^* = \arg\min_G \max_D L_{cGAN}(G,D) + \lambda L_{L1}(G),$$

where

$$L_{cGAN}(G,D) \coloneqq E_{z\sim p_z(z),c\sim p_{dat}(c)}[\log 1 - D(c,G(c,z))] + E_{c,x\sim p_{data}(c,x)}[\log D(c,x)]$$

Model	L1 error in cm	Relative L1 error	RMSE in cm
Discriminative	0.234	0.084	0.239
pix2pix	0.232	0.082	0.236
Extended pix2pix	0.171	0.064	0.175

Table 1. Results on synthetic images.

and

$$L_{L1}(G) \coloneqq E_{z\sim p_z(z),c,x\sim p_{data}(c,x)}||x - G(c,z)||_1.$$

To improve the robustness of our model when applied to real images we propose a new training paradigm for the standard pix2pix approach and input real images to the generator. As there is no ground truth depth for real images, the only loss signal remains the response of the discriminator. The generator then learns to predict realistic depth maps from real images, otherwise the discriminator would be able to identify those depth maps as false—the network is implicitly adapting to a new domain. A scheme of the architecture is depicted in Figure 2. The detailed architecture can be found in [5]. However, we omit batch-norm layers.

Training – We use TensorFlow for the implementation of our model. Training takes about 12h while inference takes 0.04 seconds for a single image on a NVIDIA Titan V GPU. We use Adam optimizer with a learning rate of $2 * 10{-}4$ and set $\lambda = 200$ as proposed in [5]. We train for 300 epochs using a batch size of 20. One element of each batch is a real example. We divide our dataset into training, validation and test data using a 6:1:3 split, resulting in approximately 9,600 training images.

RESULTS

Synthetic data – We train and compare three models: pix2pix; our extended version of pix2pix incorporating real images; and a discriminative version that has the same architecture as the generator in pix2pix. We measure the L1-distance $\|x - y\|_1$, the relative error $\|(x - y)/x\|_1$, and the root mean squared error RMSE = $\sqrt{1/N \sum_n (x_n - y_n)^2}$ between ground truth depth x and predicted depth y. Results are reported in Table 1. Additionally, we show predictions of the extended version of pix2pix in Figure 3.

Real data – We qualitatively evaluate the results on real images [6] and find that our model precisely predicts depth up to scale (Figure 4). It can be observed that the appearance of small details, such as polyps and folds, and the position of the lumen is correctly reconstructed. Further, reflections and air bubbles do not cause artifacts.

CONCLUSION AND DISCUSSION

While the results are precise on synthetic images, and look very promising on real images, we lack validation on real images. We are in the process of obtaining ground truth depth for RGB images captured with a colonoscope inside a photorealistic phantom. CT scanning the phantom with the camera inserted, we will accurately recover the shape of the imaged scene. Results on this validation set are to follow.

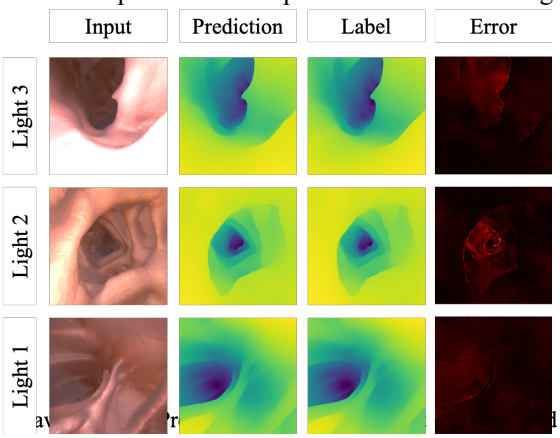

Figure 3. Results on synthetic images.

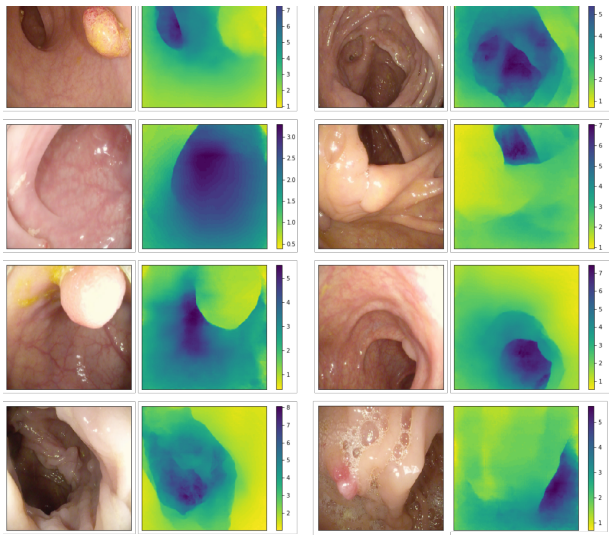

Figure 4. Results on real images [6].

Acknowledgements This work was supported by Wellcome/EPSRC Centre for Interventional and Surgical Sciences (WEISS) at UCL (203145Z/16/Z), EPSRC (EP/N027078/1, EP/P012841/1, EP/P027938/1, EP/R004080/1) and the European Commission Project-H2020- ICT-24-2015 (Endoo EU Project-G.A. number:688592).

REFERENCES

[1] D. K. Rex, "Polyp detection at colonoscopy: Endoscopist and technical factors," Best Practice & Research Clinical Gastroenterology, vol. 31, no. 4, pp. 425–433, 2017.

[2] D. Hong, W. Tavanapong, J. Wong, et al. "3d reconstruction of virtual colon structures from colonoscopy images," Computerized Medical Imaging and Graphics, vol. 38, no. 1, pp. 22–33, 2014.

[3] F. Mahmood and N. J. Durr, "Deep learning and conditional random fields-based depth estimation and topographical reconstruction from conventional endoscopy," Medical Image Analysis, 2018.

[4] M. Mirza and S. Osindero, "Conditional generative adversarial nets," arXiv preprint arXiv:1411.1784, 2014.

[5] P. Isola, J.-Y. Zhu, T. Zhou, et al. "Image-to-image translation with conditional adversarial networks," arXiv preprint, 2017.

[6] J. Silva, A. Histace, O. Romain, et al. "Toward embedded detection of polyps in wce images for early diagnosis of colorectal cancer," International Journal of Computer Assisted Radiology and Surgery, vol. 9, no. 2, pp. 283–293, 2014.

Novel capacitive-based sensor technology for augmented proximity detection

M. Chiurazzi, G.G. Garozzo, P. Dario, G. Ciuti

The BioRobotics Institute, Scuola Superiore Sant'Anna, Pisa, Italy
marcello.chiurazzi@santannapisa.it

INTRODUCTION

Embedded and environmental sensors are widely used to provide information regarding human-robot and robot-robot cooperation within unstructured environment. Worldwide, several research laboratories and companies are focusing on researching and developing autonomous self-adaptive machines capable of cooperating and interacting in swarm-based configurations and/or with human beings (*e.g.* autonomous vehicle, collaborative industrial and also medical robots). On this regard, a robust knowledge and awareness of the environment the robotic agent operates in, has been one of the main bottleneck for the diffusion of robotic cooperative systems, either in industrial or medical scenarios.

In order to provide such information, based on contact and proximity detection, Tonietti *et al.* [1] proposed to enhance human-robot interaction through variable impedance actuators (VIA) embedded onto robotic manipulator, whereas De Maria *et al.* [2] developed a force/tactile sensor for monitoring the interactive forces of a robotic end-effector with the external environment. Still relying on contact/pre-contact detection (up to 20 mm) Mazzocchi *et al.* [3] developed a sensorized external skin used for covering industrial manipulators and providing closed-loop force/pressure information through piezoresistive sensors. Moving to proximity technologies, Ye *et al.* [4] developed a capacitive technology capable of detecting proximity of an iron bullet at a maximum distance of 600 mm. These are just a few significant examples of developed sensor technologies, but more details are reviewed and reported in [5]. Other technologies, such as optical, ultrasound and laser are mainly integrated and applied into mobile robotic platforms, as presented in [6], [7], and [8], even if they are strongly affected by the shape and the material of the object to be detected.

For enabling environmental awareness for robotic agents and human beings, this work focused on the design and characterization of a novel capacitive-based technology for high-range proximity detection.

MATERIALS AND METHODS

The capacitive technology, presented in this work, is composed of two main units: a first one, named "reading sensor", on which the maximum detectable distance will be computed through the analysis of the distortion of the electrical field generated by the sensor itself, and a second active unit, named "bracelet", that interacts with the first one for enhancing the proximity response; the aforementioned units have to be used in combination. The reading sensor can be integrated into any non-regular surface, whereas the bracelet can be easily worn by a human operator. The complete system, patented on July 2018 (deposit number: IT 102018000007150), considered, as a possible application, the bracelet worn by a human operator, while reading sensors were installed on the external surface of a robotic anthropomorphic arm. However, it is worth mentioning that the bracelet can be integrated in other wearable, or even not, units, such as t-shirts, gloves, etc.

As a first step of the design phase, several geometries for the reading sensor were analyzed and physical parameters (*i.e.*, electrode dimension, distance between the electrodes) were tested in order to optimize sensor performances. Analysis leads to a bio-inspired geometry based on a multi-layer honeycomb-based structure (concentric hexagonal spirals) made up by a first conductive layer (A) lying on a insulate plate (B) made of Kapton. A third soft silicone layer (C), with specific features (*e.g.*, elastic module, thickness), was intended and designed as shock absorber for reducing the energy transferred during the collision between the robot and the human being, according to the thresholds regulated in the ISO/TS 15066. Finally, an active conductive layer (D) was added in order to force the electric field propagation along a specific direction. The bracelet is made by a soft foam layer, on which two conductive elements (made by iron) are arranged and powered to generate a specific electrical field (**Figure 1**).

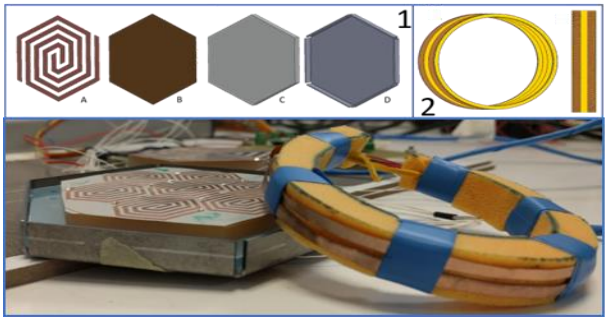

Figure 1- Multi-layer structure of the reading sensor and wearable bracelet

First, the reading sensor was characterized in simulation and in real environment, then the entire system was tested placing the two units (sensor with bracelet) at different distances (0-400 mm with a 40 mm step); for each step 1000 measures of capacitance were acquired, filtered and converted into voltage values for providing statistical data (*i.e.*, mean value, standard deviation).

RESULTS

A preliminary simulation in COMSOL Multiphysics 5.3, where the reading sensor interacts with a cube (volume of 125 mm3) with electrical properties comparable with the human hand (i.e., skin resistance,

skin conductivity), was performed. The interaction was investigated at several distances (i.e., 0-165 mm with a 15 mm step) assuming air as dielectric between the sensor and the cube. The simulated behavior was compared with the response of the real prototype (powered with 1 Vpp sinusoidal wave at 50 kHz), both showing a logarithmic trend in agreement with the state of the art (**Figure 2**)

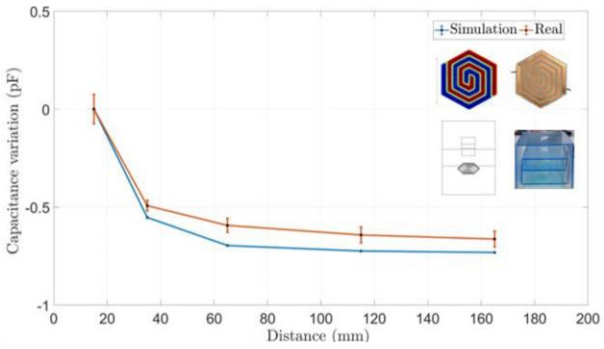

Figure 2 - Simulated vs. real curve of response from 0 mm (contact) to 165 mm

The maximum detectable distance achieved was 165 mm; it means that in the current configuration the sensor cannot detect a human hand further than 165 mm. Additionally, the sensitivity range increases with the conductivity of the detected element increases. This concept paved the way to the solution proposed within the paper, where, to increase the human hand conductivity the bracelet was developed in order to be worn by the human being while generating a specific electrical field. The maximum achievable distance, assuming to power the reading sensor with a first 1Vpp sinusoidal wave at 50kHz and the bracelet with a second sinusoidal wave in counter phase with respect to the first one, is about 400 mm. It means, 2.5 times the sensitivity range achieved with the sensor interacting only with the hand. The curve of response of the reading sensor interacting with the human hand with and without the bracelet are compared in ***Figure 3***.

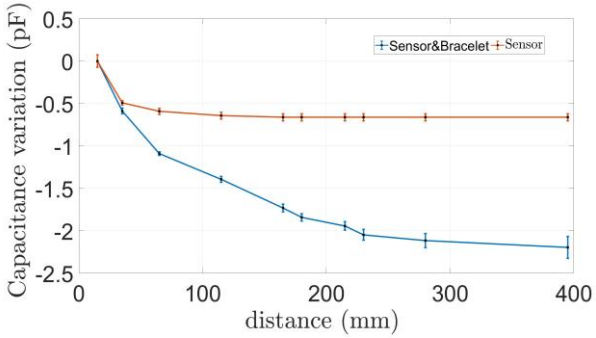

Figure 3 - Reading sensor interacting with the bracelet (blue line) vs. reading sensor (red line)

CONCLUSION AND DISCUSSION

The work describes the preliminary result of the development of a novel capacitive-based technology for high-range proximity detection, composed of a reading sensor unit, embeddable onto any non-regular surface, and interacting with a wearable active bracelet. The combined system demonstrated a maximum sensitivity range from 0 to 400 mm and it can be used either for pressure or high range proximity detection; the latest represents a noteworthy result in comparison with the current state of the art where capacitive sensors, similar in dimension, usually have a sensitivity range of a few centimeters (*i.e.*, mainly used for pre-contact detection). Prototype result shows, with respect to the simulated one, an error lower than 8%, probably due to environmental conditions, neglected in the simulated environment.

Due to the high sensitivity range achieved, the technology, still providing a local information, can allow to detect and re-map an obstacle in the environment for avoiding collisions and/or for re-planning *on-line* motion trajectories reducing the gap with the environmental sensors. The developed system has to be intended as modular; this means that the sensor unit can be designed and arranged as an array of multiple elements adaptable, in dimension and shape, with any non-regular surface according to the requested performances. The first designed capacitive-based technology paves the way to future implementations, where the wearable bracelet can become a sensorized t-shirt or a printable tattoo, due to its compact dimension and low-cost. On the other hand, the reading sensor dimension can be scaled up or down in order to be integrated into any non-regular surfaces, such as robotic arm/gripper. This re-scaling will clearly affect sensor performances thus, a trade-off between mechanical/electrical features and sensor performances has to be considered. Moreover, arrays of reading sensor with compact dimension could be developed and used in applications of gesture recognition, 3D reconstruction and, in perspective, used to recognize the material of different objects with different electrical properties.

REFERENCE

[1] G. Tonietti - *IEEE International Conference on Robotics and Automation*, pp. 526-531, 2005.

[2] D. M. Giuseppe - *IEEE International Conference on Robotics and Automation*, Vols. 2015-June, pp. 3883-3889, 2015.

[3] T. Mazzocchi - *IEEE International Conference on Intelligent Robots and Systems*, pp. 837-843, 2015.

[4] Y. Ye - *Sensors*, p. 699, 2016.

[5] R. Bogue - *Industrial Robot: An International Journal*, vol. 42, no. 5, pp. 386--391, 2015.

[6] F. Chen - *Optical Engineering*, vol. 39, no. 1, pp. 10-23, 2000.

[7] J. Guivant - *Journal of Robotic Systems*, pp. 565-583, 2006.

[8] F. Fahimi - *Robotica*, pp. 189-198, 2009.

[9] Y. A. Chizmadzhev - " *Biophysical Journal*, vol. 74, no. 2, pp. 843--856, 1998.

Drowsiness detection among surgeons: development of a wearable EEG device

T. Banfi[1], A. Cignoni[1,2], G. Ciuti[1]

[1]*The BioRobotics Institute, Scuola Superiore Sant'Anna*

[2]*Department of Information Engineering, University of Pisa*

t.banfi@santannapisa.it

INTRODUCTION

Sleep plays a crucial role in physical and cognitive wellbeing of individuals: physiologically the average human being spends roughly a third of her/his life sleeping. Sleep curtailment or reduced sleep quality (*e.g.* due to shift work) are linked to detrimental consequences particularly marked for attention and working memory capabilities [1]. Central to this contribution is not sleep itself but drowsiness, that is the intermediate state between alert wakefulness and sleep [2]. Drowsiness and sleep deprivation (SD) consequences are of main concern in safe sensitive occupations. Within the medical field, surgeons are traditionally exposed to considerable levels of SD, raising significant concerns on safety issues associated with sleepy surgeons [3], [4]. Drowsiness is also a major threat to personal security of surgeons and physicians as it has been shown to be linked to raised risk while commuting back home after shift work [5], and is deemed to generally play a role in up to 20% of road crashes [6]. Hence, being able to measure and possibly track drowsiness among surgeons, can play a role in the mitigation of accident risk for both surgeons and possibly patients. Physiological measures can be used to detect, measure and track drowsiness and sleep. Recently, miniaturized single channel EEG systems were able to distinguish with high accuracy sleep-drowsiness in aviation pilots during long-haul flights [8]. The aim of this study is to assess if this kind of approach could be effectively replicated on surgeons thorough a specifically-designed wearable EEG system.

MATERIALS AND METHODS

The designed system is composed by a wearable EEG recorder and an external Linux-based data processing unit (Raspberry Pi 3B+), the wireless communication between the two modules is encapsulated in a TCP/IP protocol (Fig. 1). A prototype has been created as a proof of concept of the integrated wearable EEG recorder. The components were chosen following the technical specifications for EEGs system dictated by the IEC 60601-2-26-2012 standard [9]. The prototype acquires EEG signals using an array of 10 microelectrodes (*cEEGrids*, [10]) comfortably placed around the ear, in a non-hair bearing area of the skull to maximize subject comfort and system usability in the field, also reducing overall system complexity. The cEEGrid has a flat connector that is attached to an analog front-end (ADS1299, Texas Instruments). The analog front-end has 8 input channels plus the bias and reference ones, a 24-bit ADC, 8 programmable gain

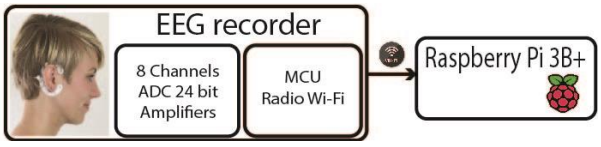

Figure 1. Schematic representation of the system

amplifiers with a small footprint (10 x 10 mm) and has a low input reference noise<1V_{pp} at maximum gain (24). The wearable EEG recorder uses a SoC that embeds an MCU (Photon, Particle; 120 MHz ARM Cortex M3 and Broadcom BCM43362 Wi-Fi radio). The MCU establishes a TCP connection with the external unit, configures the ADS1299 registers for EEG signal acquisition through SPI, stores the retrieved EEG data in a buffer and sends it through the TCP/IP connection. The MCU firmware can be flashed over the air, and remote basic diagnostic is also available (*e.g.* free MCU flash, or Wi-Fi RSSI).

Nor the wearable EEG recorder neither the external compute unit need any calibration. EEG data are received in chunks by the external compute unit at 1.12Hz. Data received are then buffered until 30s of EEG signals are available. Then we pre-process the data and, using the embedded GPU on the Rpi, we calculate the EEG signal spectrum. The filtered EEG signals and their spectra are fed to an artificial neural network (NN) classifier to classify behavioural state. The NN is implemented in Keras (2.2.4) TensorFlow (1.11.0). The network was trained using a public EEG dataset (https://physionet.org/physiobank/database/challenge/2018/) of 50 subjects for the training set and 50 subjects for the test set. The NN architecture uses both a 1D convolutional plus batch normalization cell and a recurrent one built using Gated Recurrent Units. The convolutional cell takes bandpass filtered (in the 0.5-30Hz band) EEG data as input, while the recursive branch is fed with the spectrum of those signals. The architecture was designed trying to maximize the computational efficiency through the minimization of the number of parameters of the network. The current implementation has a computational cost of 682.825 FLOPs. Three experiments were carried on comparing the performance of the prototype with a medical grade EEG amplifier (Morpheus, Micromed). *Exp.1* - EEG of one subject was recorded using cEEGrid electrodes that were connected to both our prototype and to the medical grade EEG recorder (Fig.2). *Exp.2* - 4 subjects were recruited (average age 25±2yrs). Each participant wore the cEEGrid electrodes connected to our prototype, as well as 7 standard EEG electrodes attached to the Morpheus. The latter group of electrodes were located on the skull following the standard 10-20 system

scheme (Fig.2). During the first two experiments, participants were asked to sleep for 30 min and 1 hour respectively during an afternoon nap. *Exp.3* - three standard Au wet electrodes were used to record an EEG signal from behind the ear, to verify the functionality of the prototype. The bias electrode was placed over the mastoid bone. The subject sat relaxed and was asked to perform two tasks (60 seconds each): *i)* eyes continuously open, *ii)* eyes continuously closed. EEG was recorded during each task.

RESULTS

Exp.1 - we calculated Pearson correlation coefficient over 30 minutes of recording obtaining an average rho of 0.92±0.02 ($p<0.001$) for all channels, meaning that there is a strong linear relationship between the EEG signals acquired with our prototype and the medical grade Morpheus amplifier.

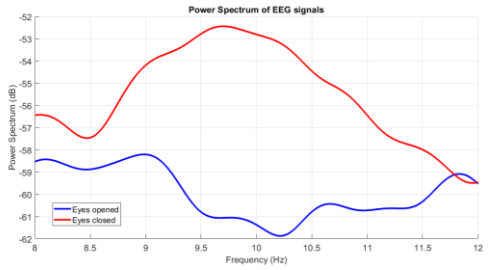

Figure 2 Power spectrum for EEG signals: eyes open (blue), eyes closed (red). Y-axis represents

Exp. 3 - Fig.3 shows the power spectrum of the two EEG signals recorded with our system during the tasks. The spectrum is centred on the alpha band range (8-12 Hz). It can be seen an increment in the alpha band with closed eyes with respect of the other task (eyes open). Alpha waves mainly originate in the occipital visual cortices: this area is distant from current electrodes' placement. Nevertheless, changes in frequencies are detected. The NN reached an average F1 score of 0.69, concordance of 0.88 and a ROC auc of 0.94 on the test set of 50 subjects.

CONCLUSION AND DISCUSSION

This preliminary finding are consistent with available evidence from the literature [11] suggesting that this architecture may be suitable for our purpose. As this is a preliminary implementation of the system, we are currently scheduling a set of experimental procedures to record EEG signals from a group of subjects while fully alert and in a drowsy state. Subjects enrolled will act as their own control, each of them will be tested twice during the same day: once during the post prandial dip of alertness and again during the Zenith of alertness physiologically around 8PM. In this phase the system will be validated against standard polysomnography and EEG data recorded with the prototype will enable a fine tune training of the current classification model. The results from the first experiment suggest that our prototype had very similar acquisition performance as the medical grade amplifier. In the prospective of detecting drowsiness, it is usually required to detect changes in certain EEG frequency bands, especially the lower ones (delta, theta, alpha). The presence of alpha and theta waves paired with slow rolling eye movements in an awake individual indicates a higher sleepiness. Now, our prototype had comparable acquisition performance to a medical grade amplifier enabling reliable EEG data collection. The NN model is in his early training phase providing good performance, future development will embed a prediction inference mode (prediction horizon 30s ahead) to enable early detection of drowsiness and subsequent feedback to the wearer or his team. Furthermore, the upgraded version of the system will use a mesh network instead of the current Wi-Fi standard, enabling self-organization and self-configuration of the network with an efficient routing of data between devices and no single point of failure in the network itself. This new communication standard will also help to reduce the power consumption of the EEG recorder to around 70mA (~50% reduction as of now). The system will be embedded in a PCB (sized 23x50x5 mm) embedding all the components. We plan to integrate the PCB in a lightweight ad hoc eyeglasses frame to improve comfort and the ease of use.

REFERENCES

[1] A. J. Krause *et al.*, "The sleep-deprived human brain," *Nat. Rev. Neurosci.*, vol. 18, no. 7, pp. 404–418, 2017.

[2] J. F. D. and C. A. Czeisler, "Effect of Light on Human Cicardian Physiology," *Sleep Med Clin*, vol. 4, no. 2, pp. 165–177, 2009.

[3] C. P. Landrigan *et al.*, "Effect of Reducing Interns' Work Hours on Serious Medical Errors in Intensive Care Units," *N. Engl. J. Med.*, vol. 351, no. 18, pp. 1838–1848, 2004.

[4] M. J. Zinner, "Surgeons, Sleep, and Patient Safety," *JAMA*, vol. 310, no. 17, p. 1807, Nov. 2013.

[5] C. Anderson *et al.*, "Self-reported drowsiness and safety outcomes while driving after an extended duration work shift in trainee physicians," *Sleep*, no. December 2017, pp. 1–11, 2017.

[6] S. G. Klauer *et al.*, "The Impact of Driver Inattention On Near Crash/Crash Risk: An Analysis Using the 100-Car Naturalistic Driving Study Data," *Analysis*, no. April, p. 226, 2006.

[7] J. Lynn Caldwell, J. F. Chandler, and B. M. Hartzler, "Battling fatigue in aviation: Recent advancements in research and practice," *J. Med. Sci.*, vol. 32, no. 2, pp. 47–56, 2012.

[8] F. Sauvet *et al.*, "In-flight automatic detection of vigilance states using a single EEG channel," *IEEE Trans. Biomed. Eng.*, vol. 61, no. 12, pp. 2840–2847, 2014.

[9] A. J. Casson, S. Smith, J. S. Duncan, and E. Rodriguez-Villegas, "Wearable EEG: what is it, why is it needed and what does it entail?," *2008 30th Annu. Int. Conf. IEEE Eng. Med. Biol. Soc.*, no. June, pp. 5867–5870, 2008.

[10] M. G. Bleichner and S. Debener, "Concealed, Unobtrusive Ear-Centered EEG Acquisition: cEEGrids for Transparent EEG," *Front. Hum. Neurosci.*, vol. 11, no. April, pp. 1–14, 2017.

[11] K. B. Mikkelsen *et al.*, "Machine-learning-derived sleep–wake staging from around-the-ear electroencephalogram outperforms manual scoring and actigraphy," *J. Sleep Res.*, no. April, 2018.

A Comparison of Expert and Novice Performance in Obstetric Ultrasound Using Probe Tracking Systems: Data to Improve Training.

Brian P Dromey [1], Shahanaz Ahmed [1], Francisco Vasconcelos [2], Evangelos Mazomenos[2], Anna L David[1], Danail Stoyanov[2], Donald M Peebles[1]

[1]*Institute for Women's Health, University College London, UK.*

[2] *Wellcome/EPSRC Centre for Interventional and Surgical Sciences (WEISS)*
b.dromey@ucl.ac.uk

INTRODUCTION

Ultrasound is a dynamic, real-time investigation, but is operator dependent and has high inter-operator variability**[1]**. Operator training and competence assessment are therefore, of great importance for safe clinical practice. Globally, standards for training and assessment have been suggested by bodies such as the American Institute of Ultrasound in Medicine (AIUM), The International Society of Ultrasound in Obstetrics and Gynaecology (ISUOG). In Europe, countries such as France, Germany and Switzerland require operators to have performed a minimum number of scans. The French National College of Gynaecologists and Obstetricians (CNGOF) require practitioners to pass a national, examination of ultrasound skills to obtain certification. Meanwhile in Sweden and Italy there is neither a formal curriculum in obstetric ultrasound, nor a minimum number of scans to complete.

Training in ultrasound and fetal medicine procedures are, inevitably pressured by clinical workload and worktime regulations for junior doctors. An arbitrary minimum threshold places considerable pressure on learners, their trainers, the hospitals they work in and provides no assessment of competence.

This study aimed to define measurable differences between expert and novice ultrasound operators and to understand how these metrics could be applied to define a specific, measurable and reproduceable performance goal for training in ultrasound.

MATERIALS AND METHODS

We undertook a prospective, observational study. We recruited a total of twenty participants. Half of whom were experts (n=10, >200 ultrasound examinations) and half of whom were novice operators (n=10, <25 ultrasound examinations). The study was undertaken at the Obstetric Ultrasound Unit at The University College London Hospitals NHS Foundation Trust. All participants were doctors in Obstetrics & Gynaecology at UCLH. All participation was voluntary and informed consent was obtained from each participant.

Each participant was asked to obtain three common cross-sectional images of the fetus. These views are the most common used for estimation of fetal weight. The required views were of the transventricular plane, corresponding to Head Circumference (HC), the transabdominal plane, corresponding to the Abdominal Circumference (AC) and a view of the femur (FL). The scan was performed using a GE Voluson E8 ultrasound scanner (Chicago, Illinois, United States) and a commercially available second trimester phantom (SPACE-FAN ST, Kyoto Kagaku Co., Ltd, Kyoto, Japan) was scanned.

The position of the probe was tracked using an Aurora electromagnetic tracking system (NDI Inc, Ontario, Canada). To track the probe a 5 degree-of-freedom sensor was attached to the ultrasound probe by means of a custom 3-D printed holder and the phantom was placed on an Aurora planar field generator.

Prior to commencing, each participant was given written instructions, including images of the required planes and up to five minutes to familiarise themselves with the operation of the ultrasound scanner. Participants were permitted to refer to these instructions during the task, if they wished to.

The captured images were transferred to the research database and were scored using the scoring tool described by Salomon et al [2] for quality control in fetal biometry.

RESULTS

Novice operators were able to achieve image quality and measurement accuracy approaching that of an expert operator when allowed unlimited time to complete the task and given access to visual prompts.

	Expert ± SD	Novice ± SD	*p*
BPD (mm)			
58 (Manufacturer Spec)	60.21±1.54	62.59±3.21	0.03
AC (mm)			
177 (Manufacturer Spec)	181.52±4.05	183.12±5.95	0.79
FL (mm)			
37 (Manufacturer Spec)	44.32±1.87	44.04±2.50	0.56
Image Score	11.8±1.87	10.2±1.46	0.04
Time (sec)	176.46±47.31	666.935±490.36	0.0004
Probe Path Length (mm)	521.23±27.41	2234.82±188.50	0.007

Table 1 - Mean biometry results as achieved by Expert and Novice Operators.

There was a difference in the process by which novice and expert operators acquired the required ultrasound image. The novice operators took 2.8 times longer to complete the task. The ultrasound probe travels 3.3 times as far, this is displayed graphically in Figure 1, which depicts the 'journey' of the probe during the scan. When scanned by an expert the probe makes three distinct

pauses, corresponding to an anatomical plane at which a measurement was made. The probe travel distance for a novice operator is longer, the pauses relating to measurement planes were lost and a tracing of the gravid abdomen was seen.

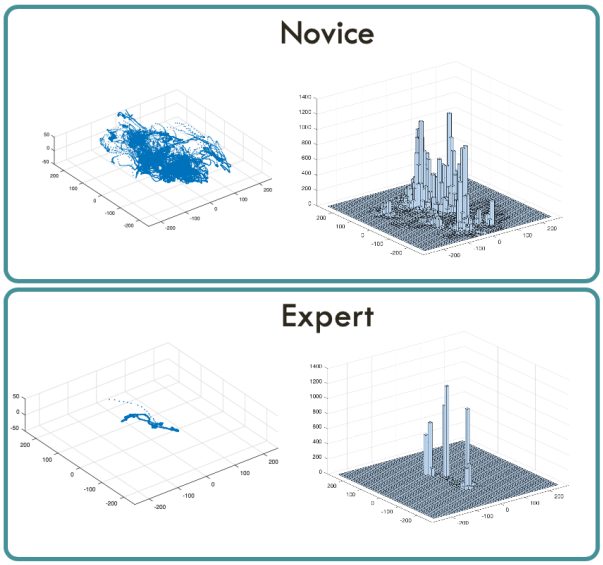

Figure 1. Path Length and Probe Travel in both groups.

We also assessed Dimensionless Jerk (DJ), a derivative of acceleration with respect to time and distance but dimensionless, so that there is no dependency of movement duration, extent, and spurious peaks [3]. DJ has been described in endoscopic surgery as a means to discriminate between expert and novice operators[4]. Figure 2 demonstrates the difference in dimensionless jerk when plotted against time for the novice and expert groups. The resulting ellipses have a small area of overlap, indicating that consideration of time and dimensionless jerk together can differentiate novice from expert performance.

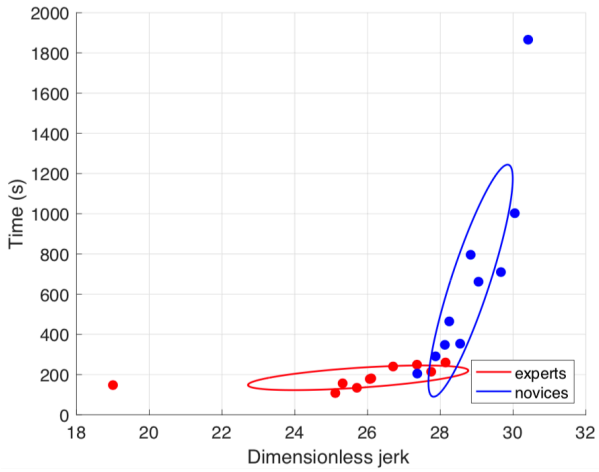

Figure 2. Dimensionless Jerk Plotted Against Time

CONCLUSION AND DISCUSSION

We found that the process of performing an ultrasound is more discriminatory between our expert and novice groups than the images acquired.

Our results show a series of metrics by which training progress could be assessed. We demonstrate that if the probe journey is considered in the context of deliberate pauses related to planes of interest, the smoothness of the probe and the time taken, that expert and novice groups can be told apart.

Ultrasound also requires a detailed understanding of the technical abilities and limitation of ultrasound to capture medical images, the ability to manipulate settings within the machine and a detailed understanding of both fetal and maternal anatomy, favouring the expert operator. The use of metrics such as jerk, path length and total time taken cannot, at this stage, be advocated as conferring competence.

This study was limited by small numbers, but is a first step in demonstrating performance differences which could form the foundation of standardised, validated training outcomes in obstetric ultrsound. The phantom used in this study did not simulate cardiac activity or fetal movements. Additional variables, such as fetal position, maternal body habitus and fetal movements could affect results such as time to complete the scan. Performing a scan in a clinical environment may induce stress or distractions which also impact on operator performance.

Contemporary training in obstetric ultrasound is evolving to include simulation, but remains an extension of "see one, do one, teach one" rather than a reflection of modern approaches to medical education. The metrics described in this paper can be measured in a clinical setting to demonstrate improvement in technique, progress towards competence and give confidence to trainers and learners that they are advancing towards independent practice. Our methods could also be used for quality control or for practitioners to demonstrate ongoing competence in ultrasound.

REFERENCES

[1] Pajkrt E, Mol B, Boer K, Drogtrop A, Bossuyt P, Bilardo C Intra- and interoperator repeatability of the nuchal translucency measurement *Ultrasound in Obstetrics and Gynecology*; 2000 vol: 15 (4) pp: 297-301

[2] Kholinne, Erica et al. 2018. "The Dimensionless Squared Jerk: An Objective Parameter That Improves Assessment of Hand Motion Analysis during Simulated Shoulder Arthroscopy." *BioMed Research International* 2018: 1–8. https://www.hindawi.com/journals/bmri/2018/7816160/ (December 14, 2018).

[3] N. Hogan and D. Sternad, "Sensitivity of Smoothness Measures to Movement Duration, Amplitude, and Arrests," *Journal of Motor Behavior*, vol. 41, no. 6, pp. 529–534, 2009.

[4] Kholinne, Erica et al. 2018. "The Dimensionless Squared Jerk: An Objective Parameter That Improves Assessment of Hand Motion Analysis during Simulated Shoulder Arthroscopy." *BioMed Research International* 2018: 1–8. https://www.hindawi.com/journals/bmri/2018/7816160/ (December 14, 2018).

Autonomous Pre-Planned Lift-and-Place of a Novel Robotic Surgery Imagining Rail Using the dVRK Platform*

C. D'Ettorre[1], A. Stilli[1], G. Dwyer[1], M. Tran[2], D. Stoyanov[1]

[1]*Wellcome/EPSRC Centre for Interventional and Surgical Sciences, University College London,*

[2]*Department of Surgical Biotechnology, Division of Interventional Science, Royal Free Hospital*
c.dettorre@ucl.ac.uk

INTRODUCTION

Robotic-Assisted Partial Nephrectomy (RAPN) is a surgical procedure where a part of the kidney is resected to remove cancerous cells. During this procedure, typically performed with the da Vinci Surgical System (Sunnyvale, CA) [1], a "drop-in" ultrasound (US) imagining probe is used to identify and outline the target tumor intraoperatively. The probe is grasped and controlled using the EndoWrist® Prograsp™ Forceps tool. The teleoperation of the probe significantly increases the cognitive load of surgeons: an optimal scanning orientation should be maintained to ensure the contact and slippages are common, hence, repositioning of the probe is frequently required. In September 2018 the authors have presented at CRAS in London for the first time the Pneumatically Attachable Flexible Rails (PAF Rails), a novel soft robotic system designed to improve the outcome of the intra-operatory imaging procedure described before. In [2] the authors have presented a detailed design study of the proposed system. This paper builds on the work presented in [2]: focusing on the integration of the proposed system with the da Vinci Surgical System (Sunnyvale, CA) the authors have developed a custom software architecture to automate its deployment on the kidney surface. With this work, we aim at the automatization of the grasping and placing of the PAF rails on the kidney surface so that the surgeon is actively operating only during the swiping step, to further decrease his/her workload and ease the procedure.

The automatization of surgical tasks is a topic widely investigated by different research groups worldwide: in [3] Pratt et al. designed a new framework for automatic tumor dissection for a planar tissue surface using the intraoperative US; in [4], the camera motion and tissue deformation are simultaneously estimated based on a respiratory model of the tissue motion. Recently Zhang et al. [5] proposed a novel system for autonomous ultrasound scanning under tissue motion.

In this work we propose the use of: 1 - a calibrated environment with an initial comparison of two surface registration techniques (reference frames used in the calibrated environment detailed in Fig.1 bottom); 2 - an imaging process algorithm for system detection 3 - a pre-operative point-to-point trajectory planning supported by a real-time control scheme based on visual feedback to monitor the position of the surgical tool (grasper) holding the system. To the best of our knowledge, this represents the first work in terms of automation with the proposed system which has never been used before in research work, clinical studies or practice.

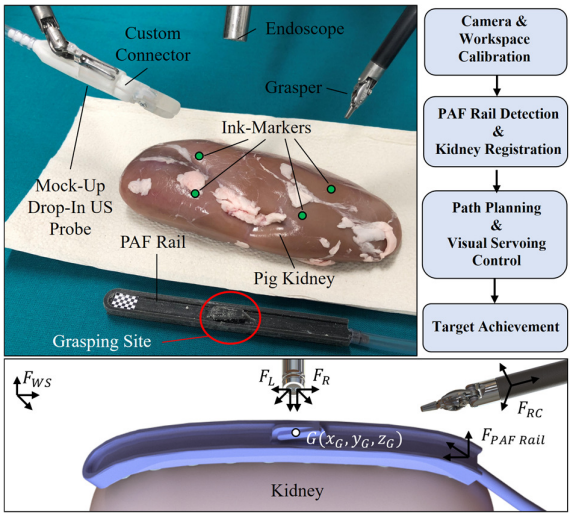

Figure 1 – *Left: Experimental setup for PAF rails autonomous placement tests including: pig kidney, the robotic tools, the stereo endoscope, the PAF rail and the drop-in US probe (mock-up). The mock-up probe is already paired with the custom clip-on connector that enables probe grasping and swiping along the PAF rail. Four ink markers used for surface registration are highlighted on the kidney surface. Right: ROS node architecture. Bottom: the five ref. frames considered in the calibrated environment are displayed on a CAD of the system: workspace (F_{WS}), grasper remote centre (F_{RC}), endoscope (F_L and F_R) and PAF rail ($F_{PAF\ Rail}$).*

MATERIALS AND METHODS

The experimental procedure here presented is performed using the daVinci Research Kit (dVRK) [6]. The ROS node architecture developed is shown in Fig. 1 (right).

Camera and Workspace Calibration

the reference frames used are shown in Fig.1 (bottom). The stereo endoscope has been calibrated through the Matlab toolbox [7] using a checkerboard. The workspace (WS) calibration has been performed as in [8], probing the intersections of a 3D printed checkerboard and saving the values of the encoder. The points were then registered with the known checkerboard dimension for each Patient Side Manipulator (PSM) tools. The test setup is shown in Fig. 1 (left), displaying the starting configuration.

PAF Rail Detection and Kidney Registration

the PAF rail is equipped with a checkerboard (see Fig.1 left) the position of which is located and tracked inside the workspace through Matlab. For the kidney registration, we extended the methodology proposed in [9] to an ex-vivo pig kidney using biocompatible ink markers. The results coming from each method are compared in terms of distances between the detected markers and the real ones representing the ground truth.

*This research is supported by the Wellcome / EPSRC Centre for Interventional and Surgical Sciences (WEISS) and from the EPSRC Impact Acceleration Accounts (IAA) 201720: Discovery-to-use funding.

Trajectory Planning and Visual Servoing

two elements are required to autonomously grasp the system in the targeted area: 1 – the generation of an ergonomic trajectory to reach and grasp the system; 2 – the development of a real-time control system to optimize the operational performance. A point-to-point trajectory has been implemented using as initial point a defined "home" position of the tooltip and as a final, the configuration corresponding to the rail correctly located on the kidney. The trajectory in-between these two points has been divided into three steps: STEP I – the robotic tool (grasper) approaches the grasping site from the "home" position. The cartesian position corresponding to this point is detected by the stereo-camera and successively triangulate in the 3D space. STEP II – the tool, holding the rail, moves back to the predefined home position. STEP III – the tool places the PAF rail on the kidney surface, allowing the system to anchor to it using the suction cup(s) as detailed in [2]. Some kinematics constraints related to the pick-up phase in STEP I and the target approaching phase in STEP III have been defined filtering and averaging the values coming from user demonstrations. Furthermore, to account for uncertainties and minor errors and to enhance the performance of the tool driving, visual feedback is added from STEP I onwards. Nonetheless, the system does not present any tool tracking node; once the relationship between the rail and the tool is geometrically established during the grasping phase, it is possible to compute the same information. The position of the tooltip is extracted dynamically and transposed in the workspace frame F_{WS} and compared to the position acquired through the dVRK and transposed in the same space.

RESULTS

Regarding the kidney registration procedures, accuracy is quantified by the error in the markers reconstruction for each method [9] in terms of Euclidean distance between the markers themselves. Unsurprisingly, given the small intraocular distance of 5.4 mm between the stereo camera in the da Vinci endoscope, localization registration with PSMs (1.23 ± 0.44 mm) was more accurate than with endoscope-based technique (4.10 ± 0.88 mm). In this preliminary test, we focused on the repeatability of the task in order to be sure the kinematic can be used to guide the dVRK. Six different acquisitions were recorded for the same task with the same initial and boundary conditions. The PAF rail is positioned in the field of view of the endoscope with the tooltip starting from the "home" position. The task is considered successfully completed when the tool grasps the PAF rail, precisely places it in on the kidney surface and moves back to the "home" position. The boxplots in Fig.2 shows the mean values of the three Cartesian coordinates in the workspace frame F_{WS} of the point G (rail grasping site) when the grasper is paired. It is possible to notice that the values related to the z-axis are greater than the other two axes, highlighting that the main error component is due to depth estimation error from during the reconstruction. A dataset of 40 acquisitions has been recorded to test the overall architecture. The task is considered concluded

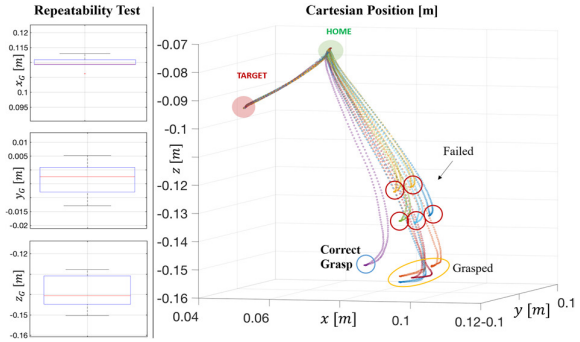

Figure 2 – *Boxplots for the coordinates of G (see Fig.1) when the grasper tooltip is paired with the PAF rail during the repeatability tests (left). Cartesian positions of G in the workspace during 10 out of 40 acquisitions (right) (only one correct grasp displayed)*

once the PAF rail is in contact with the kidney surface on the side of the suction cup. The acquisitions partially displayed in Fig.2 show a success rate of 35/40; in the remaining 5/40 the tooltip was not able to reach the rail. In 4 of the 35 successful cases, the task was correctly completed but a lower z_G was estimated, generating a small sliding of the rail before the grasp, showed by the horizontal drift (yellow circle). The average travel time among all the acquisitions was 42 seconds.

CONCLUSION AND DISCUSSION

The preliminary results here presented show that the proposed algorithm is reliable and robust with a high success rate. The described calibrated environment and the pre-planned trajectory generated allow the system to autonomously position the PAF rail on the kidney, reducing the workload of the clinician as intended.

REFERENCES

[1] "Intuitive Surgical - Frequently Asked Questions." [Online]. Available: http://www.davincisurgery.com/da-vinci-gynecology/da-vincisurgery/frequently-asked-questions.php. [Accessed: 12-Dec-2018].

[2] A. Stilli, D. Emmanouil, C. D'Ettorre, M. Tran, and D. Stoyanov, "Pneumatically Attachable Flexible Rails for Track-Guided Ultrasound Scanning in Robotic-Assisted Partial Nephrectomy – A Preliminary Design Study - (ICRA 2019 + RA-L, under review). Available here: https://bit.ly/2C6QdCH"

[3] P. Pratt *et al.*, "Autonomous ultrasound-guided tissue dissection," in *International Conference on Medical Image Computing and Computer-Assisted Intervention*, 2015, pp. 249–257.

[4] P. Mountney and G.-Z. Yang, "Motion compensated SLAM for image guided surgery," in *International Conference on Medical Image Computing and Computer-Assisted Intervention*, 2010, pp. 496–504.

[5] L. Zhang, M. Ye, P. Giataganas, M. Hughes, and G.-Z. Yang, "Autonomous scanning for endomicroscopic mosaicing and 3d fusion," in *2017 IEEE International Conference on Robotics and Automation (ICRA)*, 2017, pp. 3587–3593.

[6] P. Kazanzides, Z. Chen, A. Deguet, G. S. Fischer, R. H. Taylor, and S. P. DiMaio, "An open-source research kit for the da Vinci® Surgical System," in *Robotics and Automation (ICRA), 2014 IEEE International Conference on*, 2014, pp. 6434–6439.

[7] J.-Y. Bouget, "Camera Calibration Toolbox for Matlab; 2010," *Softw. available http//www. vision. caltech. edu/bouguetj/calib_doc*, vol. 80, 2011.

[8] C. D'Ettorre *et al.*, "Automated pick-up of suturing needles for robotic surgical assistance," *arXiv Prepr. arXiv1804.03141*, 2018.

[9] J. M. Ferguson *et al.*, "Toward image-guided partial nephrectomy with the da Vinci robot: exploring surface acquisition methods for intraoperative re-registration," in *Medical Imaging 2018: Image-Guided Procedures, Robotic Interventions, and Modeling*, 2018, vol. 10576, p. 1057609.

Toward a knowledge-based framework for task automation in surgery

Michele Ginesi*, Daniele Meli*, Hirenkumar Nakawala*, Andrea Roberti*, Andrea Calanca, Paolo Fiorini

Department of Computer Science, University of Verona, Italy
paolo.fiorini@univr.it

INTRODUCTION

The automation of complex human tasks by an intelligent robotic system has been investigated widely in the last years, thanks to the advances in machine learning [1]. In surgery, many challenges are involved, including the design of a robotic system which executes safe and precise movements, understands the surgical workflow, makes autonomous decisions and adapts to unexpected changes within the environment, guaranteeing soundness and reliability. Fully automated robotic systems have been tested on real patients, notably in orthopaedics[1], e.g., for bone milling. However, interaction with soft tissues in complex and safety-critical surgical scenarios, e.g., laparoscopic surgery, is still a challenging task for an autonomous robot. Moreover, only elementary surgical tasks, e.g., needle insertion [2], have been automated. This paper addresses the automation of a complex task, where multiple actions must be coordinated. This requires the integration of different hierarchical layers, from the task-level reasoning on the model to the online adaptive motion planning, both depending on the continuous stream of sensor data. To test the feasibility of the proposed framework, we chose a prototypical peg transfer scenario from the Fundamentals of Laparoscopic Surgery (FLS), consisting of 4 different colored pegs and rings. The task consists of multiple pick-and-place in a pre-defined sequence, using a redundant manipulator. While several authors have tried to implement it, only partial automation has been achieved so far [3].

MATERIALS AND METHODS

An overall schema of the framework is shown in Fig. 1a. It consists of four units: a predefined *model* of the task, an *ontology-based reasoner* to drive the execution, a *camera* for sensing, and *Dynamic Movement Primitives (DMPs)* as motion planner. The task is modeled by a deterministic *Finite State Machine (FSM)*. Referring to the standard granularity levels in the description of the surgical workflow [4], the FSM defines the actions, namely the atomic operations to be performed in order to accomplish the task, as well as the switching conditions among them. The structure of the FSM is adapted from [5], where the two-arm execution is described. Each pick-and-place consists of four normal actions: *move* (the end effector goes to the ring), *grasp* (the gripper closes), *carry* (the end effector goes to the peg) and *leave ring* (the gripper opens). Anomalous events may be managed by task re-planning with recovery states in the FSM. The vision system

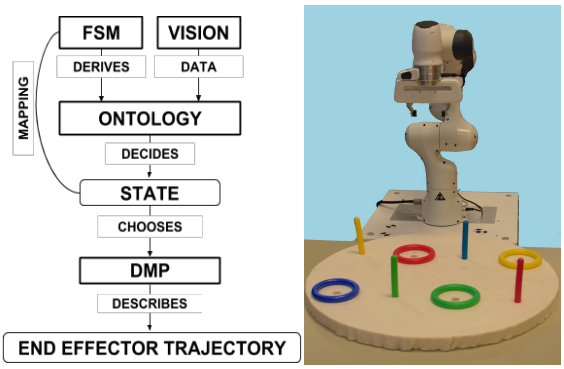

(a) (b)

Figure. 1. (a) Proposed framework for knowledge-based task automation; (b) experimental setup (the camera, in front of the robot, is omitted for visualization purpose).

consists of a hand-eye configuration with an RGB-D sensor which observes the entire scene. After having performed the calibration necessary to have a common framework for the robot and the camera, we segment and label the scene according to the requests sent by the ontology to identify the peg and the ring. Once the point cloud relative to the ring is obtained, we send it to Grasp Pose Detection (GPD) [6] algorithm; then we track the ring while approaching to the correct peg for checking correct execution. To monitor and execute the task, we designed an *ontology* which represents all possible entities (e.g., "Peg", "Ring", "Spatial information", "State", etc.) as abstract classes with properties (e.g., "hasColour", "hasShape", etc.), as well as states and transition rules from the FSM. Based on the task model and constraints, the ontology selects the current state to be executed and queries the vision system for object and target point detection. Detected objects are represented as instances of classes through symbolic anchoring and reasoning is performed on their properties. At each state of the FSM, a continuous trajectory has to be executed. To encode such trajectories, we decided to use the framework of DMPs [7]. DMPs allow learning a trajectory that is easily generalizable in space (different start and final position) and time (faster or slower execution). In the learning phase, the robot learned eight trajectories (one *move* and one *carry* for each color) via kinesthetic teaching. When a particular trajectory is needed (depending on the current state triggered by the ontology), its execution is generalized for the particular goal position (e.g., grasp point) provided by the reasoning engine.

RESULTS

Fig. 1b shows the real setup used to test the components of our framework, with a 7-DOF industrial manipulator

[1] TSolution One (https://thinksurgical.com/)

*authors contributed equally and in the alphabetical order

"Panda" from Franka Emika (Germany). The robot is controlled with a ROS/MoveIt interface. The FSM is implemented using SMACH package, while the ontology is encoded in RDF/XML (Resource Development Framework/eXtensible Markup Language), SWRL (Semantic Web Rule Language) rules, Pellet[2] reasoner and OWL API[3]. The point clouds are acquired from a calibrated RGB-D Intel Realsense D415 camera. We processed the data for tracking the rings using the Point Cloud Library (PCL) and OpenCV. The sequence of colors is red-green-blue-yellow. As shown in Fig. 3, we were be able to segment pegs and rings with the precision of 100%. Using our custom Cartesian DMPs[4], the robot is able to repeat human movements, while reacting instantaneously to high-level commands coming from the ontology reasoner, which analyzes the camera stream online. An example of trajectory generalization is shown in Fig. 2.

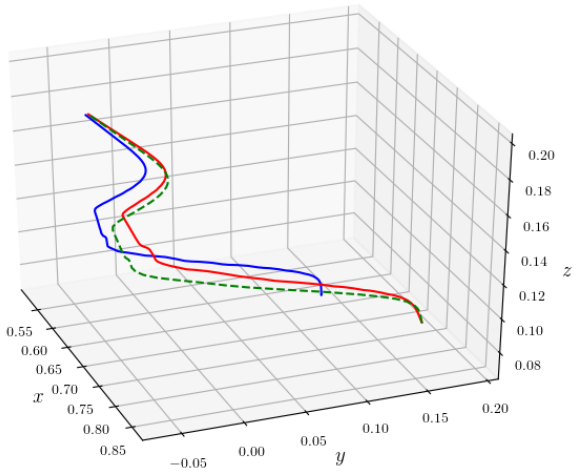

Figure. 2. Example of generalization of DMPs. The learned trajectory (*carry* of the green ring) is shown in blue, a different green carry (with different grasping and leaving points) is shown in red, while the generalization of the learned trajectory to the new critical points is shown in dashed green.

CONCLUSION AND DISCUSSION

In this work, the automation of a FLS peg-transfer task has been implemented on a real setup with a redundant manipulator. A novel hierarchical framework has been presented, integrating task-level ontology reasoning on a predefined task FSM with low-level information from the camera and adaptive motion planning with DMPs. This framework could be useful in real surgical applications, where safety shall be guaranteed by a supervisor model-based reasoning on real-time sensory information with reactive task and motion planning to crucially operate in uncertain dynamic environments. Moreover, DMPs can easily learn human movements, which is advantageous to replicate typical surgeons' gestures, e.g., knot-tying. To our knowledge, this is the first successful attempt to introduce full automation in a surgical relevant scenario. In the future, we will test this framework by adding uncertainties in the scenario (e.g., rings with different shapes and mixed colors) and handling exit conditions within the task. We will exploit the scalability of DMPs and ontology, and probabilistic information to reproduce the task with the da Vinci research kit (dVRK).

REFERENCES

[1] Galceran et al. "Multipolicy Decision-Making for Autonomous Driving via Changepoint-based Behavior Prediction: Theory and experiment" in Autonomous Robots, 2017, 41 (6): 1367-1382.

[2] Muradore et al. "Development of a cognitive robotic system for simple surgical tasks" in Int J of Advanced Robotic Systems, 2015, 12(4): 37.

[3] Berthet-Rayne et al. "Hubot: A three state Human-Robot collaborative framework for bimanual surgical tasks based on learned models" in Robotics and Automation (ICRA), 2016 IEEE International Conference on., 2016. p. 715-722.

[4] Lalys et al., "Surgical process modeling: a review" Int J CARS, 2014, 9 (3): 495-511.

[5] Hong et al., "Modeling of a transfer task in computer assisted surgical training" in MSM'16 Proceedings of the Modeling and Simulation in Medicine Symposium, 2016. p. 4.

[6] Pas et al. "Grasp Pose Detection in Point Clouds". The International Journal of Robotics Research, 2017, 36 (13-14): 1455-1473.

[7] Park et al. "Movement reproduction and obstacle avoidance with dynamic movement primitives and potential fields" in Humanoid Robots, 2008. Humanoids 2008. 8th IEEE-RAS International conference on. IEEE, 2008, pp. 91-98.

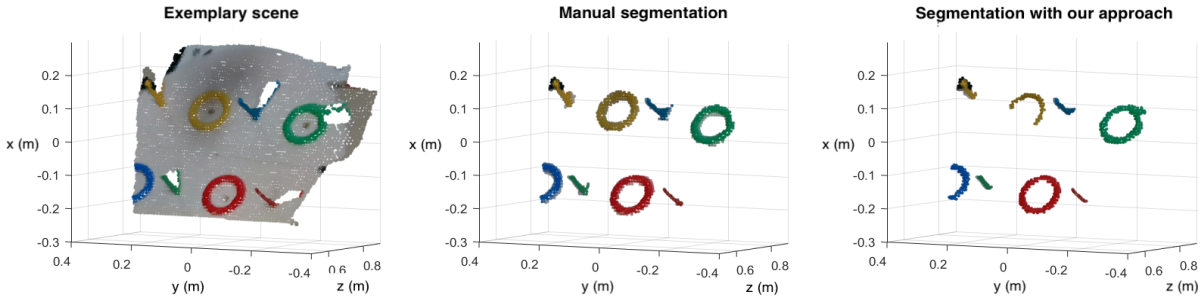

Figure. 3. Results on the segmentation of four rings and pegs. "Exemplary scene" shows an acquired raw point-cloud of the scene, "manual segmentation" was done by extracting the points that fall inside of a 2D polyline once it is projected on screen.

[2] https://www.w3.org/2001/sw/wiki/Pellet
[3] https://github.com/owlcs/owlapi
[4] https://github.com/mginesi/dmp

Intra-operative navigation in Minimally Invasive Surgery: accuracy assessment of the tracking performance of a surgical pointer

M. Aricò[1], G. Morel[1]

[1]*Sorbonne Université, CNRS, INSERM, ISIR-Agathe,*
mario.arico@sorbonne-universite.fr

INTRODUCTION

Laparoscopy is a minimally invasive technique in which surgery is performed by means of long, rigid instruments inserted into the patient's abdomen through a set of trocars. Although endoscopic cameras are used to provide visual feedback, the loss of direct vision makes this procedure complex to perform. Augmented Reality has proven beneficial in restoring visual information and providing intra-operative guidance (e.g., overlay pre-operative images on the surgical scene) [1]. During surgery, the surgeon might utilize the surgical instrument as an active pointer to modify the onscreen contents, to register new anatomical structures as points of interest, to draw [2] cutting trajectories, or to define forbidden areas. Pointers were first introduced in orthopedic surgery and for gait analysis [5] to register points over the bones surface and compute the rotation axes of a joint (e.g., knee). For a surgical tool to be used as a pointer two conditions apply: it is equipped with a marker whose 3D pose has to be measurable by a navigation system and the tip coordinates have to be estimated via a pre-calibrated transformation from the marker to the tip. In laparoscopy, instruments are tracked via optical or magnetic systems. Although these systems provide highly precise raw measures, the reconstruction accuracy is limited by geometric factors [4]. For example, for a standard 40cm-long laparoscopic tool, tip reconstruction errors can exceed 2mm [1]. In this case, the tool length imposes a distance between the markers and the tip, inducing a lever-like effect that magnifies the errors in the measures. In this study, we quantify these effects on the tracking performance of a pointer for Minimally Invasive Surgery (MIS). In a first phase, the pointer is calibrated using an optical tracking system. In a second phase, the pointer is manipulated and the tracking performance is evaluated. Moreover, we take into account whether calibrating the pointer in a specific area of the camera increases the performance with respect to a general calibration that spans the entire workspace.

MATERIALS AND METHODS

An instrumented (or navigated) pointer is a surgical tool used for the intra-operative estimation of the 3D position of anatomical landmarks. The pointer is equipped with a unique marker configuration identifying a local reference frame, whose pose is intra-operatively measured by the navigation system (frequently an infrared stereo-camera). The pointer tip is calibrated into this local frame and is used to estimate the coordinates of the point of interest:

$$^{w}\boldsymbol{P} = {}^{w}T_{in}\ {}^{in}\boldsymbol{P} \quad (1)$$

where $^{in}\boldsymbol{P}$ are the homogeneous coordinates of the tool tip in the marker frame, $^{w}T_{in}$ is the current homogeneous transform of the instrument marker and $^{w}\boldsymbol{P}$ are the resulting coordinates of the tip in the navigation system frame. The accuracy of the tip reconstruction (Eq. 1) is mostly influenced by geometric factors, such as the number and spatial distribution of the marker geometry and the relative marker-tip distance [4]. Other sources of error arise from the intrinsic accuracy of the navigation system and the calibration method. Calibration is usually carried out by pivoting the instrument around a fixed divot [3] and indirectly estimating the tip as the center of rotation. If the tip is directly measurable, the calibration is found by inverting the linear system of Eq. 1 and by averaging the results. Despite this direct end-effector measure, the tracking accuracy is still affected by non-linear errors due the distortions of the imaging system, which introduce rotation errors in the pointer pose [5], that are magnified at the tip level. The optimized pointer geometry would be obtained by equally spacing the markers around the tip [4]. However, in a MIS scenario, this is impossible as the markers are confined close the instrument handle, 40cm away from the effector.

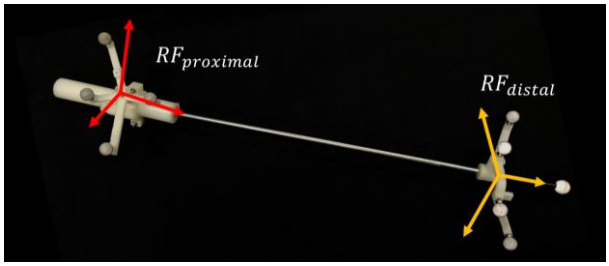

Figure 1. Laparoscopic pointer equipped with proximal markers (red frame, real surgical conditions), distal markers (yellow frame) and a fiducial at the end-effector as a ground truth.

The use of a laparoscopic instrument as an intra-operative pointer is, therefore, limited by the precision required in the current surgical task and the size of the region of interest: for instance, marking coarse boundaries for an organ requires less precision than targeting vessels or localize tumors. A quantitative evaluation of the tracking accuracy has been carried out by deploying the pointer shown in Fig. 1. It is a 40cm rigid instrument, equipped with two marker geometries; a proximal (P) geometry attached to the handle, and a distal (D) geometry close to the effector. Both geometries are composed of four markers. An ulterior marker represents the tip and provides the ground truth for comparative results. The

optical system Atracsys is used to track the surgical pointer. The system is characterized by a measurement accuracy comprised in the interval [0.09-0.15] mm RMS across the working volume. The experimental evaluation consists of two phases: the pointer calibration and the end-effector tracking. During the calibration phase, the optical tracker records the pointer movements to estimate the end-effector coordinates in the local frame. In the tracking phase, the pointer is manipulated through the trocar and the end-effector reconstruction is compared against its true position.

RESULTS

In the calibration phase, two conditions have been tested:

- The estimation of the proximal (P) or distal (D) marker geometry (see Fig. 1); the corresponding end-effector coordinates in this reference frame;
- The amplitude of the recorded movements. The first set of movements is recorded by spanning the entire working volume of the optical system (G). A second set of movements is recorded by manipulating the pointer through a trocar (T), therefore in a much narrower working volume.

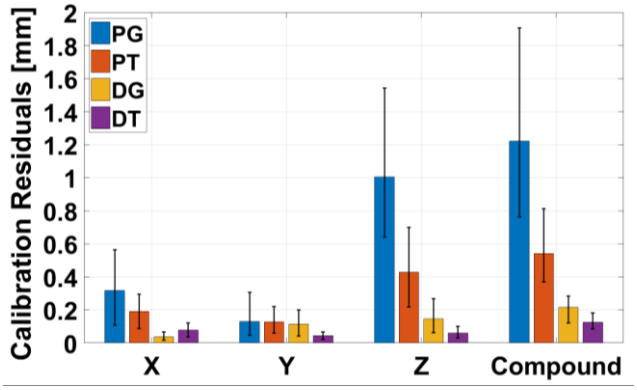

Figure 2. Component-wise and compound calibration residuals. Four configurations have been tested: Proximal (P) and Distal (D) marker positions; tool manipulation across the general workspace (G) and through a Trocar (T).

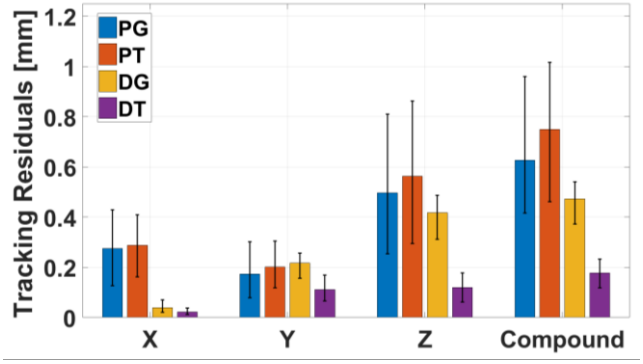

Figure 3. Component-wise and compound tracking residuals. Four configurations have been tested: Proximal (P) and Distal (D) marker positions; tool manipulation across the general workspace (G) and through a Trocar (T).

Results of the calibration phase are shown in Fig. 2: the accuracy is evaluated in terms of median residual error (bar height) and the 1st and 3rd quartiles of the distribution (whiskers). The use of proximal markers (blue and red bars) degrades the calibration accuracy, showing the negative impact of the tool length in locating the end-effector. Median errors go up to 1.2mm (Compound, blue bar), while are below 0.2mm when placing the markers as close as possible to the tip. This degradation effect is partially mitigated by manipulating the pointer through a trocar (blue vs red bars), therefore, performing the calibration in a restricted volume of the workspace of the optical system. Tracking results are shown in Fig. 3: the surgical pointer is manipulated through a trocar and the end-effector reconstruction is compared to the current measured position of the tip marker. Also in this tracking case, the highest accuracy is obtained in the distal configuration, where the length is reduced to less than 5cm. For proximal markers, 25% of the measures exceed 1mm tracking error (3rd quartile) attaining maximum values of 2.28mm and 1.85mm for the PG and PT configurations, respectively.

CONCLUSION AND DISCUSSION

A laparoscopic instrument can be used as intra-operative surgical pointer in Augmented Reality interfaces to register the coordinates of anatomical landmarks into pre-operative images. It might, also, be used as a tele-mentoring tool [2] to highlight relevant anatomies and to show correct gestures to novel surgeons. The pointer is tracked by the navigation system and the effector position is reconstructed via the pre-operative calibration. Despite the accuracy of the reconstruction depends on several factors, the main limitation is the instrument length, which account for errors exceeding 2mm. This degradation effect can be partially mitigated by performing the calibration in the same area of the camera workspace where the pointer will be tracked. Despite the high precision of the optical measurements, the uncertainty on the reconstruction does not enable the use of laparoscopic instruments as pointers to finely register anatomical structures.

REFERENCES

[1] Bernhardt, Sylvain, et al. "The status of augmented reality in laparoscopic surgery as of 2016." Medical image analysis 37 (2017): 66-90.

[2] Hung, Andrew J., et al. "Telementoring and telesurgery for minimally invasive procedures." The Journal of urology 199.2 (2018): 355-369.

[3] Yaniv, Ziv. "Which pivot calibration?" Medical Imaging 2015: Image-Guided Procedures, Robotic Interventions, and Modeling. Vol. 9415. International Society for Optics and Photonics, 2015.

[4] West, Jay B., and Calvin R. Maurer. "Designing optically tracked instruments for image-guided surgery." IEEE transactions on medical imaging 23.5 (2004): 533-545.

[5] Tawy, Gwenllian Fflur, and Philip Rowe. "Is the instrumented-pointer method of calibrating anatomical landmarks in 3D motion analysis reliable?" Journal of biomechanics 53 (2017): 205-209.

Design and Study of a Next-Generation Computer-Assisted System for Transoral Laser Microsurgery

N. Deshpande[1], A. Acemoglu[1], G. Peretti[2], F. Mora[2], L. Guastini[2], J. Lee[1], G. Barresi[1], D. G. Caldwell[1], and L. S. Mattos[1]

[1]*Advanced Robotics, Istituto Italiano di Tecnologia, Genova, Italy*

[2]*Department of Otorhinolaryngology, Università degli Studi di Genova, Genova, Italy*
nikhil.deshpande@iit.it

INTRODUCTION

With the introduction of the transoral laser microsurgery (TLM) in the field of surgical laryngology [1], the key surgical functions of control (laser manipulation) and perception (visualization of the site) have relied on the effective coordination of the following: (1) a manual laser micromanipulator (MaLM) to move the free-beam surgical laser (CO_2 is the prevalent variety) in an area about 20 x 20 mm^2, (2) visualization through a surgical microscope, and (3) laser activation through a footswitch. Towards addressing the challenges and limitations of this traditional setup, including problems of poor ergonomics and discomfort of operating in a constrained space, previous investigations by the authors of this paper have resulted in two prototypes that successfully replaced the manual mechanisms with stylus-based systems, providing heretofore-impossible levels of accuracy, uniformity, and ease-of-use [2-4]. Taking that previous research forward, the objective of this paper is two-fold:

(I) introducing the next generation Computer Assisted Laser Microsurgery (CALM) concept towards improving the usability, efficiency, and controllability; and

(II) presenting a first-of-its-kind study in characterizing the system through ex-vivo pig larynx trials with surgeon subjects.

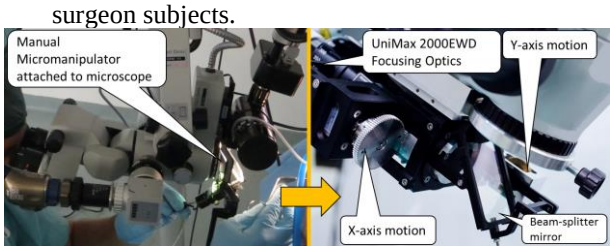

Figure. 1. *Left*: Traditional TLM setup; *Right*: CALM setup.

MATERIALS AND METHODS

The CALM Concept

Figure 1 shows the CALM concept. The concept includes the following components:

1. The novel motorized laser micromanipulator (MoLM) overcomes the limitations of earlier generation prototypes [4] by including a spherical orienting mechanism using anti-backlash gears and high-resolution encoders. The mechanism actuates the beam-splitter mirror in two orthogonal dimensions and is compatible with state-of-the-art commercial microscopes and laser systems. The MoLM provides high accuracy (35 µm), a working area (40 x 40 mm^2 @ 400 mm distance), and user-definable scanning speeds (up to 0.1 m/s).
2. A touch tablet with stylus controls the MLM device, aiming the surgical laser in real-time, replacing the MaLM.
3. State-of-the-art commercial equipment: (a) the Leica 2 surgical microscope for binocular surgical site visualization; (b) the UniMax 2000EWD reflective laser focusing optics; (c) the DEKA SmartXide2 C60 CO_2 laser system, with HiScan Surgical scanning unit; and (d) the footswitch activates the high power laser.

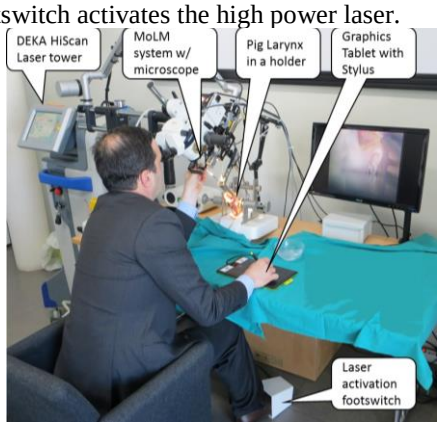

Figure. 2. Integrated CALM in simulated surgical scenario.

Figure 2 shows the integrated system. The CALM system offers an innovative feature: programmable scans for the laser beam, termed as *preview mode*. In this mode, the surgeon can intra-operatively program long incision paths of desired shapes using the stylus itself. The MoLM executes these paths automatically at user-definable speeds, giving the surgeon a preview of the intended cut.

Experiment Design

For evaluating the CALM system, a representative microsurgical setup was prepared. In a first-of-its-kind study, ex-vivo pig larynxes were utilized as simulated targets due to their resemblance to human larynxes. The arrangement of the experiment, the specially designed holder, and other details are seen in Figure 2. Fifty-seven international surgeons (average age = 41.33 years; 45 males, 12 females) from the laryngology and head & neck specialties were chosen as subjects. Based on their experience, the subjects were classified as: experts (10+ years TLM experience; 25 subjects) and non-experts (<10 years TLM experience; 32 subjects).

The non-expert subjects were asked to perform a partial cordectomy, incising one layer off the vocal fold mucosa. The expert subjects were asked to perform either a Type-

I or Type-II cordectomy. The surgeons used regular TLM microsurgical forceps for tissue manipulation. The subjects took 3-5 minutes to adapt to the CALM system with the stylus, before beginning the surgical trial. The subjects were asked to use the *preview mode* for incisions.

Subjective Measures

For the evaluations, a new questionnaire was devised based on System Usability Scale and NASA-TLX [5, 6], with a 7-point Likert scale. The questionnaire accounted not only for the ergonomics and intuitiveness aspects of the system, but also the suitability and perceived usefulness of the features of the system in relation to TLM. The questionnaire is listed in Table I.

Table. 1. Subjective Measures for CALM evaluation

Item	Question/Statement		Overall	Expert	Non-expert
	USABILITY				
S1.	It was easy to control/use the system.	Mean	6.30	6.44	6.19
		STD	1.17	0.96	1.33
S2.	I found this system was easy to learn, so I could start using it quickly.	Mean	6.58	6.72	6.47
		STD	0.75	0.46	0.92
S3.	I would like to use the system again for this kind of task.	Mean	6.32	6.24	6.38
		STD	0.94	1.09	0.83
S4.	My performance in this task with this system was satisfying.	Mean	6.26	6.28	6.25
		STD	0.85	0.89	0.84
S5.	I would recommend this system to a colleague.	Mean	6.04	5.88	6.16
		STD	0.14	1.36	0.95
	CONTROLLABILITY				
S6.	The system control was precise.	Mean	6.25	6.08	6.38
		STD	0.92	1.04	0.83
S7.	The system was safe to use.	Mean	6.02	6.00	6.03
		STD	1.67	1.68	1.71
S8.	It was easy to make errors with this system.	Mean	2.37	2.80	2.03
		STD	1.46	1.56	1.33
	WORKLOAD				
S9.	The control of the system induced fatigue in my hand.	Mean	1.60	1.60	1.59
		STD	1.14	1.26	1.07
S10.	Maintaining attention to what I was doing was difficult.	Mean	1.72	1.84	1.63
		STD	1.21	1.46	1.01
S11.	I was stressed, irritated, and annoyed using this system during the task.	Mean	1.23	1.12	1.31
		STD	0.65	0.33	0.82
	SUITABILITY TO TLM				
S12.	The system allows laser operations not previously possible.	Mean	3.44	3.48	3.41
		STD	1.71	1.83	1.66
S13.	The system is not appropriate for fine resections.	Mean	1.86	2.32	1.50
		STD	1.26	1.57	0.84
S14.	The system is an improvement over current laser microsurgery devices.	Mean	6.04	5.80	6.22
		STD	1.12	1.29	0.98
S15.	The system does not allow all laser operations I am used to performing.	Mean	2.26	2.64	1.97
		STD	1.92	2.16	1.71
S16.	The system is appropriate for large resections.	Mean	5.93	6.00	5.88
		STD	1.41	1.26	1.56

RESULTS

Table I shows the overall results for the questionnaire.

Usability Sub-group: The average score here is 6.29 (sd= 0.97). All 5 statements show a favourable scoring, close to the high score.

Controllability Sub-group: The system scored an average 5.96 (sd= 1.35). Even so, all 3 statements are scored favourably for the positive and negative statements.

Workload Sub-group: Here, the system scored an average of 1.51 (sd= 0.99) demonstrating a favourable evaluation of the system in terms of mental and physical workload.

Suitability to TLM Sub-group: The average score for suitability is 5.46 (sd= 1.48). Although most sub-scales are evaluated favourably, the sub-scale on the possible surgical operations with CALM shows uncertainty, at 3.44 (sd= 1.70; p= 0.117).

Expert vs. Non-expert Surgeon Scores

The non-parametric Wilcoxon Rank Sum test was used to compare the scores of experts vs. non-experts. Table I shows the differences.

Usability: Here, the experts and non-experts assign scores that are statistically indistinct: ease-of-use (p= 0.4453), easy-to-learn (p= 0.5056), and satisfactory in performance (p= 0.7346).

Controllability: The simulated testing scenario implies a divergence of opinion (p= 0.0386) indicating that the experts do not agree with the non-experts significantly. Even so, both the safety and error sub-scales show agreement.

Workload: The experts agree that the system is comfortable and not stress-inducing. The ease-of-attention sub-scale is scored favorably (p= 0.9797).

Suitability: As seen, the experts' scores agree with the overall scores for CALM's improvement and suitability to large resections. Yet, the experts diverge from the non-experts for the system permitting fine resections (p= 0.0107). On deeper consultation, the experts noted the limitation of the system not being able to orient the high-speed scan patterns easily.

CONCLUSION AND DISCUSSION

The CALM concept allows surgeons to perform operations using a stylus instead of the traditional manual micromanipulator joystick, making laser aiming more intuitive and consistent. It augments the surgeons' fine manual skills through gesture scaling and magnification, thereby improving safety of the surgical procedures. The system offers automatic execution of intra-operative, programmable scans (*preview mode*) combined with the high-speed scanning feature. The subjective evaluation with 57 international surgeons demonstrated the preference for the CALM system in TLM, especially with respect to ease-of-use, ease-of-learning, safety, reduced mental effort, and its suitability for the execution of uniform, fine, and long resections. It is now important to account for the limitations of the system and the feedback from the surgeons to improve CALM for TLM.

REFERENCES

[1] Strong MS, Jako GJ. Laser surgery of the larynx: early clinical experience with continuous CO2 laser. The Annals of Otology, Rhinology, and Laryngology 1972; 81:791-798.

[2] Mattos LS, Dagnino G, Becattini G, Dellepiane M, Caldwell DG. A Virtual Scalpel System for Computer-assisted Laser Microsurgery. Proceedings of Intl. Conf. on Intelligent Robots and Systems (IROS 2011); 1359–1365.

[3] Mattos LS, Deshpande N, Barresi G, Guastini L, Peretti G. A Novel Computerized Surgeon-Machine Interface for Robot-assisted Laser Phonomicrosurgery. The Laryngoscope 2014; 124(8):1887-1894.

[4] Deshpande N, Mattos LS, Caldwell DG. New Motorized Micromanipulator for Robot-assisted Laser Phonomicrosurgery. Proceedings of Intl. Conf. on Robotics and Automation (ICRA 2015); 4755-4760.

[5] Brooke J. SUS: a "quick and dirty" usability scale. In: Jordan PW, Thomas B, Weerdmeester BA, McClelland AL, eds. Usability Evaluation in Industry. 1996:189-194, Taylor & Francis, London, UK.

[6] Hart SG, Staveland LE. Development of NASA-TLX (Task Load Index): Results of Empirical and Theoretical Research. In: Hancock PA, Meshkati N, eds. Advances in Psychology: Human Mental Workload. 1988; 52:139-183.

A Hybrid Visual Servoing Approach for Robotic Laser Tattoo Removal

D. Salerno[1,3], V. Penza[1], C. Fantacci[2], A. Acemoglu[1], G. Muscato[3], L. S. Mattos[1]

[1]*Biomedical Robotics Lab, Advanced Robotics, Istituto Italiano di Tecnologia, Genova*

[2]*Humanoid Sensing and Perception, Istituto Italiano di Tecnologia, Genova,*

[3]*DIEEI, Università degli Studi di Catania, Catania.*
damiano.salerno@iit.it

INTRODUCTION

According to a survey conducted in 2015 by The Harris Poll, 29% of US adults have at least one tattoo with an increase of 8% from 4 years earlier. It is very popular among young people, with nearly half of millennials reporting having at least one tattoo [1]. However, human nature is inclined to changes: one-fourth of people with tattoos regret getting them, and the increasing demand of tattoo removal creates the need of non-invasive techniques. Recent advances have led to the use of more efficacious laser technologies, which present fewer side effects with respect to surgical excision, dermabrasion, and chemical destruction, many of which cause damages to surrounding tissue [2]. However, the current practice has some drawbacks: (i) dependence on the manual skills of the medical doctor, (ii) pain during the procedure, and (iii) need of more than one treatment for a complete tattoo removal, affecting the patient psychologically, physically and socially.

This paper introduces *DeTattoo*, an innovative system to autonomously perform laser tattoo removal by automatizing and optimizing the treatment. The system combines robotics and image processing in order to (i) identify the tattoo, (ii) plan the optimal laser path to avoid tissue thermal damage and (iii) control the robotic arm and laser scanning system [3] to accurately perform the laser tattoo removal. Image processing is used to identify salient characteristics of the unknown tissue surface and to define the trajectory to follow. The final aim of this system is to achieve the following benefits compared to the current procedure: a reduced number of treatments due to an improvement in the removal strategy and reduced tissue damage due to a precise and automatic laser positioning, with an error in the order of the millimeter.

This work is focused on the control of a robotic arm to accurately position the laser scanning system based on visual feedback information. To jointly maximize the laser efficiency and minimizing thermic tissue damages, the control strategy has to guarantee the correct pose of the laser with respect to the tattooed tissue while compensating body motions. To this end, preliminary results of a hybrid visual servoing approach, validated in a simulated environment, are presented.

MATERIALS AND METHODS

The system setup is shown in Fig. 1. A robotic arm is equipped with an RGB-D camera and a magnetically actuated laser scanning system [3]. An *eye-in-hand* configuration [4] is used in order to avoid target occlusion during the execution of the trajectory.

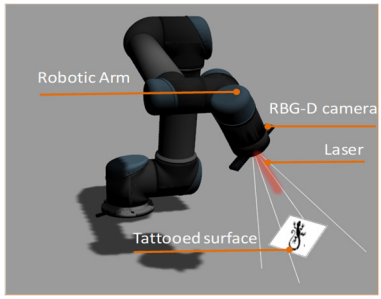

Figure 1 *DeTattoo* system.

A vision-based control strategy is necessary to ensure:

- A constant laser-tissue working distance;
- Laser perpendicularity to the surface;
- Compensation of body motion during the operations.

The aim of vision-based control schemes is to define a relationship between the end-effector velocity and changes that occur in the observed object, in order to minimize an error $e(t)$ [4], defined as:

$$\boldsymbol{e(t) = s - s^*}$$

where $\boldsymbol{s}$ is the vector of k visual and/or geometrical features identified in the object and $\boldsymbol{s^*}$ contains their desired values. In *image-based visual servoing (IBVS)* [4], $\boldsymbol{s}$ consists of a set of visual features extracted from the image and consequently its error trajectory is defined in the image plane. *IBVS* relies on the online calculation of the *image (or feature) Jacobian* and on the distance between the target object and the camera, which may be difficult to estimate [5]. In *position-based visual servoing (PBVS)* [4, 5], $\boldsymbol{s}$ consists of a set of 3D parameters estimated from image measurements, and its error trajectory is defined in the Cartesian frame. PBSV depends on the optical parameters of the visual system and it is very sensitive to calibration errors [5]. To overcome these drawbacks, $2\,^1/_2\,D$ *hybrid visual servoing approach* was introduced in [6], combining a set of 2D and 3D features in $\boldsymbol{s}$. This approach combines object pose estimation and image information, improving the robustness of the control.

Keeping into account the aforementioned considerations, a *hybrid approach* has been chosen to control the robotic arm based on the information retrieved from the RGB-D camera. In the contest of our application, the object shape (i.e., the tattooed surface to scan) is unknown and 2D and 3D features must be detected online.

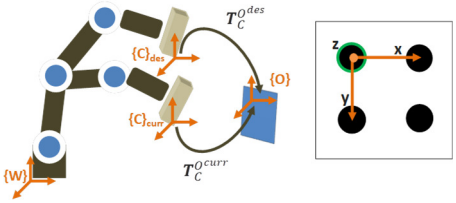

Figure 2 Reference frames and transformation involved in the computation of the object pose {O} with respect to the camera frame {C}.

2D feature extraction: RGB images are used to extract 2D features. At the current development of the system, a flat chessboard is used as the tattooed surface with black circles as features (see Figure 2). Initial position of the features in the image is set manually, followed by an automatic segmentation and tracking during the process. 3D feature extraction: depth images provided by the RGB-D camera are used to obtain a 3D reconstruction of the object and to extract the following 3D features:

- *Orientation* (θu) expressed as axis/angle parametrization of the rotation that the camera has to perform to reach the desired pose. It can be defined as:

$$T_{curr}^{des} = T_C^{O^{des}} \cdot T_O^{C^{curr}}$$

where $T_C^{O^{des}}$ and $T_C^{O^{curr}}$ are respectively the desired and current transformation between the camera and the object, as shown in Fig. 2. The object pose, thus, has to be computed. The origin of its reference frame $\{O\}$ is placed on the selected feature. The z axis is considered as the normal of the plane estimated from a subset of neighbor 3D points using RANSAC. x and y axes are taken as the projection of the camera axes, assuring orthonormality with z axis.

- *Depth* which defines the current depth (z) with respect to the desired depth (z_d) as $log\frac{z}{z_D}$.

The resulting vector of features is expressed as:

$$s = \left[x, y, \theta u_x, \theta u_y, log\frac{z}{z_D}\right].$$

Based on this set of features, the laser positioning relies on 2D feature coordinates and depth, while the laser orientation with respect to the object is assured with θu estimation. A velocity controller is used to control the robot trajectory. The camera spatial velocity is denoted by $\boldsymbol{v}_c = (v_c, w_c)$. The relationship between $\dot{s}$ and $\boldsymbol{v}_c$ is:

$$\dot{s} = L_s \boldsymbol{v}_c$$

where $L_s \in \mathbb{R}^{kx6}$ represents the *interaction matrix*. Considering $\boldsymbol{v}_c$ as input to the robot controller, and to ensure an exponential decrease of the error (i.e., $\dot{e} = -\lambda e$), we obtain:

$$\boldsymbol{v}_c = -\lambda L_s^{\dagger} e$$

Using the robot Jacobian (J^W) and the transformation (V_W^C) between the camera {C} and the robot {W}, joint velocities are computed as:

$$\dot{q} = (J^W)^{-1} V_W^C v_c .$$

RESULTS

The system was simulated in Gazebo - ROS Kinetic on Ubuntu 16.04. It is composed of Universal Robot UR5 and RealSense Depth Camera D435. ViSP library (https://visp.inria.fr/) is used for the visual servoing control, while the image processing is managed with OpenCV and PCL libraries (http://pointclouds.org/). Performances of the object pose estimation and control system have been evaluated varying the orientation of the chessboard on x or y axis (30°, 45°, 60°) and measuring three errors: (i) object pose error in terms of estimated *normal*, (ii) error between current and desired *2D feature* and (iii) *depth* error. z_D is set to 0.35 m, while λ is equal to 1.2. The execution of the system is stopped when *2D feature* error is $< 1\ mm$, orientation error $< 0.001°$ and *depth* error $< 0.1\ mm$. Errors averaged over 12 trials are reported in Table 1.

Table 1 Averaged errors involved in the object pose estimation (Normal) and control strategy (2D Point, Depth).

		x axis rotation [°]			y axis rotation [°]		
Errors		**30**	**45**	**60**	**30**	**45**	**60**
***normal* [°]**		-0.37	0.001	0.27	-1.68	-1.62	-1.73
***2D feature* [mm]**	x	-0.969	0.436	0.443	-0.192	-0.041	0.036
	y	0.067	0.162	0.097	0.096	-0.980	0.401
***depth* [mm]**		$1.37e^{-5}$	$1.37e^{-5}$	$1.37e^{-5}$	$1.37e^{-5}$	$1.37e^{-5}$	$1.37e^{-5}$

CONCLUSION AND DISCUSSION

This paper presented a preliminary evaluation of a hybrid visual servoing approach to control the motion of a robotic arm for laser tattoo removal in a simulated environment. The proposed implementation uses a combination of online estimated 2D and 3D features to demonstrate the potential to fulfil the *DeTattoo* requirements of a constant laser-tissue working distance, laser perpendicularity to the surface and motion compensation. The global positioning error in the order of sub-millimeters and the orientation error less than 0.1° satisfy the application requirements. Future work will focus on the improvement and validation of this algorithm on a synthetic real scenario, integrating more advanced vision processing for automatic tattoo segmentation and tracking.

REFERENCES

[1] Naga L. I., and Tina S. A. "Laser tattoo removal: an update." American journal of clinical dermatology 18.1 (2017): 59-65.

[2] Bernstein, E.F. "Laser tattoo removal." Seminars in plastic surgery. Vol. 21. No. 3. Thieme Medical Publishers, 2007.

[3] Acemoglu A., Deshpande N., and L.S. Mattos. "Towards a Magnetically-Actuated Laser Scanner for Endoscopic Microsurgeries." *Journal of Medical Robotics Research* 3.02 (2018): 1840004.

[4] Chaumette, F., & Hutchinson, S. (2006). Visual servo control. I. Basic approaches. IEEE Robotics & Automation Magazine, 13(4), 82-90.

[5] Chaumette, F., & Hutchinson, S. (2007). Visual servo control, Part II: Advanced approaches. IEEE Robotics and Automation Magazine, 14(1), 109-118.

[6] E. Malis, F. Chaumette and Sylvie Boudet, "2 1/2 D Visual Servoing", *IEEE Transactions on Robotics and Automation*, vol. 15, no.2, pp. 238-250, 1999.

A Robotic Platform for Neuroendoscopic Procedures in Neo-Natal and Infants

Nabeel Kamal[1], Armando Cama[2], Leonardo S. Mattos[1]

[1]*Istituto Italiano di Tecnologia, Genoa, Italy*

[2]*Istituto Giannina Gaslini, Genoa, Italy*

nabeel.kamal@iit.it

INTRODUCTION

It has been more than three decades since the inception of robotic surgery. However, literature on robotic surgery on neo natal and babies are still noticeably absent [1]. This is the case especially for neurological surgery, which was the application area of the first recorded robotic surgery: a neurological biopsy performed in 1985 [2]. The robot was only used as a stable platform, which could be oriented according to need. Soon after, in 1987, NeuroMate was introduced as the first commercially available image-guided neurosurgical robot [3]. Another early neurosurgical robot, the Minerva [4], was guided using intraoperative images, but the surgery had to be performed inside a CT scanner.

Before neurosurgical robots, surgeons performed freehand neuroendoscopy. At that time, the quality of surgery mostly depended on the experience and skills of the individual surgeon. Luckily, robotic technology for neurosurgery advanced at a relatively quick pace [5], bringing accuracy, precision, enhanced dexterity and reducing the invasiveness of these surgeries [6], [7].

Today, robotic systems are regularly used in several neurosurgical procedures such as neurological biopsies, deep brain stimulation (DBS), hydrocephalus, stereo electroencephalography (SEEG) and Endoscopic Third Ventriculostomy (ETV). The latter is, in fact, one of the most common minimal invasive transcranial surgeries. It is practiced since 1923 [8].

Neurosurgical robots improved ETV enormously. Today, there are a number of commercially available robots that can assist such procedures, including Medtech's Rosa, Renishaw's Neuromate and iSYS's iSYS1. These systems can be used for children and adults, but are not appropriate for young babies and newborns. The reason is the delicate nature and softness of the skull of these very young patients. This makes it impossible to use stereotactic frames. Moreover, bone markers cannot be used in neo-natal surgeries. Thus, no option is left for treating Hydrocephalous and performing ETV besides free hand endoscopy.

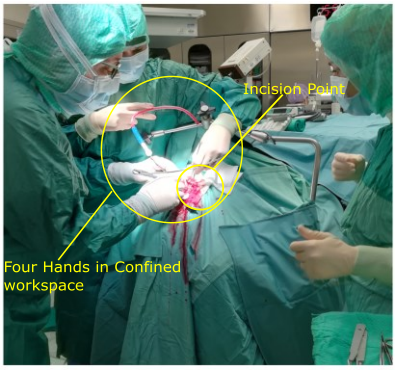

Figure 1. Manual Endoscopic Third Ventriculostomy.

At this time, no commercial robot exists for pediatric neurosurgery, forcing surgeons to perform the operations freehand as in the early days of adult neurosurgery. Further challenges include the need for teamwork (two or three surgeons) in a small workspace (Fig. 1); very small operating area (the diameter of babies' heads are about 10-12cm); and the absence of optimal (rigid and robust) endoscope holders. These challenges and the typical long operating time (about 3-4 hours) make procedures like ETV extremely difficult for surgeons.

Some of the reasons for the lack of surgical robots for pediatric neurosurgery are the need to lock the patients head in space and the size of the robots, which are enormous comparable to the size of the patients. The robots must also have enough clearance from other instruments in the operating room [1]. Nonetheless, the need for robot assistance in these delicate operations is clear, which justify investments towards the development of a robotic platform for this specific patient group.

ROBOTIC SYSTEM REQUIREMENTS

The design of the new robotic platform started with observing real surgeries and the environment of the operation room (OR). An analysis of the current state of the art surgical setup allowed the definition of major requirements to guide such design. These include the size of the workspace, the required number of degrees of freedom, the range of motion and the size of the robot required for ETV and cerebral shunt.

MRI images from babies' were used to calculate the ideal workspace of the robotic system. The MRI's were also helpful in defining the kinematic workspace for the end effector as shown in Figure 2.

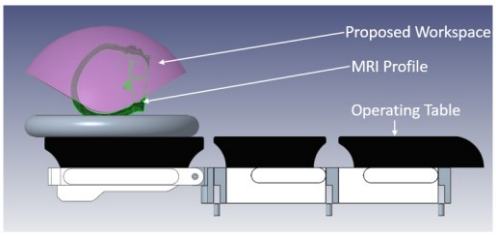

Figure 2. Required kinematic workspace.

Table 1. Design Specifications

#	Design Specification	Value
1	Max. robot size	1000 x 1000 x 600 mm
2	Degrees of Freedom	6
3	Precision	100 microns

For maximizing the potential surgical indications, the robotic system should provide sufficient degrees of freedom to safely reach lesions anywhere inside the skull. This means that the system should have at least 6 degrees of freedom (DOF). In addition, the DOFs must be sufficiently rigid to provide a stable support to the endoscopic tools during surgery. However, they must also allow fine intraoperative adjustments through a Remote Center of Motion (RCM) at the incision point. Finally, the robotic system must not interfere with the electromagnetic neuro-navigation system used during the procedures.

This analysis lead to the definition of the design specifications presented Table 1.

ROBOTIC SYSTEM DESIGN

To satisfy the system requirements, we propose the development of a system with completely decoupled six DOFs. The structure's RCM is established by using a semicircular rail placed on a rotational axis. The iso-center of this structure is the RCM of the system, which can be maintained fixed in space while allowing pitch, yaw and translation through this point. To keep the system simple and sleek, it is designed to be anchored to the neurosurgical bed.

The precise positioning of the RCM on the skull's incision point is achieved through three linear axes that can be independently actuated and locked in position. All actuation mechanisms are positioned under the surgical bed, keeping the workspace as free as possible for the surgical team and minimizing disruptions to the surgical workflow.

To avoid interference to navigation equipment, the robotic system will be fully constructed using non-magnetic stainless steel and plastics.

RESULTS

The robotic system was completely designed using CAD and its kinematic structure and workspace were successfully validated through simulations. Preliminary analysis indicates it is more rigid and stable than currently used tool holders.

Subsequently, an initial proof-of-concept prototype was developed using stereolithography (Figure 3). The size of the robot above the operating table is only 380 x 612 x 167 mm and the phantom of the baby is actual size. This prototype allowed physical verification of the system with pediatric neurosurgeons and a newborn baby phantom. Positive feedback was received and now the system is being manufactured using proper materials and tolerances.

Figure 3. Scale down Proof-of-Concept of Robotic System

DISCUSSION AND CONCLUSION

A novel robotic system for pediatric neuroendoscopy was designed based on a close collaboration between neurosurgeons and engineers. The initial proof of concept prototype validated the proposed kinematic structure and demonstrated the decoupled DOFs. The prototype also demonstrated to be a potential efficient replacement for the conventional tools, offering all the degrees of freedom and precision required for delicate pediatric neurosurgeries. The next step of this research will focus on verifying the achievement of the design specifications and the usability of the system, which is expected to be useful also for Ventricular Shunt, Biopsy, Deep Brain Stimulation and Needle insertion.

REFERENCES

[1] J. J. Meehan, "Robotic Surgery for Pediatric Tumors," *Cancer J.*, vol. 19, no. 2, pp. 183–188, 2013.

[2] Y. S. Kwoh *et al.*, "A robot with improved absolute positioning accuracy for CT guided stereotactic brain surgery," *IEEE Trans. Biomed. Eng.*, vol. 35, no. 2, pp. 153–160, 1988.

[3] A. L. Benabid *et al.,* "Computer-driven robot for stereotactic surgery connected to CT scan and magnetic resonance imaging. Technological design and preliminary results.," *Appl. Neurophysiol.*, vol. 50, no. 1–6, pp. 153–4, 1987.

[4] D. Glauser, H. Fankhauser, M. Epitaux, J. -L. Hefti, and A. Jaccottet, "Neurosurgical robot Minerva: First results and current developments," *J. Image Guid. Surg.*, vol. 1, no. 5, pp. 266–272, 1995.

[5] M. Hoeckelmann, I. J. Rudas, P. Fiorini, F. Kirchner, and T. Haidegger, "Current capabilities and development potential in surgical robotics," *Int. J. Adv. Robot. Syst.*, vol. 12, 2015.

[6] S. Lama and G. R. Sutherland, "Robotics for Image-Guided Neurosurgery," in *Image-Guided Neurosurgery*, Elsevier, 2015, pp. 475–497.

[7] C. S. Karas and E. A. Chiocca, "Neurosurgical robotics: a review of brain and spine applications," *J. Robot. Surg.*, vol. 1, no. 1, pp. 39–43, Mar. 2007.

[8] Y. Yadav, V. Parihar, S. Pande, H. Namdev, and M. Agarwal, "Endoscopic third ventriculostomy," *J. Neurosci. Rural Pract.*, vol. 3, no. 2, p. 163, 2012.

Robotic Control of All-Optical Ultrasound Imaging

G. Dwyer[1], E.J. Alles[1], R.J. Colchester[1], E. Maneas[1], S. Ourselin[2], T. Vercauteren[2],
J. Deprest[3], E. Vander Poorten[4], P. De Coppi[1], A.E. Desjardins[1], D. Stoyanov[1]

[1]*Wellcome / EPSRC Centre for Interventional and Surgical Sciences, University College London*

[2]*School of Biomedical Engineering and Imaging Sciences, Kings College London*

[3] *Dept. Obstetrics and Gynaecology, University Hospital Leuven,*

[4] *Dept. Mechanical Engineering, KU Leuven*

george.dwyer@ucl.ac.uk

INTRODUCTION

Many surgical procedures are performed minimally invasively, with the use of miniaturised devices, such as catheters and endoscopes. One such procedure is fetoscopy for both diagnostic and therapeutic purposes. Miniature imaging probes are essential for procedures performed during pregnancy to avoid surgical complications and improve outcomes. Current instrumentation is based on thin rigid endoscopes comprising working channels that can be used to deliver instrumentation into the workspace.

Recent research has focused on improving intrauterine visualisation; one such way is using all-optical ultrasound (OpUS), where ultrasound is both generated and received using light [1]. OpUS can provide high resolution imaging from small form factor devices. Current devices typically contain a single transducer element and hence provide only A-scans. Combination with robotics shows potential for performing accurate imaging sweeps during surgical procedures [2].

This paper presents the design and operation of a rigid, robot-mounted endoscope that integrates an OpUS sensor. Through a ROS interface, A-scans and kinematic information are acquired simultaneously and in real-time during robotic manipulation. After performing a calibration between the sensor and the robot, a tissue mimicking phantom with anatomically realistic vascular structures was imaged using various scanning trajectories, and the resulting 3D data were collected, processed and displayed in real-time.

MATERIALS AND METHODS

An instrument with a diameter of 5mm and length of 300mm was developed with a stainless-steel shaft. The tip of the endoscope was printed in stainless steel with channels for a stereo CMOS camera (Naneye Stereo, ams AG, Austria), fibre optic lighting channels, and a 1.1mm working channel. The instrument shaft is held in a housing made from PLA using an Ultimaker 3, (Ultimaker BV, Netherlands), this housing provides the interface to mount the instrument to a robot flange.

An all-optical ultrasound probe comprising a fibre optic ultrasound transmitter and a fibre optic ultrasound receiver was fabricated. The two optical fibres were held adjacent, and heat shrink tubing was used to align their distal end surfaces. This pair of optical fibres was housed within an acoustically transparent polymer tube (TPX, outer diameter: 1.2mm) for robustness. This OpUS imaging probe achieved an axial imaging resolution of 60μm[3]. In this instance, the OpUS sensor could not be placed within the working channel of the endoscope due to the protective TPX sheath around the sensor. It was therefore mounted to the side of the instrument shaft, thus increasing the overall diameter of the endoscope to 6.2mm. The assembled endoscope, which can be seen in Fig. 1, was mounted to a KUKA LBR iiwa 14 R820 robotic manipulator (KUKA AG, Germany), which is a 7 DOF manipulator with a payload of 14kg, a repeatability of ±0.15mm, and a reach of 820mm.The instrument is controlled through a ROS interface, where the robot manipulator is controlled through a high speed joint interface (500hz, Fast Robot Interface, Kuka). The instrument is constrained to a virtual Remote Centre of Motion (RCM) placed at the incision point on the body using a custom written interface based on the motion planning framework MoveIt. A-scans are sent from the OpUS processing cart using the LabVIEW ROS package, where each A-scan is converted to a point cloud message in the RCM coordinate system and published. These A-scans are then cumulatively merged as they are published and processed through a voxel filter to prevent overlapping points.

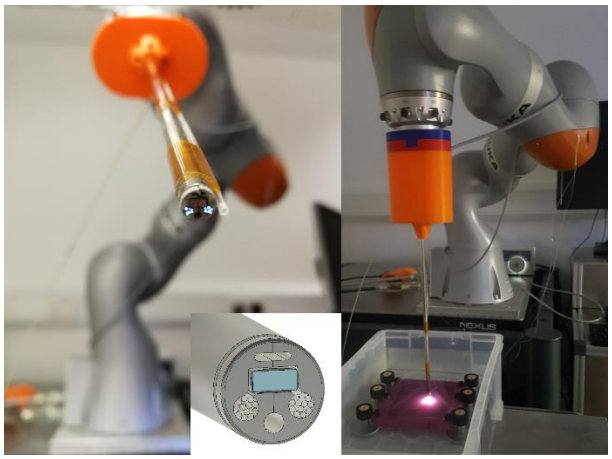

Figure. 1. Left - close-up of assembled endoscope tip showing the Naneye stereo camera, lighting channels, OpUS imaging probe and robotic manipulator. **Inset -** CAD model of endoscope tip. **Right -** Photograph of the rigid endoscope positioned above an acoustic placenta phantom.

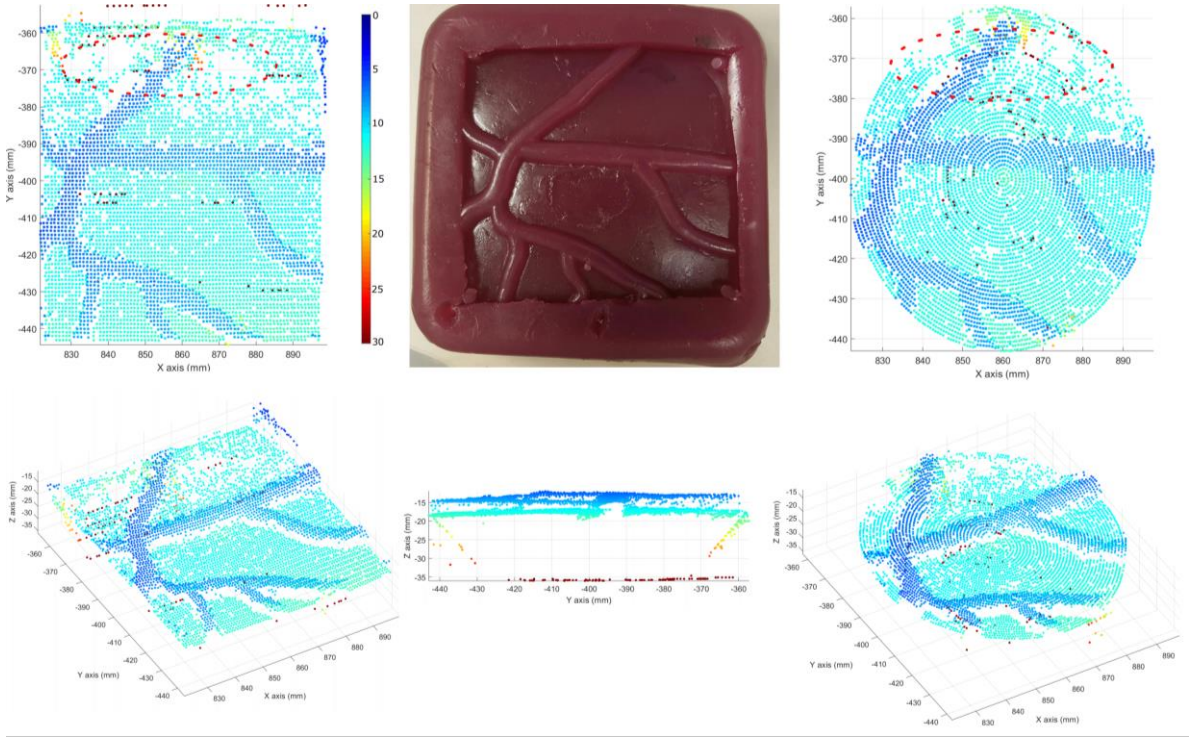

Figure. 2. 3D visualisation of the OpUS images of the placenta phantom acquired through robotic probe manipulation. A photograph of the ultrasound placenta phantom is shown in the centre of the top row **Left column -** 3D OpUS images obtained using a raster scan pattern, in top-down (top) and angled (bottom) view. **Right column -** 3D OpUS images obtained using a spiral scan pattern. **Bottom centre -** side-view of the 3D OpUS image obtained using a spiral scan pattern. In each image the distance of the points from the endoscope tip are colour-encoded using the colourbar (in mm) displayed in the top left panel.

RESULTS

A placenta phantom was fabricated using gel wax as a tissue-mimicking material. The phantom featured clinically realistic acoustic properties such as propagation speed of sound, echogenicity, and speckle pattern [4]. This phantom was placed into a water bath onto an acrylic sheet and clamped down with metal posts along the side of the phantom.

The phantom was scanned using the endoscope with two independent scanning trajectories: a raster and a spiral trajectory. The RCM was placed approximately in the center of the phantom and 160mm above the phantom. The raster scan was generated on a plane over the entire 80mm x 80mm area in 1mm increments at approximately 10mm from the phantom. The spiral scan was limited to a total diameter of 80mm and comprised 40 cycles around the start point to yield a similar scan point density. The resulting 3D OpUS images are shown in Fig. 2.

CONCLUSION AND DISCUSSION

This paper has presented the design, control, and operation of a multimodal robotic endoscope with integrated white light and optical ultrasound imaging. The endoscope consists of a miniature stereo camera, fibre optic light channels and an optical ultrasound sensor within a 6.2mm overall diameter; whilst being manipulated by a robot arm, constrained through software to a RCM.

The endoscope is demonstrated through generating scanning paths over a gel wax placenta phantom. A-scans acquired by the OpUS sensor are processed into 3d surfaces using the kinematics of the endoscope. The vessels can be clearly discriminated from the main body of the placenta. To the authors' knowledge, the OpUS scans presented in Fig. 2 are the largest presented in literature. Future work will focus on minaturisation of the endoscope while introducing an internal channel for the OpUS sensor together with therapeutic laser light delivery. In addition, the integration between the imaging sensors and robot manipulator will be utilised to constrain the robot to the surgical scene and to introduce adaptive scanning and treatment trajectories.

REFERENCES

[1] R. J. Colchester, E. Z. Zhang, C. A. Mosse, P. C. Beard, I. Papakonstantinou, and A. E. Desjardins, “Broadband miniature optical ultrasound probe for high resolution vascular tissue imaging,” *Biomed. Opt. Express*, vol. 6, no. 4, p. 1502, Apr. 2015.

[2] C. Gruijthuijsen, R. Colchester, A. Devreker, A. Javaux, E. Maneas, S. Noimark, W. Xia, D. Stoyanov, D. Reynaerts, J. Deprest, S. Ourselin, A. Desjardins, T. Vercauteren, and E. Vander Poorten, “Haptic Guidance Based on All-Optical Ultrasound Distance Sensing for Safer Minimally Invasive Fetal Surgery,” *J. Med. Robot. Res.*, p. 1841001, Mar. 2018.

[3] M. C. Finlay, C. A. Mosse, R. J. Colchester, S. Noimark, E. Z. Zhang, S. Ourselin, P. C. Beard, R. J. Schilling, I. P. Parkin, I. Papakonstantinou, and A. E. Desjardins, “Through-needle all-optical ultrasound imaging in vivo: a preclinical swine study,” *Light Sci. Appl.*, vol. 6, no. 12, p. e17103, Dec. 2017.

[4] E. Maneas, W. Xia, D. I. Nikitichev, B. Daher, M. Manimaran, R. Y. J. Wong, C.-W. Chang, B. Rahmani, C. Capelli, S. Schievano, G. Burriesci, S. Ourselin, A. L. David, M. C. Finlay, S. J. West, T. Vercauteren, and A. E. Desjardins, “Anatomically realistic ultrasound phantoms using gel wax with 3D printed moulds,” *Phys. Med. Biol.*, vol. 63, no. 1, p. 015033, Jan. 2018.

Surgical Robotic Platform for Endoscopic Dissection

M. Brancadoro[1*], C. Quaglia[1], H. Abidi[1], M. A. Bonino[2], A. Arezzo[2], A. Menciassi[1]

[1]*The BioRobotics Institute, Scuola Superiore Sant'Anna, Pisa, Italy*

[2]*Department of Surgical Sciences, University of Torino, Turin, Italy*

**margherita.brancadoro@santannapisa.it*

INTRODUCTION

Endoscopic Submucosal Dissection (ESD) is an effective and less invasive treatment for colorectal cancer [1]. This clinical technique allows for an en-bloc removal of lesions of the gastrointestinal (GI) tract. ESD is performed using a traditional flexible endoscope, through which surgical tools can be introduced. These procedures are typically time consuming due to the difficult control of the tools, and they often require around 95 min for removing lesions, that can reach 3-4 cm in diameter. The probability of intestinal perforation exceeds 18% and the hemorrhage risk ranges from 3.5% to 15.5% [2]. A procedure supported by a flexible robotic endoscope may offer a solution to overcome these limitations, thus improving the degrees of freedom (DoFs) and the overall operational efficiency [3].

Within this clinical panorama, the aim of this paper is presenting the development of a novel miniaturized robotic device to be coupled to the tip of a traditional endoscope for the surgical dissection of GI neoplasms (Figure 1).

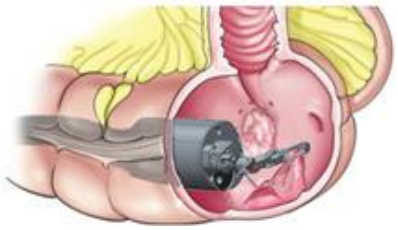

Figure 1. Concept of the miniaturized robotic device for the surgical dissection of the GI neoplasms.

MATERIALS AND METHODS

The robotic platform consists of the miniaturized robot, the actuator housing (hereafter called external platform), the control unit and the master console to allow the user driving and control (Figure 2). During the operation, one surgeon (Surgeon A in Figure 2) stands close to the patient to maneuver the endoscope for exploring the GI tract and reaching the target area. Another surgeon (Surgeon B in Figure 2) operates the miniaturized robot through the master console, carrying out the surgical procedure.

The key feature of the proposed robot is that traditional endoscope and instruments can be utilized: the device can be easily attached to and detached from the endoscope. Indeed, the miniaturized robot has been designed to be coupled to the tip of traditional flexible endoscopes in the range of 11.5 - 14.5 mm in diameter. The robot exploits the flexibility of the endoscope for navigation through the intestine and integrates two-active robotic arms (*i.e.*, cautery and gripper) extending the DoFs, and thus enhancing the efficiency during complex tasks such as manipulation and surgical tissue dissection. Furthermore, the endoscope provides the optical system for visual feedback and one working channels for conventional instruments.

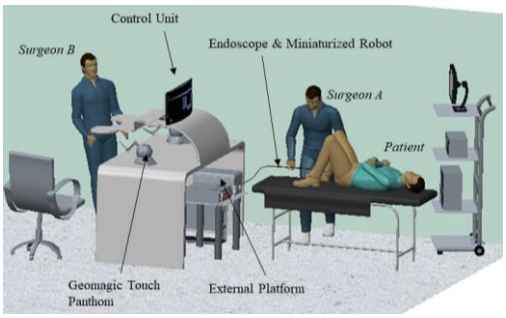

Figure 2. An overview of the endosurgery scenario.

The proposed technology is a two-armed robot with a total of six DoFs. The left arm is in the form of a gripper able to grasp and lift the tissue of the patient. This arm is featured by 3 DoFs (*i.e.*, slide, pitch and open/close of the gripper). The right arm is a mono-polar cautery with 3 DoFs (*i.e.*, slide, roll and pitch) employed to cut the lesion. The workspace generated from the DoFs of the two-activated robotic arms (*i.e.*, cautery and gripper) is shown in Figure 3. The green and blue shells are formed by the motion range of the tip of the right and left arm, respectively. The workspace covers a large part of the endoscope field of view thus allowing to reach the target area for performing a proper tissue dissection. The orientation of the gripper arm is driven by external cables (*i.e.*, one cable for the open/close, two cables for the slide and two cables for the pitch) managed by three external motors located into the external platform. Differently, three miniaturized motors have been integrated in the cautery arm to provide motion.

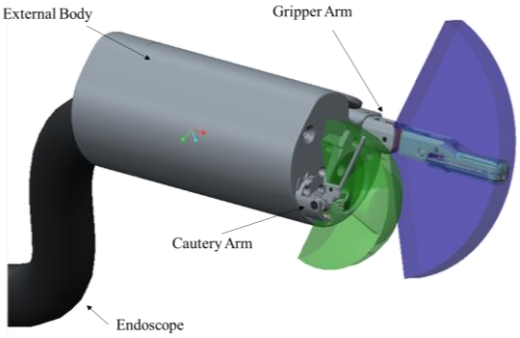

Figure 3. Workspace of the two-activated robotic arms.

The motors are controlled through 2 haptic interface devices, which are interfaced using LabVIEW. One of the devices is used for controlling the cautery system. The other one is fitted with a custom adaptor designed as a handle for the endoscopic surgical gripper.
While navigating through the intestine, the two-active robotic arms are retracted inside the body of the miniaturized robot; when the target area is reached, the arms are outside of the body and they can start to operate. The external shape of the cap body is 26 mm in diameter (including the endoscope tip) and has a total length of 50 mm; these sizes have been defined considering anatomical constraints (*i.e.*, dimension and shape of the anus and intestine). The internal endoscope is like any other traditional endoscope and can be pushed or controlled as usual. As users interface, the miniaturized robot supports two Geomagic Touch phantoms (3D System, Inc.).
To verify the feasibility of the design solution, a mock-up that faithfully reproduces the miniaturized robot has been realized using a 3D printer machine (ProJet MJP 3600, 3D System, Inc.). Moreover, the mock-up has been fixed on the tip of a traditional endoscope (Evis Exera III Colonovideoscope, Olympus) and inserted in a Transanal Endoscopic Microsurgery (TEM) simulator to verify the field of view of the endoscope once integrated.
Finally, the authors have prepared the mechanical drawing and assembled all fabricated components. Each part is made in metal materials (*i.e.*, stainless steel) with numerical control machine tools.

RESULTS

Figure 4a shows the mock-up of the miniaturized robot lodged on the tip of the endoscope. After dexterity tests performed by an expert surgeon, we could confirm that the motion capability of the endoscope was unchanged after integration and the workspace of the two arms seemed suitable for carrying out a surgical operation. The surgeon carried out in-vitro tests on colon simulator (Figure 4b) and confirmed that the field of view of the endoscope was not affected by the robot encumbrance.
After verifying the potentiality of the 3D printed prototype, a final device, with the same features (*i.e.*, DoF and geometry) of the 3D printed prototype, has been designed, fabricated and assembled (Figure 5). The miniaturized robot is made up of 87 steel components. The gripper arm is expected to generate around 3 N of lifting force and 10 -14 N of gripping force. Around 1.5 N is available at the cautery tip, based on preliminary modelling.

CONCLUSION AND DISCUSSION

A robotic platform including a miniaturized robot for the dissection of gastrointestinal neoplasms has been developed thanks to a deep collaboration between engineers and medical doctors.
Considering the weak points of the current medical techniques, the proposed robot guarantees instrument triangulation and tissue manipulation as in TEM procedure, and it should be also able to remove the lesions in all colon tract. As in the ESD technique, it is compatible with traditional endoscopes and the general anaesthesia is not mandatory, thus a traditional endoscopic room is enough for carrying out a complete surgical operation. Consequently, the hospitalization times, and hence the general hospital costs, could be significantly reduced.
For the future, the functionality of the robot will be validated with bench tests and in-vivo experiments will be conducted to prove the clinical advantages of the proposed system.

REFERENCES

[1] Arezzo A, et al. "Systematic review and meta-analysis of endoscopic submucosal dissection versus transanal endoscopic microsurgery for large noninvasive rectal lesions." Surgical endoscopy 28.2 (2014): 427-438.
[2] Akintoye E, et al. "Colorectal endoscopic submucosal dissection: a systematic review and meta-analysis." Endoscopy international open 4.10 (2016): E1030.
[3] Yeung BPM, and Philip WYC. "Application of robotics in gastrointestinal endoscopy: A review." World journal of gastroenterology 22.5 (2016): 1811.

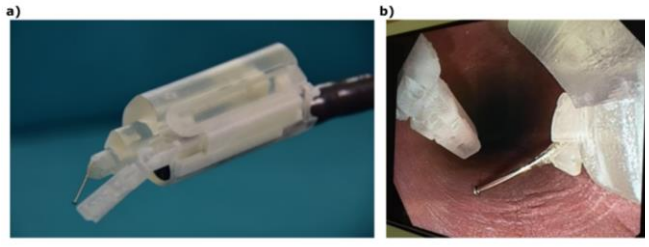

Figure 4. a) Miniaturized robot mock-up mounted on the endoscope tip and b) picture during in-vitro test in a TEM simulator.

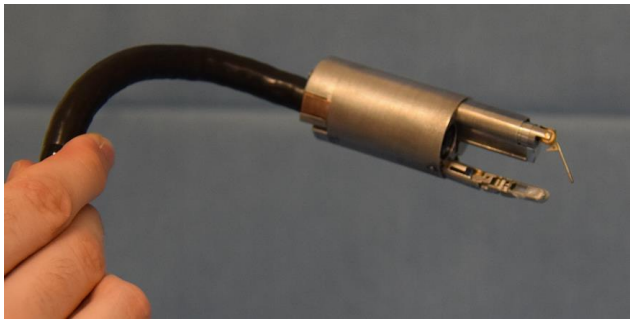

Figure 5. Final prototype of the miniaturize robot.

Towards the Development of a Novel Handheld Robotic Tool for the Expanded Endoscopic Endonasal Approach*

E Dimitrakakis[1], G Dwyer[1], HJ Marcus[2], NL Dorward[2], D Stoyanov[1]

[1] *Wellcome/EPSRC Centre for Surgical and Interventional Sciences (WEISS), University College London*

[2] *National Hospital for Neurology and Neurosurgery, London*

e.dimitrakakis@ucl.ac.uk

INTRODUCTION

The transphenoidal approach is one of the best examples of keyhole brain surgery. This surgical procedure is done through the nose and is used to treat tumours within the pituitary gland, which lies deep within the base of the brain. In recent years, surgeons have also described the use of an Expanded Endoscopic Endonasal Approach (EEEA) for treatment of other tumours around the base of the brain [1]. The benefits of this approach, however, are largely theoretical, and most surgeons still find operating in this way with non-articulated tools, very difficult.

In our study, we aim to develop a handheld tool with an articulated robotic instrument at the tip. General surgery has greatly benefited from advancements in precise robotic surgical platforms and tools that allow for smaller incisions, thus faster recovery time, shorter hospital stay, reduced pain and smaller risk of infection. Their application in neurosurgery, however, is limited because a complete redesign must take place to account for the minimal workspace in the human skull and the low forces applied. In [2], an extensive review of robotic systems used in neurosurgery is provided and potential problems that need to be solved before their wide adoption in surgical theatres are listed.

Despite the success of existing surgical robotic platforms, there is a shift towards developing handheld robotic tools that are completely ungrounded and are manipulated by surgeons in free space while being compact and requiring minimal setup time. Trends in handheld medical robotics are described in [3], while the famous handheld robotic tool for general surgery 'FlexDex' is developed in [4]. The 'FlexDex', although a handheld and easy to use tool, cannot be used in neurosurgery, due to its size and mechanical constraints.

The goal of this paper is to design a novel robotic handheld tool for Endonasal Approaches. The difference between our tool and the readily commercially available tools is the articulation ability that the robotic instrument at the tip of the tool will provide. Modern rigid instruments have just a gripper as an end-effector and operate under fulcrum, according to the studies conducted in [5]. The robotic end effector at the end of our tool will give the surgeon the ability to reach places on the surface of the brain that were not reachable with those pre-existing instruments.

In this abstract, we present a preliminary design of the tool, we solve the kinematic problems of the robot manipulator and we showcase its workspace.

MATERIALS AND METHODS

I. DESIGN OF THE HANDHELD TOOL

A 3D rendition of the design of the EEEA robotic tool is shown in Figure 1 (top), whereas a rendering of how the tool is going to be used in a surgical scenario is shown in Figure 1 (bottom). Since the work space inside the human skull, which is the hollow space behind the nasal passages and below the brain called sphenoid sinus, is limited and the nasal passages themselves are narrow, our end-effector must be exceptionally small.

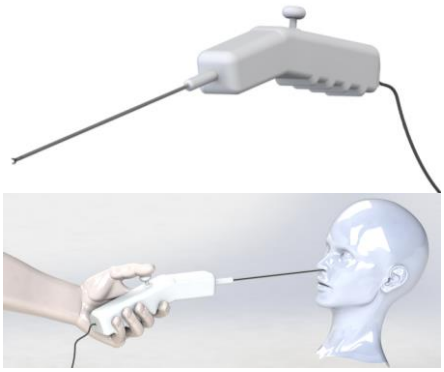

Figure 1. A rendering of the handheld robotic tool (top), a concept rendering of how the tool is going to be used in a EEEA surgical scenario (bottom).

The robot manipulator at the tip of the tool is approximately $1.37cm$ long and has an outer diameter of $3mm$. It consists of 2 Degrees of Freedom (DoF) giving the surgeon more articulation capabilities than commercially available tools. A shaft of $25cm$ in length is used for insertion of the instrument to the operating cavity, and a $1mm$ middle channel is utilized to allow for the tendons that control the gripper to pass through.

The tool is antagonistically controlled in a tendon-driven configuration. Four channels are created at a $0.9mm$ radius, from the centre of each joint, utilizing tendon passages. An antagonistic tendon pair passing opposite channels is used to actuate each DoF.

The actuation system will consist of three motors; one motor for each DoF in a pulley-driven antagonistic configuration, and a third one for the movement of the gripper. This system is located inside the handle of the tool as depicted in Figure 2 (right). Also on the handle, a 2 DoF joystick is placed that will move the motors and thus, the robot. Finally, a rerouting mechanism that will reroute the tendons from their starting point at the top of each motor, to the appropriate passage channels on the

manipulator is implemented inside the handle, shown in Figure 2 (right) as well.

II. KINEMATIC ANALYSIS

The Denavit-Hartenberg (DH) kinematic parameters for the 2-DoF robotic manipulator at the tip of the tool, as depicted in Figure 2 (left), are shown in Table 1.

Table 1. The DH parameters of the articulated tool.

Link	θ_i	a_i	α_i	d_i
$i = 1$	θ_1	$0\ mm$	90^o	$0\ mm$
$i = 2$	θ_2	$11\ mm$	-90^o	$0\ mm$

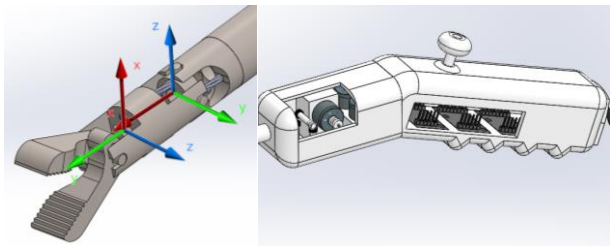

Figure 2. The articulated instrument (left) and a semi-cross section of the body and handle of the tool (right).

The inverse kinematics position problem was solved using a numerical approach algorithm for a more generic and easily expandable solution, in case we need to expand the number of DoF of the robot in the future.

A numerical approach was implemented for the calculation of the angle-vector $\theta(t^+) = [\theta_1^+, \dots, \theta_N^+]$ at time t^+. Given the current angles $\theta(t^-) = [\theta_1^-, \dots, \theta_N^-]$ at time t^- and the desired position vector of the end-effector $P_0^{N,d}(t^+) = \left[P_x^d(t^+), P_y^d(t^+), P_z^d(t^+)\right]^T$ at time t^+, the computation is cast as an Eucledian distance optimisation problem [6] defined as:

$$\min_{\theta} \|\theta(t^+) - \theta(t^-)\|,$$

$$subject\ to\ \left\|P_0^{N,d}(t^+) - P_0^N\right\| = 0$$

where P_0^N is the resulting end-effector's position. In a typical experiment $t^+ - t^-$ corresponds to the sampling period T_s.

Assuming the computed joint space angle-vector, the tendon stroke of each antagonistic pair must be computed. For each rotational DoF there are two tendons running from the robot's base, passing through holes at each joint, and ending at the counter-diameter holes at the corresponding joint to be rotated. To compute the tendons' lengths, it is crucial to compute the length of the path of each tendon, which necessitates the computation of the locations of the passing-through holes in 3D space.

For an N DoF robotic tool, each link has 2N symmetrically positioned channels at a radius r from its centre of symmetry. The computation of the tendon's path length is computed by expressing each hole in 3D space and then using the resulting homogeneous transformation matrix of each hole alongside with Euclidean geometric calculations.

RESULTS

Shown in Figure 3, is the resulting work space of our tool based on the kinematic analysis presented in the previous section with angle limits at $[-45^o\ 45^o]$. It is evident that the surgeon's abilities could be widely enhanced with the tool we propose, due to the expanded work space it provides compared to that of the traditional tool. A much larger area can be covered by manipulating the robotic instrument without having to constantly reposition the shaft.

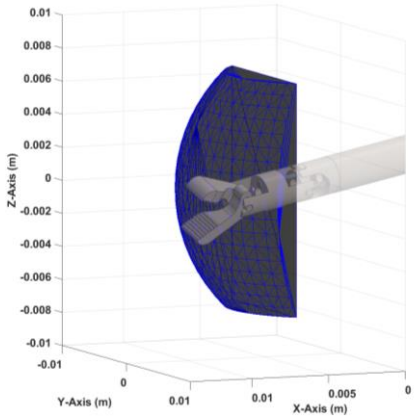

Figure 3. The workspace of the end-effector of the tool

CONCLUSION AND DISCUSSION

In this abstract, we presented our design and the kinematic analysis for a novel handheld robotic tool for EEEA surgical procedures. Our goal is to take advantage of its articulation ability to remove tumors from the surface of the brain that traditional tools struggle to remove. The immediate next step of our study is to 3D print the body and the manipulator of the tool and assemble it, in order to prove our concept and perfect our design before progressing to clinical studies.

REFERENCES

[1] A. B. Kassam, C. Snyderman, P. Gardner, R. Carrau, and R. Spiro, "The expanded endonasal approach: a fully endoscopic transnasal approach and resection of the odontoid process: technical case report," *Oper. Neurosurg.*, vol. 57, no. suppl_1, pp. E213–E213, 2005.

[2] J. J. Doulgeris, S. A. Gonzalez-Blohm, A. K. Filis, T. M. Shea, K. Aghayev, and F. D. Vrionis, "Robotics in neurosurgery: evolution, current challenges, and compromises," *Cancer Control*, vol. 22, no. 3, pp. 352–359, 2015.

[3] C. J. Payne and G.-Z. Yang, "Handheld medical robots," *Ann. Biomed. Eng.*, vol. 42, no. 8, pp. 1594–1605, 2014.

[4] S. Awtar, T. T. Trutna, J. M. Nielsen, R. Abani, and J. Geiger, "FlexDex™: a minimally invasive surgical tool with enhanced dexterity and intuitive control," *J. Med. Device.*, vol. 4, no. 3, p. 35003, 2010.

[5] H. J. Marcus, T. P. Cundy, A. Hughes-Hallett, G.-Z. Yang, A. Darzi, and D. Nandi, "Endoscopic and keyhole endoscope-assisted neurosurgical approaches: a qualitative survey on technical challenges and technological solutions," *Br. J. Neurosurg.*, vol. 28, no. 5, pp. 606–610, 2014.

[6] J. J. Moré and D. C. Sorensen, "Computing a trust region step," *SIAM J. Sci. Stat. Comput.*, vol. 4, no. 3, pp. 553–572, 1983.

XGBOOST implementation to handle missing values in large surgical datasets

L. Migliorelli[1], S. Moccia[1,2], E. Frontoni[1]

[1]*Department of Information Engineering, Università Politecnica delle Marche, Ancona (Italy)*

[2]*Department of Advanced Robotics, Istituto Italiano di Tecnologia, Genoa (Italy)*
l.migliorelli@pm.univpm.it

INTRODUCTION

Electronic Health Records (EHRs) today gather huge amounts of clinical and surgical data from several subjects and clinical centers. Analyzing EHRs potentially has strong impact in improving both (1) the the quality of screening and diagnosis, surgery and follow-up analysis and, more in general, (2) the advancement of the scientific research in the field of large-dataset analysis with Machine-Learning (ML) approaches.

When processing huge amount of data, some complexities arise, such as the presence of large-rate of missing data due to incomplete or inaccurate EHR filling. To avoid the presence of missing data hampering the use of standard statistical / ML analysis, many approaches based on data imputation and data deletion have been proposed in literature [1, 2]. However, these approaches may be harmful for clinical applications as imputing variables may modify relationship between variables and data deletion may exclude clinically relevant instances and lower data availability for ML-algorithm training [2].

The goal of this work is to present a ML-based model, intrinsically able to tackle missing values (i.e., without requiring either deletion or imputation), that analyses preoperative and operative variables from a sparse-annotated large multicenter dataset, accounting for 32812 patients, for predicting mortality at 30 days after surgery.

MATERIALS AND METHODS

From a practical and theoretical point of view, when dealing with a large amount of data with missing values, adopting different learners in parallels could reduce the risk of badly selecting a classification model [3]. In this work, inspired by [3], eXtreme Gradient BOOSTing (XGBOOST) [4] was used.

XGBOOST is a tree-based ensemble learner whose main hyperparameters are the number of estimators (i.e., the number of trees) and the max depth (i.e., the max allowed depth for each tree). XGBOOST builds a strong model by combining "weak" ones in an iterative way. At any instant *t*, the model outcomes are weighed based on the outcomes of the previous instant *t-1*. Misclassified instances get more weight so, in the subsequent iterations, more learners will concentrate on them trying to reduce the classification error.

When XGBOOST encounters missing data, it learns from data the best path to take in future, resulting one of the most effective methods in handling sparse dataset.

To possibly avoid overfitting, XGBOOST can be trained using the DART implementation. More specifically, with XGBOOST, the trees added at later iterations tend to *overspecialize* on a small subset of data and this may induce overfitting. For overcoming this problem, DART adopts dropout strategies, randomly dropping boosting-tree members at each iteration [5].

In this work, both XGBOOST and DART were investigated to classify the post-operative mortality.

EXPERIMENTAL PROTOCOL

Both the proposed methodologies (i.e. XGBOOST and DART) were tested on a thoracic-surgery dataset made of 32812 patients, among which all the deceased patients (1269 patients) were selected for the analysis. An equal number of survived patients was randomly chosen for ensuring a balanced training.

The dataset presented 34 variables, both categorical (as gender and cardiac comorbidities) and numerical (as body mass index, age at the surgery). Among the numerical variables, there were five alveolar variables. Examples include forced expiratory volume-one second (FEV1) and carbon monoxide lung diffusion capacity (DLCO) or forced vital capacity (FEVC).

The 34 variables had a mean missing-value rate of 23.7% with a peak of 65.54% in DLCO and no missing values in gender feature.

Considering the limited size of the dataset, for robust training issues, stratified 3-folds Cross Validation (CV) was performed. To search the optimal-model hyperparameters, hyperparameters tuning was implemented using the 3-folds CV technique. The following values were used to build the grid-search space: [200,250,300,350,400,450,500,550,600] for number of estimators and [3,4,5,6,7] for max depth.

Four experiments were carried out:
-Experiment A (EA): classification with XGBOOST
-Experiment B (EB): classification with DART

-Experiment C (EC): imputing missing values for categorical (training set mode) and numerical (training set mean) variables, applying XGBOOST
-Experiment D (ED): EC with DART.

The performance of the proposed method were evaluated in terms of recall-scores and area (AUC) under the Receiver Operating Characteristic (ROC).

All the experiments were implemented using scikit-learn (https://scikit-learn.org) ML libraries.

RESULTS

The ROC analysis revealed that EA and EB both had a mean AUC of 0.81, outperforming EC and ED (AUC = 0.80).

Observing the recall boxplots (Fig. 1), median values and Inter-Quartile Ranges (IQRs) for death and alive patients were, respectively: 0.74 (IQR=0.02) and 0.73 (IQR=0.01) in EA, 0.74 (IQR=0.02) and 0.73 (IQR=0.02) in EB, 0.73 (IQR=0.01) and 0.71 (IQR=0.02) in EC, 0.75 (IQR=0.02) and 0.71 (IQR=0.005) in ED.

CONCLUSION AND DISCUSSION

In this work XGBOOST algorithm was implemented to avoid data imputation and variables/subject deletion.

The four conducted experiments showed acceptable results in term of mean AUC: EA and EB, achieved slightly better results (AUC=0.81) with respect to EC and ED (AUC= 0.80).

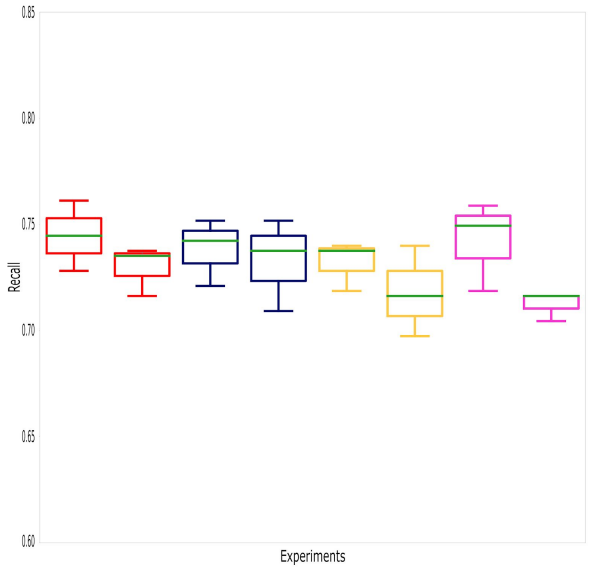

Fig. 1. Recall boxplots of the four experiments: in red Experiment A (EA), in blue Experiment B (EB), in yellow Experiment C (EC), in magenta Experiment D (ED). The left boxplot represents deceased patients, the right boxplot represents alive patients.

Considering recall boxplots, EA and EB, showed more reliable results. Hence, as observable in Fig. 1 (and confirmed by IQRs and median values) they did not outperform in predicting one class with respect to the other. Conversely, despite ED reached the highest median value for deceased patients (Fig. 1), the boxplots and the IQRs showed that EC and ED were more consistent in predicting respectively deceased patients and alive ones.

To offer all possible support for the surgery planning, it is acknowledged that further research is required, e.g., to improve classification performances. Future research directions may include application of incremental learning, to exploit the numerosity of the dataset without excluding survived patients, or deep-learning based strategies whose non-linearity is suitable to tackle the complexity of sparse dataset. However, the results presented here, are surely a promising step towards a helpful automatic method to assist the surgeon in analysing operative risks prematurely.

REFERENCES

[1] Kelley R. R., Mattingly W. A., Wiemken T. L., Khan M., Coats D., Curran D., Chariker J.H., Ramirez J. "Visual grids for managing data completeness in clinical research datasets" Journal of Biomedical Informatics 54 2015; 337-344.

[2] Pedersen, A. B., Mikkelsen, E. M., Cronin-Fenton, D., Kristensen, N. R., Pham, T. M., Pedersen, L., Petersen, I. “Missing data and multiple imputation in clinical epidemiological research” Clinical Epidemiology 9 2017; 157-166.

[3] Polikar R. "Ensemble based systems in decision making" IEEE Circuits and Systems Magazine 6.3 2006; 21-45.

[4] Chen T., Guestrin C. "Xgboost: A scalable tree boosting system" in Proceedings of the 22nd acm sigkdd international conference on knowledge discovery and data mining (ACM) 2016; 785-794.

[5] Rashmi, K. V., Gilad-Bachrach, R. “Dart: Dropouts meet multiple additive regression trees” International Conference on Artificial Intelligence and Statistics 2015; 489-497.

A deep-learning strategy for informative-frame selection and early-stage cancer diagnosis in laryngoscopic videos

I. Patrini[1*], M. Ruperti[1*], E. De Momi[1], L. Mattos[2], E. Frontoni[3], S. Moccia[2,3]

[1]*Department of Electronics, Information and Bioengineering, Politecnico di Milano, Milan (Italy),*

[2]*Department of Advanced Robotics, Istituto Italiano di Tecnologia, Genoa (Italy),*

[3]*Department of Information Engineering, Università Politecnica delle Marche, Ancona (Italy)*

ilaria.patrini@mail.polimi.it, michela.ruperti@mail.polimi.it

**The two authors contributed equally to this work*

INTRODUCTION

Squamous cell carcinoma (SCC) is the most common cancer of the laryngeal tract. SCC is characterized by the presence, in the mucosa surface, of dot-like vessels, known as intraepithelial papillary capillary loops (**IPCL**), and longitudinal hypertrophic vessels (**Hbv**). Other modifications are related to the thickening and whitening of the epithelial layer, condition known as leukoplakia (**Le**).

SCC patients' mortality and morbidity rate could be reduced with an early-stage diagnosis. Narrow-band imaging (NBI) endoscopy is currently considered the gold standard for SCC screening purposes. NBI is an optical-biopsy technique that allows an enhanced view of both superficial blood vessels and mucosa surface.

From the clinician's side, reviewing the NBI video can be a labour-intensive operation and small tissue lesions may pass unnoticed to the clinicians' eye. The video review process could be further prolonged and compromised by the presence of uninformative video frames, such as frames with saliva or specular reflections (**S**), blurred frames (**B**), underexposed frames (**U**) where the laryngeal anatomy cannot be clearly seen.

In the context of computer-assisted systems for real time diagnosis during intraoperative examination procedures, the surgical-data-science community has recently proposed methodologies that, by exploiting machine-learning (ML) techniques, are able to (i) automatically select laryngeal informative (**I**) frames over uninformative ones and (ii) classify healthy/SCC laryngeal tissues in **I**-frames. These methodologies usually exploit handcrafted texture-based information and standard ML approaches (e.g. support vector machines (SVMs)) [1],[2]. Advancements in other medical fields, however, showed that learned features may be more powerful than handcrafted ones [2],[3].

Thus, the aim of this work is to verify if (**H1**) features learned with deep learning (DL) algorithms, and in particular with Convolutional Neural Networks (CNNs) that are pre-trained on natural images, can provide better performance than the handcrafted ones (when classified with standard ML approaches for multi-class classification). This work also aims at verifying if (**H2**) CNN-based classification, after proper fine-tuning implementation on the pretrained CNNs, can be more powerful than standard ML method classification. The hypotheses are investigated for both the selection of **I**-frames in NBI endoscopic videos and the diagnosis early-stage SCC in these frames.

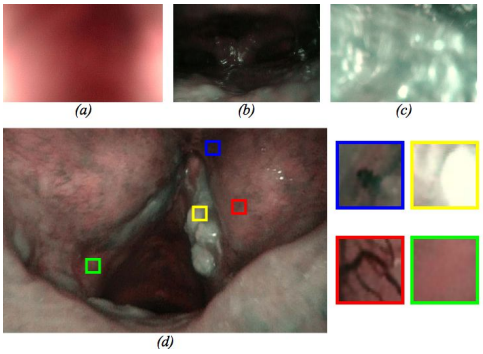

Figure. 1. Samples of laryngeal video frames in NBI-InfFrames dataset (**D1**). (a) **B**: blurred, (b) **U**: underexposed, (c) **S**: with saliva or specular reflections, (d) **I**: informative. Samples of image patches of Laryngeal dataset (**D2**), retrieved from **I**-frames. **He**: healthy tissue (green box), **Le**: leukoplakia (yellow box), **Hbv**: hypertrophic vessels (red box), **IPCL**: intraepithelial papillary capillary loops (blue box).

MATERIALS AND METHODS

Four pre-trained CNNs were investigated to test **H1** and **H2**. The CNNs were chosen among the best performing in the context of the Large Scale Visual Recognition Challenge (ILSVRC): 1) ResNet V1 101, 2) ResNet V1 152, 3) VGG 16, 4) Inception V4. For fair comparison, all the CNN models used were pre-trained on the ImageNet dataset[1]. The deepest layer of each CNN was considered as feature extractor.

When testing **H1**, feature classification was performed exploiting SVMs with the Gaussian kernel. To implement multi-class SVM classification, the *one-vs-rest* scheme was used. The SVM parameters were retrieved via grid-search and cross-validation. To test **H2**, the best performing architecture for **I**-frame selection and the best one for SCC diagnosis (according to **H1**) were fine-tuned and used for classification.

[1] http://www.image-net.org/

Experimental analysis

Two datasets were evaluated (both divided in four classes): (**D1**) NBI-InfFrames dataset[2] composed by 720 video frames (subdivided in: **B**, **I**, **S**, **U**) extracted from 18 NBI endoscopic videos referring to 18 different patients affected by SCC and (**D2**) Laryngeal dataset[3] composed by 1320 patches of healthy (**He**) and early-stage cancerous laryngeal tissues (**Le**, **IPCL**, **Hbv**) extracted from 33 narrow-band laryngoscopic images of 33 different patients. Samples of images contained in the dataset can be seen in Fig. 1.

For robust evaluation, 3-fold cross-validation was performed separating data at patient level, as suggested in [1],[2]**.** Confusion matrices were computed highlighting the class-specific recall (Rec_{class}) for each CNN model. The area (AUC) under the receiver operating characteristic (ROC) was also computed.

In order to investigate **H1**, feature extraction was implemented with *TensorFlow* and *scikit-learn*. All the TensorFlow CNN-model files and the CNN weights were downloaded from the *TensorFlow-Slim* image classification model library[4].

For **H2**, CNNs were fine-tuned using the *Gradient Descent* optimizer for **D1** and *Stochastic Gradient Descent* plus *Nesterov* and *Momentum* optimizer for **D2**. The best model during training was selected according to the maximum *categorical accuracy* and the minimum *categorical cross-entropy* (loss) on the validation set.

RESULTS

Regarding **H1**, both datasets registered comparable results with respect to the state of the art ([2],[1]), but improvements were noticed when focusing on **I** and **He**, where the classification performance *Rec* was 0.9100 and 0.9800 for **I** and for **He**, respectively.

For **D1,** the best performance was achieved with the VGG 16 learned-feature set with a *Rec* for **I** of 0.9722 (median *Rec* among the four classes was 0.9361). AUC for **I** was 0.9973. A few misclassifications occurred mainly between **S** and **I**, probably due to the presence of image-intensity edges in **S** frames as in **I**-frames.

For **D2,** the best performance was achieved with the ResNet V1 152 learned-feature set, with a *Rec* for **He** of 0.9939 (median *Rec*=0.9205). AUC among the four classes was 0.9805. Misclassification mainly occurred between **IPCL** and **Hbv**. However, it is worth noticing that both classes refer to early-stage SCC tissues.

H2 was verified for both the datasets. Best results achieved for **D1** presented values of *Rec* for **I** of 0.9778 and AUC for **I** of 0.9928. For **D2**, the achieved values of *Rec* for **He** was of 0.9969 and 0.8758 for **IPCL** (which was also the class that presented most difficulties in being correctly predicted in [1]). AUC among the four classes was 0.9900. Aforementioned results are summarized in Fig. 2 and Fig. 3.

[2] DOI: 10.5281/zenodo.1162784

[3] DOI: 10.5281/zenodo.1003200

[4] https://github.com/tensorflow/models/tree/master/research/slim

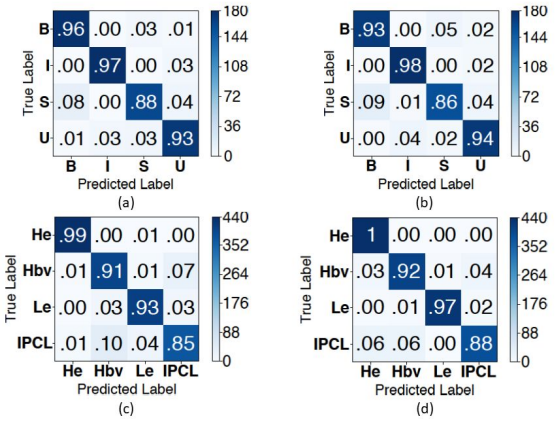

Figure. 2. Confusion matrices of (a) **D1** classified with SVMs, (b) **D1** classified with VGG 16, (c) **D2** classified with SVMs, (d) **D2** classified with ResNet V1 152.

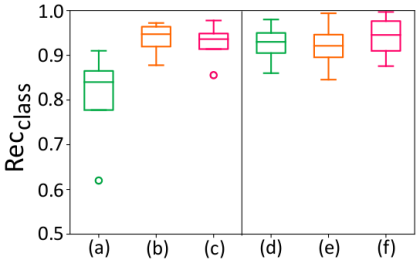

Figure. 3. Boxplots of classification recall obtained for (a) [2], (b) **D1** with SVMs, (c) **D1** with VGG 16, (d) [1], (e) **D2** with SVMs, (f) **D2** with ResNet V1 152

DISCUSSION AND CONCLUSION

This paper presented and evaluated a new strategy for feature selection and classification for the analysis of NBI videos, joining and improving work presented in [1] and [2].

The achieved results highlight the potentiality of DL in learning different and complex tasks, tackling the variability of **D1** and **D2**, which were made of images of different size, content and scale.

Even though **H1** and **H2** have been verified, results of **H2** could be further ameliorated by combining different optimizers in the training phase. As future work, we also aim at enlarging **D1** and **D2** in order to potentially solve misclassification problems and investigating strategies to provide segmentation of the SCC tumoral area.

REFERENCES

[1] S. Moccia et al., "Confident texture-based laryngeal tissue classification for early stage diagnosis support," Journal of Medical Imaging, vol.4, no.3, p.034502, 2017.

[2] S. Moccia et al., "Learning-based classification of informative laryngoscopic frames," Computer Methods and Programs in Biomedicine, vol.158, pp.21–30, 2018.

[3] L. Nanni et al., "Handcrafted vs. non-handcrafted features for computer vision classification," Pattern Recognition, vol.71, pp.158–172, 2017.

APSurg: Abdominal Positioning Surgical System. A preliminary study

Veronica Penza and Leonardo S. Mattos

Biomedical Robotics Lab, Advanced Robotics, Istituto Italiano di Tecnologia, Genova
veronica.penza@iit.it

INTRODUCTION

According to the World Health Organization (WHO), among the 300 millions of surgical operations performed each year, between the 3% and 22% are affected by major complications, causing permanent damage to the patient or even death (incidence rate 0.4 - 0.8%) [1].

Despite recent advances in surgical techniques, specifically related to minimally invasive surgery (MIS), surgical complications are very frequent. Adverse events are mostly linked with the experience of the surgeons, their ability to be aware about the patient anatomical peculiarities, and their capability to integrate the pre-operative plan within the intra-operative scenario. The most serious intra-operative laparoscopic complications are related to vascular injuries, with a 9–17% mortality rate [2]. Risk factors are attributed to the surgeon's skills, instrument sharpness and patient position [3].

A promising solution to decrease major complication rates involves exploiting assistive technologies during the intra-operative phase, such as Augmented Reality (AR) and Virtual Reality (VR) tools. The role of such technologies lies in enhancing the surgeon's capabilities during surgery, by providing information from pre-operative phase, monitoring the surgical site and warning the surgeon in case of situations leading to adverse events. A wide variety of methods has been proposed in the literature over the last decade in the field of laparoscopic assistive technologies [4], however a satisfactory method has not been developed yet for commercial use in the surgical room. The main reason slowing down the application of such technologies is the dynamic characteristic of abdominal organs, which strongly affects the augmentation accuracy.

This paper presents *APSurg*, an Abdominal Positioning Surgical system specifically designed to improve surgical awareness and safety during general/abdominal surgery. It consists of a VR environment that shows, in real-time, 3D models of patient-specific organs aligned and synchronized with the endoscopic view. It provides advanced functionalities, such as changing the transparency of organs to visualize internal structures (e.g., tissue abnormalities, vessel structures, etc.), offering a fundamental support in the surgeon decision-making process. The main purpose of this paper is to present a preliminary study of the usability of the system in a simulated and simplified surgical scenario. In particular, this study aims to demonstrate the benefits provided by *APSurg* in terms of improvements in the surgical field navigation abilities, and the effectiveness of the way the information is presented to the user.

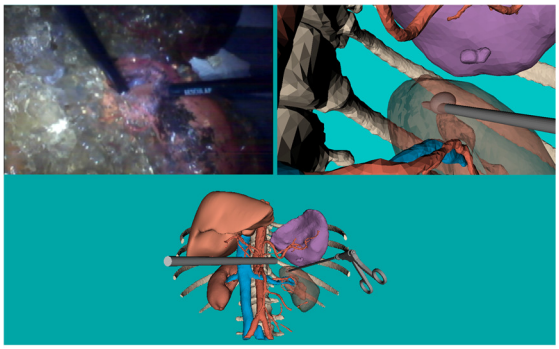

Figure 1. APSurg system: multi-view visualization. Top row: endoscopic view of a phantom of kidney with a tumor (left) and the corresponding *endoscopic virtual camera* (right). Bottom row: 3rd person view of the whole surgical scene.

MATERIALS AND METHODS

The *APSurg* system needs three sources of information:

- Pre-operative patient-specific 3D organ models;
- Run-time images captured from a surgical endoscope;
- Run-time 3D pose of the endoscope.

This information, combined with a calibration process, allows the representation of the *endoscopic virtual camera*: a virtual environment representing the virtual model of a patient-specific abdomen shown from the same point of view of the endoscopic camera. The final multi-view visualization provided to the surgeon is shown in Figure 1, where the *endoscopic virtual camera* is located side by side to the real endoscopic image, and the 3rd person view of the abdomen, including the runtime representation of the endoscope, is located below them.

The patient-specific 3D organ models are extracted from pre-operative imaging (CT Scan, MRI), commonly performed before any surgical intervention that requires the shape and position knowledge of a specific structure. *APSurg* uses these 3D models to create a virtual abdomen of the patient, hereafter called *virtual patient*.

In order to allow the intra-operative run-time visualization of the *endoscopic virtual camera*, a calibration process is necessary. This calibration consists of two steps (see Figure 2):

Endoscope-Camera Calibration. The endoscope 3D pose is tracked by a passive optical tracking system. The pose of the camera with respect to the endoscope pose is required in order to replicate the same pose in the *endoscopic virtual camera*. Hand-eye calibration method is exploited to compute this spatial transformation, ${}_{e}T^{c}$, using the method described in [5].

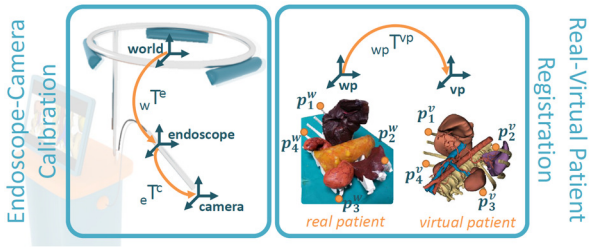

Figure 2 Representation of reference frames (green) and transformation (orange arrows) involved in *APSurg* calibrations.

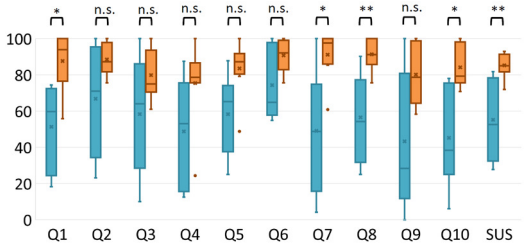

Figure 3 Boxplot representing the SUS scores for the 10 questions, green and orange without and with *APSurg*.

Real-Virtual Patient Registration. To match the position of the *real patient* with the *virtual patient* (${}_{wp}T^{vp}$), a rigid registration is computed using the same set of points in both models. Fiducial points can be selected on the ribcage, assumed to be identifiable in the real scenario.

RESULTS

An experimental validation of *APSurg* was conducted to demonstrate its (i) *accuracy*, (ii) *effectiveness* in augmenting surgical awareness, and (iii) *usability* in a simulated surgical scenario.

The setup was composed by an OptiTrack Tracking System (Natural Point Inc.) for the tracking of a custom endoscope (CMOS analogical Camera - Misumi, Taiwan), two 24'' monitors for the visualization of the configuration GUI (graphical user interface) and the multi-view window, and a phantom of human abdomen [6] placed in a laparoscopic trainer container. The corresponding *virtual patient* was loaded on the VR environment. The software was implemented in C++ and the VR environment with VTK Library, with the support of Qt Library for the GUI.

Eight subjects without surgical experience were asked to perform a simplified surgical task on the abdomen phantom. The task consisted in localizing, using real surgical MIS instruments, a tumor located in the right or left kidney, which was covered by a layer of fat reproduced with colored agar. All the subjects were informed about the pathological condition of the patient phantom and a CT scan was provided together with the segmentation of the tumor area, as in the surgical routine. In this pilot study, since the subjects were engineers, information about the kidney (appearance, location, size) was provided. Each subject performed two trials with two randomized conditions: the location of the tumor (left/right kidney) and the use of *APSurg*. Before the experiment, all subjects received verbal and written information describing the experiment and its goal. They were asked to provide written informed consent according to recommendations from the Istituto Italiano di Tecnologia and the Declaration of Helsinki.

The system *accuracy* was measured as Real-Virtual Patient Calibration error, computed as the Root Mean Square Error of point distances ($4.7 \pm 0.32\ mm$).

The *effectiveness* of the system was evaluated measuring the task execution time, while the *usability* was evaluated asking the subjects to fill the System Usability Scale (SUS) questionnaire [7], which allows the evaluation of surgical technology in terms of general usability.

Results showed a significant lower execution time when the subject was supported by *APSurg*, with an average of $4.89 \pm 2.06\ min$ against $1.94 \pm 1.07\ min$, respectively without and with the use of *APSurg*. Results related with the *usability* study are shown in Figure 3, showing a consistent advantage of the use of *APSurg*.

CONCLUSION AND DISCUSSION

This paper presented *APSurg*, an abdominal positioning surgical system aimed to enhance, intraoperatively, the surgeons' visual experience of the surgical field. A preliminary study of the *effectiveness* and *usability* of the system indicates a substantial improvement during a surgical navigation task. Although these trials have been done with engineers without surgical experience, the system shows a potential positive impact for novel surgeons, even if it does not consider yet the organ tissue deformations. Future studies will involve novel and experienced surgeons, with the aim to have more relevant evaluation of the system, including more complex and realistic tasks in accordance with the surgeons' skills.

REFERENCES

[1] Safety WHOP, Organization WH, others. WHO Guidelines for Safe Surgery: 2009: safe surgery saves lives. 2009.

[2] Opitz, Isabelle, et al. "Bleeding remains a major complication during laparoscopic surgery: analysis of the SALTS database." *Langenbeck's archives of surgery* 390.2 (2005): 128-133.

[3] Lam, Alan, et al. "Dealing with complications in laparoscopy." *Best Practice & Research Clinical Obstetrics & Gynaecology* 23.5 (2009): 631-646.

[4] Bernhardt, Sylvain, et al. "The status of augmented reality in laparoscopic surgery as of 2016." *Medical image analysis* 37 (2017): 66-90.

[5] Daniilidis, Konstantinos. "Hand-eye calibration using dual quaternions." *The International Journal of Robotics Research* 18.3 (1999): 286-298.

[6] Penza, Veronica, et al. "EndoAbS dataset: Endoscopic abdominal stereo image dataset for benchmarking 3D stereo reconstruction algorithms." *The International Journal of Medical Robotics and Computer Assisted Surgery* 14.5 (2018): e1926.

[7] Brooke, John. "SUS-A quick and dirty usability scale." *Usability evaluation in industry* 189.194 (1996): 4-7.

Surgical Gesture and Error Recognition with Time Delay Neural Network on Kinematic Data

Giovanni Menegozzo, Diego Dall'Alba, Chiara Zandona and Paolo Fiorini

University of Verona, Italy
paolo.fiorini@univr.it

INTRODUCTION

Surgical Robotic System (SRS) supports the surgeon in executing complex surgical actions with more confidence and firmness, which ultimately translates into better outcomes for the patients. Automatic surgical gesture recognition and classification is an enabling technology for improving surgeon's support in multiple applications. On-line recognition of surgical gestures will improve the training process and the overall performance thanks to user-specific feedbacks and the prompt detection of errors due to excessive fatigue or cognitive overloading [1]. Thus, surgical gesture recognition recently gained more attention from robotic and computer vision researchers, thank also by the availability of syncronized video and kinematic data acquired by reseach SRSs and surgical simulators. The introduction of new datasets and methods support generalization of results to several procedure. Zappella et al. was among the first to propose gesture recognition from video data using linear dynamical systems and bag of words [2]. Kinematic data have been firstly modeled with Hidden Markov Model (HMM) [3], then other approaches were proposed with Condition Random Field (CRF) and skip-chain CRF (SKCRF) [4]. Recent research works combine kinematics and video data to outperform gesture recognition results previously obtained [5]. However, integration of kinematic and video data is challenging due the etherogeneous nature of these data types and further research efforts is required. Actually, many research focuses on modeling the temporal information that is essential for gestures recognition. New types of neural networks have been proposed to handle videos and kinematics information, exploiting intrinsic temporal constraint as a new feature and considering multiple time steps simultaneously for a more precise context evaluation, e.g. Temporal Convolutional Networks (TCN) or Long Short Term Memory (LSTM) [6,2]. Time Delay Neural Networks (TDNN) are becoming successful due to their ability to model time relationships over long sequences while maintaining computational efficiency [7]. TDNN has a pyramidal structure with a progressively wider temporal context, i.e. the initial transforms are learnt on narrow contexts and the deeper layers process the hidden activations from a wider temporal context due to the dilatation on nodes, as shown in Figure 1.

MATERIALS AND METHODS

In Figure 1 we represent the architecture of the proposed TDNN that is composed of two blocks (layer 1 and 2 in figure) and a time distributed activation level for classification (layer 3). Each block consists of a mono-dimensional convolutional layer (with kernel filter size of 3) and a Rectified Linear Unit (ReLU) activation function. Thanks to the proposed architecture, the convolutional layer in the second block will have a dilated kernel for increasing the reception field.

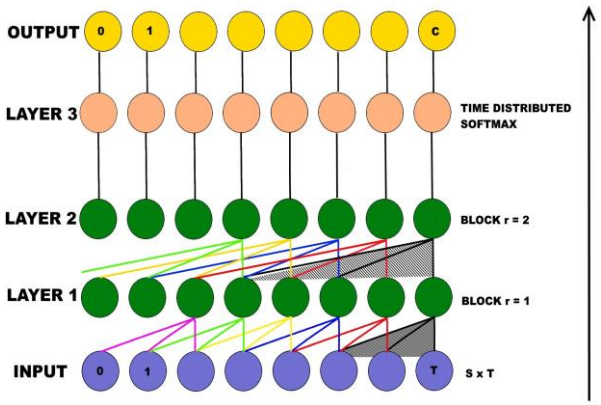

Figure. 1. *Architecture of the proposed Time Delay Neural Network (TDNN). The dark shadow shows the context pyramidal structure of the TDNN*

To evaluate the performance of the proposed method in error detection we have created the V-RASTED (Virtual Robotic Assisted Surgical Training Evaluation Dataset) dataset by collecting training exercises performed by a group of 18 medical students taking an elective course in robotic surgery. We set up an experiment to acquired synchronized kinematic data and endoscopic stereo images from the simulator developed by BBZ s.r.l. The exercise consists in lifting a ring with one robotic arm, passing the ring on the other arm and positioning it in the corresponding pole (Figure 2). This exercise replicates the one offered in standard MIS training curriculums and available in all SRS virtual training simulators.

Each student had a time slot of one hour, the first half is dedicated to practicing with the simulator interface and the second half is dedicated to the recorded trials. Each student performed from a minimum of ten to a maximum of twenty trials resulting in a total 276 sequences. The dataset included synchronized stereo images, kinematic variables for each slave manipulators simulated and some status variable for recording foot-pedals activities. To maintain consistency with JIGSAWS [5], for each slave manipulator 13 variables are provided: Cartesian position (3), rotation matrix (9), and instrument gripping angle (1). The classification classes are six and are defined as ring collection, ring transfer between surgical tools, ring

positioning in matching pole and their corresponding errors.

The dataset and more detailed documentation are available at *gitlab.com/altairLab/v-rasted.git.* The proposed TDNN implementation is based on Keras, with GPU accelerated Tensorflow framework, and it has been tested on mobile workstation equipped with Intel i7 CPU, 8GB RAM and a Nvidia Geforce 960m video card with 2GB video memory. We used ADAM stochastic optimization algorithm with categorical cross entropy loss function during training with 200 epochs and batch size of 16.

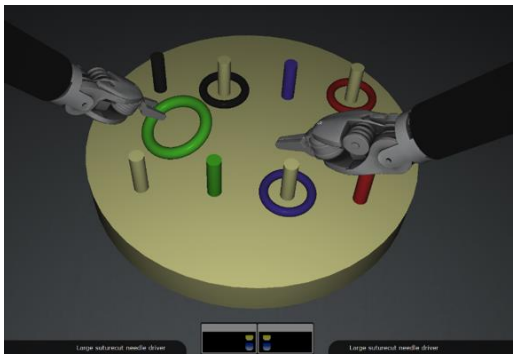

Figure. 2. *Example of image extracted from V-RASTED dataset showing the training exercise considered.*

RESULTS AND DISCUSSIONS

To evaluate the performance of the proposed method we followed the protocol described in [5] using only micro accuracy and precision. For detailed description of the experimental evaluation please refer to [5]. We obtained 68.4±6.95% on micro accuracy and 69.75±12.07 on precision evaluation. The values presented for each measure correspond to the average values (± standard deviation) of all users tested with Leave One User Out (LOUO) methodology. This means that for each user, the training and the testing set are recalculated. In Figure 3 we report the normalized confusion matrix resulted from our evaluation, it shows which types of classes are correctly recognized and which classes are the most complex to predict. In general, the results obtained on V-RASTED correspond to a good level of gesture recognition, aligned with results obtained on other datasets [2,6]. We tested our network with benchmark dataset [8]. We Most of the wrong recognitions occur between gesture and corresponding errors classes. This fact is clearly represented by the normalized confusion matrix showed in Figure 3. These results demonstrate the limits of error detection based only on kinematic variables, which can accurately represent robotic system movements, but they are unsuitable for recognizing errors deriving from interaction with the environment, such as the fall of a ring during grabbing or the incorrect positioning of the ring in the corresponding pole. To improve this result, in future works we will introduce environment sensing, based on video data as spatiotemporal features or on external sensors as marker. Moreover, the proposed V-RASTED dataset is more challenging than previously proposed ones (e.g. JIGSAWS) since its present strong class imbalance that is typical of fault/error detection. This public dataset would be an important component in the development and benchmarking of future surgical error detection methods.

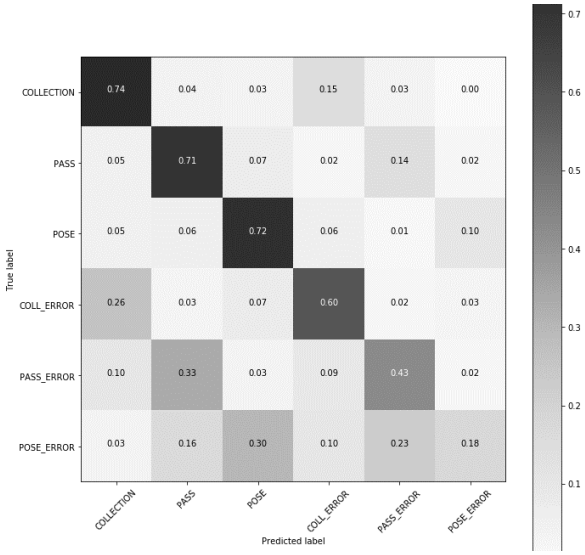

Figure. 3. *Normalized Confusion matrix obtained for the proposed method during LOUO evaluation on V- RASTED*

CONCLUSIONS

In this work we have introduced TDNN for surgical gestures and errors recognition based on kinematic data. We have evaluated the proposed method on novel V-RASTED public dataset. The obtained results demonstrate state that TDNN applied to kinematic data can be very effective in modeling instrument movements, thus they are suitable for gesture recognition, but they need to be fused with other sensing modalities for obtaining error detection performance suitable for on-line situation awareness systems.

ACKNOWLEDGEMENT

This project has received funding from ERC under the H2020 R&I programme (grant agreement No 742671).

REFERENCES

[1] Lee, G. I., et al. "Surgeons' physical discomfort and symptoms during robotic surgery: a comprehensive ergonomic survey study." Surgical endoscopy 31.4 (2017)

[2] Zappella, Luca, et al. "*Surgical gesture classification from video and kinematic data*." Med. image analysis 17.7 (2013)

[3] Rosen, Jacob, et al. "*Markov modeling of minimally invasive surgery based on tool/tissue interaction and force/torque signatures for evaluating surgical skills*."

[4] Tao, Lingling, et al. "*Surgical gesture segmentation and recognition*."

[5] Ahmidi, Narges, et al. "*A dataset and benchmarks for segmentation and recognition of gestures in robotic surgery*."

[6] DiPietro, Robert, et al. "*Analyzing and Exploiting NARX Recurrent Neural Networks for Long-Term Dependencies*."

[7] Peddinti, Vijayaditya et al. "*A time delay neural network architecture for efficient modeling of long temporal contexts*."

[8] Menegozzo, Giovanni et al. "*Surgical Gesture Recognition with Time Delay Neural Network based on kinematic data*."

A position-based framework for the prediction of probe-induced lesion displacement in Ultrasound-guided breast biopsy

E Tagliabue[1], D Dall'Alba[1], E Magnabosco[1], C Tenga[1], P Fiorini[1]

[1]*Dept of Computer Science, University of Verona,*
eleonora.tagliabue@univr.it

INTRODUCTION

The non-invasiveness and real-time capabilities of ultrasound (US) imaging make this technique appealing for guiding breast biopsy procedures. However, the fact that certain malignant lesions are often challenging to be distinguished on US has raised interest in finding some ways to combine knowledge about lesions position obtained from pre-operative modalities with real-time information provided by intra-operative US. To this purpose, several commercial and research platforms have implemented image fusion techniques able to co-register pre-operative data and US images [1]. However, none of these systems is able to account for the large deformations the breast undergoes due to the compression forces applied with the US probe by the physician to guarantee proper probe-tissue coupling and obtain acceptable image quality.

Biomechanical models represent a valuable tool to support the localization of suspicious areas identified on pre-operative imaging during US scanning, since they are able to account for anatomical deformations resulting from US probe pressure. Although the finite element method (FEM) has been extensively used in breast biomechanics, it was never employed to compensate for US probe-induced deformations, due to its incompatibility with real-time computation [2]. A valuable alternative to FEM is represented by geometry-based approaches, like the position-based dynamics (PBD). The PBD approach models objects as an ensemble of particles whose positions are directly updated as a solution of a quasi-static problem subject to geometrical constraints, thus making the method stable, robust and able to achieve real-time performances [3]. These are among the main reasons for the increasing popularity of this method in the medical field, especially for the development of surgical training simulators. The PBD scheme is used by Camara et al. to create a patient-specific biomechanical model of the kidney for the real-time simulation of intra-operative US [4]. In their work, optimal PBD parameters are estimated as those describing the deformation of kidney phantom subject to different levels of probe-induced deformations.

In this work, we present a biomechanical model of the breast based on the PBD formulation available in NVIDIA FleX. To the best of our knowledge, this is the first model able to predict in real-time the displacement of internal lesions due to the interaction with US probe. Since PBD parameters cannot be directly related to the real material properties, they are initialized with a calibration procedure performed on a phantom whose mechanical properties approximate those of the tissue of interest. In order to obtain a patient-specific description of the deformation, such parameters are then fine-tuned on the final anatomy (in our case, a realistic breast phantom) by tracking the displacement of a US-visible landmark. In this way, we obtain a patient-specific model that can accurately predict in real-time the displacement of the other internal areas during US scanning.

MATERIALS AND METHODS

The experimental data are acquired from a Freehand Ultrasound System (FUS) based on a MicrUs US device (Telemed, Vilnius, Lithuania) equipped with a linear probe (model L12-5N40) and an optical tracking system MicronTracker Hx40 (Claron-Nav, Toronto, Canada) (Figure 1). The overall probe spatial calibration error achieved is below 1mm (±0.7147).

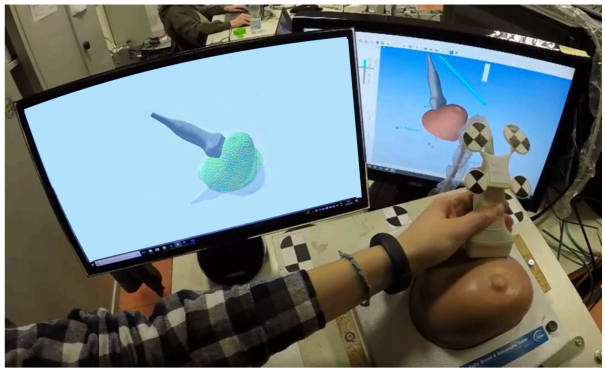

Figure. 1. The FUS system allows to map the real positions of the CIRS breast phantom and the US probe to the 3D Slicer scene (right monitor). Information about probe spatial transformation is communicated to the simulated environment in Unity (left monitor).

A box-shaped calibration phantom with three stiffer inclusions is manufactured with ballistic gel as described by Amini [5] and is used for the initial calibration of PBD parameters. In general, PBD simulations are controlled by a high number of parameters, but we focus on those closely controlling the deformable behavior of soft objects, which are related to the PBD constraint called "region-based shape matching". As a consequence, we optimize the value of *volume sampling, cluster spacing* and *cluster stiffness* parameters and we set other parameters in accordance to values reported in previous works [4]. Optimal model parameters are estimated with a greedy strategy as those minimizing the average localization error on the three internal inclusions, when applying four different input deformations with the probe

(5, 10, 15, 20 mm). Localization error is computed as Euclidean distance between the model-predicted and the real displacement provided by the FUS of corresponding fiducial points.

A realistic multi-modality breast phantom (Model 073; CIRS, Norfolk, VA, USA) is used to evaluate the capability of the PBD model to provide correct estimates of biopsy targets. Although we expect that simulation parameters obtained for the calibration phantom provide a good approximation of the breast behavior under the same kind of input deformations, it is unlikely that the same exact parameters will be optimal to describe the deformations of a structure with some major differences, mainly in shape and material properties. In order to account for the specificity of the final scenario, some experiments are conducted to refine the values of selected simulation parameters before applying the model to predict lesions displacement. This process, which we refer to as fine tuning, consists of tracking the position of a US-visible landmark (in our case, one of the internal lesions) subject to four probe-induced deformations (15, 20, 25, 30 mm) in a similar fashion to what has been done for the calibration phantom. It's worth mentioning that this fine-tuning could (and should) be performed with any internal structure which is detectable on US. The PBD model with updated optimal parameters is then used to infer the displacement of the other 9 segmented lesions under four deformations as done previously.

RESULTS

Optimal values for the volume sampling, cluster spacing and cluster stiffness parameters for the calibration phantom are 5, 10 and 0.7 respectively. The fine-tuning process for volume sampling and cluster spacing converges to values of 7 and 8. Instead, cluster stiffness is not further optimized and kept to 0.7, since changes in its value did not impact significantly the calibration results already obtained. An improvement of 16% in the overall mean target error is observed thanks to the fine-tuning process.

Figures 2 and 3 compare the performances of the proposed deformation model with a rigid one. Localization errors relative to the rigid case are computed as difference between the lesion position at rest (which always corresponds to the predicted position) and the real current lesion position, both identified on US images. Whereas, error associated to the use of the PBD model is computed as difference between the predicted position and the real position, at each deformation level. The green and orange lines in Figure 2 show the trend of the localization error at increasing deformation levels for the PBD and rigid model. It is evident that, while the errors relative to the rigid case significantly increase with the induced deformation, PBD errors never exceed the threshold of 10 mm, even when the input deformation becomes large (in the order of 30 mm). On average, the PBD biomechanical model performs better than the rigid scenario for every lesion, as emerges from Figure 3.

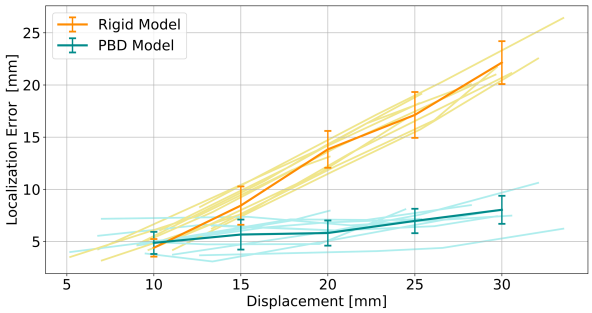

Figure. 2. Target error in mm at different levels of applied deformations for rigid (orange) and PBD (green) models. Solid lines represent the average errors on all the tumors, whereas shaded lines represent errors on each individual tumor.

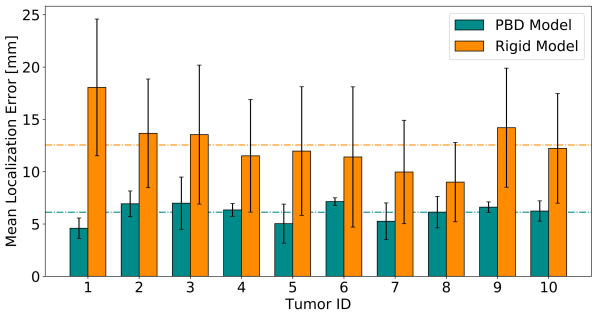

Figure. 3. Average localization error obtained for each tumor with (green) and without (orange) the PBD deformation model. Horizontal dashed lines represent the corresponding average error.

CONCLUSION AND DISCUSSION

Exploiting position-based dynamics formulation for modelling breast deformations has proved successful in predicting in real-time probe-induced displacement of internal lesions during US scanning. The proposed approach outperforms rigid models usually employed for lesion tracking in biopsy procedures. To strengthen our results, we will compare the PBD model with a FEM formulation, both in terms of accuracy and computation time. As future work, we plan to employ a more systematic multi-dimensional optimization procedure for parameters estimation and to improve the setup by replacing freehand scanning with a robotic acquisition. Finally, we will provide a more complete tool for guiding US-based percutaneous procedures by including needle insertion simulation.

REFERENCES

[1] R. Guo, G. Lu, B. Qin, and B. Fei, "Ultrasound Imaging Technologies for Breast Cancer Detection and Management: A Review," *Ultrasound Med. Biol.*, 2017.

[2] J. Zhang, Y. Zhong, and C. Gu, "Deformable Models for Surgical Simulation: A Survey," *IEEE Reviews in Biomedical Engineering*. 2018.

[3] M. Müller, B. Heidelberger, M. Hennix, and J. Ratcliff, "Position based dynamics," *J. Vis. Commun. Image Represent.*, 2007.

[4] M. Camara, E. Mayer, A. Darzi, and P. Pratt, "Soft tissue deformation for surgical simulation: a position-based dynamics approach," *Int. J. Comput. Assist. Radiol. Surg.*, 2016.

[5] R. Amini, "A novel and inexpensive ballistic gel phantom for ultrasound training," *World J. Emerg. Med.*, 2015.

Minimally Invasive Surgery Eversion Overtube

F. Putzu[1], T. Abrar[1], J. Konstantinova[1], K. Althoefer[1]

[1]*Centre for Advance Robotics @ QMUL, Queen Mary University of London,*
(f.putzu; t.abrar; j.konstantinova; k.althoefer)@qmul.ac.uk

INTRODUCTION

During minimally invasive surgery (MIS), a patient undergoes small incision and the operation involves small tubes, miniature surgical instrument and tiny cameras to be inserted. To protect the patient from sharp or otherwise potentially harmful objects during the insertion and retrieval of instruments during MIS, overtubes are used for endoscopic surgical procedures. The overtube has a sleeve like structure that avoids inadequate trapping of insufflate air, increases the depth of insertion and protects mucosa from trauma [1], [2]. It also facilitates in procedures which require insertions of multiple endoscopes, i.e. treatment of esophageal food impaction. The length and diameter of these devices varies from 540 – 650 mm and 14.4 – 21 mm (outer diameter), depending on the route of entry and the application area, such as esophageal or gastric surgeries. An example of the application of the overtube is the protection of the cricopharyngeal area or the airway. In this case, the overtube should be 25 cm in length. When the surgical area is far away from the point of entry i.e. stomach, a longer overtube is required [3].

Typically, overtubes are produced from semi-rigid plastic and have a flexible tip. The distal end of the overtube has a smaller diameter than the remainder of its body. The overtube body diameter usually match the outer dimeter of the surgical tool that needs to be employed. The overtube approach is used to reduce the chances of pinching or entrapment during insertion/exchanges of instruments. The standard solutions available on the market are specifically designed for deep endoscope insertion. The first example is a double-balloon enteroscopy (DBE) system that uses pneumatically activated concentric latex balloon and the second solution - the single-balloon enteroscopy (SBE) - uses a single silicone (non-latex) balloon placed at the tip of the endoscope [3]. The most reported complications associated with the use of overtubes are damages to the mucosa such as abrasion and tears [4]. This is mainly caused by the friction that occurs between the device and the biological environment, especially during insertion. Other problems reported are tissue perforations and pancreatitis during enteroscopy procedures [3]. Although overtubes are flexible, the causes of the damage are mainly due to the high stiffness of these devices.

In conventional overtubes, the lubrication of the inner and outer surfaces of the overtube and endoscope before the procedure is required. The outer lubrication is needed to minimize the friction and resistance between the overtube and the body parts. On the other hand, internal lubrication is needed to reduce the friction between the surgical tools and the inner layer of the device[3].

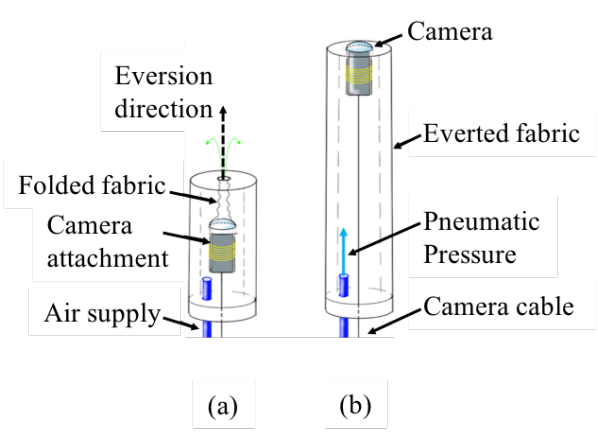

Figure 1 Illustration of fabric-based eversion overtube with embedded camera: (a) actuation of the overtube starts, (b) overtube fully elongated and the camera extending outward.

This paper describes the novel design of an overtube which can be used in both upper and lower endoscopic procedures. The proposed design is using the principles of eversion or growing at the tip [5]. Differently from more traditional devices this overtube does not require any lubrication. Due to the actuation principle, no friction occurs between the device and the biological environment, the folded part comes out during actuation and eliminates the external push of the overtube (Fig. 1).

MATERIAL AND METHODS

The proposed overtube prototype is constructed from flexible fabric with an outer diameter of 18 mm, an inner diameter of 17 mm, and the length of the tube can expand up to 1000 mm.

The airtight fabric-reinforced bladder of the overtube folds inside-out at the tip when pressure is applied, as it is shown in Figure 1. When pressurized, the fabric inside the sleeve is continuously pushed towards the tip and unfolds outwards (Fig. 1(a)). Therefore, during the process of actuation, the folded fabric that is inside is everted out to the outer surface (Fig. 1(b)). The advantages of this devices are the following:

Friction between the tube and the environment is removed due to the employment of the eversion (growing) principle. This frictionless overtube also avoids the abrasion and tears of biological tissues as the objects are not dragged or directly in contact with the surrounding body. During insertion and retraction, the eversion effects plays an important role as the overtube unfolds (insertion) and folds back (retraction) without any friction, the camera cable can work as a tendon in a similar way presented in [5].

The overtube is constructed from entirely soft material, and it allows the overtube to adapt its shape to the environment without applying undesired forces, as well as avoiding punctures and perforations. The length of the device can be adjusted controlling the pressure inside the fabric sleeve. Low cost materials are being used and, hence, the overtubes based on the eversion principle are disposable.

EXPERIMENTAL STUDIES AND RESULTS

The entry points to the human body are biological orifices or in laparoscopic surgery trocar ports. In MIS they are placed into the abdomen and represent the access for the surgical tools to the human body. Overtubes have to pass through the trocar port and extend inside the body. The first experiment performed to study the feasibility of the prototype was passing of the overtube through a standard trocar port. A standard 12 mm trocar port was used (Fig. 2). Our flexible overtube (18mm diameter), was able to travel through the trocar port and extend into

Figure 2 Eversion overtube passing through the trocar port. The esented overtube has a camera embedded at the tip.

the space behind. This experiment proves the ability of an eversion-type overtube to pass through narrow openings. Moreover, the same overtube can be used for the trocar ports of different dimensions. The second experiment is evaluating the bending capability of the overtube. The straight path is blocked by an obstacle placed in front of the overtube. Further on, the response of the overtube elongation was observed (Fig. 3(a)). It was found that the device easily bends when the straight path is obstructed. In addition, the obstacle and further bending does not influence the elongation capabilities of the overtube. Thus, the tube can bend and carry on extending until fully extended or reached another obstacle (Fig. 3 (b), 4). The natural bending of the overtube excludes the need of tendon, which in some cases are used to control the bending movement of overtube [5].

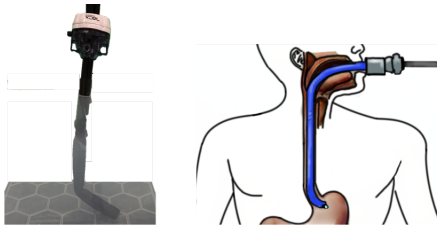

(a) (b)

Figure 3 Bending of the overtube; (a) Overtube enters in the body when the straight path is closed it bends, (b) artistic impression of the overtube bending.

RESULTS

Despite having a diameter greater than the Trocar, the overtube was able to pass through the narrow inner lumen of the Trocar port. The softness of the material allows it to bend when hitting an obstacle, enabling it to extend further and, at the same time, ensuring the safety of the human internal body and its organs as shown in Figure 4.

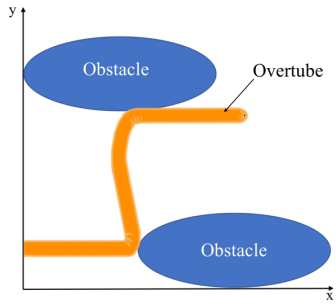

Figure 4 Behaviour of the Eversion Overtube facing obstacles observed in experiment 2.

Once deployed, the hollow inside of the eversion-type overtube can be used as guide for surgical instruments to enter and be directed to the area of interest. The results presented here are promising and show the feasibility of the proposed eversion-type overtube. Further experiments are needed to confirm its suitability for MIS.

CONLCUSION

The design and procedure of this innovative overtube is to provide ease and simplicity in the surgical procedure. Insertion of objects (endoscope or other potentially sharp tools) can take minutes but employing the proposed eversion-type overtube the procedure is expected to be done much more quickly. Our overtube is soft and, hence, the amount of trauma is reduced. The experiment was designed for a camera to pass through, but it can be used for transporting other tools as well. The experiment performed and the result discussed in this paper are an initial feasibility study showing promise. In future, the aim is to study the internal friction caused by the instruments during their insertion and use this overtube in a surgical procedure. Those procedures will endorse the effectiveness and usefulness of overtube.

ACKNOWLEDGEMENTS

This work was supported in part by the EPSRC in framework of the NCNR (National Centre for Nuclear Robotics) project (EP/R02572X/1) and WormBot project by Q-Bot (IUK 2308/104059).

REFERENCES

[1] "Technology Status Evaluation Report: Endoscopic Retrieval Devices," *Gastrointest. Endosc.*, vol. 50, no. 6, pp. 932–934, Dec. 1999.

[2] M. Goldschmiedt, G. Haber, G. Kandel, P. Kortan, and N. Marcon, "A safety maneuver for placing overtubes during endoscopic variceal ligation," *Gastrointest. Endosc.*, vol. 38, no. 3, pp. 399–400, May 1992.

[3] W. M. Tierney *et al.*, "Overtube use in gastrointestinal endoscopy," *Gastrointest. Endosc.*, vol. 70, no. 5, pp. 828–834, Nov. 2009.

[4] F. Y. Hondo *et al.*, "Transgastric access By balloon overtube for intraperitoneal surgery," *Surg. Endosc.*, vol. 21, no. 10, pp. 1867–1869, Sep. 2007.

[5] F. Putzu, T. Abrar, and K. Althoefer, "Plant-Inspired Soft Pneumatic Eversion Robot," in *2018 7th IEEE International Conference on Biomedical Robotics and Biomechatronics (Biorob)*, Enschede, Netherlands, 2018, pp. 1327–1332.

Electrical Bio-impedance Proximity Sensing for Intra-ocular Surgery

L. Schoevaerdts[1], D. Reynaerts[1], E. Vander Poorten[1]

[1]*Robot-Assisted Surgery Group, Mechanical Department, KU Leuven*
laurent.schoevaerdts@kuleuven.be

INTRODUCTION

Intra-ocular surgery is a particularly challenging type of micro-surgery where surgeons work minimally invasively at the back of the patient's eye. As a case study, retinal vein occlusion (RVO) is one the most widespread eye vascular diseases. According to the literature up to 16.4 million people are affected by this disease worldwide [1]. RVO is an obstruction of the retinal vessels due to blood clots. As a consequence, blood leaks underneath the retinal layers. This leakage causes blind spots in people eyesight, eventually leading to blindness. A current promising treatment consists of the injection of a thrombolytic agent inside the clotted vessel during a few minutes [2]. Surgeons need to display extreme dexterity during such procedure as the targeted vessels with diameters ranging from 50 to 400 µm are very fragile. Puncturing a retinal vein requires forces below 20 mN [3]. This is thus below the human perceptual threshold.

Recently, robotic systems have been successfully used to assist a surgeon in performing a retinal vein cannulation in clinical trials on humans. The surgeon manipulated a dedicated needle mounted on a co-manipulation system. The robot dampened out the motion and forces applied to the instrument [4]. During this surgery, the surgeon relies on a stereoscopic microscope placed above the eye lens of the patient. The inside of the eyeball is illuminated by a small chandelier which is introduced into the eyeball nearby the targeted site. While the microscope allows a stereoscopic vision, the quality of the depth perception is limited. Due to the poor depth estimation there is a considerable risk of piercing through the vessel, creating a `double puncture'. If unnoticed the clot-dissolving agent would be injected underneath the retina which would affect the patient's eyesight very negatively. By embedding sensors in the dedicated instruments, depth awareness could be tackled to reduce surgical risks.

However current sensor technology is often complex, expensive and difficult to integrate. The state of the art reports two main concepts for distance sensing: intra-operative Optical Coherence Tomography [5] (iOCT supplying A-scans and B-scans) and electrical bio-impedance. Here, we focus on the latter technology due to its potential to be more affordable. Within eye surgery, the electrical impedance is mainly used for proximity sensing between an implant and the retina. Ray conducted in-vivo experiments in rats, moving an insulated probe forward and backward over a range of 500 µm to the retina, reporting a rise in impedance magnitude when approaching [6]. Majdi *et al.* reported similar results on *ex-vivo* rabbit retinas measuring over a range of 1 mm away from the retina [7].

In the following we introduce a new bio-impedance sensor that was developed to detect retinal proximity over a larger range. Our measurements on *ex-vivo* pig eyes expose a specific impedance pattern that may lead to a simple and robust way to keep distance to safety-critical structures in the eye. To the best of our knowledge, current literature only reported impedance magnitudes within a close proximity of the retina, and hence failed to discover and exploit the full impedance spectrum.

MATERIALS AND METHODS

A cannulation needle previously validated in clinical trials forms the basis of this work [4]. The needle consists of a glass pipette sputtered with an electrically conductive coating. A stainless steel protective sleeve is slid over the needle tip to protect it during its insertion inside the eyeball as shown on **Figure. *1***.

A setup, as depicted in **Figure. *2***, is made for the experiment consisting out of three parts. First, the needle is fixed on a 3 Degrees of Freedom (DoF) system made out of 3 linear stages (M-423, Newport, USA) and Vernier Micrometer handles (SM – 25, Newport, USA). Two stages in the XY plane are used to align the instrument tip with an incision in the pig eye to enter the vitreous chamber. The third stage actuates the needle along its longitudinal axis to approach the retina. A laser distance sensor mounted on this stage (OADM12I6460 S35A, Baumer, Switzerland) measures the needle insertion. Second, an *ex-vivo* pig eye is positioned in a support. The eye can be oriented by rotating it about rotational axis parallel to the ground. Third, a chandelier lighting system is held by a positioning arm after being inserted through a trocar to illuminate the vitreous chamber. A clear view upon the retina is available by looking through the eye lens with a stereoscopic microscope (HS Hi-R NEO, Haag-Streit Surgical, Switzerland) and an EIBOS (90D NIR, Haag-Streit Surgical) magnifying lens that also compensates for the pig eye lens optics.

The electrical bio-impedance is measured between the needle tip and the retina. On one hand, the sleeve sliding over the glass pipette is connected to a *V+* source. The sleeve being in contact with the conductive coating, *V+* is also applied until the very tip of the needle so that the impedance measures the tip - retina distance. On the other hand, a crocodile clip attached to the eye optic nerve is put under the *V-* voltage. Voltages are applied and impedances measured with a Quadra Impedance Spectroscopy (Eliko company) system at excitation frequencies ranging from 1 kHz up to 349 kHz, measuring data at 1kHz sampling rate.

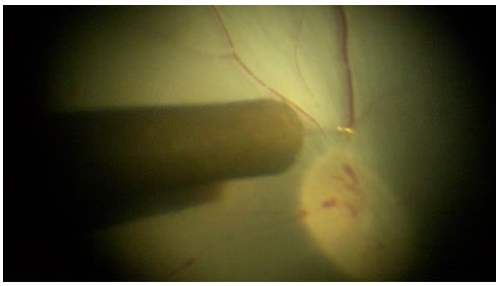

Figure. 1. Retina observed through the eye lens. The needle is pointing at a blood vessel laying on top of the retina.

RESULTS

In order to characterize the behavior of the bio-impedance, 10 round trips were executed by moving the needle between a fixed position in the vitreous chamber towards the blood vessel (**Figure. *1***). The traveled range was about 7 mm. The contact with the blood vessel was established visually as the blood inside would be flushed away when touching it with the needle. This moment was used as a reference to zero the distance measurement.

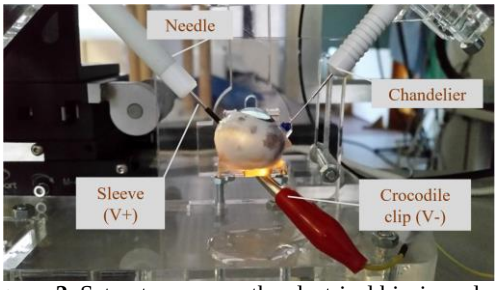

Figure. 2. Setup to measure the electrical bio-impedance while approaching the needle tip towards the retina

Figure. *3* shows a general trend how the impedance magnitude (red) is correlated to the relative distance (blue) to the vessel. The impedance magnitude was measured at 349kHz to minimize any capacitive parasitic effect. From the figure it can be seen that the magnitude decreases as the needle is getting closer to the vessel. Additionally, a repetitive bump-like pattern appeared in the impedance magnitude when approaching the blood vessel. The rise in impedance has been reported earlier and it finds its origin in the neuronal response from the retina [7]. Latter structure is made out of different neurons processing signals from the environment. The impedance drop beforehand and the resulting bump-like behaviour have not been reported. The impedance decrease when approaching the retina comes from the resistance decrease of the saline solution between the needle tip and the retina. For the given setup and needle, the experiment showed that the bump appeared approximately 600 µm away from the blood vessel. The amplitude of these bumps (i.e. from rise to contact with the retina) varied from 0.5 to 2.5 Ω. We expect that compared to the magnitude this pattern forms a much more robust means to keep the distance to the surface.

CONCLUSION AND DISCUSSION

This work introduced an innovative proximity bio-impedance sensor integrated in a cannulation needle. Experiments on a closed *ex-vivo* pig eye with this needle showed repetitive measurement of a pattern at an average distance of 600 µm between the needle tip and a blood vessel. Whereas impedance magnitude is highly variable, detecting this bump would be a robust way to report retinal proximity. Indeed changing the needle geometry or the contact surface between the crocodile clip and the optic nerve would significantly impact the impedance magnitude but not the bump-like pattern. We expect that by detecting this specific pattern, proximity could be robustly estimated merely by using affordable bio-impedance sensing techniques. Future work aims at developing more sophisticated algorithms to detect the bump and alert the practitioner of the retinal proximity. In addition, the optic chiasm is a natural electrical path from one eye to another, involving the optic nerve. In this way we expect to be able to conduct in-vivo measurements by measuring the electrical impedance between the two eyes.

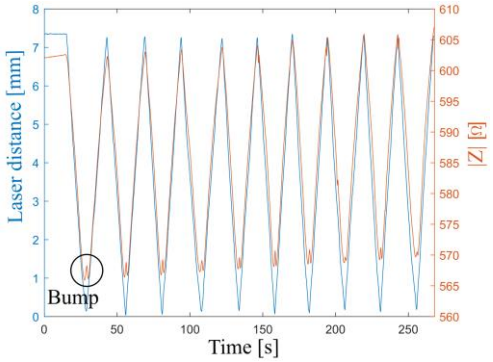

Figure. 3. The bio-impedance magnitude shows a repetitive bump when getting close to a blood vessel

REFERENCES

[1] S. Rogers et al. and International Eye Disease Consortium, "The prevalence of retinal vein occlusion: pooled data from population studies from the united states, europe, asia, and australia," *Ophthalmology*, vol. 140, no. 2, pp. 313-319, 2010.

[2] K. Van Overdam et al., "Updated cannulation technique for tissue plasminogen activator injection into peripapillary retinal vein for central retinal vein occlusion," *Acta Ophthalmologica*, vol. 93, pp. 739-744, 2015.

[3] A. Gijbels et al., "Development and experimental validation of a force sensing needle for robotically assisted retinal vein cannulations," in *IEEE ICRA*, pp 2270–2276, 2015.

[4] A. Gijbels et al., "In-human robot-assisted retinal vein cannulation, a world first," *Annals of Biomedical Engineering, vol. 46, no. 10, pp 1676–1685*, May, 2018.

[5] G. Borghesan et al., "Single fiber oct-based retina detection for robot-assisted retinal vein cannulation," *CRAS*, 2016.

[6] A. Ray et al., "Impedance as a method to sense proximity at the electrode-retina interface, " *TNSRE*, vol. 19, p. 696 – 699, 2011.

[7] J. A. Majdi et al., "Access resistance of stimulation electrodes as a function of electrode proximity to the retina, " *Journal of Neural Engineering*, vol. 12, 2015.

A physical/virtual anatomical platform for hysteroscopy training

A. Hernansanz[1], R. Martínez[2], R. Rovira[3], A. Casals[1,2]

[1]*Research Centre for Biomedical Engineering, UPC*

[2]*Institute for Bioengineering of Catalonia*

[3]*Hospital de la Santa Creu i Sant Pau, Barcelona, UAB*

albert.hernansanz@upc.edu

INTRODUCTION

Minimally Invasive Surgery (MIS), which consists in operating through small orifices, reduces the patients' pain, complications, recovery time and scarring. However, while providing many benefits, the skills required in MIS are especially difficult to learn. Unfortunately, current training methods for such techniques have not progressed at the same pace as surgical advances. Insufficient surgical skills acquisition translates into complications during procedures, which not only harm the patient, but also increases the derived costs of interventions and their follow up.

Traditionally, surgical skills training consisted in the model „see one, do one, teach one". This method was practically unchanged until the introduction of simulators, which allow students to practice before entering the operating room, but it still relies on the classical apprenticeship model. Having an expert constantly supervising the training is unsustainable, and the reality faced by residents is the lack of enough practising time [1] [2].

MIS training presents specific challenges that are not addressed by traditional methods. In hysteroscopy, an endoscopic diagnostic and interventional procedure, the hysteroscope is inserted through the vagina and the cervix to examine the uterus. Normally, surgeons have to interpret a 3D operating area through a 2D display monitor, with the consequent lack of depth perception. The instruments, which are introduced through the working channel, provide limited tactile and kinaesthetic feedback, making their control difficult [2].

Current simulators can be divided into two categories: physical simulators, also known as box trainers, and virtual reality simulators. Box trainers consist of anatomical reproductions that can have realistic tactile and visual properties. However, performance assessment has to be carried out by an observer mentor, and therefore, the evaluation is subjective.

Virtual reality simulators offer a wide range of clinical cases and keep track of the performance, but they lack of realistic haptic feedback and physical behaviour. The validity and applicability of skills acquired with virtual simulators is still an open discussion in the scientific and medical community. In addition, there is a noteworthy price difference between the two types, which makes virtual simulators unaffordable for most formative centres [3].

This work presents HysTrainer (HT), a training module for hysteroscopy, which is part of the generic endoscopic training platform EndoTrainer (ET). This platform merges both technologies, with the benefits of having a physical anatomic model and computer assistance for augmented reality and objective assessment. Further to the functions of a surgical trainer, EndoTrainer provides an integral education, training and evaluation platform.

MATERIALS AND METHODS

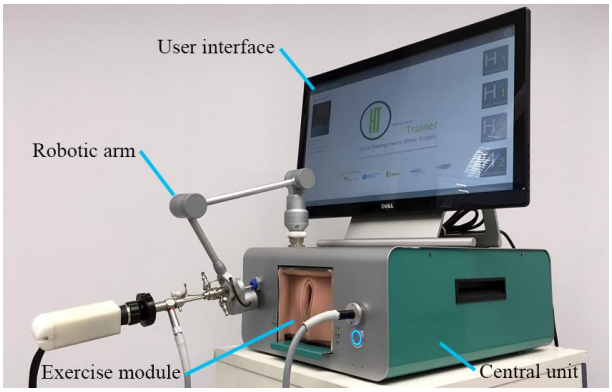

Figure 1. HT parts

Device: ET is a multi-speciality modular training device that can be used for hysteroscopy, cystoscopy and trans-anal surgery. The device consists of a central unit, which connects with the rest of the modules; an exercise module, which contains an anatomic model and elements to train specific skills; a robotic arm, which tracks the movements of the tool inside the anatomic model; and a user interface, which allows the user to interact with the device, visualise the exercise and revise the results.

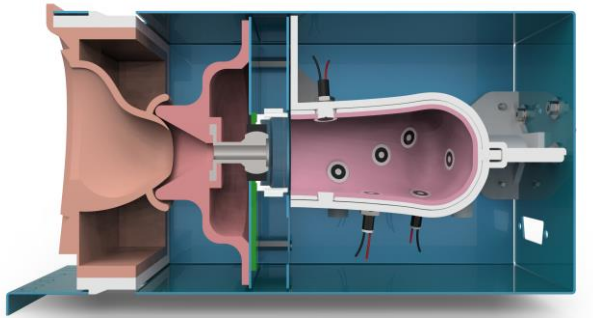

Figure 2. Reaching targets exercise module (section view).

The exercise modules consist of an anatomical model of a female reproductive system built from soft materials that emulate the appearance and physical properties of

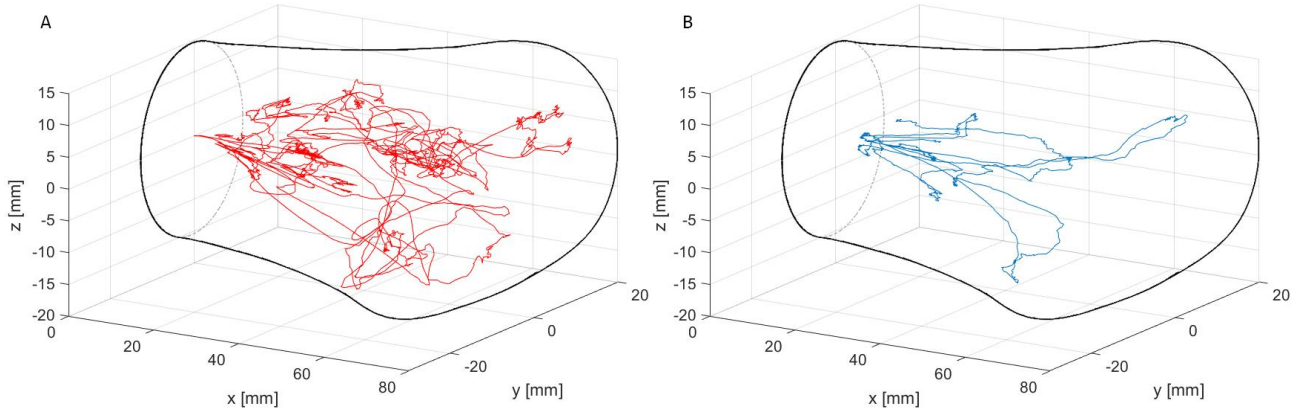

Figure 3. Hysteroscope tip trajectory pattern in the first execution (A) and after 30 repetitions (B) of a user.

the different tissues. They also include sensors and actuators to measure the interaction of the tool with the simulated organ. These modules are independent, and thus, new exercises can be introduced in the future.

The current prototype includes two exercises, corresponding to HYSTT 1-2 from the European Soc. for Gynaecological Endoscopy's formative programme [4]:

a. Reaching targets: the user has to reach 10 targets, located in key anatomical points, presented in random order. The exercise aims to train spatial cognition and camera navigation with a 30-degree angle of view hysteroscope. Quantitative metrics are used to assess the performance: time to reach the target; quality, understood as correct positioning and orientation of the tool; and economy of movement, compared to the optimal trajectory.
b. Polyp removal: the user has to remove 10 polyps with a micro grasper. This exercise aims to train in the use of auxiliary tools. Each polyp has a sensor to detect when it was extracted and the time spent to reach each polyp is measured.

Testing: the device was tested in the setup shown in Figure 1. The subjects were asked to perform 30 repetitions of the Reaching targets exercise. The tests were conducted with 25 subjects of different expertise level: 16 subjects were novices with no prior experience and 9 subjects were gynaecologists with previous experience in hysteroscopy.

RESULTS

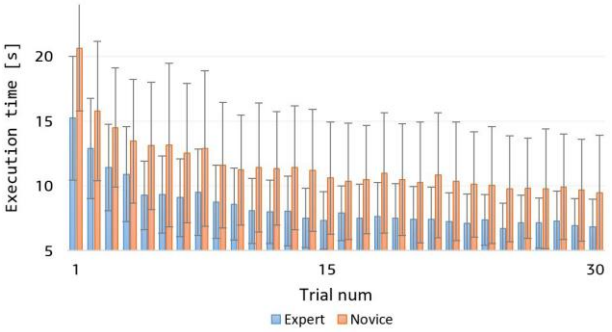

Figure 4. Execution time per target

Figure 3 shows that initially, the user followed random trajectories around the uterus cavity. After 30 repetitions, the user mainly used the central area and diverted the trajectory to reach each target. Using the central channel to observe the uterus denotes mastery in the use of the 30-degree hysteroscope and reduces the risk of harming or perforating the uterus' walls.

Regarding the execution time, the learning curve is stabilised around the 15th trial (figure 4), but there is a reduction in the variance until the last trial in both groups. There is a difference of 11,2 seconds between the 1st and 30th trial in the experts and 8,4 seconds in novices. In all trials, experts needed less time to reach each target.

CONCLUSION AND DISCUSSION

This study proposes a hybrid anatomical platform to train MIS skills applied to gynaecological surgery. The combination of physical and virtual technologies offers the benefits of performing the training exercises in a realistic anatomical model with haptic feedback, while also provides objective measurements and performance assessment.

The proposed training device increases the skills needed to perform MIS in a safe manner. The training proves to be useful regardless of previous experience since both the mean execution time and the dispersion of the results decrease after 30 trials in both groups. The fact that the curves of experts and novices do not intersect also supports the validity of the training.

REFERENCES

[1] Kolkman W, Wolterbeek R, Jansen FW. "Gynecological laparoscopy in residency training program: Dutch perspectives." Surg Endosc; 2005; 19(11):1498-502.

[2] Janse J, Driessen S, Veersema S, Broekmans FJM, Jansen FW, Schreuder HWR. "Training of Hysteroscopic Skills in Residency Program: The Dutch Experience. J Surg Educ; 2014; 72(2).

[3] Lahanas V, Georgiou E, Loukas C. "Surgical Simulation Training Systems: Box Trainers, Virtual Reality and Augmented Reality Simulators." Int J Adv Robot Automn; 2016; 1(2): 1-9.

[4] HYSTT. Hysteroscopic Skills Training and Testing method, *Accessed on 20th December 2018*. https://europeanacademy.org/training-tools/hystt/

SENTISIM: A hybrid training platform for SLNB in local melanoma staging

A. Hernansanz[1], T. Pieras[2], L. Ferrandiz[3], D. Moreno[3] A. Casals[1,2]

[1]*Research Centre for Biomedical Engineering (CREB-UPC), Barcelona*

[2]*Institute for Bioengineering of Catalonia (IBEC), Barcelona*

[3]*Melanoma Unit, Hospital Universitario Virgen Macarena, Seville*
albert.hernansanz@upc.edu

INTRODUCTION

Sentinel Lymph Node Biopsy (SLNB) has been established as an accurate procedure for regional melanoma staging. SNLB has a diagnostic significance as biopsy-based staging identifies patients with nodal metastases who may benefit from immediate complete lymphadenectomy and prolongs disease-free survival for all patients. Among patients with intermediate-thickness melanoma, this procedure provides significantly improve, over the 10-year disease-free survival rate, compared to the lymphadenectomy for nodal relapse (71.3±1.8% vs. 64.7±2.3%). This improve is also observed among patients with thick melanomas (50.7±4.0% vs. 40.5±4.7%) [1].

Optimal SLNB combines radionuclide and blue dye detection to identify the sentinel node and, during the procedure, a hand-held gamma probe is used to locate the sentinel nodes for their extraction [2]. These skills are unfamiliar to many surgeons and inexperience could lead to misdiagnosis, and thus follow an inadequate treatment, and increasing costs at the long term. Previous studies recommend a minimum of 30 cases as training phase to master SNLB due to its characteristic learning curve [3]. The estimated cost of educating a surgeon simply in added time in the operating room has been estimated at about $50.000 during the five-year residence period [4].

Surgical training platforms have emerged in the latest years as an alternative to enhance surgical training outside the operating room and even to certify procedure knowledge and ability. Up to date, some physical training models have been reported using synthetic material [5][6] or a human cadaver torso [7]. The main problem with those models is the use of radionuclide, such as technetium-99m (^{99m}TC), that entails a security protocol requirement and high costs. In addition, these platforms lack evaluation metrics to measure the exercise quality and that can worsen the training evaluation. Virtual training platforms allow to practice a surgical procedure, while they gather data of the performance to evaluate the quality of the exercise. Their main disadvantage is the loss of real feedback, which can drive to an unrelated perception of the real procedure.

Training platforms, virtual or physical, are a perfect complement to conventional training such as dissection practices that usually provide limited availability and result in high cost. The use of these platforms reduces the risk of complications and the cost of training. This work presents a new training platform for SLNB in local melanoma staging, that solves the previous problems maintaining a realistic scenario, at the same time that measures a series of important parameters to determine the quality of the surgery.

MATERIALS AND METHODS

SENTISIM is a hybrid simulation platform for training and evaluation of SLNB that combines a virtual and a physical environment, taking the advantages of both approaches. SENTISIM allows the user to train the key aspects of SNLB in a realistic scenario: hand-held gamma probe navigation, node identification, tissue dissection, node extraction and final suture. In addition, the system allows the practice of critical situations like vascular suture for femoral artery accidental dissection.

The system consists of three main modules: a multi-layer pad that simulates the inguinal region; a custom hand-held active navigation probe for node detection, and a software application to receive, analyze and store data from different sensors (e.g. probe), to generate signals for pad actuators and user interface.

The inguinal module is an anatomically realistic multi-layered pad constructed using advanced soft plastic and silicon materials reproducing textures and dynamic properties. The multi-layer composition simulates skin, fat, fascia and subcutaneous tissue, muscle, tendons, nerves, blood vessels and lymph nodes (Fig. 1).

The surgery is performed on the anatomic pad using real tools and provides realistic feedback of the passive behaviour from the different anatomic structures. Active behaviour such as cardiac pulse or muscular contractions caused by local nerve stimulation are also simulated.

Figure. 1. Section and full views of the multi-layer pad.

The custom hand-held probe (Fig. 2) simulates the gamma probe, and is used to identify and locate the nodes inside the anatomic pad. The target sentinel nodes have miniaturized magnets inserted. The simulation of the node detection is carried out through a magnetic sensor (Hall effect) located at the tool tip, that detects the

magnetic emission of the node reproducing the behaviour of the gamma probe when detecting radionuclide. More magnetic elements are present in the platform to simulate the background count and residual detection. The probe provides acoustic and visual feedback of the sensor value to improve node detection understanding. Tracking of the probe is done using an 9DoF IMU. Sensors data is sent to the user interface to enhance the training experience and later evaluate the navigation performance.

Figure. 2. Hand-held gamma probe simulation module.

The software (virtual part of the system) collects all the data from the sensors, guides the exercise through a user interface which displays the counting of the detection probe along with its reference value and other information such as like heart beat signal, vascular circuit blood level and nerve integrity (Fig. 3). Once finished the exercise, the software evaluates the training session through performance data. Gathering information of the training and comparing over evaluation metrics is essential to measure the quality of an exercise. The evaluation metrics considers time, precision of detection, probe sweeping area, correct node extraction and accidents (vessel or nerve cut). This evaluation is combined with an ocular inspection from a supervisor.

Figure. 3. First version of SENTISIM user interface.

RESULTS

The presented platform, that is under patent process, has been tested in the 2nd edition of MelaTX; a 3-day workshop in Sevilla (June of 2018) focused on a full review and training of medical-surgical treatment of locally advanced melanoma. Twenty-two dermatologists (resident and experienced) from various Spanish hospitals participated in this test. The test was performed in a two-round practical session where the participants worked in pairs, one assuming the role of the surgeon and the other that of an assistant. In the second round, the roles were exchanged. Evaluation metrics gathered during the practice permitted a better overall assessment of the exercise. E.g., tracking of the probe provided a density map of the navigated zone, where the hot spots coincide with the location of the nodes (Fig. 4). Compared to a pre-operatory gammagraphy can give a matching percentage. A small group of experts, that were invited to the workshop as speakers tested and validated the platform. The feedback received from the participants remarked the realism of the platform from the node identification and the surgical procedure on the pad. The majority expressed an increase in self-confidence in their SLNB skills. Usability tests will be done in near future to analyze impact in learning curves.

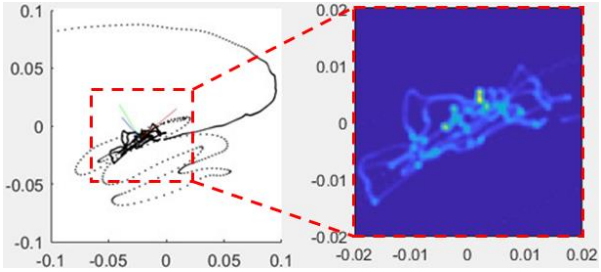

Figure. 4. Tracking of the probe (left) and density map (right).

CONCLUSION AND DISCUSSION

This paper has presented SENTISIM training platform for SLNB. The platform combines virtual and physical advantages thanks to its modular approach. Its main characteristics are realism, tissue behaviour, continuous feedback interaction, probe navigation, etc. The platform allows performing a complete surgical procedure, training all main key aspects and emergency situations.
Avoiding the need of radionuclide material usage for node detection eases the access to training sessions thanks to its reduced costs and security protocols.
SENTISIM has demonstrated its validity during the MelaTX course. A group of 22 participants and another of 8 experts performed the practical session using the platform. SENTISIM obtained the face-validity from the experts group.

REFERENCES

[1] Morton DL, et al. “Final trial report of sentinel-node biopsy versus nodal observation in melanoma.” N Engl J Med; 2014 370:599-609

[2] Motomura K, Inaji H, Komoike Y, et al. “Combination technique is superior to dye alone in identification of the sentinel node in breast cancer patients.” J Surg Oncol; 2001; 76:95-9.

[3] Clarke D, Newcombe RG, Mansel RE. “The learning curve in sentinel node biopsy: the ALMANAC experience.” Ann Surg Oncol; 2004; 11 (Suppl 3):211S-5S.

[4] Bridges M, et al. (1999) “The financial impact of teaching surgical residents in the operating room.” Am J Surg; 177:28-32.

[5] Baker PA, Sillitoe AT, et al. “Training simulators for sentinel lymph node biopsy in malignant melanoma.” Journal of Plastic, Reconstructive & Aesthetic Surgery; Volume 61, Issue 8, 976-979

[6] Keshtgar MRS, Chicken DW, et al. “A training simulator for sentinel node biopsy in breast cancer: a new standard”. European Journal of Surgical Oncology; Volume 31, Issue 2, 134-140

[7] Dunnington GL. “A model for teaching sentinel lymph node mapping and excision and axillary lymph node dissection.” J Am Coll Surg; 2003; 197:119-21.

Combined Force- and Pose Sensing to Characterize Vaginal Wall Stiffness during Laparoscopic Sacrocolpopexy

J. De Smet[1], J. Deprest[2,3], E. Vander Poorten[1]

[1]*KU Leuven, Department of Mechanical Engineering, Leuven, Belgium*

[2]*KU Leuven, Department of Development and Regeneration, Leuven, Belgium*

[3]*UZ Leuven, Department of Obstetrics and Gynaecology, Leuven, Belgium*

jef.desmet@kuleuven.be

INTRODUCTION

During sacrocolpopexy (SCP) vaginal vault prolapse, a type of pelvic organ prolapse (POP), is repaired by fixating the vaginal vault to the sacrum with a synthetic graft/mesh, restoring its anatomical position. Anatomical success rates of open or abdominal sacrocolpopexy (ASCP) exceed 90 % [1], which is better than those after sacrospinous vault fixation (SVF) whereby the vaginal vault is sutured directly to the sacrospinous ligament. However, ASCP has a higher morbidity rate, longer operation times and increased hospital cost when compared to SVF [2]. Laparoscopic sacrocolpopexy (LSCP), the minimally invasive counterpart of ASCP, appears to be the logical solution to decrease morbidity and blood loss [3]. Observational studies and systematic reviews have shown that LSCP is as effective as its open counterpart (ASCP) [4] and therefore it has gained a lot of popularity in the last decade. During LSCP at least three people are present around the operation table: A surgeon and an assistant that operate the laparoscopic instruments through four or five cannulas in the abdominal wall; and a second perineal assistant that is positioned between the legs of the patient and uses a vaginal manipulator to position and tension the vaginal vault. Manual vaginal vault manipulation has shown to be a fatiguing task and the quality of vaginal vault exposure varies depending on the experience of the perineal assistant. A common error during vaginal vault manipulation is inappropriate response to the surgeon's positioning- and tensioning instructions, leading respectively to bad vault exposure and possibly over-tensioning. These errors require additional instructions or often a manual correction by the surgeon himself/herself, which leads to extended operation times and increased stress levels for the surgical team. Recently, robot-assisted surgery (RAS) has gained a lot of popularity in gynaecology [5] as a means to give the surgeon full control over the surgical site. However, design requirements concerning the workspace of the vaginal manipulator and the required- and safe tensioning forces for a surgical robot are unknown.

This work describes the results of an in-vivo study whereby a force sensor, developed in [6], is attached to the vaginal manipulator and equipped with a pose sensing probe to obtain design requirements for a vaginal vault manipulating robot.

MATERIALS AND METHODS

After characterization [6] the force sensor was equipped with a pose sensing probe which can be tracked by an electromagnetic field generator (Aurora System, Northern Digital Inc., Canada). The operation room (OR) setup is shown on Figure 1. Care was taken to have minimum influence on the surgery by performing the study. Therefore, an appropriate location for the field generator was found under the operation table (non-sterile zone), between the legs of the patient. The total length of the modified vaginal manipulator attached and force sensor is equal to the total length of the standard vaginal manipulator. All other recording hardware is placed away from the surgical site, next to the already present OR-equipment. At the beginning of the intervention the position of the vaginal vault entrance is stored during a landmarking procedure whereby the assistant has to point to the vaginal vault entrance with the manipulator head.

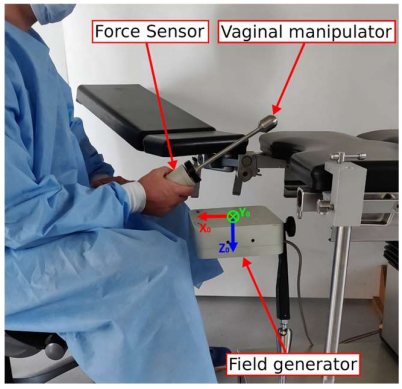

Figure 1: Clinical trial setup. The pose of the force sensor can be tracked by an electromagnetic field generator. The perineal assistant holds the force sensor housing while using the vaginal manipulator.

Figure 2 gives the data flow diagram. Force- and pose samples are combined based on timestamps. Force data is recorded with a field-programmable gate array (FPGA) (cRIO-9045, National Instruments, United States) and sent to a computer over a UDP-connection. This computer is also connected to the pose tracking system with a USB-connection. The recording and post-processing is done by a combination of LabVIEW, Python and Robot Operating System (ROS) software. A

total of eight LSCP interventions were recorded and analyzed for vaginal wall stiffness, manipulator workspace and tensioning force range.

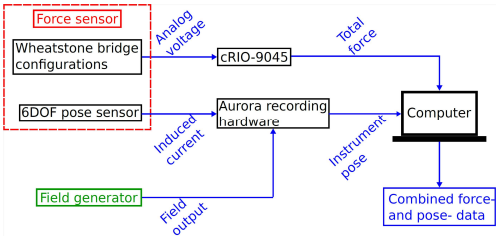

Figure 2: Data flow diagram. force- and pose samples are recorded and combined based on timestamps.

RESULTS

Table 1 summarizes the results of eight LSCP recordings. Vaginal wall forces, stiffness and manipulator workspace are all expressed in the coordinate frame of the field generator (x_0,y_0,z_0), as indicated on Figure 1. This frame coincides with the operation table plane and thus the directional stiffness and forces can be expressed w.r.t. the patient's functional anatomy.

Table 1: Vaginal wall average stiffness and total maximum forces.

	k_x [N/mm]	k_y [N/mm]	k_z [N/mm]	$F_{tot,max}$ [N]
Study 1	8.1	7.5	8.3	47.3
Study 2	12.7	8.1	6.3	25.5
Study 3	3.7	3.4	5.1	36.7
Study 4	6.8	9.6	9.0	35.7
Study 5	1.5	1.0	2.2	20.8
Study 6	8.9	12.1	12.5	26.4
Study 7	7.1	8.9	10.0	46.4
Study 8	4.0	2.7	3.4	24.7
Average	**6.6**	**6.7**	**7.1**	**32.9**

The stiffness k in every direction is calculated as:

$$k = \frac{\Delta F}{\Delta d} \quad (1)$$

Where ΔF and Δd is the difference between two consecutive force- and position samples respectively. Only samples inside the vaginal vault were used during stiffness calculation and care was taken not to include out-of-range or unreasonably high values. The total maximum interaction force with the vaginal wall is displayed in the last column of Table 1. The average workspace of the manipulator head inside the patient can be confined in a bounding box of *163 mm x 212 mm x 128 mm* (x_0,y_0,z_0). Figure 3 visualizes the workspace results of study 8. The positions of the vaginal manipulator head are color coded based on the present interaction force at that location: green for forces below 10 N, yellow for forces between 10 N and 20 N and red for forces higher than 20 N. The instrument handle is indicated in blue and the vault entrance in purple.

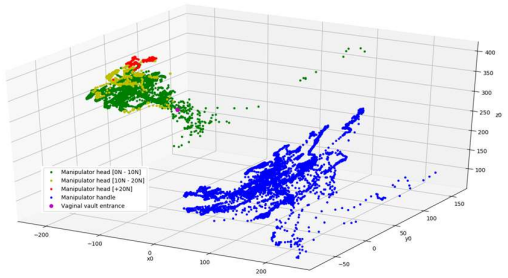

Figure 3: Vaginal manipulator workspace and corresponding interaction forces. Blue: instrument handle; Manipulator head color coded in green (< 10 N), yellow (< 20 N) and red (> 20 N).

CONCLUSION AND DISCUSSION

It is hypothesized that the vaginal vault stiffness is dependent on the degree of vaginal vault prolapse. Where a high degree of prolapse corresponds with more stretched and thus more flexible tissue, resulting in a lower stiffness. The direction of highest stiffness varies between trials, resulting in a somewhat homogenous result when looking at the average directional stiffness in the last row of Table 1. The average maximal force is 32.9 N but total maximal forces vary greatly between studies. From analyzing force data it was clear that these force peaks occur mostly during the suturing phase when the mesh is connected to the vaginal vault. A total of thirty LSCP interventions will be recorded to obtain design requirements for robotic assistants for vaginal vault positioning. Results of this study can also be used for the training of surgeons, providing them with force feedback during vaginal vault manipulation to prevent them from over-tensioning the tissue.

ETHICAL APPROVAL

All procedures performed in studies involving human participants were in accordance with the ethical standards of the institutional and/or national research committee and with the 1964 Helsinki declaration and its later amendments or comparable ethical standards. Clinical Trial Center UZ Leuven has approved this study under number S61346. Informed consent was obtained from all individual participants included in the study.

REFERENCES

[1] I. E. Nygaard *et al.*, "Abdominal Sacrocolpopexy: A Comprehensive Review," *Obstet. Gynecol.*, vol. 104, no. 4, pp. 805–823, Oct. 2004.

[2] C. Maher, B. Feiner, K. Baessler, and C. Schmid, "Surgical management of pelvic organ prolapse in women," in *Cochrane Database of Systematic Reviews*, C. Maher, Ed. Chichester, UK: John Wiley & Sons, Ltd, 2013.

[3] J. Deprest *et al.*, "The challenge of implementing laparoscopic sacrocolpopexy," *Int. Urogynecol. J.*, vol. 25, no. 9, pp. 1153–1160, Sep. 2014.

[4] A. M. Ganatra *et al.*, "The Current Status of Laparoscopic Sacrocolpopexy: A Review," *Eur. Urol.*, vol. 55, no. 5, pp. 1089–1105, May 2009.

[5] G. Callewaert *et al.*, "Laparoscopic versus robotic-assisted sacrocolpopexy for pelvic organ prolapse: a systematic review," *Gynecol. Surg.*, vol. 13, no. 2, p. 115, 2016.

[6] J. De Smet, J. Deprest, A. Thys, and E. Vander Poorten, "Force Sensing for Measuring Vaginal Wall Interaction Forces during Laparoscopic Sacrocolpopexy," in *8th joint workshop on New Technologies for Computer/Robot Assisted Surgery*, 2018, pp. 73–74.

Residual networks for inter-foetus membrane segmentation in fetoscopy

A. Casella[1,2], D. Paladini[4], E. De Momi[1], L. S. Mattos[2], S. Moccia[2,3]

[1]*Department of Electronics, Information and Bioengineer, Politecnico di Milano (Italy)*

[2]*Department of Advanced Robotics, Istituto Italiano di Tecnologia (Italy)*

[3]*Department of Information Engineering, Università Politecnica delle Marche (Italy)*

[4] *Department of Fetal Medicine and Surgery, Istituto Giannina Gaslini (Italy)*

alessandro5.casella@mail.polimi.it

INTRODUCTION

Twin-to-twin transfusion syndrome (TTTS) is a rare (estimated incidence ~15%) but lethal disease that may affect monochorionic twin pregnancies. TTTS is mainly caused by blood-flow imbalance among fetuses due to inter-placental anastomoses. If the syndrome is not treated, the risk of perinatal death of one or both of the fetuses can exceed the 80%, while more than 50% of survived foetuses could encounter physical or neurological morbidity. [1] The elected treatment for TTTS consists of selective-vessel laser photocoagulation performed in fetoscopy. [6] The placental membrane, which separates the two fetuses, is used as a reference by surgeons to navigate through vessels and locate that have to be treated. [1]

Membrane identification can be a burdensome task also for expert surgeons due to issues related to: (i) in-vivo image acquisition (e.g., limited field of view, different camera poses with respect to the membrane), (ii) image quality (e.g., noise, varying illumination level, specular reflections) and (iii) treated anatomical district (amniotic fluid, high patient variability).

Recent advances in deep learning, in particular in the field of Convolutional Neural Networks (CNNs), proposed for intraoperative-image analysis may be suitable to tackle such issues. [2]

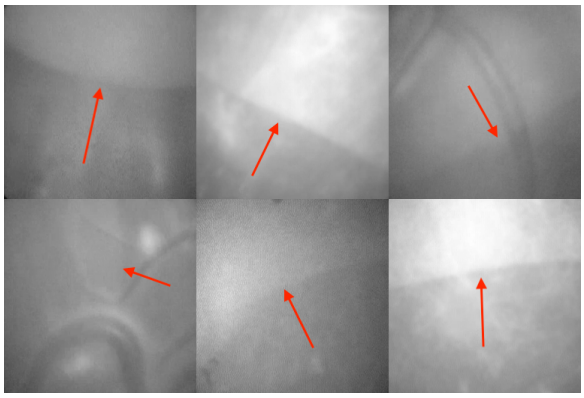

Figure 1: Samples of placental membranes (showed by red arrows) for six different women.

MATERIALS AND METHODS

In this work, a Fully Convolutional Neural Network (FCNN) based on ResNet [7] and U-Net [4] was investigated. Specifically, the proposed architecture takes advantages from both U-Net copy layers and ResNet residual skip connections.

The proposed FCNN architecture is made by a descending and an ascending path, symmetric to each other. The descending path extracts features, while the ascending one performs up-convolution and segmentation. The descending path consists of 5 layers made of 3x3 convolutional kernel with 2x2 strides. The ascending path has 3x3 convolutional and up-sampling layers. [4] Copy layers was introduced to link the descending and the ascending path to retrieve the information lost in the descending path, while the skip connections work as an identity shortcut to skip a block when it is not useful for a particular class allowing to build much deeper architectures layers reducing memory cost. [3]

To the best of authors knowledge, there is no previous work for this application and no suitable dataset for placental membrane segmentation was available to train the proposed FCNN. For this reason, a new dataset was created.

Experimental Protocol

The dataset created and used to test the proposed approach consisted of 671 frames of intraoperative videos manually extracted and labelled. A total of 600 frames (120 per patient, for 5 patients) were used as training set and a 6th patient (120 frames) was used as test set. The training images were merged, randomly shuffled and divided in training (80%) and validation (20%) set. Images were resized from 720x576 pixels to 256x256 pixels, to smooth noise and speed up training. The dataset was manually annotated under the supervision of an expert surgeon. Sample images are shown in Fig. 1. Prior to training, data augmentation was performed (by rotating the images by 45, 90, 180 and 270 degrees).

To train the FCNN, dice similarity coefficient (DSC) was used as loss function and Adam [8] was used as optimization algorithm.

$$DSC = \frac{2TP}{2TP + FP + FN} \quad (1)$$

Table 1: Performance of segmentation using proposed FCNN and U-Net. The results represent median values obtained from the test set. PPV: positive predictive value, DSC: Dice Similarity Coefficient

	PPV	DSC
U-Net [4]	97.05% (IQR 2.83%)	95.65% (IQR 6.47%)
Proposed FCNN	**98.98% (IQR 1.48%)**	**97.77% (IQR 9.01%)**

Where TP and FP are membrane pixels correctly and wrongly segmented, respectively while TN and FN are background pixels correctly and wrongly segmented, respectively.

The initial learning rate (LR) was set to 0.0001. Mini-batch gradient descent technique was used as a trade-off between training convergence time and memory usage. Batch size was set equal to 32 and the network was trained for 200 epochs.

Keras (https://keras.io) with TensorFlow (https://www.tensorflow.org) backend was used for training and testing purposes.

Segmentation performance of our protocol was quantitatively evaluated with respect to manual membrane tracing in terms of positive predictive value (PPV) and DSC and compared with results obtained using U-Net considered as gold standard in segmentation protocols.

$$PPV = \frac{TN}{TN + FP} \qquad (2)$$

RESULTS

The results of the approaches investigated are shown in Table 1. Proposed FCNN achieved best median results. Sample segmentation images are shown in Fig. 2.

DISCUSSION AND CONCLUSIONS

Membrane Segmentation for TTTS is a challenging task. As can be observed in Table 1, Proposed FCNN achieved very good results, over performing the use of U-Net alone. Nonetheless, we believe further improvements are possible and needed for clinical application. Despite data augmentation, the limited number of patients affects segmentation performance. Building a larger dataset will likely result in better segmentation performance and make the FCNN more robust against inter-patient variability.

In 31 cases out of 120, such as the one shown in the 4th row of Fig. 2, the membrane was not correctly segmented due to low membrane contrast and presence of major vessels. In the clinical practice, such cases are addressed by surgeons through the analysis of temporal information. Thus, as future work, a 2D FCNN taking into account temporal information will be investigated to solve these problems. To further increase segmentation performance, adversarial networks will be also investigated, as they showed promising results in other medical-image analysis fields. [5]

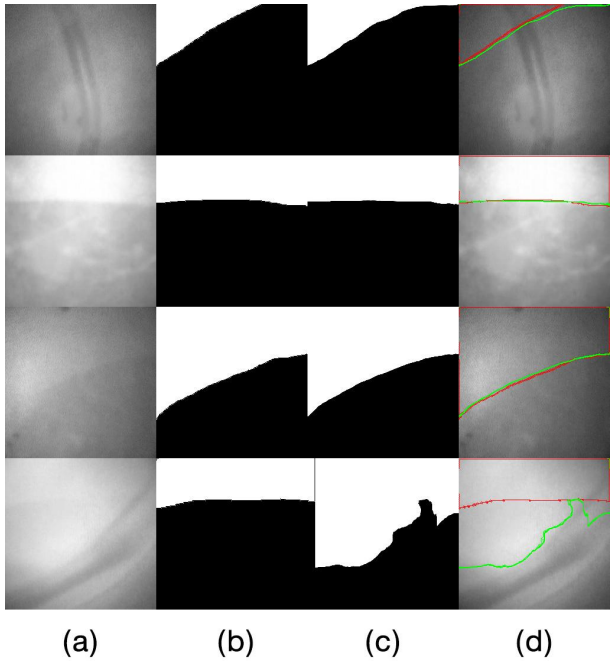

Figure 2: Some sample images of segmentation outcomes. (a) original images, (b) ground-truth manual segmentations, (c) achieved segmentation, (d) comparison between ground-truth (red) and segmentation outcomes (green).

REFERENCES

[1] D. Roberts, S. Gates, M. Kilby, JP. Neilson, "Interventions for Twin–Twin Transfusion Syndrome: a Cochrane Review." *Ultrasound in Obstetrics and Gynecology*, vol. 31, no. 6, pp. 701–711 (2008).

[2] S. Moccia, E. De Momi, S. El Hadji, L. S. Mattos, "Blood vessel segmentation algorithms — Review of methods, datasets and evaluation metrics." in *Computer Methods and Programs in Biomedicine*, Volume 158, 2018, Pages 71-91, ISSN 0169-2607

[3] M. Drozdzal, E. Vorontsov, G. Chartrand, S. Kadoury, C. Pal. "The importance of Skip Connections in Biomedical Image Segmentation." in *Lecture Notes in Computer Science* (2016): 179–187

[4] O. Ronneberger, P. Fischer, T. Brox, "U-net: Convolutional networks for biomedical image segmentation." in *International Conference on Medical image computing and computer-assisted intervention*. Springer, Cham, 2015

[5] I. Goodfellow, J. Pouget-Abadie, M. Mirza, B. Xu, D. Warde-Farley, S. Ozair, A. Courville, Y. Bengio, "Generative adversarial nets." in *Advances in neural information processing systems*. 2014. p. 2672-2680.

[6] MV. Senat, J. Deprest, M. Boulvain, A. Paupe,N. Winer, Y. Ville "Endoscopic laser surgery versus serial amnioreduction for severe twin-to-twin transfusion syndrome". 2014 in *New Engl J Med 351(2):*136–144

[7] K. He, X. Zhang, S. Ren, J. Sun, "Deep residual learning for image recognition." in *Proceedings of the IEEE conference on computer vision and pattern recognition,* 2016, pp 770–778

[8] D. P. Kingma, J. Ba, "Adam: A Method for Stochastic Optimization" in *3rd International Conference for Learning Representations*, San Diego, 2015

Transferring automatic polyp detection to the clinical domain

P Brandao[1], OF Ahmad[1,2], E Mazomenos[1], LB Lovat[1,2], D Stoyanov[1]

[1] *Wellcome/EPSRC Centre for Interventional & Surgical Sciences (WEISS), University College London,*

[2] *Gastrointestinal Services, University College London Hospital*
patrick.brandao.15@ucl.ac.uk

INTRODUCTION

Colorectal cancer (CRC) is the third most common form of cancer and the second deadliest in the whole world [1]. The survival rate of CRC patients is lower than 7% when the disease reaches an advanced stage, however, in cases of early diagnosis, with successful treatment, it increases to almost 90% [2].

In recent years, computer-aided diagnostic (CAD) systems have made big strides in the CRC detection by using artificial intelligence. These advances are mainly due to an increase in public available data, such as the MICCAI GIANA challenge dataset [3], composed of still high-quality frames or very short polyp video sequences. While the current top polyp detection methods perform extremely well in this kind validation sets, there is still limited information of how well they translate to a more realistic clinical scenario. During a full colonoscopy exam, images are frequently out of focus, overexposed or appear with interlacing artefacts. Some of these scenarios are exemplified in Figure 1.

In this work, we evaluate how one of the top methods in the MICCAI GIANA dataset performs in complete withdrawal colonoscopy videos and highlight some of the current barriers for its real clinical application.

MATERIALS AND METHODS

We use our previously developed FCN-ResNet-101 [4] trained on the MICCAI 2015 polyp detection challenge dataset as a baseline for this study. This method performs very competitively in the ETIS-Larib dataset with a detection precision and recall of 83.70 and 88.20, respectively.

Dataset

We created a new dataset using 17 complete colonoscopy withdrawal videos, previously unseen by the CNN, containing 83 unique polyps consisting of 83,716 frames (14,634 polyp and 69,082 non-polyp) using Olympus EVIS LUCERA CV290(SL) processors and colonoscopes. Polyps present in white light frames were manually annotated by an expert videoendoscopist. Low quality frames (blurred/indistinguishable image) were also labelled. Half the procedures were randomly selected to create a testing set consisting of 27,236 frames (4,804 high quality polyp images, 2640 polyp images with visual artefacts and 19,792 non-polyp).

Implementation and training details

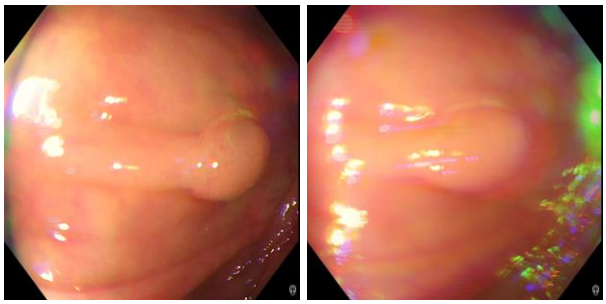

Figure. 1. Example of two sequential frames in a colonoscopy video. The second image is significantly more challenging for automatic detection methods due to blurring and interlacing artefacts.

We fine-tuned our model by SGD with a 0.99 momentum and all layers were updated by back-propagation, with a learning rate of 10^{-8}. Classes probabilities are calculated with Softmax function and cross-entropy was used as the loss function. We used a batch size of 8 for training and we resized all images to a 512x512 pixel size. Convergence was achieved after 50K iterations. All models were trained and tested using the Caffe software library [5] in a single NVIDIA TESLA GPU.

RESULTS

We evaluate our model before and after transferring its domain to the new dataset. For training, low quality images were excluded. We score a true positive detection when the computer-generated segmentation overlaps with the bounding box. A false positive indicates a non-overlapping location (more than one can occur per frame). The performance of the models in our testing set is presented in Table 1 and a few examples of the produced detections are illustrated in Figure 2

Table 1. Precision (Prec.), recall(Rec.) and false positive per frame (FPPF) values obtained in our testing set. We present the performance before (GIANA ResNet) and after (Fine-tuned ResNet) fine-tuning in our training set. The results are split for polyp images that were considered blurred or poor quality by the videoendoscopist

	Good Quality		Blurred Images		FPPF
	Prec.	Rec.	Prec.	Rec	
GIANA ResNet	56.78%	76.6%	53.23%	60.43%	0.2264
Fine-tuned ResNet	79.65%	84.5%	58.76%	62.41%	0.075

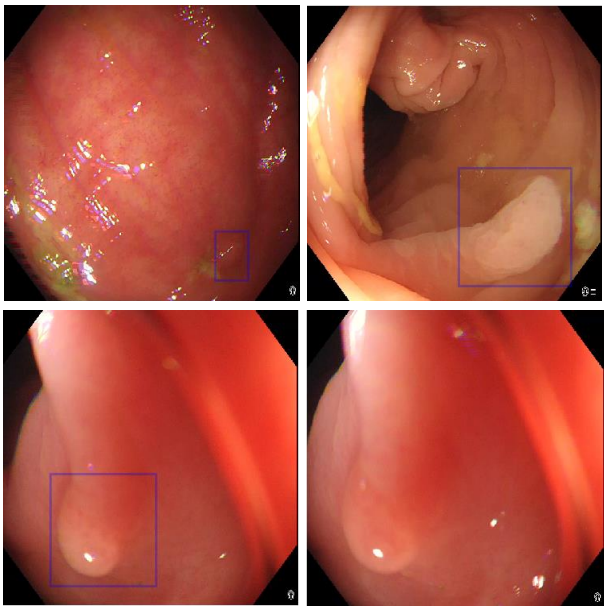

Figure. 1. Detections obtained by our FCN-ResNet fine-tuned on the training dataset.

CONCLUSION AND DISCUSSION

Whilst the CNN achieved excellent results on the public still image dataset, it is more challenging to generalize results to complete colonoscopy withdrawals. When looking exclusively at the high-quality testing sub-set, the model performs substantially worse than in the MICCAI testing set. This gap is even wider when we consider blurred polyps, where the recall drops to 60.43%. Furthermore, the model generates a huge number of false positives due to the increase of background diversity of our complete withdrawals video data.

Fine-tuning using our dataset led to improved performance. For the good quality images subset, all metrics improved considerably. While small improvements are always expected when transferring the domain of a CNN to a new dataset, these differences highlight the low generalization ability of the current public datasets. This is especially evident when we look at the big decrease in false positives, showing that the high variability of the colon and of different image acquisition systems is still poorly represented in the present datasets.

Table 1 shows that our models severely underperform when we consider lower quality images. Because datasets are mainly composed from high quality images, small visual artefacts tend to be enough to deceive the detection algorithm. For example, even though the last two images of Figure 1 are sequential, the small blurriness of the second image is enough for our CNN to completely miss it. Because we also excluded blurred images from our training set, fine-tuning did not result in major improvements of the model in this testing subset. This represents a major obstacle to clinical application when we consider that more than 35% of our polyp frames acquired in a standard colonoscopy setup were considered with subpar quality.

In conclusion, we showed that the quality of automatic polyp detection is still highly dependent of the quality of the dataset used for training. A high variability of image acquisition systems, colon views and image qualities are essential for a CNN model to be able to do large scale detection. In our future work we intend to tackle these obstacles in three-fold: continuing to increase our dataset; expand the model to accurately classify low quality images so they can be automatically discarded; incorporate temporal information instead of doing single frame detection.

ACKNOWLEDGEMENT

This work was supported by the EU-Horizon2020 project Endoo(H2020-ICT-2015-688592),
the EPSRC (EP/P012841/1) and the Wellcome/ EPSRC Centre for Interventional and Surgical Sciences (WEISS) at UCL (203145Z/16/Z).

REFERENCES

[1] Bray, F. , Ferlay, J. , Soerjomataram, I. , Siegel, R. L., Torre, L. A. and Jemal, A. (2018), Global cancer statistics 2018: GLOBOCAN estimates of incidence and mortality worldwide for 36 cancers in 185 countries. CA: A Cancer Journal for Clinicians, 68: 394-424.

[2] G. Ciuti, R. Caliò, D. Camboni, et al., “Frontiers of robotic endoscopic capsules: a review,” *J. Micro-Bio Robot.*, pp. 1–18, May 2016.

[3] Bernal, Jorge, et al. "Comparative validation of polyp detection methods in video colonoscopy: results from the MICCAI 2015 Endoscopic Vision Challenge." *IEEE transactions on medical imaging* 36.6 (2017): 1231-1249.

[4] Brandao, P., et al. "Towards a Computed-Aided Diagnosis System in Colonoscopy: Automatic Polyp Segmentation Using Convolution Neural Networks." *Journal of Medical Robotics Research* 3.02 (2018): 1840002.

[5] Jia, Y., Shelhamer, E., et al., Cae: Convolutional Architecture for Fast Feature Embedding, Proc. ACMMM ,675-678 (2014).

Including temporal information in deep-learning based joint estimation of surgical instruments

E. Colleoni[1], S. Moccia[2,3], X. Du[4], E. De Momi[1], D. Stoyanov[4]

[1]*Department of Information, Electronics and Bioengineering, Politecnico di Milano, Milan (Italy)*

[2]*Department of Advanced Robotics, Istituto Italiano di Tecnologia, Genoa (Italy)*

[3]*Department of Information Engineering, Università Politecnica delle Marche, Ancona (Italy)*

[4]*Centre for Medical Image Computing, University College London, London (UK)*

INTRODUCTION

Instrument-pose estimation is a challenging but crucial task in robot-assisted Minimally Invasive Surgery (MIS) to provide useful information for surgeon-skill analysis or surgical-action recognition.

Many methods have been proposed in literature for pose estimation, mainly exploiting laparoscopic images in combination with iterative approaches that uses 3D models of the surgical robot [1] and deep-learning algorithms [2]. In particular, deep learning has the potentiality of tackling the high intra- and inter-patient variability of surgical images.

An interesting solution has been recently proposed in [2], where a bi-branch Fully Convolutional Neural Network (FCNN) coupled with a regression network for precise joint localization has been proposed for 2D pose estimation starting from monocular laparoscopic images. The objective of the FCNN presented in [2] is to exploit the segmentation performed by the FCNN to assist the regression network in the generation of the instrument-joint probability maps, improving the detection probability of both instrument joints and the connections between them. Despite the promising results achieved in [2], no temporal information was included in the processing, limiting useful information to be exploited for pose estimation. To our knowledge, despite temporal information being widely exploited in several CNN-based video analysis tasks, e.g. for human-action recognition [3], it has never been investigated for instrument pose estimation.

In this paper, inspired by [2], we proposed an innovative architecture that uses 3D FCNN in order to extract spatio-temporal features for pose estimation starting from laparoscopic images acquired during MIS with the DaVinci surgical system.

MATERIALS AND METHODS

The instrument joints considered in this work were five: Left Clasper Point (LCP), Right Clasper Point (RCP), Head Point (HP), Shaft Point (SP) and End Point (EP) and the connections are: LCP – HP, RCP – HP, HP – SP, SP – EP.

The proposed FCNN was composed by a first segmentation bi-branch sub-network that generates nine binary maps, highlighting the neighborhood of all the detected joints and connections between joints of every tool in all the images of the input clip. A single frame example is shown in Fig. 1.b, where all the nine binary maps were put together for illustrative purposes.

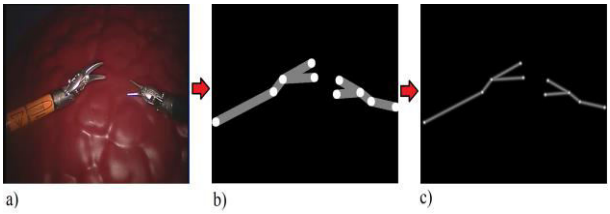

Figure 1: Example of an input frame (a). The detection network generates a binary map for each joint and connection, highlighting the neighbors of each component. The illustration (b) represents the superimposition of all the binary maps generated by the segmentation network. The regression network receives as input the raw clip and the output of the detection network and generates a probability map for each joint and connection between joints. An example of the maps is represented in (c).

This result is concatenated with the input clip and then processed in the regression sub-network, that produces a probability map for the location of every joint and connection between joints in the clip, as shown in Fig. 1.c.

Every joint probability map is then processed with a Non Maximum Suppression (NMS) algorithm in order to extract all the possible joint candidates points for every frame and then the skeleton of the instruments is generated using the pose estimation algorithm shown in [2].

The structure of the whole network is presented in Fig. 2.

Experimental protocol

To evaluate the proposed approach, the 10 videos from the EndoVis Challenge, MICCAI 2015, were used. We also included further 8 videos, acquired with a DVRK at UCL. We used the annotations provided in [2] in order to generate the gold standard for the MICCAI dataset, while we manually labeled the frames of the custom dataset.

We used ≈70% of the whole dataset for the training, ≈10% for validation and ≈20% for the test, where each set was made of videos from both the two datasets.

Every video was fragmented into clips using a sliding window of eight frames with a stride of four frames. Frames were resized to 256x320 pixels.

We trained both the proposed network and the network presented in [2] using a learning rate of 0.01 with a decay of 5% every 5 epochs, a momentum of 0.98 and a batch size of 2. The chosen loss functions was the binary cross-entropy for the segmentation network and the mean squared error for the regression network, using the Stochastic gradient descend as optimizer. We selected the model with the smallest loss on the validation dataset for both the networks.

The FCNN segmentation performance were evaluated in terms of Dice Similarity Coefficient (DSC). The DSC is defined as $\frac{2*TP}{2*TP+FP+FN}$, where TP is the number of pixels correctly classified as joints neighbor, FP is the number of pixels misclassified as joints neighbor and FN is the number of pixels misclassified as background. We also computed segmentation precision as $\frac{TP}{TP+FP}$ and recall as $\frac{TP}{TP+FN}$.

The performance of the proposed FCNN were compared with those achieved by our competitor in the state of the art, i.e. [2].

RESULTS

Figure 3 shows the results achieved on the test set by the proposed 3D network and the state of the art competitor [2].

We achieved statistically significant different results (p-value < 0.01, Wilcoxon signed-rank test) for DSC and precision, with an increase of 5% and 10% of the median values, respectively, and a decrease of the InterQuartile Range (IQR) of 5% for both the quantities. No significant differences were found when comparing the recall achieved with the two FCNNs. With the proposed approach, a median recall of 90% was achieved.

Even so recall statistics showed very good results, with a median value around 90% and IQR ≈ 7%.

DISCUSSION AND CONCLUSION

The proposed 3D FCNN outperformed the joint-segmentation results obtained in [2] in terms of precision and DSC. Such results support the hypothesis that including temporal information may be helpful with a view to recover instrument pose estimation.

Future work will deal with the integration of this work with the design of the regression network using 3D convolutional layers, employing an architecture similar to the one developed in [2] in order to obtain instrument pose estimation from the achieved segmentation.

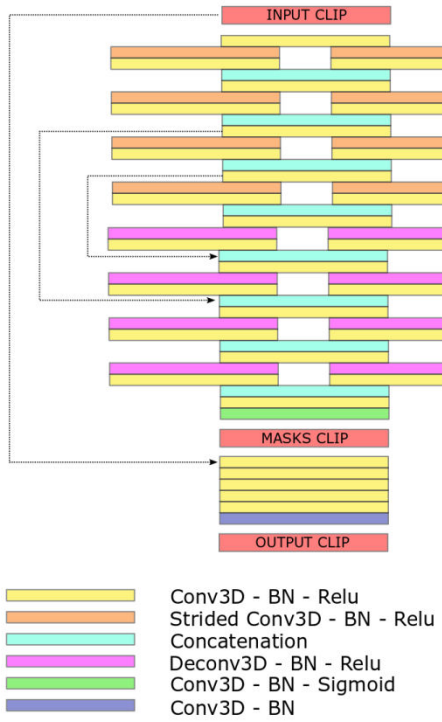

Figure 2: Architecture of the proposed FCNN.

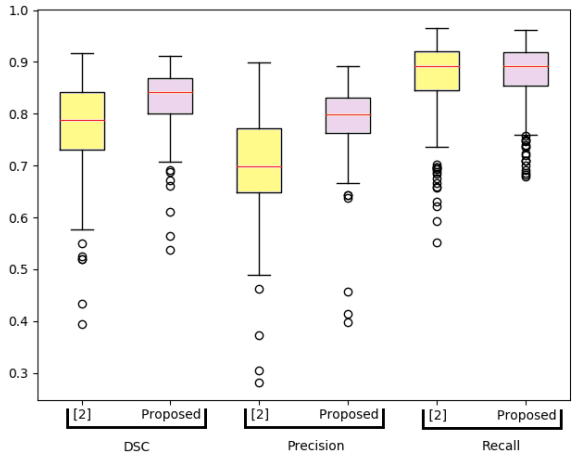

Figure 3: Boxplot of the considered scores. The test set was processed using the network developed in [2] (purple blocks) and the proposed one (yellow blocks). The results of the segmentation are shown in terms of precision, recall and DSC.

REFERENCES

[1] Allan, M et al., '3-D pose estimation of articulated instruments in robotic minimally invasive surgery' *IEEE Transactions on Medical Imaging*, vol. 37, no. 5, pp. 1204-1213.

[2] Du, X et al., 'Articulated multi-instrument 2-d pose estimation using fully convolutional networks' *IEEE Transactions on Medical Imaging*, vol. 37, no. 5, pp. 1276-1287.

[3] Hou, R. et al., 'An end-to-end 3D convolutional neural network for action detection and segmentation in videos'. *arXiv preprint arXiv:1712.01111*.

Contact Force Compensation of a Catheter Tip for Minimally Invasive Cardiovascular Surgery

O. Al-Ahmad[1,2], M. Ourak[1], J. Vlekken[2] and E. Vander Poorten[1]

[1]*KU Leuven University, Department of Mechanical Engineering, Leuven, Belgium,*

[2]*FBGS International NV, Bell-Telephonelaan 2H, 2440 Geel, Belgium*
omar.alahmad@kuleuven.be

INTRODUCTION

Nowadays, heart disease has become the leading cause of death worldwide [1]. It has been undergoing a significant widespread to the extent that it is considered to be a global epidemic [2]. Clinicians and interventionalists around the world continuously look for contemporary solutions to confront such diseases. As a result, with the advent of Minimally Invasive Surgery (MIS) comes the need to develop novel robotic technologies to serve this purpose. Catheters, sheaths and guidewires have become the standard tools used in catheterization procedures. For example, they are employed in coronary bypass surgeries and Radio-frequency Ablation (RFA). The catheter is inserted into the patient's vasculature and navigated towards the heart. In previous work, a catheter drive system has been presented that can achieve this task [3]. The innovative design allowed for continuous catheter motion with adequate and non-damaging gripping force. For interventions where the catheter tip directly interacts with cardiac tissue, it is very important to maintain a constant contact force. Excessive contact forces can cause severe tissue damage and various cerebrovascular complications, whereas too low forces can have no effect on the cardiac tissue. The highly dynamic environment within the beating heart in addition to complementary effects such as friction and backlash prove this to be a non-trivial task. It has been shown that standard closed-loop force control methods usually cannot be employed solely for this purpose [4]. The reason is mainly due to the high actuator bandwidth requirements and vibratory modes. Moreover, the catheter and heart wall are compliant bodies which further influence the contact behavior. A generally proposed approach is to have an additional environmental measurement which can then be passed as a feed-forward term in the control loop [5]. This was implemented in cardiac catheter applications where position measurements were obtained using 3D ultrasound imaging [4], [6]. However, in some given situations it is not possible to directly measure heart motion. Therefore, we present an approach using our previously developed catheter drive system to estimate the motion of the heart as a periodic sinusoid. A description of how the sinusoidal parameters are estimated is provided. Furthermore, the results of feed-forward control using position/velocity terms in combination to an adequately-tuned closed-loop force controller are demonstrated and compared to the exclusive closed-loop controller.

MATERIALS AND METHODS

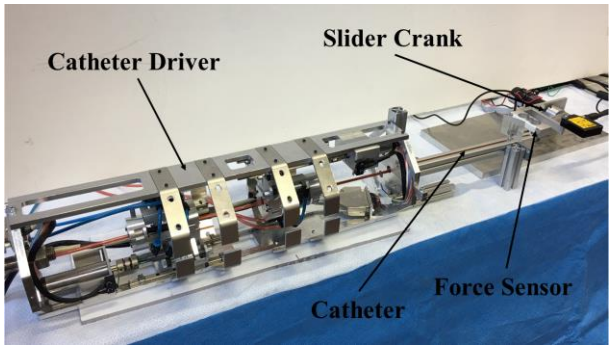

Figure. 1. Experimental setup incorporating the catheter drive system, catheter and slider crank mechanism to imitate the beating heart motion.

The catheter drive system illustrated in Figure 1 is used to maintain a constant contact force between the catheter tip and slider crank wall (imitating the heart wall). The system comprises a pair of sleeve-based pneumatically actuated grippers. These are used to firmly grasp the catheter and propagate it as demanded. This is achieved using motors, linear guides and screws. A slider crank mechanism was designed to generate a sinusoidal motion profile which will be employed to imitate the motion of the heart wall. A force sensor (load cell) is rigidly mounted on the slider crank. The sensor provides contact force measurements with respect to the catheter tip. The first step towards force compensation/tracking is to have a reasonably accurate estimation of the heart's wall motion. In this paper, the motion is assumed to be sinusoidal and estimated as:

$$\hat{x}(t) = \hat{A}\sin(\hat{\omega}t + \hat{\varphi}) \qquad (1)$$

Where $\hat{A}$, $\hat{\omega}$ and $\hat{\varphi}$ are the estimated sine amplitude, angular frequency and phase shift respectively. The procedure to obtain these parameters is explained as follows: Starting from a no-contact position, the catheter slowly moves towards the beating heart (slider crank with load cell here). At a certain point, a contact force peak will be detected. If the peak magnitude is larger than a certain threshold, the catheter gradually retreats until the peak contact force is within a certain predefined limit. Once in position, forces are recorded for a given number of force peaks. The time at which these peaks occur is recorded and an average period T_{avg} is computed.

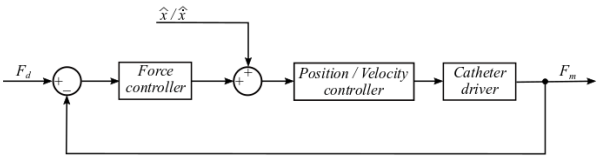

Figure. 2. Block diagram for the closed-loop force control with position/velocity feedforward.

The angular frequency $\hat{\omega}$ can then be simply found as $\hat{\omega} = 2\pi/T_{avg}$. The phase shift $\hat{\varphi}$ is computed as $\hat{\varphi} = \hat{\omega} \cdot (t_{ref} - (t_p - T_{avg}/4))$. Where t_p is the time when the peak occurs and t_{ref} is a reference time where the first force measurement is recorded. An average for all force peaks is computed. The amplitude $\hat{A}$ is estimated using an iterative trial approach. An initial estimate for $\hat{A}$ is provided and the forces are recorded respectively. The catheter tip amplitude is then gradually increased up to a certain maximum. For tip amplitude values smaller than the actual heartbeat amplitude, a force peak is observed at the crest of the sine (i.e. heart fully expanded) with minimal contact. On the other hand, for amplitude values greater than the actual amplitude, a force peak is observed at the trough of the sine (heart fully contracted). Here depending on how large the amplitude is, the contact force can exceed the predefined force threshold. The optimal situation occurs when the amplitude is closely in the proximity of the actual amplitude. There will be force contact in both the crest and trough sides of the sine. To quantify this, the normalized force values are consecutively summed. An additional sign is given to the force value depending if the sine position was on the crest side or the trough side (similar to an integral). The amplitude which yields a summation value closest to zero is the nearest to the actual amplitude and is taken as $\hat{A}$. The complete heartbeat motion is now estimated. The estimated motion can then be given as a feedforward term to a position/velocity controller. This inner loop is then closed by an outer force control loop. The block diagram schematic for this approach is illustrated in Figure 2.

RESULTS

The main emphasis during this procedure lies in obtaining a highly accurate estimation of the angular frequency $\hat{\omega}$. This is because it has a larger influence on the feedforward term and the system stability. $\hat{\omega}$ was estimated several times for different frequencies with error values below 0.5%. Similar results were also obtained for the phase shift $\hat{\varphi}$ and amplitude $\hat{A}$. Figure 3 shows force measurements for different control scenarios. The slider crank's frequency was set to 1Hz and amplitude to 10mm peak-to-peak. The result illustrates the poor behavior of single-handed closed-loop force control. As mentioned previously, the system would require a very high bandwidth in order to cope with the hyperfast changes in force. As the heart wall moves away from the catheter tip, the catheter tries to follow it and maintain contact. The contact force here would be very low or zero (i.e. loss of contact).

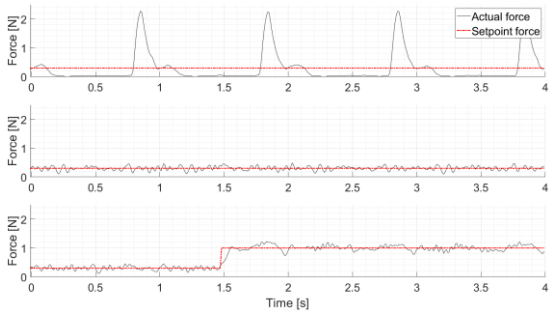

Figure. 3. From top to bottom: Closed-loop force control only; Closed-loop force control with feedforward (fixed setpoint); Closed-loop force control with feedforward (changing setpoint).

When the heart wall changes direction, a sudden force peak is observed (due to fast "collision"). The catheter then tries to overcompensate for this force peak. Eventually, contact is lost and the cycle repeats. Conversely with feed-forward, the system already "predicts" and follows the motion of the heart. The external force controller makes sure the demanded force setpoint is reached. The result is significantly improved and the catheter maintains contact at all times. For the given setpoint of 0.3N, the mean error was less than 1% and a maximum variation of ±0.2N. When the setpoint was increased (0.3N to 1.0N), the mean error and maximum variation remained the same after stabilization.

CONCLUSION AND DISCUSSION

A catheter drive system was used to maintain a constant contact force between a catheter tip and cardiac tissue. A technique to estimate sinusoidal heart motion parameters was provided with accurate results. Estimated motion feed-forward in combination with closed-loop force control showed a remarkable improvement in maintaining constant contact forces. The dynamic behavior proved to be quite adequate. Generally, the higher the force setpoint the larger the error would be as the catheter and heart are compliant bodies. Further effects such as friction and backlash will be characterized and added to improve system behavior.

REFERENCES

[1] WHO, World Heart Federation, and World Stroke Organization, "Global Atlas on Cardiovascular disease prevention and control," 2011.

[2] G. Y. H. Lip, P. Kakar, and T. Watson, "Atrial fibrillation - The growing epidemic," *Heart*, 2007.

[3] O. Al-Ahmad, et al., "Development of an Innovative Sleeve-Based Robotic Catheter Driver," in *8th Joint Workshop on New Technologies for Computer/Robot Assisted Surgery*, 2018.

[4] S. G. Yuen, et al., "Force tracking with feed-forward motion estimation for beating heart surgery," *IEEE Trans. Robot.*, 2010.

[5] J. De Schutter, "Improved Force Control Laws for Advanced Tracking Applications," *Control*, 1988.

[6] S. B. Kesner, and R. D. Howe, "Design and Control of Motion Compensation Cardiac Catheters," in *2010 IEEE International Conference on Robotics and Automation*, 2010, pp. 1059–1065.

An Artificial Neural Network Differential Pressure Flow Predictor to Measure Intra-Aortic Flow for REBOA

Alok Mehta[1], Akash Mehta[1], Diana Velazquez-Pimentel[1], Jack McAlinden[2], Samy Sadek[3], Kaspar Althoefer [2]

[1]*Barts and the London School of Medicine, Queen Mary University of London,*

[2]*Centre for Advanced Robotics @ Queen Mary University of London,*

[3]*Royal London Hospital, London's Air Ambulance, The Institute of Pre-Hospital Care*
a.mehta@smd13.qmul.ac.uk

INTRODUCTION

Haemorrhage accounts for up to 50% of trauma deaths in the world. 33-56% of these patients die before reaching hospital[1]. Non-compressible torso haemorrhage constitutes a major cause of this, making it particularly challenging to stop the bleeding**.** A solution to this problem is resuscitative endovascular balloon occlusion of the aorta (REBOA), where a balloon tipped catheter is inserted and inflated in the aorta reducing distal blood flow. A major limitation of this device however involves the ischaemic damage to end organs after prolonged balloon occlusion[2,3,4]. A solution to this problem is variable occlusion REBOA (VO-REBOA), allowing a low flow of blood to pass distally[5,6].

According to Poiseuille's equation there is a power 4 relationship between diameter and flow rate, so small changes in balloon volume can lead to drastic changes in aortic flow. To achieve optimal VO-REBOA outcomes a fully autonomous robotic device that can continuously monitor the intraarterial environment and modulate the balloon maximising distal flow is needed to prevent ischaemic damage and exsanguination simultaneously[7]. The greatest challenge in this is measuring flow accurately.

Flow measurement is particularly difficult due to size constraints and the environment it must operate in. A differential pressure flow sensor is therefore proposed, measuring distal and proximal pressure, using the catheter and introducer sheath. During VO-REBOA the balloon will deflate and inflate continuously, thereby changing the orifice diameter and geometry as the balloon is a soft, deformable restrictor. This means the discharge coefficient will be variable, a constant that is required for differential pressure flow sensing[8]. Artificial neural networks (ANN) can attain trends and predictive value from relatively complex, unintuitive data that a fixed formula may struggle with. Because of this, an ANN is proposed to create an intuitive solution to the problem.

MATERIALS AND METHODS

A model aorta was made using 25mm and 6mm diameter PVC and silicone tubes, with pressure sensors (Honeywell 24PCBFA6G) and flow sensor (RS Pro flow-meter 0.01-4L/min, 447-4449) connected as seen in Fig 1. A syringe driver was used to control the ER-REBOA™ balloons volume using an Arduino Uno at a rate of 0.18 ml/s. A water tap was used to modulate flow of water. 1867 sets of data were collected over 31 min at 1s intervals, however 98 were removed due to anomalies arising from experimental limitations leaving 1769 sets. A 3 layer backpropagation ANN was created using Simbrain (Fig 2). The ANN was given four data inputs, the proximal high pressure, the distal low pressure, the diameter of the tube and volume of fluid in the balloon with flow being the target.

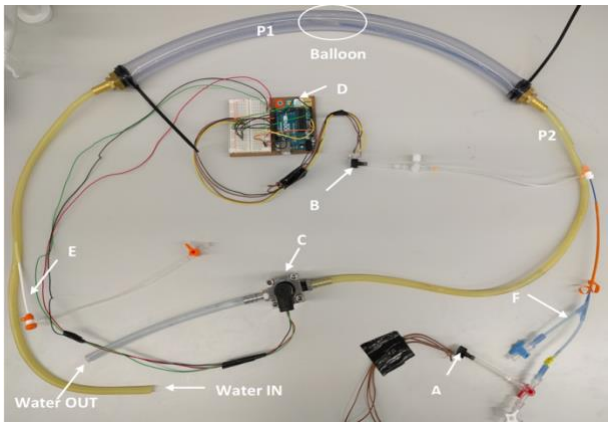

Figure. 1. Model aorta. Proximal (A) and distal (B) pressure sensors attached to the balloon. P1 shows where inside the tube the proximal pressure is being read from while P2 shows where the distal pressure is being read from. The flow sensor (C) is attached to the end of the circuit. These sensors communicate to an Arduino Uno (D). The high-pressure bypass (E) is an introducer sheath connected to the proximal tube. The ER REBOA™ catheter (F) is introduced into the distal silicone tube.

RESULTS

The sensor data was converted into a value between 0-1 by dividing all values by the maximum in the group – 3400 for the flow, 13 for pressure, 24 for balloon volume and 32 for diameter. This data was then randomised. The ANN was trained on a training set of 1415 data points (first 80%) and iterated over 5000 times to reach a root mean squared error (RMSE) of 0.0059. The next 20% was used to test the data – totalling 354 data points.

The test data results show that a sensor in the range of 0-3400 ml/min with an RMSE of 0.039 (132 ml/min) has been demonstrated. Figure 3 shows the spread of the predictions for this. The greatest output variance was 724 ml/min flow when the true flow was 400 ml/min with a minimum predicted at 179 ml/min and maximum at 903 ml/min. There is little variance at the high flow range while the mid-flow rate still has significant variance. The ideal fit graph (y=x) shows what the perfect response of the network should have been. This can be compared to the best fit line from the actual fit data representing an R^2 of 0.95.

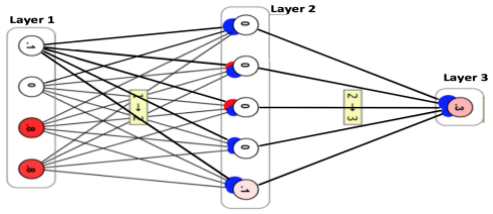

Figure. 2. – 3 Layer ANN with 4 inputs

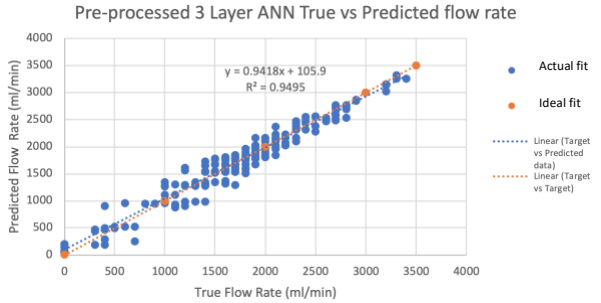

Figure. 3. – The graph shows the predictions vs the ideal flow value for the 3-layer ANN. A trend is evident for the data as a whole. The graph shows the results after processing of data to eliminate obvious anomalous results that were usually after rapid changes in balloon volume or tap flow rates.

CONCLUSION AND DISCUSSION

Differential pressure flow sensors are simple sensors by design that require pre-determined coefficients and predictable environments to operate in. A solution for differential pressure use in a dynamically changing environment was hypothesised. The results indicate that flow can be predicted using the four inputs including differential pressure to a relatively high accuracy using an ANN. To the authors knowledge this work is the first time a differential pressure flow sensor incorporating a neural network has been developed. It has been demonstrated that relatively simple hardware using equipment already being used in medical practice can be used to develop a flow sensor with little modification of the current hardware.

The number of limitations of current generation velocity sensors can be overcome using this method. Thermal flow sensors are affected by dilution and changes in the thermal coefficient of the blood with limited ranges for velocity (>100 cm/s)[9]. Smaller catheter diameters usually limit workable surface area for sensors to operate on; however, the flow sensor proposed won't be limited by this as pressure sensors are operable at very small catheter diameters.

There were however some limitations in the experimental setup. PVC tubes are not equivalent to an aortas mechanics. Abrupt changes in either high or low flow, or inflation of the balloon lead to lagging of sensing data and could give quite ambiguous data. This could be rectified by modifying the experimental set-up by connecting the flow sensor closer to the balloon or using wider tube diameters to connect the flow sensor to the model aorta. This work needs to be repeated in an in-vivo porcine model to further train the ANN and allow the system to operate in a realistic model.

An autonomous robotic system now needs to be developed that can monitor all the sensor inputs and balloon volumes, run an ANN that can predict the flow rate and modify the balloons diameter via a syringe driver in real-time to maintain a pre-determined flow rate. This system would cognitively offload physicians in the austere field and significantly change REBOA practice to improve outcomes for exsanguinating patients.

REFERENCES

[1] Kauvar DS, et al. "Impact of hemorrhage on trauma outcome: an overview of epidemiology, clinical presentations, and therapeutic considerations." J Trauma; 2006; 60(6 Suppl)**:** S3-11.

[2] DuBose JJ, et al. "The AAST prospective Aortic Occlusion for Resuscitation in Trauma and Acute Care Surgery (AORTA) registry: Data on contemporary utilization and outcomes of aortic occlusion and resuscitative balloon occlusion of the aorta (REBOA)." J Trauma Acute Care Surg; 2016: 81(3)**:** 409-19.

[3] Morrison JJ, et al. "The inflammatory sequelae of aortic balloon occlusion in hemorrhagic shock." J Surg Res; 2014; 191(2)**:** 423-31.

[4] Saito N, et al. "Evaluation of the safety and feasibility of resuscitative endovascular balloon occlusion of the aorta." J Trauma Acute Care Surg; 2015; 78(5)**:** 897-903; discussion 904.

[5] Russo RM, et al. "Partial Resuscitative Endovascular Balloon Occlusion of the Aorta in Swine Model of Hemorrhagic Shock." J Am Coll Surg; 2016a; 223(2)**:** 359-68.

[6] Russo RM, et al. "Extending the golden hour: Partial resuscitative endovascular balloon occlusion of the aorta in a highly lethal swine liver injury model." J Trauma Acute Care Surg; 2016b; 80(3)**:** 372-8; discussion 378-80.

[7] Williams TK, et al. "Extending REBOA: Endovascular Variable Aortic Control (EVAC) in a Lethal Model of Hemorrhagic Shock." J Trauma Acute Care Surg; 2016; 81(2): 294-301

[8] Beck SBM, Mazille J. "A study of a pressure differential flow meter that is insensitive to inlet conditions." Flow Measurement and Instrumentation; 2002; 12(5)**:** 379-384.

[9] Klinker L, et al. "Balloon catheters with integrated stretchable electronics for electrical stimulation, ablation and blood flow monitoring". Extreme Mechanics Letter; 2015; 3**:** 45-54.

Four degrees of freedom soft manipulator module driven by tendons for minimally invasive surgery

H Godaba[1], A Ataka[2], K Althoefer[1,2]

[1]*School of Electronic Engineering and Computer Science, Queen Mary University of London*

[2]*School of Engineering and Materials Science, Queen Mary, University of London.*
h.godaba@qmul.ac.uk

INTRODUCTION

Soft robots are growing in popularity due to the myriad of advantages they offer such as high manoeuvrability, inherent compliance and reduced complexity of mechanical design [1]. Unlike their rigid counterparts, they are less likely to cause injury when they impact against body tissues. Owing to these advantages, soft manipulators have been proposed for minimally invasive surgery (MIS) [2], [3].

In MIS or keyhole surgeries, manipulators with sensors or tools mounted at the tip are inserted through ports placed at incisions in the human body. The size of the incisions must be as small as possible to minimize patient trauma and to reduce the recovery time of the patient after surgery [4]. This places emphasis on designing mechanical systems that can pass through these tiny openings and exhibit high controllable degrees of freedom to enable versatile manoeuvres required for surgery. In previous works, 3-dof controllable pneumatically actuated manipulators were proposed for minimally invasive surgery [3], [5]. In this methodology, a soft elastomer body with three air chambers was utilised to achieve linear elongation and bending in the two transverse directions. However, many MIS systems utilize four degrees of freedom – penetration (or elongation), pan (or roll), tilt (or pitch) and spin, to achieve various surgical manoeuvres[6]. Achieving additional degrees of freedom in pneumatically actuated structures increases the space requirements and complexity of the actuators.

Maghooa et. al. designed a 3-dof continuum manipulator actuated by tendons and air pressure based on the antagonistic principle[7]. Actuation using tendons offers additional degrees of freedom without adding to the space requirements of the manipulator as they can be integrated along the body of the manipulator. Moreover, the tendon lengths and air pressure can also be controlled to vary the stiffness of the manipulator so as to ensure the stability of the manipulator after the desired position and orientation have been reached [8]. In this paper, we present a preliminary proof of concept for the development of a 4-dof manipulator module actuated using tendons and pressure that is capable of elongation, bending and twisting.

MATERIALS AND METHODS

The manipulator module consists of a hyperelastic bladder made of latex which is covered on the outside by a fabric sleeve made of inextensible material (Fig. 1a). A hollow tubing through which air can be pumped in, is attached to the pneumatic bladder. The outer fabric sleeve has three longitudinal channels, stitched into the fabric, spaced 120 degrees radially apart from one another. Another helical channel runs clockwise around the sleeve from the distal to the proximal end. As a first prototype for demonstrating the principle, only a clockwise channel is employed in this work. Four flexible but inextensible tendons are passed through the

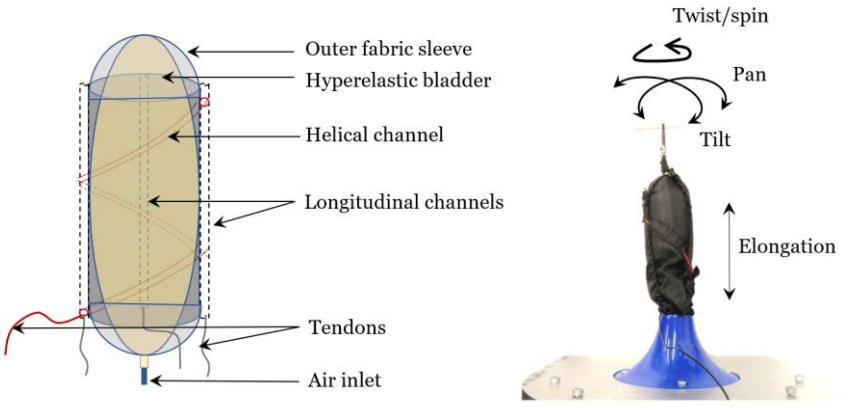

(a) Mechanical design (b) Degrees of freedom of the manipulator

Figure 1 (a) Mechanical design of the manipulator (b) Degrees of freedom exhibited by the manipulator

Figure 2 (a) The manipulator in the reference state (b) Tendon on the left of the module is actuated and the tendon bends to the left. (c) The helical tendon is actuated in conjunction with the three longitudinal tendons and the actuator twists while contracting in length. The twisting can be noted by the change in orientation of the red tube held by the forceps.

four channels and are affixed to the fabric sleeve at the distal ends of the channels. The free ends of each of these tendons are independently controlled by stepper motors. A total of four degrees of freedom- elongation, pan, tilt, and twist (or spin) can be achieved by controlling the pneumatic pressure and the tendon lengths (Fig. 1b).

RESULTS

The actuation principle of the manipulator is as follows. The pneumatic bladder is initially deflated such that the manipulator length is at its minimum. When air is pumped into the extensible bladder, the latex chamber inflates extending the length of the manipulator. The expansion of the bladder is constrained in the radial direction by the fabric sleeve forming a backbone for the manipulator (Fig. 2a). When a longitudinal tendon is actuated, the manipulator bends towards the tendon (Fig. 2b). When the tendon passing through the helical channel is actuated in conjunction with the three longitudinal tendons, the manipulator twists in the counterclockwise direction (as shown in Fig. 2c). One may note that the face of the red tube held by the forceps is distinctly visible in Figs. 2a and 2b. However, in Fig. 2c, the manipulator twists around the central axis so that only a smaller projection of the tube is visible.

CONCLUSIONS AND DISCUSSIONS

In this paper, we demonstrate a preliminary prototype for 4-dof extendable soft manipulator module. It can be compressed to fully deflate and can exhibit twisting motion besides extension, and bending along two planes. The proposed system offers several advantages: 1) the actuation strain is large as the manipulator can be fully deflated 2) additional degrees of freedom are achieved at no extra space cost, and 3) the redundancy in the system can be exploited to achieve stiffness controllability.

It is interesting to note that the bending and twisting motions of the manipulator are coupled together. The kinematics of the system needs to be established to achieve the control of this type of manipulator. In our future work, we shall investigate fabrication of miniaturised manipulators that can pass through small trocar ports and characterise the workspace, force and torque capabilities of the manipulator. We hope that this work can serve towards improving the dextrousness and functionalities of soft manipulators to further their applications in robot-assisted surgery.

REFERENCES

[1] R. F. Shepherd, F. Ilievski, W. Choi, S. A. Morin, A. A. Stokes, A. D. Mazzeo, X. Chen, M. Wang, and G. M. Whitesides, "Multigait soft robot," *Proc. Natl. Acad. Sci.*, vol. 108, no. 51, pp. 20400–20403, Nov. 2011.

[2] M. Cianchetti and A. Menciassi, "Soft robots in surgery," in *Soft Robotics: Trends, Applications and Challenges*, Springer, 2017, pp. 75–85.

[3] M. Cianchetti, T. Ranzani, G. Gerboni, T. Nanayakkara, K. Althoefer, P. Dasgupta, and A. Menciassi, "Soft robotics technologies to address shortcomings in today's minimally invasive surgery: the STIFF-FLOP approach," *Soft Robot.*, vol. 1, no. 2, pp. 122–131, 2014.

[4] G. Dogangil, B. L. Davies, and F. Rodriguez y Baena, "A review of medical robotics for minimally invasive soft tissue surgery," *Proc. Inst. Mech. Eng. Part H J. Eng. Med.*, vol. 224, no. 5, pp. 653–679, 2010.

[5] J. Fraś, J. Czarnowski, M. Maciaś, J. Główka, M. Cianchetti, and A. Menciassi, "New STIFF-FLOP module construction idea for improved actuation and sensing," in *Robotics and Automation (ICRA), 2015 IEEE International Conference on*, 2015, pp. 2901–2906.

[6] C.-H. Kuo and J. S. Dai, "Robotics for minimally invasive surgery: a historical review from the perspective of kinematics," in *International symposium on history of machines and mechanisms*, 2009, pp. 337–354.

[7] F. Maghooa, A. Stilli, Y. Noh, K. Althoefer, and H. A. Wurdemann, "Tendon and pressure actuation for a bio-inspired manipulator based on an antagonistic principle," in *Robotics and Automation (ICRA), 2015 IEEE International Conference on*, 2015, pp. 2556–2561.

[8] A. Shiva, A. Stilli, Y. Noh, A. Faragasso, I. De Falco, G. Gerboni, M. Cianchetti, A. Menciassi, K. Althoefer, and H. A. Wurdemann, "Tendon-based stiffening for a pneumatically actuated soft manipulator," *IEEE Robot. Autom. Lett.*, vol. 1, no. 2, pp. 632–637, 2016.

Vision-based Virtual Fixtures Generation for MIRS Dissection Tasks

R. Moccia[1], M. Selvaggio[1], B. Siciliano[1], A. Arezzo[2], and F. Ficuciello[1]

[1]*Department of Electrical Engineering and Information Technology, Università degli Studi di Napoli Federico II*

[2]*Department of Surgical Sciences, University of Torino*

rocco.moccia@unina.it

INTRODUCTION

Nowadays, cancer and precancerous lesion are major health problems. Assistive polyp dissection is a possible solution to accomplish high quality intervention while lowering down the surgeon fatigue. It could be performed in three stages: (i) polyp detection from images; (ii) safe margins definition around the polyp; (iii) path planning for assisted cutting. Vision-based procedures extract region of interest directly from the images, exploiting texture and color information as region descriptors. Modern developments in deep learning, e.g. the use of convolutional neural networks (CNNs) have made major advances in this field [1]. This paper proposes a vision-based pipeline for assistive polyp dissection. Our approach starts from stereo endoscopic images processing, including detection and segmentation of the region of interest, and leads to the definition of accurate points needed in path planning for assistive/autonomous cutting. In this work, we use the generated path as Virtual Fixture (VF), i.e. a constraint that restrict the motion of the robot manipulator along the path through haptic guidance forces rendered to the user. The goal of the work is to propose a functioning pipeline for assistive polyp dissection, exploiting basic computer vision concepts and impedance control to enforce the VF constraint. The work is a natural continuation of [2] towards a fully autonomous surgical interventions exploiting vision-based methods.

MATERIALS AND METHODS

As shown in Figure 1, our system is composed by the da Vinci Research Kit and an experimental setup replicating a surgical scene containing a polyp (blue object). We define an inertial word reference frame $(O-x_w y_w z_w)$, performing Zhang's stereo calibration [3] and identifying the transformation between $(O-x_w y_w z_w)$ the camera reference frame $(O - x_c y_c z_c)$. Then, acquiring images with the tool in different positions, we identify the transformation between $(O-x_w y_w z_w)$ and PSM (Patient Side Manipulator) frame $(O-x_t y_t z_t)$ by using the absolute orientation formulation, which allows defining 3D object points and robot tool positions in the same coordinate system [4].

A. Vision algorithm

Figure 2 represents an overview of our system, that takes endoscopic stereo images as input. A segmentation step is adopted restricting the acquired images to the object of interest. We apply a Watershed transformation on left gray-scale image, defining the polyp region, later used as seed point to apply the widespread *GrabCut* segmentation method [5], obtaining polyp's binary mask. We adopt a modifications of this algorithm, solving the minimization problem by a graph cuts minimization algorithm and defining the statistical models for the data energy function as a Gaussian Mixture Models based on color distribution. Simultaneously, Semi-Global Matching and Mutual Information (SGBM) is used for disparity computation from stereo images, with post-process enhancement via weighted least squares filter. The obtained disparity map is segmented using the previously computed polyp's binary mask. This allows calculating two different disparity map, one related to the object and other one to the background. Then, disparity information are reprojected in 3D space, producing object's point cloud and background point cloud. We identify the 3D centroid of the polyp in the space as a 3D vector. After that, the maximum distance from centroid is computed, allowing defining four extreme points of the object. A Sample Consensus method is selected to estimate a plane model from the background point cloud approximating the surface on which the robot's tool will perform the cutting path. This approximation is adopted due to the small curvature of the background.

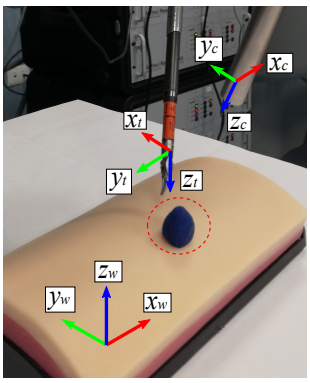

Fig. 1: Experimental setup, recreating patient's anatomy using phantom. The blue object represents a polyp.

B. Path Planning and Virtual Fixture

The object 3D points are projected on the surface model and their coordinates transformed to be defined in PSM reference frame $(O - x_t y_t z_t)$. Particularly, the object ex-

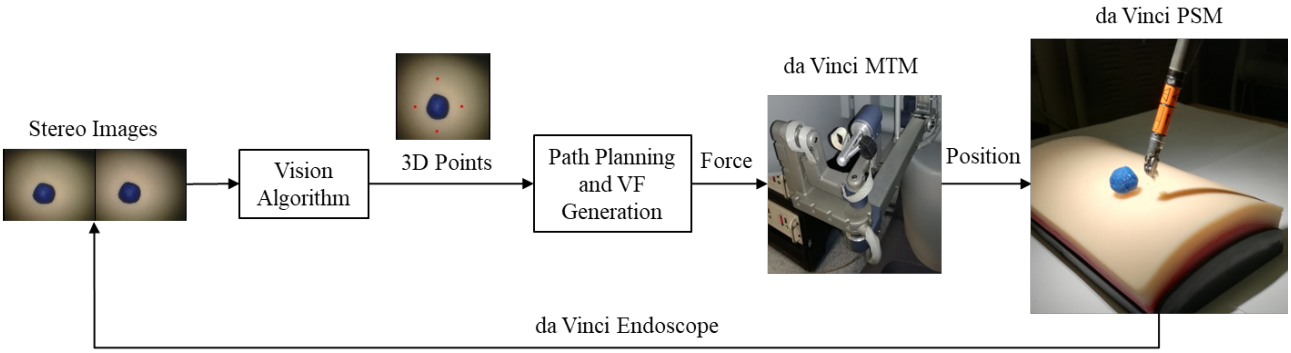

Fig. 2: Overview of the method.

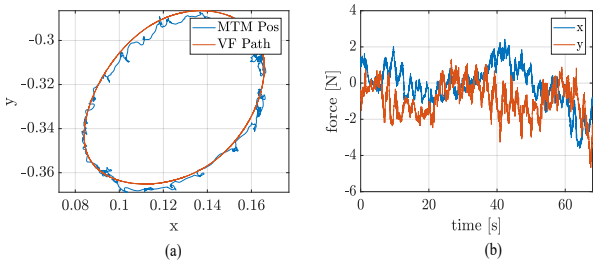

Fig. 3: (a) Virtual Fixture path (red line) and Master Tool Manipulator (MTM) position during the dissection task; (b) Estimated Haptic guidance forces displayed to the user through the MTM.

treme points coordinates are adjusted with a security margin, that allows performing the cutting in safe conditions avoiding collisions between the tool and the polyp. Once these 3D points are determined, they are used to build the VF geometry. Similarly to [2], we formulate the path for cutting through a parametric curve. In this work, we adopt a closed B-Spline curve defined by:

$$\Gamma(s) = \sum_{i=0}^{n} N_{i,k}(s)\, p_i \qquad (1)$$

where $\Gamma(s)$ denotes the curve, k its order, $s \in [0, 1]$ is the normalized curve parameter and $N_{i,k}$ are its basis function. The 3D points identified by our vision algorithm are used as controls points of the curve (p_i). Finally, a simple constraint enforcement method is adopted, i.e. a spring-damper like force is imposed onto the VF path that thus exhibits attractive behavior, i.e.: $f = K_p(x_d - x) - K_d\dot{x}$. To this end, Newton-Raphson method is used to find the nearest point on the curve x_d starting from the current robot TCP position. The attractive force f is displayed through impedance control of the Master Tool Manipulator (MTM) robot, realized thanks to the identification of the dVRK dynamic model [6].

RESULTS

The proposed vision-based assistive control is evaluated executing multiple dissection tasks. As previously explained, four polyp's extreme points are computed directly from the images, and their coordinates are adjusted by adding a secure margin of 1 cm. These points are used to define the B-Spline representing the dissection path. Graph in Figure 3 (a) contains a VF path and the MTM end-effector position in the xy plane of the MTM reference frame. As it is possible to notice, the user follows the determined path during the procedure thus improving its precision and accuracy. Figure 3 (b) shows the estimated haptic guidance forces to the user through the master side (MTM) during the tasks.

CONCLUSIONS AND DISCUSSION

In this paper, a vision-based assistive dissection procedure is presented, which finds application in polyp resection. The overall technique uses online generated VFs to constraint the robot to follow an optimal dissection path, created via specific points obtained directly from images of the surgical scene. The presented method aims at the full automation of polyp/tumor dissection. The obtained results suggest the feasibility of the proposed pipeline for polyp dissection. As future works, more advanced computer vision techniques will be considered, overcoming the inaccuracies in 3D reprojection, which could occur in more realistic surgical conditions. Also, an accurate study on medical procedures for polyp dissection will be considered for a correct definition of safe security margins for cutting.

REFERENCES

[1] J. Bernal and D. Stoyanov et al, "Comparative validation of polyp detection methods in video colonoscopy: Results from the miccai 2015 endoscopic vision challenge," *IEEE Transactions On Medical Imaging*, vol. 36, no. 6, 2017, pp.1231 - 1249.

[2] M. Selvaggio, A. G. Fontanelli, F. Ficuciello, L. Villani, and B. Siciliano, "Passive virtual fixtures adaptation in minimally invasive robotic surgery," *IEEE Robotics and Automation Letters*, vol. 3, no.4, 2018, pp.3129 - 3136.

[3] Z. Zhang, "Flexible camera calibration by viewing a plane from unknown orientations," *Computer Vision, 1999. The Proceedings of the Seventh IEEE International Conference*, vol. 1, 1999, pp.666-673.

[4] L. Zhang, M. Ye, C. Chan, and G. Z. Yang, "Real-time surgical tool tracking and pose estimation using a hybrid cylindrical marker," *International Journal of Computer Assisted Radiology and Surgery*, vol. 6, 2017, pp.921-930.

[5] C. Rother, V. Kolmogorov, and A. Blake, "Grubcut: Interactive foregroud extraction using graph cuts," *ACM Transactions on Graphics (TOG)*, vol. 23, 2004, pp.309-314.

[6] G. A. Fontanelli, F. Ficuciello, L. Villani, and B. Siciliano, "Modelling and identification of the da vinci research kit robotic arms," *IEEE/RSJ International Conference on Intelligent Robots and Systems (IROS)*, 2017, pp.1464–1469.

Shared Control of an Automatically Aligning Endoscopic Instrument Based on Convolutional Neural Networks

A. Ahmad[1], C. Gruijthuijsen[1], M. Ourak[1], J. Deprest[2], T. Vercauteren[3], S. Ourselin[3], E. Vander Poorten[1]

[1]*KU Leuven University, Department of Mechanical Engineering, Leuven, Belgium*

[2]*University Hospital Leuven, Department of Development and Regeneration, Leuven, Belgium*

[3]*King's College London, Imaging and Biomedical Engineering, London, United Kingdom*
mirzaawais.ahmad@kuleuven.be

INTRODUCTION

Endoscopic surgery is a video-based procedure that is less invasive, less strenuous for patients, and is a great alternative to open surgery in many situations. With the evolution of endoscopic surgery, flexible endoscopy has also seen a growth in popularity over the past two decades. Flexible endoscopy was introduced purely as a diagnostic tool, yet with the advance in surgical tools and therapeutic technologies, it has evolved to even replace some surgical procedures. [1].

Although frequently used in narrow intra- or transluminal applications e.g. in colon, esophagus or gastric tubes, this research discusses the application of flexible endoscopes in in-utero fetal surgery which offers a relatively open workspace. As compared to a marrow path, such an open workspace offers less visual ques for the surgeon to re-orient the scope. This introduces unique challenges for the control of a flexible endoscope. To improve the usability in this work, a shared control approach is proposed where the control is shared between a human and a robot.

This abstract deals with the use of the endoscopic instruments in photocoagulation therapy using lasers for Twin-to-twin Transfusion Syndrome (TTTS). In the current approach, rigid instruments are inserted into the uterine cavity. Which has a few shortcomings including: inability for orthogonal orientation of the endoscope and laser in case of anterior placenta resulting in suboptimal ablation; the need to change scopes over different interventional stages; image instability in the absence of motion compensation when carried out at close proximity to prevent inadvertent ablation or tissue contact and feto-placental hemorrhage [2].

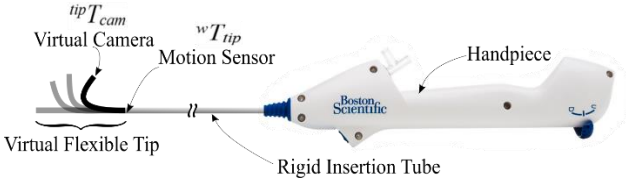

Figure 1: A semi-rigid scope with virtual flexible tip.

In order to overcome all these challenges, a semi-rigid scope is proposed as shown in Fig. 1. This scope has a long rigid insertion tube that is inserted through a trocar into the uterine cavity. The rigid part of the scope gives more control to the surgeon inside the uterus as they are trained to use rigid scopes. The flexible tip at the end can be bent in only one direction. This gives the surgeon more freedom to access hard to reach areas in the uterus, but remains still somehow tractable for the surgeon as there are not that many possible configurations.

Within this abstract we propose a shared control approach to further improve the usability. Namely the proposed approach allows the surgeon to take care of the gross motion whereby the bending of the flexible tip and the rotation of the instrument about the axis of insertion tube are actuated automatically. These two degrees of motion are shown in Fig. 2. This research presents the development of sensing and control techniques for the actuated flexible distal tip. The sensing is to detect the orientation of the camera with respect to the scene, in this case, a placenta. The controller is then to re-orient the camera such that it is directed normal to the placenta. It is expected that such shared control operation reduces the mental load of the clinician who only has to focus on navigation. The developed method is validated and compared to a traditional manual operation in a virtual reality environment where the flexible tip is simulated.

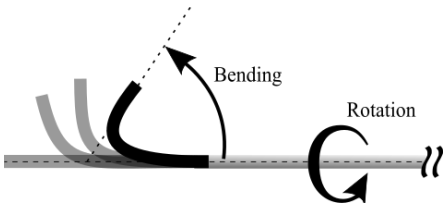

Figure 2: The insertion tube with two degrees of freedom i.e. bending and rotation.

MATERIALS AND METHODS

The endoscope shown in Fig. 1. consists of 3 main parts. The handpiece contains a lever that controls the bending of the flexible distal tip for manual operation. The rigid insertion tube is a metal tube with an electromagnetic sensor inserted at the tip. The position and orientation of

the sensor, ${}^{w}T_{tip}$, is used in the virtual reality simulator to know where the distal tip of the rigid portion of the instrument is in the world reference frame. The position of the virtual camera at the flexible tip, ${}^{tip}T_{cam}$, is known based on the kinematics of the flexible instrument. The control actions are generated by the control algorithm in the automatic operation mode or by the lever and the shaft orientation in manual mode.

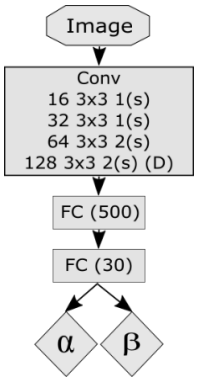

Figure 3: Design of the CNN. 4 convolutional layers and 3 fully connected layers. The number preceding (s) is stride and (D) represents dropout. NxN is the size off the kernel and the number preceding it is the number of filters.

As the pose of the placenta with respect to the world frame is not known we need to directly estimate the value of ${}^{p}R_{cam}$, as shown in Fig. 4. A Convolutional Neural Networks (CNN) [3] has been developed to estimate the orientation of the camera with respect to the placenta. To avoid needing to introduce additional sensors, the developed network is trained to predict the orientation, after training, based on a single 2D endoscopic image. The proposed network is shown in Fig. 3. In Virtual Reality such data-set can be tailored such that it is well-distributed and can be created in huge numbers with no human cost.

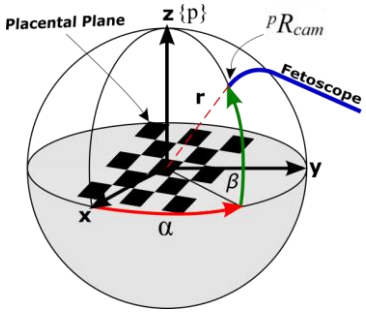

Figure 4: Orientation information of the image plane with respect to the endoscope

The network is trained to output two out of the three Euler angles represented as α and β as shown in Fig. 4. The rotation about the axis of the camera is redundant and these two angles are enough to generate the ${}^{p}R_{cam}$ which is the rotation matrix of camera with respect to the placenta. This matrix is used by the controller to generate new bending and rotation corrections according to the following equation.

$$ {}^{tip}R_{p} = {}^{tip}R_{cam} \times {}^{cam}R_{p} \qquad (1) $$

The matrix ${}^{tip}R_{cam}$ is the rotation of the camera with respect to the motion sensor on the tip and is known by the previous control action. The rotation matrix ${}^{tip}R_{p}$ is then used to calculate bending and rotation corrections based on the kinematics of the instrument.

RESULTS

Two different placenta images were used to generate a dataset at different orientations and distance of the camera. The network was trained over 5000 randomly selected images out of this dataset. The results in Fig. 5. represent the output of testing with the dataset. It can be seen that the network was able to predict the value of both angles within the acceptable error of 5 degrees.

For validation of the CNN and the controller in real time, a task has been designed in the virtual reality simulator. Users were asked to coagulate a series of letters printed on the image of placenta. The feasibility of the approach was validated as estimates were offered in real time and used by the controller. As the user moved the shared control kept the orientation perpendicular to the surface.

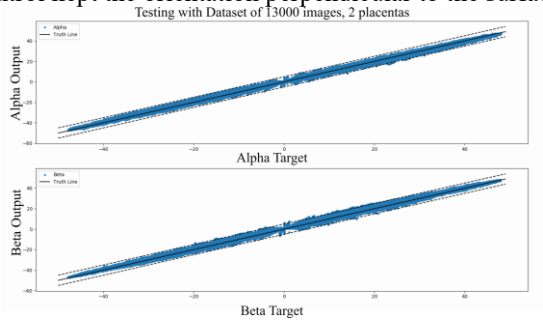

Figure 5: Output of testing the trained CNN over the dataset of 13400 images. Images used for training and testing at 200x200 pixels.

CONCLUSION AND DISCUSSION

The CNN performed well even when the scope was moved with freehand. As the network was trained with images generated within a range of distance of the camera from the images, the CNN did not perform well when the scope was moved too far from the placenta.

For future work, the network needs to be trained over a larger range of data that may be encountered in a real surgical application as opposed to controlled data set that was used here.

REFERENCES

1. Chand, Bipan, Joshua Felsher, and Jeffrey Ponsky. "Future trends in flexible endoscopy." *Seminars in laparoscopic surgery.* Vol. 10. No. 1. Sage CA: Thousand Oaks, CA: Sage Publications, 2003.

2. Huber, A., et al. "Laser coagulation of placental anastomoses with a 30° fetoscope in severe mid-trimester twin–twin transfusion syndrome with anterior placenta." *Ultrasound in Obstetrics and Gynecology: The Official Journal of the International Society of Ultrasound in Obstetrics and Gynecology* 31.4 (2008): 412-416.

3. LeCun, Yann, Yoshua Bengio, and Geoffrey Hinton. "Deep learning." nature 521.7553 (2015): 436.

Comparing Users Performances in a Virtual Reality Surgical Task under different Camera Control Modalities: a Pilot Study Towards the Introduction of an Autonomous Camera

Andrea Mariani[1, 2], Giorgia Colaci[1], Nicole Sanna[1], Eleonora Vendrame[1], Arianna Menciassi[2], Elena De Momi[1]

[1] *Department of Electronics, Information and Bioengineering, Politecnico di Milano, Milan, Italy*

[2] *BioRobotics Institute, Scuola Superiore Sant'Anna, Pisa, Italy*

andrea.mariani@santannapisa.it

INTRODUCTION

Robot-Assisted Surgery (RAS) enhances the depth perception of the surgical field and, as a consequence, the surgeon's dexterity, especially in minimally invasive surgery. This improved vision has been shown to better surgeon's performance by restoring proper hand-eye coordination, allowing an immersive view of the operational scene and providing an intuitive correspondence with manipulators [1]. In current robotic surgery, the operator directly controls both the tools and the camera with the same handles (Fig.1.a). This can lead to increasing errors, as well as to longer operating times [2]. An autonomous camera navigation modality (Fig.1.b), which performs a smart and automatic positioning of the camera, has been proposed to overcome these limitations [3-4]. The aim of this work is to compare the performances of novice and expert users in a Virtual Reality (VR) task under two conditions: manual and autonomous control of the camera. In this way, the advantage of autonomous methods to control the camera can be discussed, as well as its influence on subjects with heterogeneous levels of expertise.

MATERIAL AND METHODS

Hardware and Software

In order to carry out the experimental session, we employed the master console of a da Vinci Research Kit (dVRK, by Intuitive Surgical Inc., Sunnyvale, US). This console includes a foot-pedal tray, a stereo viewer and two master manipulators.

The VR exercises were designed using our Assisted Teleoperation with Augmented Reality (ATAR) framework [5].

Virtual Reality Task and Performance Assessment

We created a virtual reality task (Fig.2) that involves fundamental skills of robotic surgery (hand-eye coordination, depth perception, object manipulation and wrist articulation). The user grabs a needle and performs an instrument to instrument exchange through randomly oriented rings, simulating a rigid suturing. While conducting the transfer, he/she has to keep the needle orthogonal with respect to the ring's plane and passing through the ring's center. In order to assess the user's performances, we considered three metrics: the *translation error* (i.e. the average distance between the needle point crossing the ring section and the centre of the ring), the *orientation error* (i.e. the average angle between the needle and the vector orthogonal to the ring plane) and the *total time* to accomplish the task.

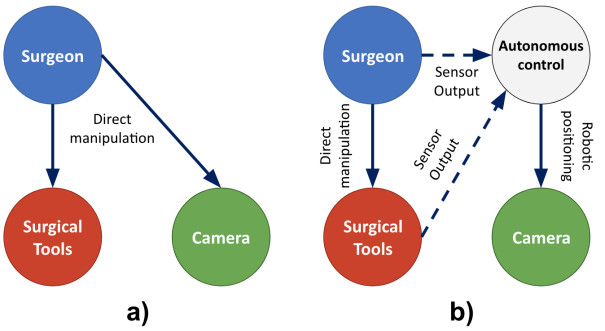

Figure 1. a) Current Manual Camera Control; b) Autonomous Camera Control (from [2]).

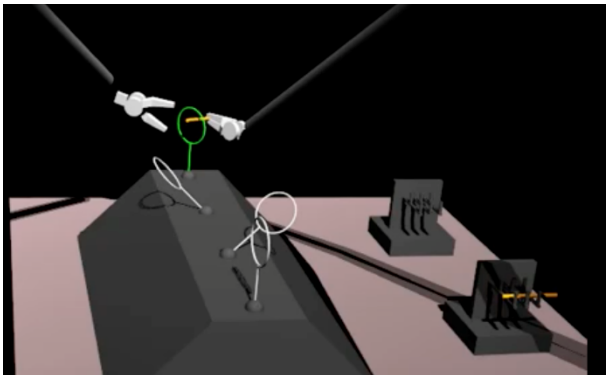

Figure 2. VR 'Rigid Suturing' Task.

Camera Control

We integrated in this task two modalities of camera control: the *manual* and the *autonomous* one. In the former mode, the operator can move the camera by himself, using the master manipulator and the foot-pedals of the console. While keeping the camera pedal pressed, the user controls the camera position in the VR environment by moving the right manipulator and the camera orientation using the left one. Moreover, the user can zoom in and out by exploiting the plus and minus pedals. In the *autonomous* mode, the movement of the camera is solely the result of the following control algorithm. Similarly to [4], the midpoint of the centres of mass of the two tools is set as the focal point of the camera. Additionally, while interacting with a target object, the camera zooms in till reaching a minimum threshold from the object.

Experimental Protocol

The user study involved 10 non-medical volunteers. Half of them were novice to teleoperation, while the remaining ones had more than 50 hours of previous practical experience with robotic devices. The research outline was explained prior to enrollment and all the participants gave informed consent. Initially, the subjects were introduced to the dVRK console and they were shown videos of a successful execution of the task. Then, each user was asked to perform the VR exercise 10 times: during 5 repetitions they were provided with the possibility to control the camera, while in the remaining trials they experienced the autonomous camera control. To prevent training effects, the order in which they underwent the 2 modalities was randomized. Finally, each participant was asked to fill in a NASA-TLX [6] survey to evaluate their experience.

Statistical Analysis

Due to the small sample size, non-parametric statistical significance tests were used to compare the performances of the users under the two different modalities. The Wilcoxon rank sum test was employed using MATLAB and statistically significant effects were assessed at $p < 0.05$.

RESULTS

The main outcomes of the study are shown in Fig.3. In case of expert users, the autonomous camera allowed to obtain statistically significantly lower translation and orientation errors with respect to the manual mode; considering the novice subjects, the orientation error and the task execution time were significantly lower. The variability of the accuracy metrics was reduced by the autonomous control of the camera both in expert and novice users. Comparing the two classes of subjects, the novice users were characterized by higher variability across all the metrics. It is possible to notice that while in the manual control modality, the experts achieved higher performances with respect to the novices, the autonomous control attenuated this difference. The results of the NASA-TLX test showed that the global score (corresponding to the workload) was significantly higher for the task performed in the manual mode with respect to the autonomous one.

CONCLUSION AND DISCUSSION

This pilot study highlights the promising introduction of an autonomous camera control in complex visuo-motor tasks. This camera control modality allowed to improve the time-accuracy performances of both novice and expert users while conducting a VR task involving fundamental skills of robotic surgery. This was assessed to be correlated with the cognitive load, which the autonomous camera allowed to decrease according to the users' feedbacks. A bigger sample size can lead to better statistical determinism; at the same time, we are going to improve the analysis of the influence of the level of expertise by imposing stricter selection criteria and initial skill assessment. In particular, autonomous camera control can potentially help novice users in the initial training stage by decreasing the cognitive load. In other words, the trainee can focus on specific

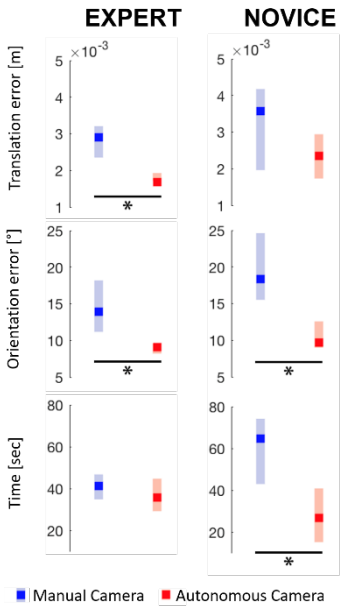

Figure 3. Average metrics across the five repetitions of expert and novice users under the two camera control modalities. The marked squares represent the medians across the population, the vertical bars stand for the variances (25th and 75th percentiles), the stars refer to statistical significant difference.

fundamental skills of robotic surgery and avoid to overlap the camera control with the instrument handling at the beginning of his/her learning curve. Further future developments can involve modifications towards the translation from a VR setup to the real environment: these could include the introduction of sensors, like an eye gaze tracker to detect targets and consequently modifying the focal point, and force sensors on the robot tooltip to identify the interaction with that object.

ACKNOLEDGMENTS

Research partially supported by FUTURA2020 project (grant agreement 801451).

REFERENCES

[1] Freschi, Cinzia, et al. "Technical review of the da Vinci surgical telemanipulator." *The International Journal of Medical Robotics and Computer Assisted Surgery*, 2013.

[2] Pandya, Abhilash, et al. "A review of camera viewpoint automation in robotic and laparoscopic surgery." *Robotics*, 2014.

[3] Park, Jae-Hyeon, et al. "Endoscopic Camera Manipulation planning of a surgical robot using Rapidly-Exploring Random Tree algorithm." *2015 15th International Conference on Control, Automation and Systems (ICCAS)*. IEEE, 2015.

[4] Eslamian, Shahab, et al. "Towards the Implementation of an Autonomous Camera Algorithm on the da Vinci Platform." *Studies in health technology and informatics*, 2016.

[5] Enayati, Nima, et al. "A Framework for Assisted Tele-operation with Augmented Reality," in *CRAS: Joint Workshop on New Technologies for Computer/Robot Assisted Surgery*, 2017.

[6] Hart, Sandra G. "NASA-task load index (NASA-TLX); 20 years later." *Proceedings of the human factors and ergonomics society annual meeting*. Sage CA: Los Angeles, CA: Sage Publications, 2006.

Modeling and Design Of An Active Assistive Exoskeletal Robot For Upper Limb Rehabilitation

Vishal Ramadoss[1], Dimiter Zlatanov, Matteo Zoppi

[1]*PMAR Robotics, University of Genoa, Italy*
austinvishal@gmail.com

INTRODUCTION

Wearable robotics is a fast growing field with assistive exoskeletons being developed for medical and industrial purposes. These exoskeletons can be used for gait rehabilitation of patients, arm rehabilitation and provide body support during training. These exoskeletal systems are anthropomorphically structured mechanisms where the rigid links form a serial kinematic chain and the cables are attached in a parallel configuration.

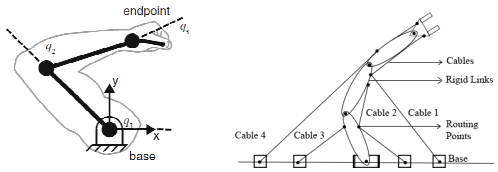

Figure. 1. A 3-link 3DOF planar cable driven serial kinematic chain.

Cable-driven system[1,2,3] eliminates the need of rigid links and mechanical joints, making the system lightweight. Due to the serial unilateral constraints, it has to be ensured that all cables remain in tension at any point of time for system functionality. This results in redundancy in the actuation system. The aim of this paper is to provide the kinematic analysis of these multilink cable-driven robots[4] (MCDRs) with fully routed cable bundles. MCDRs benefits from the actuation and reconfigurability of cable-driven manipulators and the dexterity of the serial chain. The workspace and tension analysis was performed for optimal design of cable driven exoskeletons[5]. From the information of workspace, we can check whether the cable driven exoskeleton is able to perform the desired behavior (gait motion) with positive cable tensions[6,7,8] and without violating defined constraints[9].

Exoskeletal devices are usually bulky. Even if the weight is well compensated, inertial compensation is difficult due to joint velocity and acceleration measurements. These devices require mechanical adjustments to match the link lengths to the arm segment lengths. Poorly aligned joint axes may cause large reaction forces and moments at the joints thereby causing skin sores and soft tissue damage. Therefore, precise joint axis alignment is essential for an exoskeleton to function properly for rehabilitation. The minimally routed multi-link cable driven exoskeletal devices differs from conventional designs as it does not have traditional links and joints thereby eliminating the joint axis alignments. Lightweight cuffs, cable routing rings with large range of adjustments, minimally routed cables from proximal to distal arm segments thereby providing high endpoint force and stiffness control. The cable tension planner is devised for minimum tension and maximum safety. The safety indices are ratios between actual force/moment and the minimum force/moment that would cause damage to a human at shoulder and elbow joints [10]. The smaller the safety index is, the safer it is for the human user. The safety indices are functions of cable tension.

MATERIALS AND METHODS

The purpose of a cable driven exoskeleton is to assist human motion. To check this, we need to evaluate the workspace of the cable driven system for that configuration. For cable driven serial kinematic chain, one of the key design element is the cable routing, which defines the structure matrix, of the multi-link unilateral manipulator. This structure matrix defines the torque and force produced by the serial chain based on the cable tensions. The number of cables[11,12] used in the design is crucial to the design of the structure matrix, and using minimal number of cables has the advantage of reducing the number of cables and actuators thereby reducing the weight, size and complexity of the serial chain.

In order to describe the motion of the upper limbs driven with cables, the coordinate frames F_o and F_k are attached to the origin and the link k. Cables are connected to the links with attachment points at B_i and A_i where $i = 1, \dots m$ cables. The cable vector is kinematically defined as:

$$\boldsymbol{l}_i = \boldsymbol{r}_{\boldsymbol{OG}i} + \boldsymbol{r}_{\boldsymbol{A}i} - \boldsymbol{r}_{\boldsymbol{B}i} \quad (1)$$

For the cable driven serial kinematic chain with routing through multiple links, the cable segment vectors are added since the routed cable consists of multiple cable segments passing through the attachment points. The length of the cable i with routed segment j can be expressed as:

$$\boldsymbol{l}_i = \sum_{j=0}^{jmax} |\boldsymbol{l}_{\mathrm{ij}}| \quad (2)$$

The cable structure matrix can be evaluated by using the differential relationship:

$$\dot{\boldsymbol{l}} = J\dot{\boldsymbol{q}} \quad (3)$$

where q is the joint configuration of the exoskeleton and J is the Jacobian of the cable driven system. In order to resist any external wrench applied on the system, the cables must create unilateral tension forces to achieve

equilibrium. Applying the principle of virtual work, the kinetostatic equilibrium is defined as:

$$\boldsymbol{J^T t = W} \quad (4)$$

where J^T is called the cable structure matrix, $\boldsymbol{t}$ is the column vector containing cable tensions and $\boldsymbol{W}$ is the sum of all external forces and moments including weight, inertial forces and moments. The wrench closure workspace is defined as the set of poses in which the cable driven manipulator can sustain any arbitrary external wrench. Mathematically, it is defined as:

$$WCW = (q: \boldsymbol{w = J(q)^T t}, \exists \boldsymbol{t} \geq 0) \quad (5)$$

Various methods have been proposed for the workspace analysis of cable driven systems. As human gait pattern differs among individuals, we analyze the boundaries of workspace. The null space of the structure matrix is used to define the workspace. For a given point to lie within the workspace, all values of the kernel of the cable structure matrix should be either positive or negative. If one of the two conditions are satisfied, irrespective of the particular solution, we can find a scalar λ which will guarantee positive tension in all cables.

RESULTS

To control a n DOFs system, at least $n + 1$ cables are needed due to the unilateral constraint property. Therefore, for the 3 link planar CDSKC at least four cables are required. In Fig.2 cables are attached to the links of planar exoskeleton without internal routing. The workspace is calculated analytically using Cramer's rule. To find WCW, the union of regions formed from the intersection of positive and negative null spaces are considered. Figure 3. shows the SR chain (3 dof's for shoulder 1 for elbow) with five cables routed to the base.

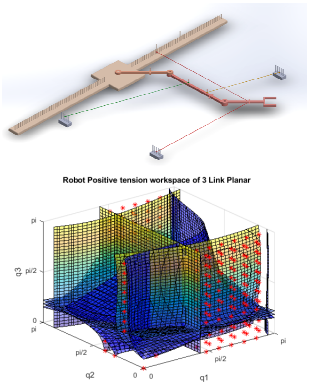

Figure.2. Simplified model of a 3-DOF planar exoskeleton and its workspace.

The WCW is identical for the single link 3-dof ball joint manipulator and two-link 4-dof manipulator, differing only in the dimension of the Jacobian matrix. For the purpose of visualization, the workspace of ball joint manipulator is shown in Figure 4.

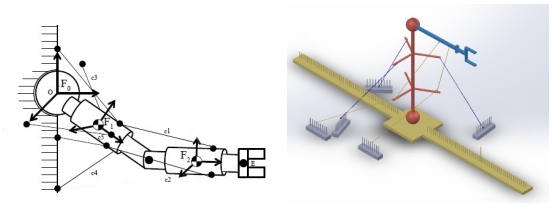

Figure.3. A 4-DOF 5-cables arm, modeling the shoulder and elbow motions.

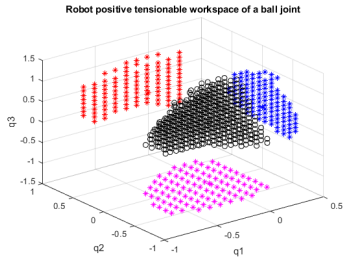

Figure.4. Workspace of cable-driven 3-DOF ball joint manipulator modeling the wrist motions.

An affordable solution for improving the workspace without adding actuators is by employing spring cables attached between the fixed ground and one of the links. Also, adding springs between links decreases the probability of interference of cables. Adding springs change the WFW by providing bounded cable wrenches through the springs. The wrenches of spring cables are treated as external wrench for analysis.

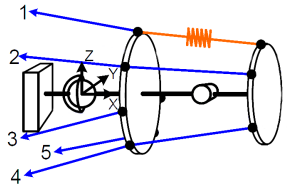

Figure.5. Spring-loaded multi link cable driven unilateral manipulators

CONCLUSION AND DISCUSSION

The work presents three cases of multi link cable driven robot architectures that can be modeled and designed for assistive technologies. The kinematics and workspace analysis of the exoskeleton models were presented. The design of SR chain was motivated by the natural arm and uses a multi link cable driven mechanism. Cable based parallel design requires additional actuation motors than the number of dofs, since cables can only transmit power in tension. This motivates in optimizing and maximizing the workspace. The ball joint manipulator was also studied to model the motions of the wrist.

REFERENCES

[1] J. Albus, R. Bostelman, and N. Dagalakis. The NIST robocrane. Journal of Robotics Systems, 10:709724, 1993.

[2] S. Bouchard and C.M. Gosselin. Workspace optimization of a very large cable-driven parallel mechanism for a radiotelescope application. In Proceedings of of the ASME IDETC, Las Vegas, Nevada, Las Vegas, Nevada, 2007.

[3] Fink J. Michael, N. and V. Kumar. Cooperative manipulation and transportation with aerial robots. In Proceedings of Robotics: Science and Systems, Seattle, Washington, USA, 2009.

[4] D. Lau, D. Oetomo, and S.K. Halgamuge. Generalized modeling of multilink cable-driven manipulators with arbitrary routing using the cable-routing matrix. IEEE Transactions on Robotics, 29:1102 1113, 2013.

[5] Y. Mao and S. K. Agrawal. Design of a cable driven arm exoskeleton (carex) for neural rehabilitation. IEEE Transactions on Robotics, 28(4):922931, 2012.

[6] S. K. Mustafa and Agrawal S. K. On the force-closure analysis of n-dof cable-driven open chains based on reciprocal screw theory. IEEE Transactions on Robotics, 28(1):2231, 2012.

[7] Lung-Wen Tsai. Design of tendon-driven manipulators. Journal of Mechanical Design, 117:8086, 1995.

[8] S. Rezazadeh and S. Behzadipour. Tensionability of an arbitrary two-link multibody. In Proceedings of of the ASME IDETC, number DETC2009- 87597, pages 7581, Las Vegas, Nevada, USA, 2009.

[9] K. Lakshminarayana. Mechanics of form closure. In Proceedings of of the ASME DETC, number ASME paper 78-DET-32, Minneapolis , MN, USA, September 1978.

[10] K. Ikuta, H. Ishii, and M. Nokata. Safety evaluation method of design and control for human-care robots. The International Journal of Robotics Research, 22:281-287, 2003.

[11] D. Zlatanov. Serial kinematic chains with unilateral external force constraints. In IFToMM World Congress in Mechanism and Machine Science, Guanajuato, Mexico, 2011.

[12] M. Zoppi, D. Zlatanov, and R Molfino. On the velocity analysis of interconnected chains mechanisms. Mechanism and Machine Theory, 41(11):13461358, 2006.

A Deep Reinforcement Learning Approach for Inverse Kinematics of Concentric Tube Robots

K. Iyengar, G. Dwyer, D. Stoyanov

Surgical Robot Vision Group, University College of London
keshav.iyengar.17@ucl.ac.uk

INTRODUCTION

Minimally invasive surgical procedures are performed with a small incision for surgical instruments to pass through to reach the stage of the procedure. Dexterous surgical instruments like concentric tube robots (CTR) are needed to steer along sensitive structures within the body and achieve minimal damage by employing a remote centre of motion (RCM) at the incision point. A CTR is a continuum robot composed of multiple telescopic, concentric, pre-curved, super-elastic tubes that can be axially translated and rotated at their base relative to each other [1]. The bending is derived from the elastic tube interactions with neighboring tubes, allowing for high dexterity while maintaining a small footprint. Along with the CTR, which is known as the distal configuration, there are outer degrees of freedom (DOF) that fix the CTR's base to a remote center of motion known as the proximal configuration. Kinematic modelling of such systems is non-trivial due to the complex interaction of individual tubes with neighboring tubes that form unique bending curves. Previously, traditional iterative approaches have been used to moderate success, but challenges include model complexity and a reliance on material constants. Previous work on introducing model-free solution include solutions with feed-forward neural networks [5]. Although these solutions are accurate, the cost of data sampling is high as all training, validation and testing is done on a physical CTR.

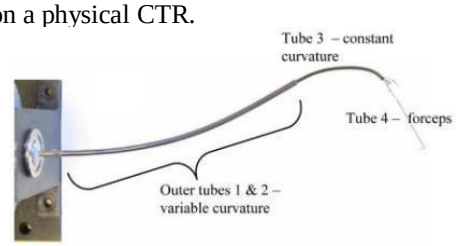

Figure. 1. Distal configuration of 3 tubes [1].

This paper presents a deep reinforcement learning approach to solving the inverse kinematics of CTRs. The approach known as deep deterministic policy gradient (DDPG) [2] has shown promising results in high dimensional, continuous control problems such as humanoid robot control [3] and RC car drifting [4]. DDPG is an off-policy, actor-critic based algorithm that uses experience replay. Fully-connected neural networks are used to model the actor and critic.

With this work, the authors investigate using DDPG for CTRs in simulation for 3 configurations, distal, proximal and full. The distal configuration consists of a rotational and prismatic DOF per tube and the proximal configuration has 3 rotational and 1 prismatic DOF to maintain a remote centre of motion.

MATERIALS AND METHODS

State, Action and Reward Definitions

The state formulation consists of the joint states, q, desired position, $X_{desired}$, and achieved position, $X_{achieved}$. The proximal configuration has three rotational DOFs, ψ, ϕ and θ about the *x*, *y* and *z* axis and a prismatic DOF, *r*, about the *z* axis. The distal configuration has a rotational DOF, γ_i, about the z-axis and prismatic DOF, l_i , about the z-axis for each tube *i* of a *n* tube CTR. The state *s* is defined in equations 1, 2, 3.

(1) $s = [q \quad X_{achieved} \quad X_{desired}]$

(2) $q_{distal} = [\gamma_1 \quad l_1 \quad \dots \quad \gamma_n \quad l_n]$

(3) $q_{proximal} = [\psi \quad \phi \quad \theta \quad r]$

(4) $q_{distal} = [\psi \quad \phi \quad \theta \quad r \quad \gamma_1 \quad l_1 \quad \dots \quad \gamma_n \quad l_n]$

The action is defined as the change in joint state, q in equation 4.

(5) $a = \Delta q$

A novel reward function was formulated specific to CTRs. α and β are normalization constants for equal weighting of the norm-distance error term and change in joint states term. α is the multiplicative inverse of the longest normal distance between two points in the achievable workspace. In most cases, the minimum and maximum joint state values provide the two points with the largest normal distance. β is the multiplicative inverse of the number of active joints depending on the configuration.

(6) $$r = -\alpha|X_{achieved} - X_{desired} - \beta\sqrt{\sum_i^n \left(\frac{\Delta q_i}{q_{i,max} - q_{i,min}}\right)^2}$$

Agent Model

The exploration strategy chosen was zero-mean Gaussian noise where the variance of the noise decreases with each time step *t*, proportional to a decay period, given the starting variance $\sigma_{max,}$ and final variance σ_{min}.

(7) $$\sigma_t = \sigma_{max} - (\sigma_{max} - \sigma_{min}) \times \min\left(1, \frac{t}{T}\right)$$

The fully-connected neural network architectures of the actor and critic (including target networks) have 2 hidden layers. The number of neurons at each hidden layer differs based on the configuration of the CTR as show in table 1.

Configuration	Hidden Layer 1	Hidden Layer 2
Distal	50	10
Proximal	100	50
Full	200	100

Table. 1. Hidden Layer Configurations.

Environment Model

The forward kinematics model utilized the dominating stiffness model [1] for CTRs which assumes that the bending stiffness of one tube is much larger than the neighboring tube, resulting in the neighboring tube conforming to the curvature of the stiffer tube. This model was used to generate achievable 3D goal positions for the end effector and track the current position of the end effector in simulation. Given k is the curvature of all tubes and l_{tip} is the length of the tip of the end effector the transformations from the remote center of motion to the end effector (l_{tip}) were formulated.

(8) $$T_{shaft}^{RCM}(\omega, \phi, \theta, r) = T_{RotX}(\psi)T_{RotY}(\phi)T_{RotZ}(\theta)T_{TransZ}(r)$$

(9) $$\mathrm{T_n^{shaft}}(\gamma_1 \quad l_1 \quad \dots \quad \gamma_n \quad l_n) = \prod_{i=1}^{n} \mathrm{T_{RotZ}}(\gamma_i)\mathrm{T_{TransX}}\left(\frac{1-\cos(\mathrm{kl_i})}{\mathrm{k}}\right)\mathrm{T_{TransZ}}\left(\frac{1-\sin(\mathrm{kl_i})}{\mathrm{k}}\right)\mathrm{T_{RotY}}(\mathrm{kl_i})$$

(10) $$\mathrm{T_{l_{tip}}^{RCM}} = \mathrm{T_{shaft}^{RCM}}(\omega, \phi, \theta, r)\mathrm{T_n^{shaft}}(\gamma_1 \quad l_1 \quad \dots \quad \gamma_n \quad l_n)$$

RESULTS

For the distal configuration with n = 1, after every 200 episodes, a 100 episode rollout was performed. The rollout gave an accuracy measure based on the number times the desired goal was reached. For the other configurations, the desired goal was never within the tolerance, so this measure was not possible. After 3000 episodes, the distal configuration rollout gave an average accuracy of 18.3%, a minimum accuracy of 13.0% and a maximum accuracy 23.3% done over 3 seeds with the error plot shown in figure 2.

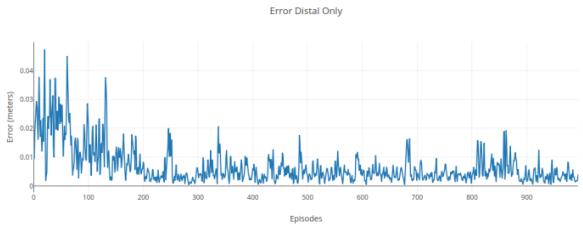

Figure. 2. Error for distal configuration.

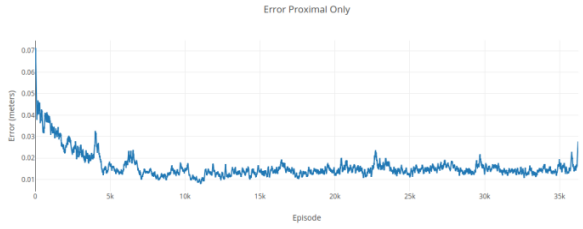

Figure. 3. Error for proximal configuration.

For the proximal configuration n = 1, after 10000 episodes, the goal tolerance was not achieved. Over 3 seeds, the average error was 0.004 meters, minimum error was 0.001 meters and maximum error was 0.005 meters. For the full configuration n = 1, after 10000 episodes, the goal tolerance was not achieved. Over 3 seeds, the average error was 0.010 meters, minimum error was 0.005 meters and maximum error was 0.013 meters.

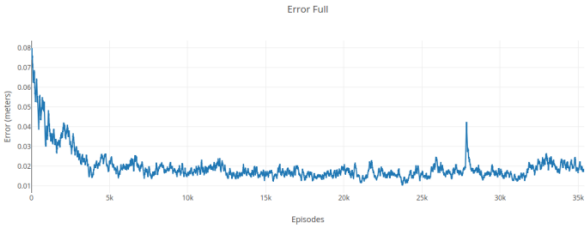

Figure. 4. Error for full configuration.

CONCLUSION AND DISCUSSION

Figure 2, 3 and 4 all demonstrate learning and optimization is occurring which is promising for future work in continuum robot control applications. Note however, the results are no where accurate to either te iterative Jacobian methods or the feed-forward neural network approach [5]. Because of the low accuracy, a physical robot was not used for experimentation. Three main domains of interest to improve the accuracy of DDPG are the exploration strategy, reward function formulation and transfer learning. First, without fully exploring the solution space, DDPG cannot find a good policy, better exploration strategies such as parameter noise exploration can be investigated. Second, the reward function can be improved upon by better representing the requirements of the solution mathematically. Last, DDPG must learn with no prior knowledge of the model resulting in long convergence. Contextualizing the learning by incrementally advancing the complexity using transfer learning could help convergence times as shown in autonomous RC car drifting [4]. In the future, a more complex model should be used along with this simple model and a physical CTR to perform deep learning with forward and reverse transfer learning. Although no expermintation was done, the results are a first step to introduce a data efficent deep learning approach for CTRs.

REFERENCES

[1] P. Sears and P. Dupont, “A Steerable Needle Technology Using Curved Concentric Tubes,” in 2006 IEEE/RSJ International Conference on Intelligent Robots and Systems, 2006.

[2] D. Silver et al, “Mastering the game of go with deep neural networks and tree search,” Nature, vol. 529, pp. 484–489, January 2016.

[3] S. Phaniteja, Dewangan, et al, “A deep reinforcement learning approach for dynamically stable inverse kinematics of humanoid robots,” 2018.

[4] M. Cutler and J. P. How, “Autonomous drifting using simulation-aided reinforcement learning,” in 2016 IEEE International Conference on Robotics and Automation (ICRA), IEEE, May 2016.

[5] Grassmann, Reinhard et al. (2018). Learning the Forward and Inverse Kinematics of a 6-DOF Concentric Tube Continuum Robot in SE(3). 5125-5132. 10.1109/IROS.2018.8594451.

Development of a 3-DOF impedance-type manipulator for cooperative surgical port alignment during microsurgery.

Jonas Smits[1], Andy Gijbels[1], Dominiek Reynaerts[1,2], Emmanuel Vander Poorten[1]

[1]Dept. of Mechanical Engineering, KU Leuven, [2]Member Flanders Make, Belgium
Jonas.smits@kuleuven.be

INTRODUCTION

Vitreoretinal surgery is a branch of microsurgery involving delicate interactions with the inner- and posterior-segments of the eye. Surgical procedures are highly challenging, and limited by human factors such as hand tremor and depth/force perception. Surgical robotic technology can offer increased precision and situational awareness through robotic assistance and smart instrumentation. First applications of robotic eye surgery have been successfully demonstrated during first-in-human clinical studies on retinal vein cannulation [1] and epiretinal membrane peeling [2].

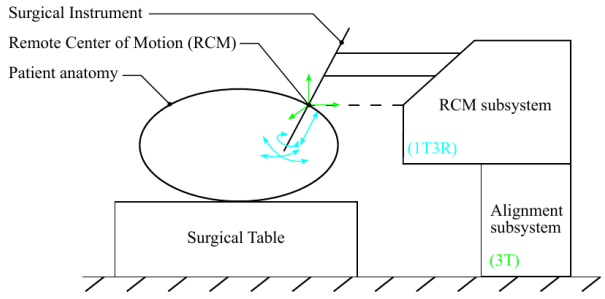

Fig. 1. Annotated illustration of a generalized MIS surgical scene using a 3R1T+3T surgical robotic system architecture.

The architecture of surgical robotic systems can often be described as a combination of two subsystems (Fig. 1). Firstly, a "Remote Center of Motion (RCM) subsystem" provides 1 translational and 3 rotational DOF's of the surgical instrument through and about a defined RCM. Secondly, an "Alignment subsystem" provides three translational DOF's to move the RCM subsystem with respect to the patient, thus enabling alignment of the RCM with the surgical port. The Leuven eye-surgical robotic system is an example of such an architecture. It's current alignment subsystem is a combination of three spindle-driven linear actuators in a Cartesian configuration. Due to low backdrivability, cooperative control options rely on an admittance control scheme, in which the RCM DOF's are locked and used to measure user forces. While this is sufficient for high-accuracy experimental procedures - such as retinal vein cannulations [1] and subretinal injections [3] - which often do not require RCM-repositioning, users indicate that having the ability to cooperatively reposition the RCM during surgery without losing instrument DOF's would be valuable in procedures where the eye is intentionally rotated. This abstract reports on the development of a novel 3-DOF impedance-type alignment subsystem towards enabling more intuitive and versatile intraoperative RCM positioning. First, the developed prototype and it's key performance specifications are briefly discussed. Secondly, an initial experimental validation of the developed alignment subsystem is reported, in which surgical port alignment accuracy is reviewed. Finally, the outcomes are discussed.

NOVEL ALIGNMENT SUBSYSTEM PROTOTYPE

The developed prototype consists of three linear translation stages assembled in a Cartesian configuration. Each stage is actuated with a brushed DC-motor-encoder combination paired with an EM-brake. The actuators are mounted via a custom assembly, featuring a capstan cable transmission. Positional resolution and force output for each DOF are 1,7 µm and 17 N respectively. Low level and high level control are implemented using Epos motor drivers + FPGA and a cRIO RT embedded controller at 10 kHz and 1kHz respectively. The RCM subsystem mass is temporarily simulated by a static load of aprox. 6 kg, using commercial barbell weights. The Z-axis is equipped with a spring-based passive gravity compensation. The residual gravitational force is identified and actively compensated with a 3rd order polynomial fit. For the purpose of this paper, a simple impedance control law is implemented with a heuristically chosen gain of 0.08 Ns/mm.

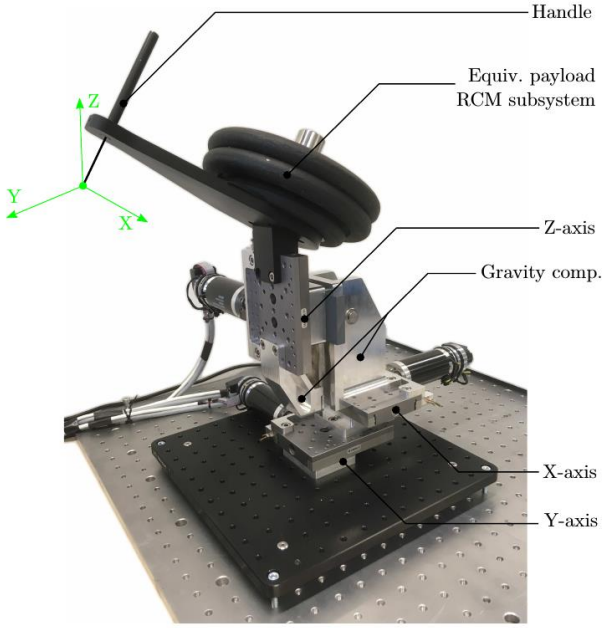

Fig. 2. Annotated overview of the novel alignment subsystem prototype.

EXPERIMENTAL VALIDATION

As a first experimental validation, relative point accuracy of surgical port alignment is reviewed. This is defined as the user's ability to position an instrument tip - visually representing the RCM - with an already present visual reference, being the surgical port. The aim is to compare cooperative alignment using the novel system with manual alignment, as well as with the prior admittance type system. The experiment is conducted as follows. The user is asked to indicate their visual target as desired with the instrument tip, using the alignment subsystem. Once indicated, an initial static measurement of 10s is taken, of which the average value is considered the user's intended target throughout the experiment. Once determined, the user is asked to move the instrument away from the target, and – for manual cases - to unmount the instrument from the alignment subsystem. At this point, the user will move the instrument tip towards the intended target, and attempt to hold the target position to the best of their ability for 10 seconds. After this, the user moves the instrument away from the target to the starting position. This cycle is performed nine times during each experiment.

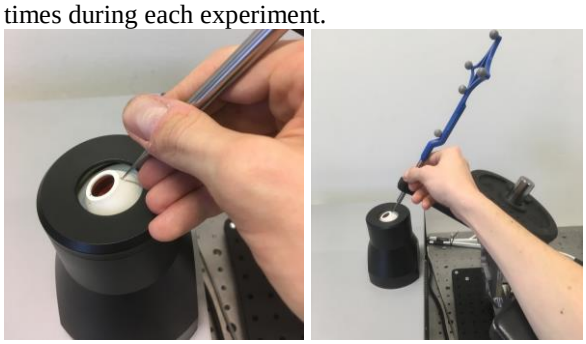

Fig. 3. Experimental validation during manual use with hand support (left) and cooperative use (right).

Data acquisition was done using a real-time optical pose-tracking system (fusionTrack 250, Atracsys) at 120 Hz, in combination with a commercially available blunt-probe instrument equipped with passive reflective spheres. For each cycle, the positional error is computed as the Euclidean distance between the actual user position and the initially declared target position. Relative point accuracy is determined per cycle as the average of the positional error.

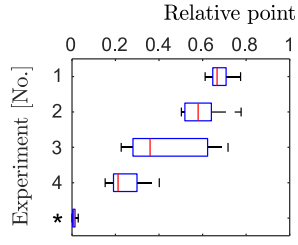

median	min	max
0.67	0.60	0.78
0.58	0.51	0.78
0.36	0.23	0.72
0.21	0.15	0.40
0.01	0.00	0.05

Fig. 4. Boxplots showing median and interquartile range of the relative point accuracy for each of the four cases and a 30s static measurement (left) and table with measurement data (right).

The described experiment is conducted for four cases: (1) manually-held instrument, with forearm support; (2) manually-held instrument, with forearm and hand support; (3) cooperatively-held instrument, no impedance control; (4) cooperatively-held instrument, with impedance control. Throughout the experiments, the user is seated in a surgical chair with configurable arm-rests. No additional means for visualization such as a camera or microscope are provided. As a preliminary analysis, a single trained user performed this campaign. A total of 36 datasets were collected (4 experiments, 9 cycles each). An additional measurement (*) of 30s with a static instrument was taken to determine static measurement noise.

DISCUSSION

The development of a novel 3-DOF impedance-type alignment subsystem is reported. The developed subsystem, when paired with an RCM subsystem, will enable more intuitive and versatile intraoperative RCM positioning. By doing so, surgical procedures requiring intentional eye rotations are feasible, thus increasing usage options of the surgical system in vitreoretinal surgery. Furthermore, this expansion will allow rendering of haptic guidance features for both instrument tip as surgical port locations. These guidance features are believed to further increase the usability and performance of the existing surgical system. An initial experimental validation of surgical port alignment accuracy was performed. Preliminary results suggest that the novel impedance-type alignment subsystem outperforms manual alignment. Furthermore, current data indicates equivalent or improved performance when compared to the prior admittance-type alignment system - ranging between 0.7 and 0.1 mm, with a median of 0.4 mm [4] - as static positioning is concerned. However, current data is collected without the presence of additional mechanical compliances due to the RCM subsystem and surgical table fixation, which could cause accuracy reduction. Further validation is required on surgical system level to confirm relative performance between the prior and novel alignment subsystem, as well as dynamic repositioning accuracy. Future work will focus on expanding the current experimental validation, the integration of the developed alignment subsystem with an RCM subsystem, and research on haptic fixtures.

ACKNOWLEDGEMENTS

Jonas Smits is funded by an SB Fellowship of the Research Foundation - Flanders (1S41517N). This research was funded by KU Leuven (3E160449).

REFERENCES

[1] A. Gijbels, J. Smits, L. Schoevaerdts, K. Willekens, E. B. Vander Poorten, P. Stalmans, and D. Reynaerts, "In-Human Robot-Assisted Retinal Vein Cannulation, A World First," *Ann. Biomed. Eng.*, vol. 46, no. 10, pp. 1676–1685, Oct. 2018.

[2] T. L. Edwards, K. Xue, H. C. M. Meenink, M. J. Beelen, G. J. L. Naus, M. P. Simunovic, M. Latasiewicz, A. D. Farmery, M. D. Smet, and R. E. Maclaren, "First-in-human study of the safety and viability of intraocular robotic surgery," *Nat. Biomed. Eng.*, vol. 2, no. September, 2018.

[3] J. Smits, A. Gijbels, K. Willekens, B. V. Stanzel, and D. Reynaerts, "Robot-Assisted Subretinal Surgery: initial in-vivo animal validation," in *Proceedings of the 11th Hamlyn Symposium on Medical Robotics*, 2018, pp. 91–92.

[4] A. Gijbels, K. Willekens, L. Esteveny, P. Stalmans, D. Reynaerts, and E. B. Vander Poorten, "Towards a clinically applicable robotic assistance system for retinal vein cannulation," in *6th IEEE International Conference on Biomedical Robotics and Biomechatronics (BioRob)*, 2016, pp. 284–291.

Robust laparoscope body calibration using hand-eye calibration methods

Chinmay Samant[1], Adlane Habed[1], Michel de Mathelin[1]

[1]*ICUBE, University of Strasbourg,*
samant@unistra.fr

INTRODUCTION

Ultrasound laparoscopes (US) are predominantly used in abdominal laparoscopic surgeries related to liver, pancreas and biliary tract. Despite being used in surgeries such as ablation procedures, they are harder to use for novice surgeons. The problem lies in understanding the proper orientation of the image with respect to the patient's body. Tracking the pose (position and orientation) of the laparoscope in real-time can address this problem. There are several solutions available [1,2,3] to this problem. All these solutions are based upon an Electromagnetic (EM) as well as optical pose tracker-based systems to track the pose of the US. In these methods, it is required to establish a chain of multiple transformations between the pose sensors. Some of them are fixed (do not change with the movement) and the rest are dynamic (change with a movement). The fixed transformations are between sensors which are mounted on the fixed part of the laparoscope as well as on the EM transmitters. The fixed transformations can be computed using 'Hand-Eye Calibration', as used in [1], which consists in estimating a fixed Euclidean transformation relating the reference frames of two rigidly attached sensors providing pose measurements. Since the EM sensors are constantly affected by different disturbances in the operation theatre, the measurements are often corrupted by noise and even worse, outlier data. Outliers are totally uncorrelated, non-synchronized measurements which together with the noise lead to faulty estimation of Hand-Eye Calibration. In this paper, we propose a robust method based on RANSAC [4] to get rid of the outlier data. We use a 'geometric' threshold for RANSAC based upon pixel error compared to the 'algebraic' one (in [8]). Due to this, we can comfortably find a value for the threshold for a wide range of datasets. We implement two state of the art methods in Hand-Eye calibration [5,6] in our RANSAC framework. In the results section, we compare the RANSAC implementations against the non-RANSAC versions of the methods.

BACKGROUND

- Magneto-Optic Hybrid Tracking:

In a typical setup of the hybrid tracking (as shown in [1]), a very thin wired EM receiver is mounted on the tip of a laparoscope. It has its paired transmitter in the vicinity. Minimum two optical tracking elements are required in this setup. They both are tracked using a camera system with a view of the laparoscope. First optical tracking element is mounted on the handle of the laparoscope and the second is mounted on the EM transmitter. In [1], they use additional EM receivers on the body of the laparoscope to estimate the transformation of the fixed body of the laparoscope. This is done by acquiring several poses of the EM sensors and optical trackers by moving the laparoscope in front of the camera and EM transmitter. The same poses are also used to compute the fixed calibration between the optical tracker on EM transmitter and the body of the EM transmitter itself. The poses are stacked into a system of equations which is used to solve the Hand-Eye Calibration.

- Hand-Eye Calibration:

The poses from the camera are stacked into A and the poses from EM sensor are stacked into B. They both are related to each other by a system of equation $AX = XB$. X is the fixed transformation. A , B and X are homogeneous transformations in $SE(3)$. Multiple recordings of A and B create an over-determined (with noisy data) system of equations. The data can also be infested with outliers especially if the data is recorded in an operation theatre with multiple sources of electromagnetic noises. We tested multiple methods of Hand-Eye calibration and selected [5,6] which are robust to the noise in the dataset. In [5], the authors use a locally optimal method to solve the problem and in [6], authors use a globally optimal method with quaternion parametrization of the rotation. We created a general RANSAC framework for Hand-Eye calibration in which these methods are incorporated.

METHOD

Our RANSAC algorithm works in following steps.

1. Choose *n* set of random samples from the dataset. In our case we select 4.
2. Compute Hand-Eye calibration using the methods [5,6]. Obtain the value of *X*.
3. Using X and Hand motions, transform all the calibrated camera motions into each camera motion one-by-one. Compute the average pixel error between the obtained camera motion and the transformed camera motion. Based on this 'geometric' threshold, determine the consistent inlier pairs eliminating the outliers.
4. Retain the largest inlier set.
5. After all the inliers are found, re-compute the Hand-Eye calibration using the largest inlier dataset.

EXPERIMENT AND RESULTS

We tested our algorithm extensively with synthetic as well as real dataset experiments. Due to the space constraints, we only present the results of the synthetic experiment with outlier infested dataset. The dataset is generated by creating random set of 3D points. 31 random camera motions are generated which capture the

3D points in each motion. A fixed calibration X is assumed (which is also the ground-truth) and 31 hand motions are created respectively. During the experiment, an increasing percentage of hand-motions are replaced with non-related wrong transformations to simulate outliers. We induce the outliers only in the hand-dataset since we believe that the EM sensors are mostly affected by them. We also introduce a nominal 0.5 Gaussian pixel noise on all the camera images, 0.01 absolute noise on quaternion transformations of hand dataset (as suggested in [7]) and 0.1% relative noise on the translation of the hand dataset. The probability value of the RANSAC is set to 0.99. Due to this, the RANSAC algorithm must find a solution if there are no time bounds, for any percentage of outliers in the dataset. But, in our experiments, we set a timer of 90 seconds after which the algorithm is forced-stop. Within this time our RANSAC algorithm finds a solution using at-least upto 50% of outlier infested dataset.

In the results, on the top, we show RMS of the errors in rotation unit quaternions $||q - q'||$ and in the middle, RMS of the relative errors in translation $\left|\left|t - t'\right|\right|/||t||$, where the q' and t' are the ground-truths. These are customary metrics used in [7] and other Hand-Eye calibration literature.

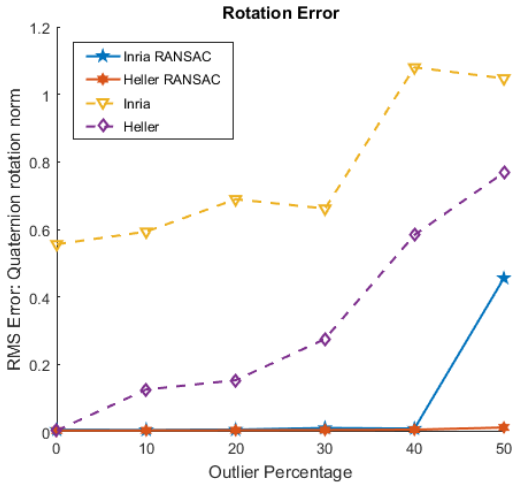

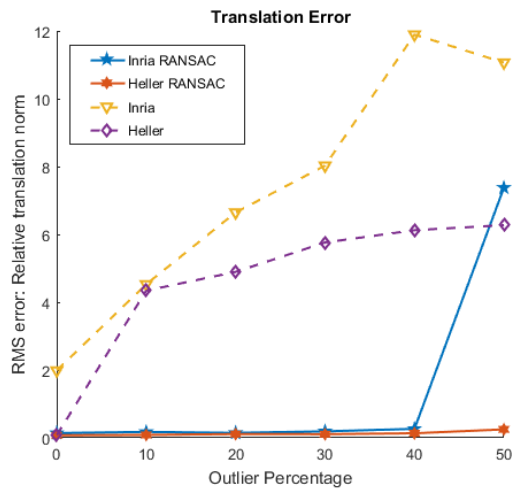

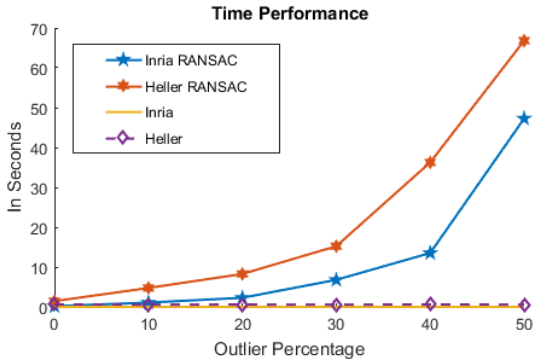

CONCLUSION AND DISCUSSION

In this paper, we presented a RANSAC framework for Hand-Eye calibration methods with a geometric threshold. Since the threshold is based upon pixel error compared to an algebraic error, it is easier to find a comfortable value for the threshold for a wide range of dataset. This framework can be used for any hand-eye calibration method with next to little modifications in the inputs to the methods. The presented results show that, the method can comfortably remove the outliers upto 50% within an acceptable computational time.

REFERENCES

[1] Feuerstein, Marco, et al. "Magneto-optic tracking of a flexible laparoscopic ultrasound transducer for laparoscope augmentation." International Conference on Medical Image Computing and Computer-Assisted Intervention. Springer, Berlin, Heidelberg, 2007.

[2] Nakamoto, Masahiko, et al. "3D ultrasound system using a magneto-optic hybrid tracker for augmented reality visualization in laparoscopic liver surgery." International Conference on Medical Image Computing and Computer-Assisted Intervention. Springer, Berlin, Heidelberg, 2002.

[3] Konishi, Kozo, et al. "A real-time navigation system for laparoscopic surgery based on three-dimensional ultrasound using magneto-optic hybrid tracking configuration." International Journal of Computer Assisted Radiology and Surgery 2.1 (2007): 1-10.

[4] Fischler, Martin A., and Robert C. Bolles. "Random sample consensus: a paradigm for model fitting with applications to image analysis and automated cartography." Communications of the ACM 24.6 (1981): 381-395.

[5] Horaud, Radu, and Fadi Dornaika. "Hand-eye calibration." The international journal of robotics research 14.3 (1995): 195-210.

[6] Heller, Jan, Didier Henrion, and Tomas Pajdla. "Hand-eye and robot-world calibration by global polynomial optimization." Robotics and Automation (ICRA), 2014 IEEE International Conference on. IEEE, 2014.

[7] Daniilidis, Konstantinos. "Hand-eye calibration using dual quaternions." The International Journal of Robotics Research 18.3 (1999): 286-298.

[8] Furrer, Fadri, et al. "Evaluation of combined time-offset estimation and hand-eye calibration on robotic datasets." Field and Service Robotics. Springer, Cham, 2018.

The design of a novel visual interface for the 3D steering of Programmable Bevel-Tip Needles (PBN) during Neurosurgery.

E. Matheson[1], R. Secoli[1], F. Rodriguez Y Baena[1]

[1]*Mechatronics in Medicine Lab, Dept. of Mechanical Engineering, Imperial College of London,*

f.rodriguez@imperial.ac.uk

INTRODUCTION

Percutaneous intervention has attracted significant interest in MIS development. In order to achieve more complex path trajectories, effort has been applied to the development of tools named flexible needles [1]. Needle designs in this category are able to successfully follow curvilinear paths to reach targets whilst avoiding critical areas. Image guidance technologies show promise for real-time navigation in 3D and steering accuracy. One common technique is to directly show the needle via MRI or ultrasound, however MRI requires significant mental effort to correlate slices to the 3D environment and requires an MRI compatible needle system. As well as this, the latency of generating MRI 3D volumes can be too high for real-time tracking of the needle [2]. Ultrasound images can also track needles in 3D [3], though they have a lower resolution than MRI, and ultrasound volumes also require mental effort from the operator to map the axes of the needle to the axes of the brain which may differ from the axes of the ultrasound view. A promising approach is to augment the imagery received from MRI or ultrasound in order to convey clearer visual information to the operator. This can be achieved with the use of overlays [4]. Inspiration for such designs can come from other areas of 3D robotic steering.

The main applications for human-machine interfaces towards 3D steering in the real world are applied to either Unmanned Aerial Vehicles (UAV) or Autonomous Underwater Vehicles (AUV), whereby a human operator still maintains some control authority. There are many existing interfaces, and some common characteristics. Such interfaces are designed to improve the situational awareness of the environment and the system [5]. The interface needs to be accurate, and often incorporates pre-mapped information as well as real-time imagery and updates. It is necessary to ensure the visual channel is not overloaded, as this can confuse the operator and lead to so called 'alarm fatigue'. Similar design guidelines can be considered to develop a medical steering application.

This paper presents work undertaken to develop a novel visual interface that allows a surgeon to intuitively control a programmable bevel-tip needle (PBN) capable of steering in 3D along a pre-defined path. The design of multiple visual interfaces are presented.

MATERIALS AND METHODS

The PBN system has been developed within the H2020 EDEN2020 project. The system has a shared controller design whereby the operator will use a haptic joystick and the visual interface to navigate the needle for convection enhanced drug delivery in neurosurgery at the target site. Positional feedback of the needle is provided by real-time US measurements fused with the MRI images, as well as by shape sensing sensors (via either ElectroMagnetic (EM) sensors or Fibre-Bragg Grating sensors (FBG)). The architecture is show in Fig 1.

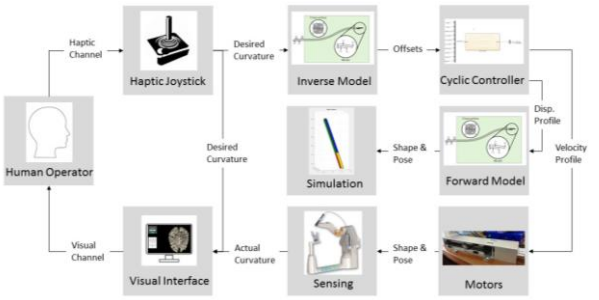

Figure. 1. EDEN2020 System Architecture. This paper focuses on the design of the Visual Interface

The final visual interface will be ported into the neuroinspire™ neurological planning software created by Renishaw. This will consist of four windows – the sagittal, axial and coronal views of the brain showing the real-time deformed MRI images, as well as a fourth window which will contain the graphical user interface (GUI) for 3D needle steering. The fourth window visual interface modalities for 3D needle steering tasks have been created with the Unity3D game engine.

MRI images of a patient are used to build a 3D arterial map. A pre-operative path planner [6] generates an optimal path for the surgeon to follow to reach the target that avoids all obstacles within a safe radius. The path the surgeon should follow, as well as the current and commanded status of the needle, can be visually depicted to the surgeon in multiple ways. The following visual cues for steering have been designed and implemented.

Method 1: Tunnel steering (Fig 3)– the operator remains in a 3D environment, passing through a tunnel of rings representing waypoints, whereby the diameter of the rings gives the operator an idea of the allowable error. The center of the tunnel represents the desired path, and the current position is indicated by a simulated needle tip. The Euclidean distance from the needle tip to the path nearest point (calculated via the KD nearest neighbor tree algorithm) is displayed.

Method 2: Tunnel steering with overlay– as in method 1, with the addition of two augmented overlays; the predicted needle curve based on the current joystick input (the 'commanded overlay'), and the curve the needle

would take based on in its current mechanical configuration (the 'actual overlay').

Method 3: Cross-hair steering (Fig 4) – the operator is given a 2D environment that abstracts the 3D path following task to a 2D space. They must aim a black cross-hair symbol (representing the current needle pose) at a moving green target cross-hair symbol (representing the desired needle pose). Any difference between the cross-hairs is the error in the respective curvature values as defined in the Bishop's frame of the needle (Fig 2).

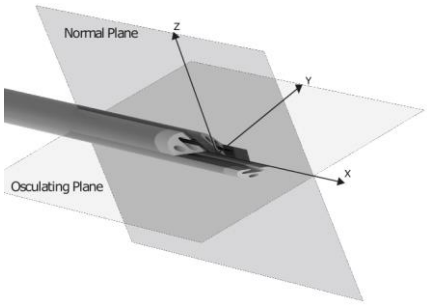

Figure. 2. PBN with an outer diameter of 2.5mm. The frame is defined at the needle tip, and is controlled via two curvatures, around Y and Z axes, with forward motion along the +ve X axis.

RESULTS

The majority of the EDEN2020 system architecture components run on a Linux GPU computer, with communication handled via the Robotic Operating System (ROS) protocols and nodes. Unity3D is a Windows software platform that uses C# or Java, and is not immediately compatible with ROS nodes. It is however necessary to regularly pass inputs such as the needle pose, array of path poses and overlay poses into the Unity interface during an insertion. For this, the Java ROS websocket plugin for Unity was used and extended to handle the ROS messages expected by our system. Communication packets are sent via UDP, ensuring that the minimum time delay is added by this porting procedure.

The MRI images are pre-processed in Slicer in order to segment the arterial tree, white matter and tumor tissue, which are then loaded into the interface before the insertion begins. For interface methods 1 and 2, the operator can choose to turn the white matter on and off, and zoom in and out of the arterial tree. The desired path is represented as a set of green waypoint rings, the diameter of which represents the safety zone used by the path planner when generating the path. The overlays are represented as blue (actual) and yellow (commanded) curves extending from the tip of the needle for method 2.

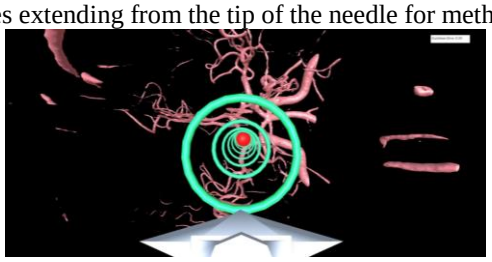

Figure 3: Method 1 interface (no overlays shown) in 3D

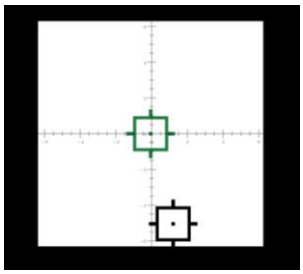

Figure 4: Method 3 interface with 2D crosshairs

Method 3 has been implemented as a separate view where the crosshairs are shown in Fig 4. The operator can also swap back to the arterial 3D tree/white matter view.

CONCLUSION AND DISCUSSION

Future work will focus on the evaluation of the visual interface with different user groups (non-medics, junior and senior surgeons). Evaluation will be undertaken via qualitative methods (Likert scale questions and the NASA Task Load Index analysis) and quantitative index measurements (path tracking error and task reaching performance).

This evaluation will first take place in simulation in order to remove effects of disturbances in the real system, and then using the real needle for insertions into phantom gelatin and ex vivo tissue. Haptic feedback will also be added to the visual user interface and evaluated for these trials.

REFERENCES

[1] Engh JA, Podnar G, Kondziolka D and Riviere CN, "Toward Effective Needle Steering in Brain Tissue," in International Conference of the IEEE Engineering in Medicine and Biology Society 2006; pp. 559-562.

[2] Ries M, de Senneville BD, Roujol S, Berber Y, Quesson B and Moonen C, "Real-time 3D target tracking in MRI guided focused ultrasound ablations in moving tissues". Magn. Reson. Med.; 2010; 64: 1704–1712.

[3] Fallahi,B, Rossa C, Sloboda RS, Usmani B, Tavakoli M, "Sliding-based image-guided 3D needle steering in soft tissue." Control Engineering Practice; 2017; pp. 34-43

[4] Cornud F, Bomers J, Futterer JJ, Ghai S, Reijnen JS, Tempany C. "MR imaging-guided prostate interventional imaging; Ready for a clinical use?"; Diagnostic and Interventional Imaging; 2018, pp. 743-753

[5] Yuan C, Recktenwald F and MallotcHA, "Visual steering of UAV in unknown environments," in IEEE/RSJ International Conference on Intelligent Robots and Systems 2009; pp. 3906-3911.

[6] Pinzi M, Galvan S, Rodriguez y Baena F. "The adaptive Hermite fractal tree (AHFT). Accepted to International Journal of Computer Assisted Radiology and Surgery, expected publication 2019

MEMS varifocal mirror for high-power laser focusing in endoscopic laser surgery

A.A. Geraldes[1,2], P. Fiorini[2], L.S. Mattos[1]

[1]*Istituto Italiano di Tecnologia, Italy*

[2]*University of Verona, Italy*
andre.geraldes@iit.it

INTRODUCTION

Today, lasers are used in many surgical interventions due to their ability of performing precise incisions and ablations. This allows surgeons to preserve more healthy tissue, which can be critical for the patient, especially in microsurgical procedures. For example, in vocal cord tumor resection, even 1 mm of additionally resected tissue can result in permanent vocal impairment [1]. Besides that, lasers possess the unique ability to cauterize small blood vessels while cutting, which reduces bleeding during the operation. This avoids complications and increases the safety and performance of the procedure.

One of the main disadvantages of laser tools, however, is that the target site must be accessed by a straight-line trajectory. This poses accessibility issues, especially when the area to be operated cannot be properly exposed. With the development of fiber-coupled lasers, endoscopic laser systems have been proposed, allowing to deliver the laser closer to the target site. These endoscopes provide improved visualization of the surgical site, while expanding the applicability of laser tools to minimally invasive procedures.

In order to ensure the precision of the cut, the laser beam must be focused at the target tissue. However, adjustable focusing systems based on moving lenses are too large and bulky to be integrated in an endoscopic setup. For this reason, fiber laser systems typically have no focusing optics and require the fiber to be in direct contact with the tissue. This ablation method decreases the precision of the cut and results in excessive thermal damage to the surrounding tissue, often leading to tissue carbonization [2]. To avoid these issues, a compact focusing unit would be necessary.

Instead of miniaturizing standard focusing units, a different approach can be obtained with adaptive optical elements, such as varifocal mirrors. Varifocal mirrors are mirrors whose curvature can be dynamically controlled in order to change the focal length of the laser beam, without physical displacement, On the last decade, several types of MEMS varifocal mirrors have been proposed for imaging systems [3], however until now, this technology has not been used for controlling high-power laser systems. In this work we propose a MEMS varifocal mirror designed for an endoscopic laser system, as illustrated in Fig. 1.

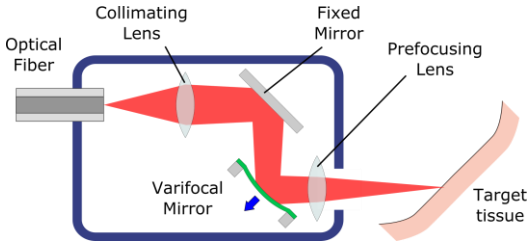

Figure. 1. Proposed focusing system with variable focal length, based on a MEMS varifocal mirror.

MATERIALS AND METHODS

The proposed varifocal mirror was designed to withstand a continuous CO_2 laser beam with 3W of power. To achieve that, the mirror was designed with large aperture (4 mm), to allow reducing the power density of the laser over the mirror. To achieve large deflection, even with a large aperture, hydraulic actuation was used, which also helps cooling the mirror.

Fig. 2 shows the conceptual design of our MEMS varifocal mirror with hydraulic actuation. The mirror consists of a freestanding flexible membrane and a fluidic chamber. The fluidic chamber is connected to a microinjection system through a microfluidic channel, which allows applying positive or negative pressure to the membrane, deflecting it in concave or convex direction. Since the pressure applied to the membrane is uniform, the mirror deflection is parabolic, which allows focusing the laser beam without inducing optical aberrations.

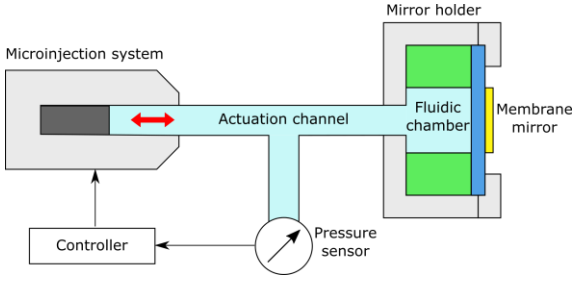

Figure. 2. Design of MEMS varifocal mirror with hydraulic actuation.

We fabricated the MEMS varifocal mirrors from silicon wafers, using a clean room facility. The microfabrication process consisted on depositing the membrane layer, etching the silicon bulk to release the membrane and create the fluidic chamber and coating the membrane with a reflective coating. The membrane used here was a

low-stress silicon nitride film with 500 nm of thickness. Since the fluidic chamber must be sealed, the silicon bulk was etched from the back side, using a combination of deep reactive ion etching and wet etching. The coating applied was a 200 nm layer of gold, deposited with a lift-off process.

RESULTS

To characterize the fabricated varifocal mirror, we irradiated it with a 10 mW probe beam and analyzed the reflected beam using a Shack-Hartmann wavefront sensor. This measurement method is convenient as the wavefront sensor can measure the focal length of the beam as well as its optical aberrations. However, one limitation of this method is that the wavefront sensor cannot analyze the beam if its focal point is too close to the imaging plane of the sensor. Therefore, there is a pressure range for which no measurements can be obtained. To avoid this problem, we performed two experiments, with and without a prefocusing lens between the mirror and the sensor. The prefocusing lens shifts the range of pressures that result in invalid measurements, allowing us to fully characterize the mirror.

Fig. 3 shows the optical power of the mirror (P_M) as a function of the applied pressure (Δp), with and without the prefocusing lens. As we can see, the optical power of the mirror changed from -28 to 31 m^{-1}, for a pressure range of ± 5 kPa. This optical power range can shift the focal length of the reflected laser beam from 9.5 to 140 mm, if a prefocusing lens with focal length of 40 mm is used. The experimental results without the prefocusing lens were fitted to the membrane deflection model [4], given by $\Delta p = A + BP_M + CP_M{}^3$. The obtained RMSE was 0.43 m^{-1}. The results with the prefocusing lens were more noisy, especially for pressure values above 4 kPa, due to improper alignment between the mirror and the prefocusing lens.

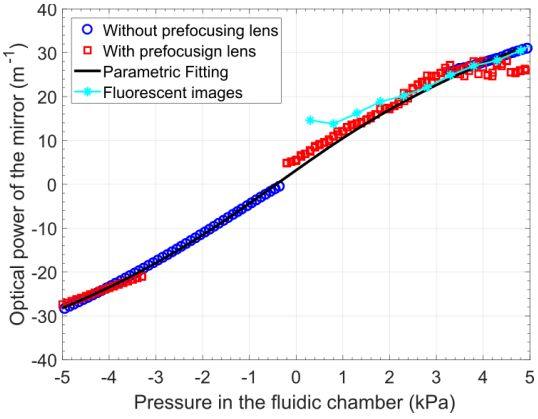

Figure. 3. Static characterization of the fabricated mirror.

To verify the focusing capability of the system, we performed a focusing demo, by replacing the wavefront sensor with a cuvette containing a solution of fluorescein in water. Fig. 4 shows some pictures of the probe beam propagating through the fluorescent medium for different values of actuation pressure. The focal point of each beam (indicated by a vertical yellow line) has been identified as the point where the beam diameter was minimal. These measurements performed on the fluorescent images are also indicated in Fig. 3. As it can be seen, there is a good agreement between the measurements of the wavefront sensor and the fluorescent images, except for the low-pressure values. However, at these points the beam is almost collimated, which makes it difficult to identify the focal point in the fluorescent images correctly, as the variation of the beam diameter around the focal point is in the order of the pixel resolution of the image.

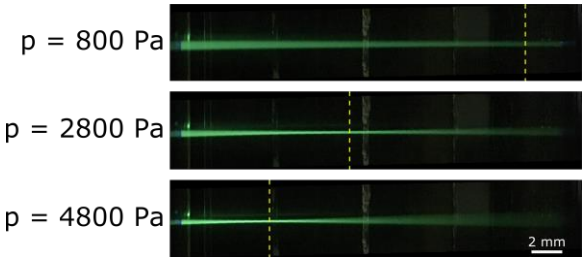

Figure. 4. Focusing of a laser beam in fluorescent medium using the varifocal mirror.

CONCLUSION AND DISCUSSION

In this paper, we presented a MEMS varifocal mirror with hydraulic actuation for focusing a high-power laser beam in an endoscopic laser system. The optical power range of the mirror is almost 60 m^{-1}, which can provide a focal length range from 9.5 to 140 mm. This optical power range is much higher than the one obtained with electrostatic mirrors of similar size for imaging applications (around 20 m^{-1}). The obtained deflection of the mirror was well described by the mirror deflection model, although the alignment between the mirror and the prefocusing lens needs to be improved to increase the precision of the mirror deflection.

REFERENCES

[1] Rubinstein M, Armstrong WB. "Transoral laser microsurgery for laryngeal cancer: a primer and review of laser dosimetry" Lasers in medical science 26.1 (2011): 113-124.

[2] Acemoglu A, Mattos LS. "Non-Contact Tissue Ablations with High-Speed Laser Scanning in Endoscopic Laser Microsurgery." 2018 40th Annual Int Conf of the IEEE Engineering in Medicine and Biology Society (EMBC). IEEE, 2018.

[3] Dickensheets DL. "Requirements of MEMS membrane mirrors for focus adjustment and aberration correction in endoscopic confocal and optical coherence tomography imaging instruments." Journal of Micro/Nanolithography, MEMS, and MOEMS 7.2 (2008): 021008.

[4] Geraldes A, Jacassi A, Fiorini P, Mattos LS. "Large-Stroke Varifocal Mirror with Hydraulic Actuation for Endoscopic Laser Surgery." 2018 7th IEEE International Conference on Biomedical Robotics and Biomechatronics (Biorob). IEEE, 2018.

Momentum-based collision detection algorithm for a biphasic media variable stiffness actuator

J.H. Lugo, M. Zoppi, R. Molfino

PMAR Robotics Group, University of Genoa
lugocalles@dimec.unige.it

INTRODUCTION

Industrial collaborative robots and service assistant robots must be flexible and versatile to help humans in complex and demanding tasks [1]. Variable stiffness actuators (VSA) are used to improve safety and performance in physical human-robot interaction (pHRI) [2]. This protection is extended to unintended interactions due to hardware failure, limitations on perception and cognition [3]. Handling of collisions is one of the main objectives in pHRI because of the possibility of damaging humans, the environment or the robot itself. Collision detection is a phase, where an algorithm is fed with specific sensor's data and a binary output denoting the occurrence of a collision is given [1]. To avoid false positives and achieve high sensitivity an appropriate threshold on the monitoring signals must be tuned according to the current robot's task. This abstract presents the application of a momentum-based collision detection algorithm (MBCDA) introduced in [1], on a biphasic media variable stiffness actuator (BMVSA). Simulations of the system were performed to demonstrate the feasibility of the algorithm.

MATERIALS AND METHODS

BMVSA has been studied, developed and manufactured in [3-6]. This technology uses pneumatic and hydraulic components, as shown in Fig. 1. The gas fraction works as nonlinear elastic element (Nitrogen), providing variation of stiffness in the system due to pressure gas changes, while the liquid one is assumed incompressible and used to provide pressure changes and motion to the output link (hydraulic oil). To keep high modularity, hydropneumatic accumulators (HPA) are used to seclude the gas. The major implementations of the system are industrial grippers for garment handling, suspension systems and surgical robotics concepts. BMVSA is modeled as a damped harmonic oscillator as shown in (1), where m is the mass of the output link of the actuator, x_p is the displacement of the piston, k_v is the coefficient of viscosity, F_p is the force generated by the difference of pressures P_1 and P_2 applied on the piston's head surface S, as display in (2), and F is the external force applied, which resembles the load on the actuator.

$$m\ddot{x}_p + k_v\dot{x}_p - F_p = F \tag{1}$$

$$F_p = (P_1 - P_2)S \tag{2}$$

Considering a uniform temperature in the system, the gas constant definitions are defined in (3) and (4), where V_{ai} represents the added/subtracted volume of fluid volume in the system's chambers.

$$C_1 = P_1\left(v_1(0) - v_{a1} - Sx_p\right) \tag{3}$$

$$C_2 = P_2\left(v_2(0) - v_{a2} + Sx_p\right) \tag{4}$$

If pressures in HPAs are the same, the gas constant can be taken as equal for both sides ($C_1 = C_2 = C$).

$$F_p = SC\left(\frac{1}{v_1} - \frac{1}{v_2}\right) \tag{5}$$

The instantaneous stiffness K of the actuator is the derivative of force generated by the difference of pressures in the cylinder with respect to displacement.

$$K = \frac{\partial F_p}{\partial x_p} = \frac{S^2}{C}\left({P_1}^2 + {P_2}^2\right) \tag{6}$$

If fluid is added to both chambers, the volume of gas reduces and the pressure in both chambers increases, increasing the stiffness. Similarly, if fluid is subtracted from both chambers, the volume of gas increases and the pressure in both chambers reduces, reducing the stiffness.

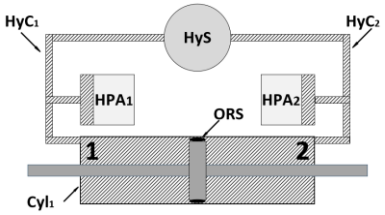

Figure. 1. BMVSA diagram. The actuator is composed of a double acting hydraulic cylinder (Cyl_1) connected to a hydraulic circuit. This circuit includes a supply and distribution system (HyS) and two hydraulic distribution lines (HyC_1) and (HyC_2) respectively connected to cylinder's chambers and insulated HPAs (AC1 and AC2). O-ring type seals (ORS) provide translation of piston without leakage. The oil is represented as the mesh while the Nitrogen is light grey.

Proprioceptive sensors for position and pressures are used during the process. Several types of control laws have been implemented regarding the position and stiffness of BMVSA [4,5]. These controllers work fine for a small working range (dual-coupled PID) or are computationally expensive (fuzzy control). An efficient model-based controller (MBC) was developed in [6], it is characterized of allowing the user to prioritize the stiffness or position tracking by means controlling the flow of liquid in the BMVSA chambers, see Fig. 2.

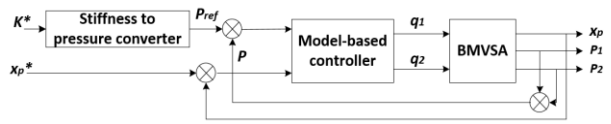

Figure. 2. Model-based controller diagram. The usual method to control position is performed by controlling the pressures in both chambers; hence, movement is done whenever the pressures are different. The approach for the stiffness is similar but it is related to the amount of pressure in each chamber: the higher the pressure, the higher the stiffness, and vice versa.

Based on the work done in [1,2], an actuator level abstraction of moment-based collision detector is implemented for BMVSA, as shown in (7). This approach does not require the computation of accelerations and is able to detect collisions even when the velocity is zero. Another advantage of this method is that no extra sensors are required, the only needed quantities are x_p and P_i.

$$p(t) = (m)\left(\dot{x}_p(t)\right) \tag{7}$$

The monitoring signal r is the residual of the momentum and it is described in (8). K_I is a design parameter that allows r to closely follow the external disturbance (F).

$$r = K_I\left(p(t) - \int\left(F_p + r\right)dt - p(0)\right) \tag{8}$$

After r is computed, its absolute value is compared with a predefined threshold in order to indicate the existance of collisions.

RESULTS

The following simulation was performed to study the MBCDA during a position and trajectory tracking task, these values correspond to design parameters used to develop a prototype. A model-based controller, tuned for stiffness tracking, priority is used. The simulated parameters are: (i) a cylinder of 0.15 m, (ii) K_v = *0.5 Ns/m*, (iii) *C= 300 Pam*^{3}, (iv) *xp (0)=0 m*, (v) *vi (0) =1.5x10*$^{-4}$ *m*^{3}, (vi) K_i*=125 s*$^{-1}$, and (vii) $r_{threshold}$*=30*. The external forces are displayed in Fig. 3. It is worth to note that the disturbances differ in magnitude and duration., and that position is measured from left end of the cylinder. The desired position is given as a sinusoidal signal with *0.05 m* amplitude and baseline on *0.075 m* at *1 Hz*, while the desired stiffness is a sinusoidal signal with *2.5x104 N/m* amplitude and baseline on *5x104 N/m* at *1 Hz*.

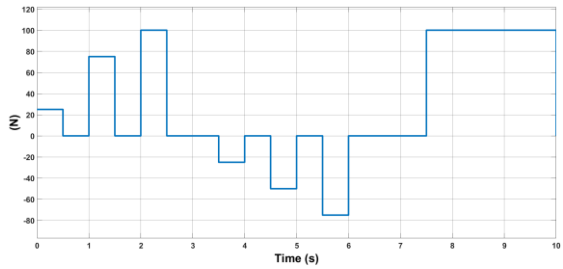

Figure. 3. External forces during the process.

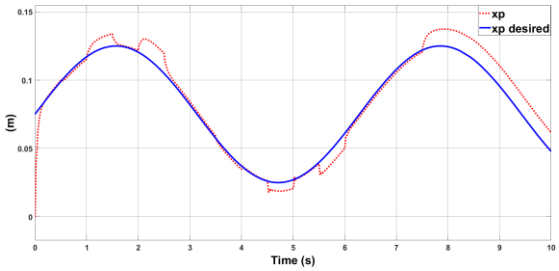

Figure. 4. Position tracking in time. The reference trajectory (blue) is reached when there is no disturbance.

The results of the simulations prove that MBC can properly track position and stiffness even when disturbances affect the system, as shown in Figs. 3, 4, and 5. The MBCDA effectively detected all the collision events whenever the absolute value of the residual overcomes to the predefined threshold.

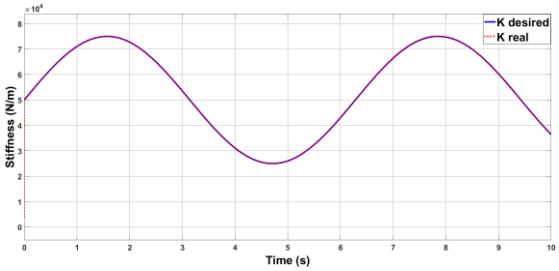

Figure. 5. Stiffness tracking in time. The reference trajectory (blue) is reached by K during the whole process due to its priority in the controller.

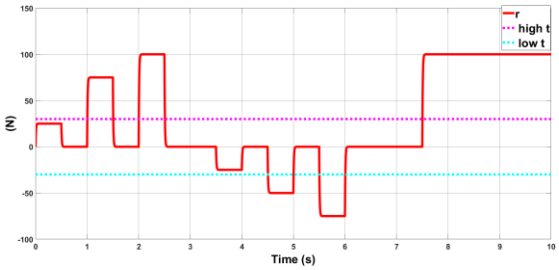

Figure. 6. Residual graph. The residual (red) accurately tracks the disturbances shown in Fig. 4. The threshold is shown as two symmetrical dotted parallel lines (pink and blue). Only the two disturbances that are between the threshold lines are not detected as collisions.

CONCLUSION AND DISCUSSION

MBCDA is a light-computing and efficient collision detector that makes use of the available sensors of BMVSA. It is important to note the high impact of tuning of K_i and selecting $r_{threshold}$. Several thresholds can be established to classify the detected external force. Currently, MBCDA is being tested on a prototype with positive results. For future work, collision classification and reaction algorithms will be implemented to ensure safety during pHRI.

REFERENCES

[1] S. Haddadin, A. De Luca and A. Albu-Schäffer, "Robot Collisions: A Survey on Detection, Isolation, and Identification," in IEEE Transactions

on Robotics, vol. 33, no. 6, pp. 1292-1312, Dec. 2017.
[2] A. De Luca, F. Flacco, A. Bicchi and R. Schiavi, "Nonlinear decoupled motion-stiffness control and collision detection/reaction for the VSA-II variable stiffness device," 2009 IEEE/RSJ International Conference on Intelligent Robots and Systems, St. Louis, MO, 2009, pp. 5487-5494.
[3] M. Zoppi, "Method for adapting stiffness in a variable stiffness actuator," US Patent 8-991-169, March 31, 2015.
[4] B. Han, M. Zoppi, and R. Molfino, "Variable impedance actuation using biphasic media," Mechanism and Machine Theory, vol. 62, pp. 1-12, 2013.
[5] B. Han, "Variable impedance actuation using biphasic media," Ph.D. Thesis dissertation, University of Genoa, 2013.
[6] J.H. Lugo, G. Cannata, M. Zoppi, and R. Molfino, "Modeling and Simulation of a Biphasic Media Variable Stiffness Actuator," International Journal of Mechanical Engineering and Robotics Research, to be published.

CBCT reconstruction based on arbitrary trajectories using TIGRE software tool

S. Hatamikia[1,2], A. Biguri[3], G. Kronreif [1], J. Kettenbach[4], W. Birkfellner[2]

[1]*Austrian Center for Medical Innovation and Technology, Wiener Neustadt, Austria*

[2]*Center for Medical Physics and Biomedical Engineering, Medical University of Vienna, Austria*

[3]*Institute of Sound and Vibration Research, University of Southampton, United Kingdom*

[4]*Department of Diagnostic and Interventional Radiology and Nuclear Medicine, Wiener Neustadt, Austria*

INTRODUCTION

Nowadays, cone beam CT (CBCT) image guidance has turned into a widespread clinical routine imaging modality in interventional and therapeutic procedures. In conventional CBCT, a circular source-detector trajectory is used to acquire a high number of 2D projections in order to reconstruct a 3D volume. However, this standard methodology has some limitations. Repetitive intraoperative 3D scans are often needed during surgery, and in complex interventions surgical or interventional devices hamper access to the patient. Here, imaging can be problematic due to the geometric constraints related to the imaging device, patient positioning table and operating room. In addition, a high number of projections is needed for adequate 3D reconstruction based on such a circular trajectory which causes a lot of radiation dose to the patient. Therefore, it is desirable to have some optimized source-detector trajectories with arbitrary orientation and minimal number of projections. Such trajectories are easier to apply in the surgery room and will give less radiation dose to the patient. CBCT reconstruction based on general source-detector trajectories is also interesting for other various applications. For example, target-based CBCT reconstruction is interesting as it gives us the opportunity to have an appropriate reconstruction at a particular region of interest. Such a target-based CBCT reconstruction requires source-detector trajectories which are beyond the standard circular imaging method. In [1,2] some trajectories with arbitrary orbital tilt as well as non-circular trajectories are introduced in order to perform task-driven CBCT imaging. Several other non-circular trajectories have been proposed in the literature to overcome the drawbacks of circular trajectories [3,4]. Furthermore, there is another limitation regarding the imaging geometry of CBCT devices for circular trajectories: the working volume of such a device is limited given the currently available x-ray detectors and is always at the center of rotation of the device. By abandoning the necessity of a fixed isocenter using a non-isocentric CBCT reconstruction, we can extend the size of the working volume and also perform the reconstruction for the areas which are not necessarily at the center of rotation. Tomosynthesis devices utilize these geometries in a limited fashion. Therefore, applying a non-isocentric CBCT reconstruction for such an applications can cause big benefits. Based on the knowledge of the authors, there is no open source CBCT reconstruction able to perform arbitrary trajectories and do reconstruction based on such trajectories. Thus, it is rewarding to provide an open source platform for researchers able to perform CBCT reconstruction based on variety of arbitrary source-detector trajectories, which can also be non-isocentric. This article shows a modification of the open source Tomographic Iterative GPU-based Reconstruction (TIGRE) Toolbox [5] to perform reconstruction from cone-beam projection images which were acquired at arbitrary orientations and positions.

MATERIALS AND METHODS

The TIGRE Toolbox is a free open source toolkit which allows fast reconstruction of CBCT geometries. It is a MATLAB-CUDA toolbox in which the forward and backward projections are implemented in CUDA, making use of fast calculations from the graphics processing unit (GPU) and the reconstruction algorithms are implemented in MATLAB. In this study, we modified TIGRE to perform arbitrary trajectories.

In order to properly specify a source-detector arbitrary rotation based on Euler angles we needed to follow some conventions as described in [6]. We modified the TIGRE CUDA codes related to forward and backward projections and implemented the Z-Y-Z convention to calculate an intrinsic rotation matrix as bellow:

$$Rot(z,\varphi z).Rot(y,\theta y).Rot(z,\psi z), \quad (1)$$

$$\begin{bmatrix} c\varphi_z c\theta_y c\psi_z - s\varphi_z s\psi_z & -c\varphi_z c\theta_y s\psi_z - s\varphi_z c\psi_z & c\varphi_z s\theta_y & 0 \\ s\varphi_z c\theta_y c\psi_z + c\varphi_z s\psi_z & -s\varphi_z c\theta_y s\psi_z + c\varphi_z c\psi_z & s\varphi_z s\theta_y & 0 \\ -s\theta_y c\psi_z & s\theta_y s\psi_z & c\theta_y & 0 \\ 0 & 0 & 0 & 1 \end{bmatrix}$$

where *c* and *s* represent *cos* and *sin* respectively.

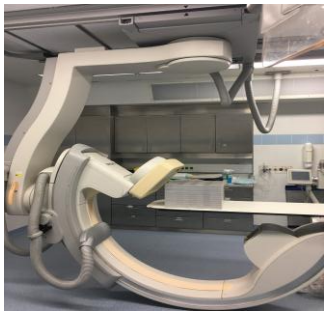

Figure. 1. Philips Allura FD20 Xper C-arm located at Department of Diagnostic and Interventional Radiology and Nuclear Medicine,Wiener Neustadt, Austria.

RESULTS

We made some experiments in order to investigate the ability of the modified codes to perform reconstruction based on arbitrary trajectories. We used an Alderson head phantom in our experiments. A Philips Allura FD20 Xper C-arm (Fig.1) was used to acquire projections by applying a sample arbitrary trajectory. We employed an image set including 264 projections at different arbitrary orientations and translations using the C-arm device. We also used a CT scan of the head phantom and used this as a digital phantom. We used this digital phantom to verify the modified software as the first standard verification step. Afterward, we also verified the modified software experimentally based on real data. We performed some simulations on the head digital phantom to acquire synthetic image projection with the same applied orientations and translations as the real data. Some examples of projections for both real and simulation data are shown in Fig.2. We investigated the reconstructed results based on the employed arbitrary trajectory for both simulated and real data. We used Adaptive-Steepest-Descent-Projection-Onto-Convex-Sets (ASD-POCS) algorithm implemented in TIGRE for CBCT reconstruction. We illustrate the results of the reconstruction for both real and simulation data as well as a standard CBCT as a ground truth in Fig.3. Our reconstruction results as shown in Fig.3 show the ability of TIGRE to successfully reconstruct images based on the arbitrary trajectory for both simulation and real data. We used Normalized-Root-Mean-Square-Error (NRMSE) to evaluate the result of reconstruction. The value of 0.28 was achieved for NRMSE between the real data reconstructed volume and the standard CBCT volume. This value was achieved for our sample trajectory and lower values of NRMSE are expected for more optimal arbitrary trajectories.

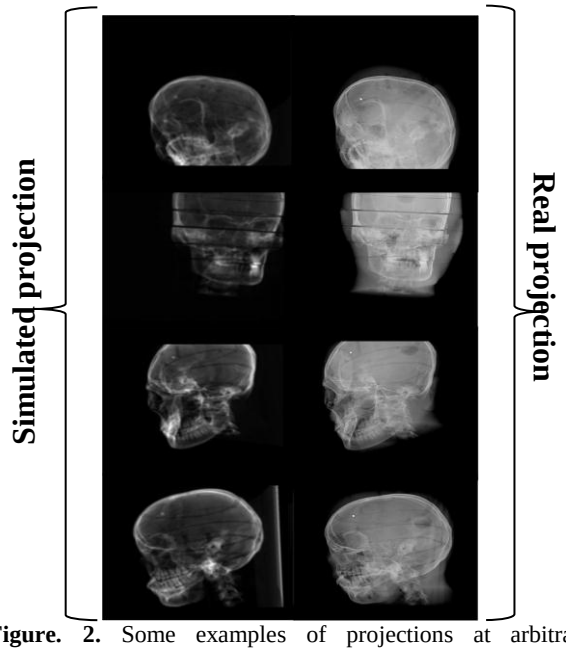

Figure. 2. Some examples of projections at arbitrary orientations and positions. Simulated projections (Left), Real data projections (Right).

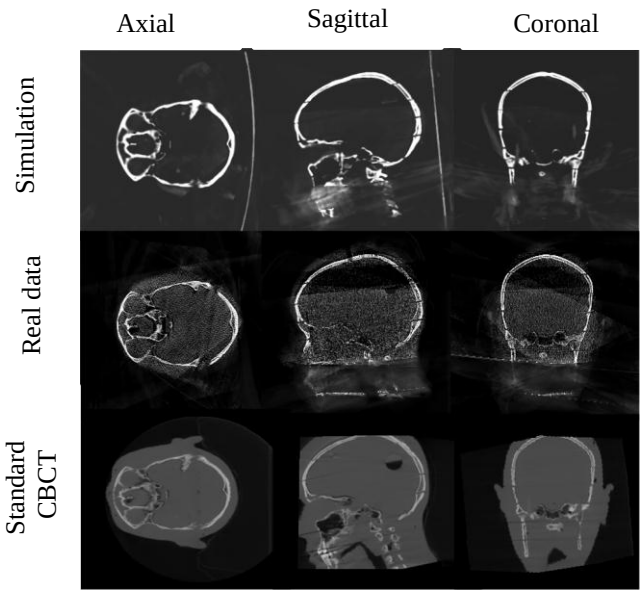

Figure. 3. Reconstruction Results related to the simulation (First row), real data (Second row) for sample arbitrary trajectory. Head phantom CBCT CT (Third row) for standard circular trajectory.

CONCLUSION AND DISCUSSION

We successfully modified TIGRE software tool to perform reconstruction based on arbitrary trajectories. We released the resulted codes freely available at https://github.com/CERN/TIGRE/releases/tag/v1.3.
This work opens new possibilities for free, fast and reliable reconstruction algorithms based on variety of arbitrary/non-isocentric trajectories to other research groups.

ACKNOWLEDGEMENT

This work has been supported by ACMIT – Austrian Center for Medical Innovation and Technology, which is funded within the scope of the COMET program and funded by Austrian BMVIT and BMWFW and the governments of Lower Austria and Tyrol. We also gratefully acknowledge the support of NVIDIA Corporation for the donation of Titan Xp GPU used for this research.

REFERENCES

[1] Gang GJ, et al. "Task driven image acquisition and reconstruction in Cone beam CT" Phys. Med. Biol. 2015; 60(8): 3129-3150.

[2] Ouadah S, et al. "Task-Driven Orbit Design and Implementation on a Robotic C-Arm System for Cone Beam CT" Proc SPIE Int Soc Opt Eng. 2017 March; 10132.

[3] Jacobson MW, et all. "A line fiducial method for geometric calibration of cone-beam CT systems with diverse scan trajectories" Phys. Med. Biol. 2018; (63): 025030.

[4] Erik A, et al. "Non-circular cone beam CT trajectories: A preliminary investigation on a clinical scanner" IEEE Nuclear Science Symposium & Medical Imaging Conference. 2010 October; 12061132.

[5] Biguri et al., "TIGRE: a MATLAB-GPU toolbox for CBCT image reconstruction," Biomed. Phys. Eng. Express, 2016; (2): 1-10.

[6] Mathworld.wolfram.com/EulerAngles.html

CRAS+SPIGC 2019 Support

ISTITUTO ITALIANO
DI TECNOLOGIA

UNIVERSITÀ DEGLI STUDI
DI GENOVA

OSPEDALE POLICLINICO
SAN MARTINO

REGIONE LIGURIA

ORDINE PROVINCIALE
DEI MEDICI CHIRURGHI
E DEGLI ODONTOIATRI
GENOVA

CRAS
Joint Workshop on Computer/Robot Assisted Surgery

SOCIETÀ POLISPECIALISTICA ITALIANA
DEI GIOVANI CHIRURGHI

ISBN 9789491857041

CRAS 2019

Proceedings of the 9th Joint Workshop on New Technologies for Computer/Robot Assisted Surgery